DTU Physics
Department of Physics

Jacob S. Bach

Theory of acoustic fields and streaming with viscous boundary layers in microsystems

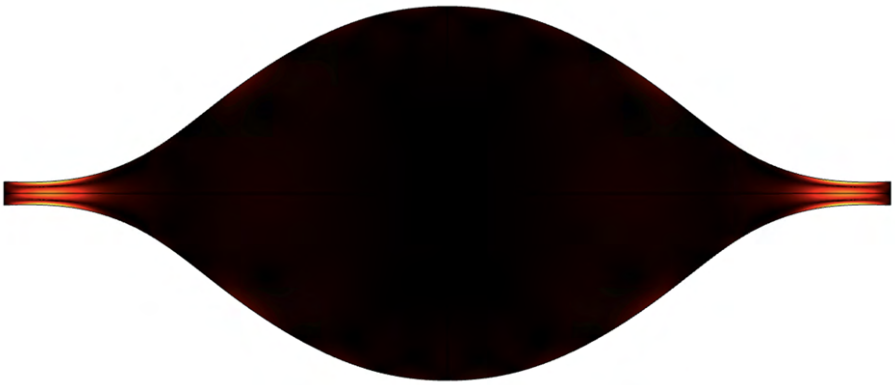

PhD thesis
Copenhagen, 29 February 2020

Advised by Professor Henrik Bruus

Cover illustration: Simulation result of acoustic streaming in the cross section of a microchannel. The theory developed in the theses lead to this peculiar cross-section shape where the streaming is dramatically suppressed, see paper V of the thesis.

Theory of acoustic fields and streaming with viscous boundary layers in microsystems

Typeset using LaTeX.

Department of Physics
Technical University of Denmark
DTU Physics Building 309, DK-2800 Kongens Lyngby, Denmark
http://www.fysik.dtu.dk/microfluidics

Abstract

When a fluid oscillates acoustically, non-linear time-averaged forces are exerted both on a given particle suspended in the fluid and on the fluid itself. The latter effect gives rise to a steady motion of the fluid, called acoustic streaming, which causes an additional force on the suspended particle in the form of viscous drag. The resulting particle motion due to an acoustic field is called acoustophoresis, and it is extensively exploited in the field of acoustofluidics for controlled handling of biological microparticles in water-filled microsystems actuated by ultrasound frequencies. A central phenomenon in these devices is the micrometer-thin viscous boundary layer forming close to a solid wall, where the fluid motion adapts to the solid motion. This boundary layer play an essential role for both viscous dissipation and for the generation of the so-called boundary-driven acoustic streaming.

In this thesis, a theory for the viscous boundary layer is developed, which extends the current boundary-layer theories of the literature in two major perspectives: First, a boundary condition on the oscillating acoustic pressure is derived, which take into account the viscous dissipation in the boundary layer. Second, the well-known slip condition on the acoustic streaming is extended to apply for a curved wall that oscillates in any direction. The derived boundary conditions constitute the so-called "*effective model*" for calculations of acoustic fields and streaming in arbitrary geometries where the boundary layer is taken into account analytically. From a numerical point of view, the effective model leads to drastic reductions in the memory requirements thus facilitating larger 3-dimensional simulations.

Inspired by reported experimental observations of acoustic streaming in closed resonating cavities, the phenomenon of bulk-driven acoustic streaming is investigated theoretically. Bulk-driven acoustic streaming is often ignored in acoustofluidic devices having length scales comparable to the acoustic wavelength. Here, it is found that bulk-driven streaming can play an essential role in such systems if the acoustic motion is rotating. Remarkably, this rotation may be induced unexpectedly even though the actuation is not rotating. Therefore, a central message of this thesis is, that bulk-driven streaming should not be ignored neither in the understanding nor in the calculations of resonating acoustofluidic devices. In this thesis, a general length-scale condition for ignoring bulk-driven streaming is provided, which is rarely satisfied in acoustofluidic systems.

Acoustic trapping in capillary tubes is a promising application of acoustofludics which has mainly been studied experimentally. Using the effective boundary conditions for the viscous boundary layer, the acoustic fields and radiation force in long straight capillary

tubes of arbitrary cross section are calculated. The analysis leads to an analytical expression for the axial radiation force and an optimal axial actuation length for the acoustic trap.

Finally, due to the effective boundary-layer model, it is possible to calculate the acoustic streaming sufficiently fast so that many different channel shapes can be examined. This advantage is exploited in an iterative algorithm that optimizes the channel shape in order to suppress acoustic streaming. The resulting optimized shape is shown on the front page of this thesis, and the corresponding streaming is suppressed by two orders of magnitude relative to conventional rectangular channels. The numerically proposed shape may allow for controlled handling of sub-micron particles by use of acoustophoresis, and as such, this final result has promising perspectives for further experimental research.

Resumé

Når en væske svinger akustisk, vil ulineære, tidsmidlede kræfter påvirke både en given partikel i væsken men også væsken selv. Den sidstnævnte effekt giver anledning til en jævn væskebevægelse, kaldet akustisk strømning, som medfører en yderligere kraft på partiklen på grund af viskøs gnidningsmodstand. Den resulterende partikelbevægelse foresaget af et akustiske felt kaldes akustoforese, og denne effekt udnyttes i vid udstrækning inden for feltet acoustofluidik, til at håndtere biologiske mikropartikler i væskefyldte mikrosystemer aktueret med ultralyd frekvenser. Et centralt fænomen i disse systemer er det mikrometertynde viskøse randlag som opstår tæt ved en væg, hvor væskebevægelsen tilpasser sig til vægbevægelsen. Dette randlag er af afgørende betydning både for viskøs dissipation og for genereringen af akustisk strømning.

I denne afhandling udarbejdes først en teori for det viskøse randlag, som videreudvikler eksisterende randlagsteorier på to afgørende måder: For det første udledes en randbetingelse for det akustiske tryk, som tager højde for den viskøse dissipation i randlaget. For det andet udvides den velkendte sliphastighedsbetingelse for den akustiske strømning til at gælde for en krum væg, som svinger i en hvilken som helst retning. De opnåede randbetingelser udgør den såkaldte "*effektive model*" til beregning af akustiske felter og strømning i arbitrære geometrier, hvor der analytisk er taget højde for randlaget. Fra et numerisk perspektiv medfører den effektive model en drastisk reduktion i den nødvendige beregningshukommelse som tillader at større 3-dimensionelle systemer kan simuleres.

Inspireret af tidligere eksperimentelle observationer af akustisk strømning i lukkede resonanskaviteter, undersøges fænomenet "bulk-drevet strømning". Denne form for strømning bliver ofte ignoreret i akustofluidiske opsætninger med længdeskala sammenlignlig med den akustiske bølgelængde. I denne afhandling konkluderes det, at bulk-drevet strømning kan spille en afgørende rolle i sådanne systemer, hvis den akustiske bevægelse roterer. Det er værd at bemærke, at denne rotation kan blive igangsat uventet, også selvom aktueringen ikke roterer. Derfor er et centralt budskab i denne afhandling at bulk-drevet strømning ikke bør ignoreres, hverken i forståelse eller i beregninger af akustofluidiske resonanssystemer. I denne afhandling gives der en generel længdeskalabetingelse, som skal være opfyldt for at forsvare at ignorere bulk-drevet strømning.

Akustisk indfangning i kapillærrør er en lovende anvendelse af akustofluidik, som hovedsageligt er blevet studeret eksperimentelt. Ved at anvende de effektive randbetingelser for det viskøse randlag, beregnes de akustiske felter og den akustiske strålingskraft i lange lige kapillærrør med arbitrær tværsnitsform. Denne analyse giver et analytisk udtryk for den aksielle strålingskraft og en optimal aktueringslængde for akustisk indfangning i disse

systemer.

Slutteligt, ved hjælp af af den effektive randlagsmodel har det vist sig muligt at beregne den akustiske strømning tilstrækkeligt hurtigt, således at mange forskellige kanalformer kan blive undersøgt. Dette bliver brugt i en iterativ algoritme, som optimerer kanalformen med målet at minimere den akustiske strømning. Den resulterende optimerede form er vist på forsiden af denne afhandling, og dens strømningshastighed er undertrykt med to størrelsesordner relativt til strømningen i konventionelle rektangulære kanaler. Denne teoretisk forslåede kanalform kan potentielt facilitere akustisk håndtering af partikler mindre end en mikrometer, og i det lys giver dette afsluttende resultat lovende perspektiver imod fremtidige eksperimentelle undersøgelser.

Preface

This thesis is submitted in candidacy for the degree of Doctor of Philosophy (PhD) from the Technical University of Denmark (DTU). The work was carried out in the Department of Physics, Section of Biophysics and Fluids, in the Theoretical Microfluidics Group, during the three years from 1 March 2017 to 29 February 2020, with Professor Henrik Bruus as main supervisor and Professor Tomas Bohr as co-supervisor. The PhD project was funded by a DTU scholarship. The project included an external research stay from September to December 2018 in the group of Professor Joel Voldman at Massachusetts Institute of Technology funded by a Visiting Scholarship (Grant No. 8052-00001B) from the Danish Agency for Science and Higher Education, as well as the Idella Foundation and the Kaj and Hermilla Ostenfeld's Foundation.

Copenhagen, 29 February 2020

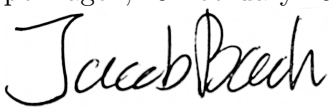

Jacob S. Bach

Acknowledgement

Several people has played an essential role for this project to become successful. A special acknowledgement goes to my supervisor Professor Henrik Bruus for his inspiring and passionate approach to theoretical physics, and for his immense dedication to me as a student. The many hours spend with Henrik at the whiteboard or doing "café physics" have given me an invaluable insight into the theory and joy physics. I would also like to thank my fellow PhD students and postdocs in the Theoretical Microfluidics Group: Nils R. Skov, André G. Steckel, Jonas H. Jørgensen, William N. Bodé, Mikkel W. H. Ley, Jonas T. Karlsen, Fabian Lickert, Massimiliano Rossi, and Wei Qiu. I am happy to have shared three years of enlightening conversations, several conference stays, and hundreds of lunch breaks with these people. Furthermore, I thank Professor Joel Voldman and his group for their great hospitality of having me at MIT for four months and ofr their recognition of me and my work. Some people in his group spend significant time on teaching me laboratory practise, for which I am particularly grateful: Jaemyon Lee, Dan Wu, Kruthika Kikkeri, and Rodger Yuan. A heartfelt gratitude I send to Hillary and Edward whom we lived with during our stay in Brookline, Massachusetts. Their impressive hospitality meant more than they know. Finally, but not least, I thank my parents, family, and friends for their support and willingness to listen to my excitement about microscale acoustics, even though this topic may seem far from their primary interests. This is especially true for my girlfriend Julie.

Contents

Publications in the PhD project

Peer-reviewed journal papers

I. J. S. Bach and H. Bruus, *Theory of pressure acoustics with viscous boundary layers and streaming in curved elastic cavities*, J. Acoust. Soc. Amer. **144**, 766-784 (2018).
Enclosed in Section 7.1, Ref. [1].

II. N.R. Skov, J. S. Bach, B.G. Winckelmann, and H. Bruus, *3D modeling of acoustofluidics in a liquid-filled cavity including streaming, viscous boundary layers, surrounding solids, and a piezoelectric transducer*, AIMS Math **4**, 99-111 (2019).
Enclosed in Section 7.2, Ref. [2].

III. J. S. Bach and H. Bruus, *Bulk-driven acoustic streaming at resonance in closed microcavities*, Phys. Rev. E **100**, 023104 1-20 (2019).
Enclosed in Section 7.3, Ref. [3].

IV. J. S. Bach and H. Bruus, *Theory of acoustic trapping of microparticles in capillary tubes*, Phys. Rev. E **101**, 023107 1-12 (2020).
Enclosed in Section 7.4, Ref. [4].

V. J. S. Bach and H. Bruus, *Suppression of acoustic streaming in shape-optimized microchannels*, Submitted to Phys. Rev. Lett., 5 pages (Feb. 2020). ArXiv preprint: 2002.11058 [physics.flu-dyn].
Enclosed in Section 7.5, Ref. [5].

Editor-reviewed journal papers

VI. J. S. Bach and H. Bruus, *Different origins of acoustic streaming at resonance*, Proceedings of Meetings on Acoustics **34**, 022005 (2018).
Enclosed in Section 7.6, Ref. [6].

Peer-reviewed conference contributions

1. J. S. Bach, M.W.H. Ley, and H. Bruus, *Effective boundary-layer modeling of acoustofluidics in 3D microchannels*, Flow17 Conference, 3-5 July 2017, Paris, France, **poster presentation**.

2. J. S. Bach and H. Bruus, *Effective modeling of acoustic boundary layers in acoustofluidic systems with curved oscillating walls*, Acoustofluidics Conference, 28-29 August 2017, San Diego, CA, USA, **poster presentation**.

3. J. S. Bach and H. Bruus, *An effective boundary condition for pressure acoustics in microfluidic systems*, 8th Sommer School Complex Motion in Fluids, 24-29 Sep 2017, Cambridge, UK, **oral presentation**.

4. J. S. Bach and H. Bruus, *Acoustic streaming in 3 dimensions*, The Swedish Center for Acoustofluidics and Cell Separation (SWECACS), 19 Dec 2017, Lund, Sweden, **oral presentation**.

5. J. S. Bach and H. Bruus, *Different origins of acoustic streaming at resonance*, 21st International Symposium on Nonlinear Acoustics, 9-13 July 2018, Santa Fe, New Mexico, **oral presentation**.
   Conference paper is published [6] and enclosed in Section 7.6.

6. J. S. Bach and H. Bruus, *Bulk-driven acoustic streaming induced by weak symmetry breaking of the grometry or by a rotating actuation*, 9th Sommer School Complex Motion in Fluids, 18-24 Aug 2019, Gilleleje, Denmark, **oral presentation**.

7. J. S. Bach and H. Bruus, *Classification of acoustic streaming in three dimensions*, Acoustofluidics Conference, 29-31 August 2018, Lille, France, **oral presentation**.

8. J. S. Bach and H. Bruus, *Double-mode resonances inducing bulk-driven acoustic streaming*, Acoustofluidics Conference, 26-28 Aug 2019, Enschede, Netherlands, **oral presentation**.

List of Figures

List of Tables

Chapter 1

Introduction

This chapter gives a brief introduction to the research field of microfluidics and its subbranch acoustofluidics, which is the topic of this PhD project. The particularly relevant phenomenon of acoustic streaming is presented and the scope of the PhD project is established. Finally, overviews of the research and thesis structure are provided.

1.1 Introduction to microfluidics

The fundamental idea in microfluidics is to process and manipulate fluids in channels or cavities having a dimension of tens to hundreds of micrometers [7]. As a technology, it is particularly interesting in the field of biochemistry as it offers a cheap and fast way to precisely handle and perform assays on tiny amounts of biological fluids, say a single drop of blood. Using different manipulation techniques, such fluids can be guided around in microchannels, mixed with other fluids, diluted, concentrated, purified etc., and the whole system constitute an automated biological laboratory on a microchip specialized for a specific purpose, often called *lab-on-a-chip*. Promising perspectives include the development of point-of-care devices that offer cheap and fast diagnostics in areas without access to conventional laboratories [8, 9], organ-on-a-chip devices used for drug testing on a personalized artificial human organ [10], or microreactors as shown Fig. 1.1(a) where many chemical reactions can be rapidly tested in parallel and under different conditions [11].

The small length scale of microfluidics makes the physical behaviour different from what we experience from every-day fluid phenomena. Most importantly, at this small length scale, viscous forces are often dominant over inertial forces, and therefore, the fluid motion is well described by a *laminar flow* where no mixing or turbulence occurs[12], see Fig. 1.1(b). This makes microfluidics advantageous for controlled handling of biological samples.

Not only may the fluid itself be controlled in microsystems, but also the suspended particles. These can be controlled by exploiting a vast variety of physical forces [12, 13] including inertial [14], gravitational [15], hydrodynamic [16], electric [17], magnetic [18], dielectrophoretic [19, 20], optical [21, 22], and acoustic forces [23]. Using these forces, suspended particles may be sorted out, trapped, or concentrated based on their physical

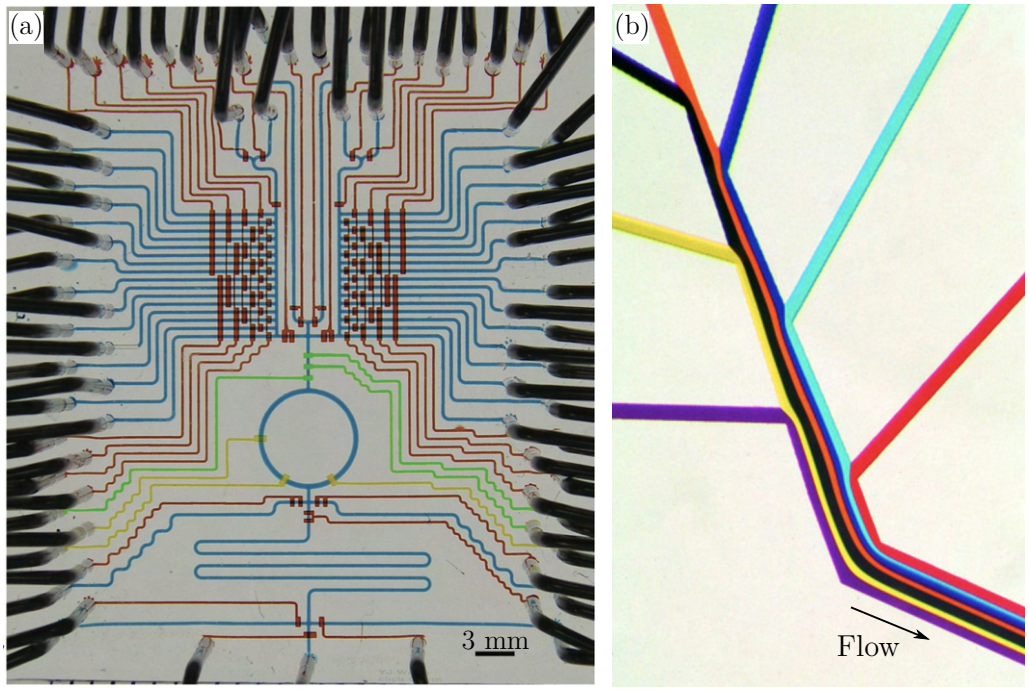

Figure 1.1: Optical images of microfluidic devices containing fluid colored with different dies. (a) A microreactor with 2×16 individually addressed reagent inlets (blue) for chemical reactions. Adapted from Wang *et al.* [11]. (b) A beautiful example of laminar flow in a microchannel. Adapted from Kenis *et al.* [24].

properties such as density, compressibility, polarizability, permittivity, size, shape, etc. From a physics point of view, microfluidics is therefore not just a study in hydrodynamics, but requires the entire toolbox of classical physics.

1.2 Acoustofluidics

Acoustofluidics is the subbranch of microfluidics where acoustic fields are used to manipulate suspended particles or the fluid itself [23]. The knowledge that sound waves can move particles dates back at least as early as 1680, where Robert Hooke observed the nodal patterns on a glass plate as he ran a bow along the edge of the plate covered with flour. The migration of particles due to sound waves is in general called *acoustophoresis* [12] and this phenomenon can be exploited in a microfluidics setting by attaching *e.g.* a piezoelectric transducer on a microchannel. The acoustic response is particularly enhanced when actuating at the resonance frequency corresponding to a half standing pressure wave across the microchannel as shown see Fig. 1.2(a). For a typical microchannel of width $\frac{\lambda}{2} = 375$ µm filled with water having the sound speed $c_0 = 1497 \frac{\text{m}}{\text{s}}$ [25], this correspond to an ultrasound frequency of around $f = \frac{c_0}{\lambda} = 2$ MHz.

Acoustofluidics has gained increased interest over the past two decades [23, 26]. The

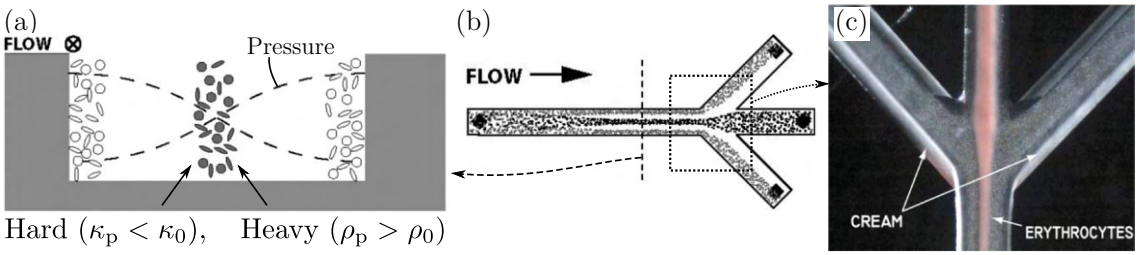

Figure 1.2: Separation of lipids from blood utilizing ultrasonic an standing wave in a microfluidic channel of width 350 µm and height 125 µm. (a) Schematic of the cross section, where hard and heavy particles are focused in the pressure node. (b) Scematic top view of the microchannel. (c) Optical image of the trifurcation region. Adapted from Petersson *et al.* [29].

method allows for gentle [27, 28] manipulation of particles in their natural fluid medium and does not require any prelabeling of the particles in order to influence them. The key working principle in acoustofluidics is the *acoustic radiation force* which acts on particles suspended in an acoustically excited fluid. One example is shown in Fig. 1.2 showing separation of lipids from blood in a microchannel utilizing an ultrasonic standing pressure wave. Particles that are heavier and harder than the surrounding fluid will be pushed by the acoustic radiation force towards the pressure node at the center of the channel, which is the case for the red blood cells in water. In contrast, particles that are lighter and softer than the surrounding medium, will be pushed to the pressure anti-nodes at the channel walls which is the case for the milk lipids in water. The key physical properties that distinguish particles in acoustofluidics are the density ρ_p, the compressibility κ_p, and the size which for a spherical particle is quantified by the radius a_p. The phenomenon of acoustophoresis has been used for many different applications within microflidics including particle separation [29–35], enrichment of prostate cancer cells in blood [36], concentration of red blood cells [37], acoustic trapping [38–48], acoustic tweezing [49–52], handling of submicron particles [42, 53–55], cell synchronization [56], handling of swimming organisms [57, 58], single cell patterning [59, 60], controlled cell aggregation [61–63], and handling of particles inside droplets [64].

Acoustic streaming

In addition to the acoustic radiation force, that acts on suspended particles, there are also time-averaged acoustic forces acting on the fluid itself. The resulting steady motion of the fluid is called *acoustic streaming*, and by the viscous drag force, suspended particles experience a drag from this flow. An example is shown in Fig. 1.3(a), where the acoustic streaming in a cross section of a microchannel is visualized from the measured velocity of small tracer particles. It is quite remarkable, that acoustic fields can be used to generate a flow inside a microchannel without using any pumps or valves. However, this flow is often not desired if the purpose is to focus microparticles with the acoustic radiation force. For

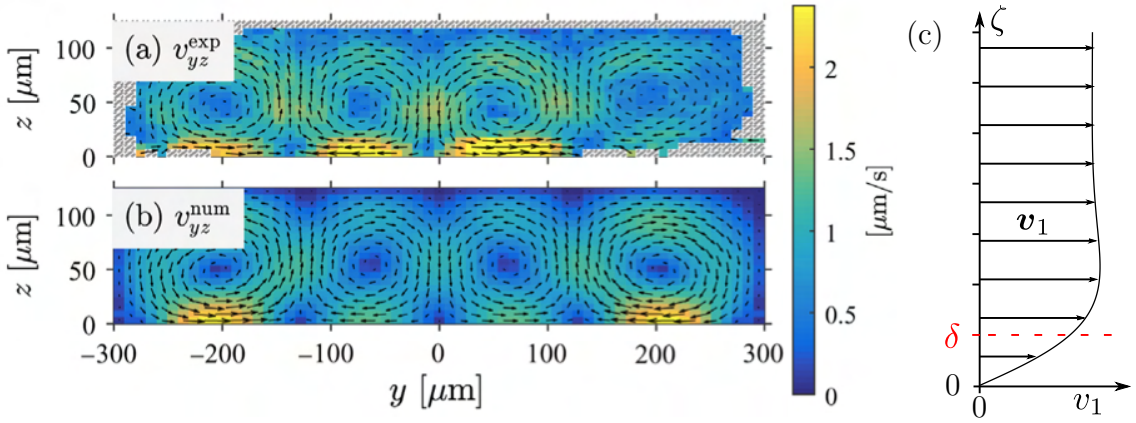

Figure 1.3: (a)-(b) Acoustic streaming in a cross section of a rectangular polymer microchannel actuated by surface acoustic waves of frequency 6.2 MHz at the bottom wall. (a) Experimentally measured velocity of particles of diameter 0.5 µm. (b) Numerical simulation of the acoustic streaming velocity. From Barnkob *et al.* [65]. (c) The velocity profile of the viscous boundary layer of characteristic length scale δ along the perpendicular coordinate ζ away from the surface.

a spherical particle, the viscous drag force scales with the radius a_p whereas the acoustic radiation force scales with the volume a_p^3. These scaling laws lead to one of the most important obstacles in acoustofluidics for particle handling; namely that particles smaller than a certain critical size follow the rotating acoustic streaming instead of being focused by the acoustic radiation force. This critical particle diameter has been determined to be around 2 µm for a spherical polystyrene particle in a standing pressure wave at 2 MHz frequency in water [66, 67]. Hence, acoustic streaming must be explored and understood in order to use acoustofluidic devices for handling of particles smaller than this size. This can be done by either suppressing the acoustic streaming or by controlling it, so it acts constructively. In particular, the suppression of acoustic streaming will be investigated in this thesis.

When analyzing acoustic streaming in microchannels, an unavoidable physical phenomenon is the *viscous boundary layer*, which is a narrow region close to a fluid-solid boundary, where the fluid velocity adapts to the solid velocity as sketched in Fig. 1.3(c). At 2 MHz frequency this width is as narrow as $\delta = 0.4$ µm which is typically two to three orders of magnitude smaller than the channel dimension. Nevertheless, significant time-averaged viscous effects occur in the boundary layer which generate both dissipation and acoustic streaming. A central goal of this PhD project is to understand the physics of the viscous boundary layer in the general case of a curved oscillating interface.

In addition to the *boundary-driven streaming* which is generated by the viscous boundary layer, viscous effects outside the boundary layer may also generate acoustic streaming, which is called *bulk-driven streaming*. This kind of streaming is often ignored in a microfluidic setting [68, 69] but as shown in this thesis, it may actually play a significant role in many cases.

1.3 Overview of the research done in the PhD project

This PhD project investigates, from a theoretical point of view, the acoustic fields and streaming in microsystems actuated at ultrasound frequencies. The overall goal is to use theoretical insight to predict and explain acoustic phenomena that are relevant for the development of acoustofluidic devices. The research is carried out in three major parts:

(1) **The viscous boundary layer and effective boundary conditions** (Paper I [1])
The viscous boundary layer is responsible for both dissipation of the acoustic fields and for the generation of steady acoustic streaming. In this part of the research, a theoretical understanding of these effects is developed with the outset in existing boundary-layer theories [70–75], which will be extended to apply for the general case of a curved wall oscillating in any direction. The work leads to effective boundary conditions on both the acoustic pressure and the acoustic streaming, which allow for numerical simulations where all the effects from the viscous boundary layer are taken into account analytically without resolving the boundary layer numerically.

(2) **Theoretical understanding of experimental observations** (Paper II-IV [2–4])
The acoustic streaming and the acoustic radiation force result from non-linear time-averaged effects of the acoustic fields which are not always trivial to predict. In this part, two different experimentally relevant observations are analyzed theoretically: First, inspired by the experimental observations of a peculiar streaming pattern in a closed cavity by Hagsäter *et al.* [76], a theory for bulk-driven acoustic streaming at resonance is developed. It is found that bulk-driven acoustic streaming can play an essential role even for systems comparable to the acoustic wave length. Second, inspired by the experimental [39–43, 45–47] and numerical [43, 45, 77] work on acoustic trapping in long straight capillary tubes, a theory is developed for the acoustic fields and the axial radiation force in theses systems. This theory is derived for any cross section and therefore allow for general insight in the phenomenon of acoustic trapping.

(3) **Suppression of acoustic streaming** (Paper V [5])
The effective boundary conditions derived in part (1) are in this final part exploited to investigate how the shape of a resonating channel influence the acoustic fields and streaming. It is found that the acoustic streaming can be dramatically suppressed by optimizing the shape of the cavity.

1.4 Thesis overview

The scientific content of this PhD project has been thoroughly written in the five published papers I-V [1–5], which I have therefore chosen to include in their original form in Chapter 7. A central part of the thesis is the boundary-layer analysis carried out in Paper I [1], and due to the comprehensive mathematical load of that paper, Chapter 3 gives a summary of the key steps and results of that paper. Similarly, Chapter 4 supplements the analysis of bulk-driven acoustic streaming carried out in Paper III [3], by presenting

the key results as well as perspectives to experimental observations. It is emphasized that the papers that are not supplemented by chapters are still significant, in particular the final Paper V [5] that presents the suppression of acoustic streaming in shape-optimized microchannels. Below, is given an overview of the chapters of the thesis.

Chapter 1: Introduction — A broad introduction to the fields of microfluidics and acoustofluidics is given as well as a motivation and scope of the research.

Chapter 2: Theoretical background of acoustofluidics — The general conservation laws of mass and momentum are presented as well as the governing equations for acoustic fields and streaming. The wall motion and the no-slip boundary condition for an oscillating wall is defined as well as the acoustic radiation force. Acoustic streaming is introduced and a historical development of the boundary-layer analysis is provided. Finally, concepts and limitations of acoustophoresis in microsystems are discussed.

Chapter 3: The viscous boundary layer at a curved oscillating surface — The key steps and results of the boundary-layer analysis carried out in Paper I [1] are provided, including the derived effective boundary conditions on the acoustic fields and streaming.

Chapter 4: Bulk-driven streaming on the wavelength scale — Complementing the findings of Paper III [3], the goal of this chapter is to emphasize that bulk-driven acoustic streaming should not be ignored in microsystems of size comparable to the acoustic wavelength. A general length-scale condition is derived for ignoring bulk-driven streaming. Three examples of observations reported in the literature are considered and it is argued that these may be classified as bulk-driven streaming.

Chapter 5: FEM modelling in COMSOL and validation — A brief introduction to the Finite Element Method (FEM) used in the numerical simulations of the thesis is given, as well as an overview of the equations and boundary conditions that are used in the models. The validity of the numerical results and how these are substantiated are discussed.

Chapter 6: Summary of results — The key results of each paper is summarized in a combined overview.

Chapter 7 Papers of the PhD project — All the published papers from I-V [1–5] and their supplemental material are provided in their original form.

Chapter 8 Conclusion and outlook — A final conclusion of the thesis is given as well as a theoretical and and experimental outlook.

Chapter 2

Theoretical background of acoustofluidics

In this chapter, the theoretical background of acoustofluidics, on which this thesis is build upon, is established, and the general concepts and limitations of acoustophoresis are described. Three places, I put a section named "This thesis" to point out where this thesis contributes with new results in the given context.

2.1 The general conservation laws

The local conservation of mass and momentum is described in the Eulerian picture in terms of the mass density $\tilde{\rho}(\boldsymbol{r},t)$, the fluid velocity $\tilde{\boldsymbol{v}}(\boldsymbol{r},t)$, and the stress tensor $\tilde{\boldsymbol{\sigma}}(\boldsymbol{r},t)$,

$$\partial_t\tilde{\rho} = \boldsymbol{\nabla}\cdot[-\tilde{\rho}\tilde{\boldsymbol{v}}], \tag{2.1a}$$

$$\partial_t(\tilde{\rho}\tilde{\boldsymbol{v}}) = \boldsymbol{\nabla}\cdot[\tilde{\boldsymbol{\sigma}} - (\tilde{\rho}\tilde{\boldsymbol{v}})\tilde{\boldsymbol{v}}], \tag{2.1b}$$

where a tilde[1] denotes a time-dependent field. Here, the stress tensor $\tilde{\boldsymbol{\sigma}}$ is defined in terms of the pressure $\tilde{p}$ and its viscous part $\tilde{\boldsymbol{\tau}}$ with the dynamic shear viscosity η_0, and the bulk viscosity η_0^{b} [12],

$$\tilde{\boldsymbol{\sigma}} = -\tilde{p}\mathbf{I} + \tilde{\boldsymbol{\tau}}, \qquad \tilde{\boldsymbol{\tau}} = \eta_0\Big[\boldsymbol{\nabla}\tilde{\boldsymbol{v}} + (\boldsymbol{\nabla}\tilde{\boldsymbol{v}})^{\mathrm{T}} - \frac{2}{3}(\boldsymbol{\nabla}\cdot\tilde{\boldsymbol{v}})\mathbf{I}\Big] + \eta_0^{\mathrm{b}}(\boldsymbol{\nabla}\cdot\tilde{\boldsymbol{v}})\mathbf{I}. \tag{2.1c}$$

As a constitutive relation, the adiabatic assumption is applied, stating that the entropy of each infinitesimal fluid particle remains constant. Hence, the change in mass density and the change in pressure are related through the isentropic compressibility κ_0,

$$\kappa_0 = \frac{1}{\rho_0}\left(\frac{\partial\tilde{\rho}}{\partial\tilde{p}}\right)_S = \frac{1}{\rho_0 c_0^2}, \tag{2.2}$$

where ρ_0 is the unperturbed mass density and c_0 is the speed of sound of the fluid. Table 2.1 provides an overview of the material parameters for water and some relevant derived quantities used in this thesis.

[1] The tilde has only been used in Paper III [3], but after confusing several reviewers, I have decided to use it to distinguish physical time-dependent fields $\tilde{\rho}(\boldsymbol{r},t)$ from time-independent fields $\rho_1(\boldsymbol{r})$, see Eq. (2.4b).

Table 2.1: Material parameters for water at 25 °C [25]. The values below the line is for the frequency $f = 1$ MHz.

Parameter	Symbol	Value	Unit
Mass density	ρ_0	997.05	kg m^{-3}
Sound speed	c_0	1496.7	m s^{-1}
Compressibility	κ_0	452	TPa^{-1}
Dynamic viscosity	η_0	0.890	mPa s
Bulk viscosity	η_0^{b}	2.485	mPa s
Boundary-layer width	$\delta \propto f^{-\frac{1}{2}}$	0.53	µm
Acoustic damping factor	$\Gamma_0 \propto f$	4.03×10^{-6}	–
Boundary-layer smallness	$k_0\delta \propto f^{\frac{1}{2}}$	2.24×10^{-3}	–

2.2 The acoustic perturbation expansion

Acoustic fields may be described as small oscillating perturbations $\tilde{\rho}_1$ in the fluid density away from the equilibrium value ρ_0, thus defining the small acoustic perturbation parameter,

$$\varepsilon_{\mathrm{ac}} = \frac{\tilde{\rho}_1}{\rho_0} \ll 1. \tag{2.3}$$

The perturbation $\tilde{\rho}_1$ in the density implies the acoustic velocity $\tilde{\boldsymbol{v}}_1$ and the acoustic pressure $\tilde{p}_1$, which are also small in the sense $\kappa_0\tilde{p}_1 \sim \varepsilon_{\mathrm{ac}}$ and $\frac{1}{c_0}\tilde{v}_1 \sim \varepsilon_{\mathrm{ac}}$. The dependent fields $\tilde{\rho}$, $\tilde{\boldsymbol{v}}$, and $\tilde{p}$ are therefore written as the perturbation expansion,

$$\tilde{A}(\boldsymbol{r},t) = A_0 + \tilde{A}_1(\boldsymbol{r},t) + \tilde{A}_2(\boldsymbol{r},t). \tag{2.4a}$$

The zeroth-order fields with subscript "0" are here assumed to be constant in space and time. The first-order fields with subscript "1" are assumed to be oscillating harmonically with the angular frequency ω and are written as a single Fourier component with the time-independent complex amplitude $A_1(\boldsymbol{r})$. The second-order fields $\tilde{A}_2$ are induced by products of first-order fields, and therefore have both a steady part $A_2(\boldsymbol{r})$ and a second-harmonic part that oscillates with the double frequency 2ω. Hence, the time-independent fields $A_1(\boldsymbol{r})$ and $A_2(\boldsymbol{r})$ without the tilde are defined by the relations,

$$\tilde{A}_1(\boldsymbol{r},t) = \mathrm{Re}\Big[A_1(\boldsymbol{r})\mathrm{e}^{-\mathrm{i}\omega t}\Big], \qquad A_2(\boldsymbol{r}) = \langle\tilde{A}_2(\boldsymbol{r},t)\rangle = \frac{1}{T}\int_0^T \tilde{A}_2(\boldsymbol{r},t)\,\mathrm{d}t, \tag{2.4b}$$

where angular brackets "$\langle\cdot\rangle$" denote time averaging over a full oscillation period $T = \frac{2\pi}{\omega}$. In particular, the time averaged product of two first-order fields is,

$$\langle\tilde{A}_1\tilde{B}_1\rangle = \frac{1}{T}\int_0^T \tilde{A}_1(\boldsymbol{r},t)\tilde{B}_1(\boldsymbol{r},t)\,\mathrm{d}t = \frac{1}{2}\mathrm{Re}\Big[A_1B_1^*\Big], \tag{2.4c}$$

where "Re" is the real part of a complex number and "$*$" denotes complex conjugation.

2.3 Wall motion and the no-slip condition

We consider a fluid domain Ω as shown in Fig. 2.1, which is embedded in an elastic solid material with a fluid-solid interface that oscillates harmonically around the equilibrium position $\partial\Omega$ or $\boldsymbol{s}_0$ with the angular frequency ω. The instantaneous position $\tilde{\boldsymbol{s}}(\boldsymbol{s}_0, t)$ and velocity $\tilde{\boldsymbol{V}}^0(\boldsymbol{s}_0, t)$ of the wall element with equilibrium position $\boldsymbol{s}_0$ are written as in Eq. (2.4b) in terms of the complex amplitudes $\boldsymbol{s}_1(\boldsymbol{s}_0)$ and $\boldsymbol{V}_1^0(\boldsymbol{s}_0)$,

$$\tilde{\boldsymbol{s}}(\boldsymbol{s}_0, t) = \boldsymbol{s}_0 + \tilde{\boldsymbol{s}}_1(\boldsymbol{s}_0, t), \qquad \tilde{\boldsymbol{s}}_1(\boldsymbol{s}_0) = \mathrm{Re}\Big[\boldsymbol{s}_1(\boldsymbol{s}_0)\mathrm{e}^{-\mathrm{i}\omega t}\Big], \tag{2.5a}$$

$$\tilde{\boldsymbol{V}}^0(\boldsymbol{s}_0, t) = \partial_t \tilde{\boldsymbol{s}} = \tilde{\boldsymbol{V}}_1^0(\boldsymbol{s}_0, t), \qquad \tilde{\boldsymbol{V}}_1^0(\boldsymbol{s}_0) = \mathrm{Re}\Big[\boldsymbol{V}_1^0(\boldsymbol{s}_0)\mathrm{e}^{-\mathrm{i}\omega t}\Big], \tag{2.5b}$$

where $\boldsymbol{V}_1^0(\boldsymbol{s}_0) = -\mathrm{i}\omega\boldsymbol{s}_1(\boldsymbol{s}_0)$ and $\mathrm{i} = \sqrt{-1}$ is the imaginary unit. Here, the superscript "0" on the surface velocity $\tilde{\boldsymbol{V}}^0$ denotes a velocity field which is only defined at the surface and therefore has no perpendicular derivative, see Section II F of Paper I [1]. When formulating the boundary condition on the fluid velocity $\tilde{\boldsymbol{v}}(\boldsymbol{r}, t)$, it is important to note that the fluid velocity $\tilde{\boldsymbol{v}}$ is Eulerian, *i.e.* it refers to the fluid velocity at the *fixed* coordinate $\boldsymbol{r}$, whereas the solid velocity $\tilde{\boldsymbol{V}}^0(\boldsymbol{s}_0, t)$ is Lagrangian *i.e.* it refers to the velocity of the wall element at the position $\tilde{\boldsymbol{s}} = \boldsymbol{s}_0 + \tilde{\boldsymbol{s}}_1$ slightly displaced from the equilibrium position $\boldsymbol{s}_0$ of evaluation, see Fig. 2.1. The no-slip boundary condition on the *instantaneous* wall position $\tilde{\boldsymbol{s}}(\boldsymbol{s}_0, t)$ is therefore [74, 78],

$$\tilde{\boldsymbol{v}}\big[\tilde{\boldsymbol{s}}(\boldsymbol{s}_0, t), t\big] = \tilde{\boldsymbol{V}}^0\big(\boldsymbol{s}_0, t\big), \qquad \text{at } \boldsymbol{s}_0. \tag{2.6a}$$

For wall displacements $\tilde{\boldsymbol{s}}_1$ much smaller than the length scale of variations in the fluid velocity $\tilde{\boldsymbol{v}}$, this condition may be written by inserting $\tilde{\boldsymbol{s}} = \boldsymbol{s}_0 + \tilde{\boldsymbol{s}}_1$ from Eq. (2.5) on the left-hand side and Taylor expanding,

$$\tilde{\boldsymbol{v}}(\boldsymbol{s}_0, t) + \big(\tilde{\boldsymbol{s}}_1 \cdot \boldsymbol{\nabla}\big)\tilde{\boldsymbol{v}} = \tilde{\boldsymbol{V}}_1^0, \qquad \text{at } \boldsymbol{s}_0, \tag{2.6b}$$

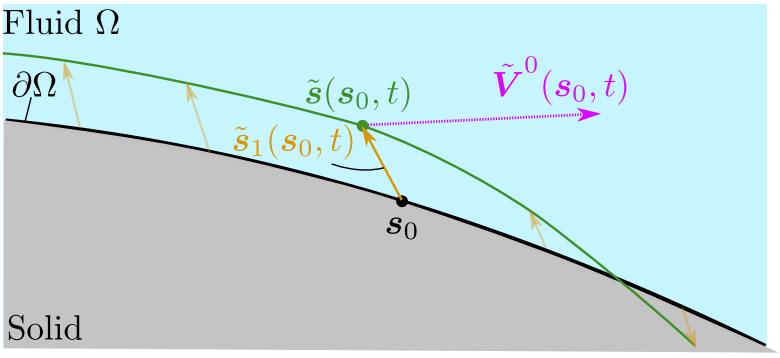

Figure 2.1: Sketch of the interface (wall) between the fluid domain Ω (blue) and the solid domain (grey). The equilibrium position of the wall is called $\partial\Omega$ or $\boldsymbol{s}_0$ (black line), the instantaneous position of the wall is $\tilde{\boldsymbol{s}}(\boldsymbol{s}_0, t)$ (green line), and the instantaneous displacement displacement of the wall is $\tilde{\boldsymbol{s}}_1(\boldsymbol{s}_0, t)$ (orange arrows). The Lagrangian wall velocity $\tilde{\boldsymbol{V}}^0(\boldsymbol{s}_0, t)$ (magenta arrow) is the velocity at the instantaneous position $\tilde{\boldsymbol{s}}(\boldsymbol{s}_0, t)$.

where $\tilde{\boldsymbol{V}}^0 = \tilde{\boldsymbol{V}}_1^0$ from Eq. (2.5b) was used. Combining this result with the acoustic perturbation expansion described in Section 2.2 leads to the no-slip boundary condition on the time-independent velocity fields $\boldsymbol{v}_1(\boldsymbol{r})$ and $\boldsymbol{v}_2(\boldsymbol{r})$ defined in Eq. (2.4b),

$$\boldsymbol{v}_1 = \boldsymbol{V}_1^0, \qquad \boldsymbol{v}_2 + \langle(\boldsymbol{s}_1 \cdot \boldsymbol{\nabla})\boldsymbol{v}_1\rangle = \boldsymbol{0}, \qquad \text{at } \boldsymbol{s}_0. \tag{2.6c}$$

Using this Lagrangian no-slip condition allows for *local* time-averaged mass flux at the boundary equilibrium position $\boldsymbol{s}_0$, but the *global* time-averaged mass flux vanishes as required, see Appendix A for details.

2.4 The acoustic fields

The first-order acoustic fields $\tilde{\rho}_1(\boldsymbol{r},t)$, $\tilde{v}_1(\boldsymbol{r},t)$, and $\tilde{p}_1(\boldsymbol{r},t)$ all have the time-harmonic form given in Eq. (2.4b) with the time-independent complex amplitudes $\rho_1(\boldsymbol{r})$, $\boldsymbol{v}_1(\boldsymbol{r})$, and $p_1(\boldsymbol{r})$. They are governed by the first-order expansion of Eq. (2.1) and the boundary condition (2.6c), which for a homogeneous fluid become [1],

$$-\mathrm{i}\omega\kappa_0 p_1 = -\boldsymbol{\nabla}\cdot\boldsymbol{v}_1, \qquad \text{for } \boldsymbol{r}\in\Omega, \tag{2.7a}$$

$$-\mathrm{i}\omega\rho_0\boldsymbol{v}_1 = \boldsymbol{\nabla}\cdot\boldsymbol{\sigma}_1 = -(1-\mathrm{i}\Gamma_0)\boldsymbol{\nabla}p_1 - \eta_0\boldsymbol{\nabla}\times(\boldsymbol{\nabla}\times\boldsymbol{v}_1), \qquad \text{for } \boldsymbol{r}\in\Omega, \tag{2.7b}$$

$$\boldsymbol{v}_1 = \boldsymbol{V}_1^0, \qquad \text{for } \boldsymbol{r}\in\partial\Omega, \tag{2.7c}$$

where the vector identity $\nabla^2\boldsymbol{A} = \boldsymbol{\nabla}(\boldsymbol{\nabla}\cdot\boldsymbol{A}) - \boldsymbol{\nabla}\times\boldsymbol{\nabla}\times\boldsymbol{A}$ was used, as well as the relation $p_1 = c_0^2\rho_1$ from Eq. (2.2). In Eq. (2.7b) the dimensionless bulk damping coefficient Γ_0 is,

$$\Gamma_0 = \left(\frac{4}{3} + \frac{\eta_0^{\mathrm{b}}}{\eta_0}\right)\eta_0\omega\kappa_0. \tag{2.8}$$

The velocity field $\boldsymbol{v}_1$ is eliminated from Eq. (2.7) by taking the divergence of Eq. (2.7b) and using Eq. (2.7a) leading to a Helmholtz equation for the pressure p_1,

$$\nabla^2 p_1 + k_{\mathrm{c}}^2 p_1 = 0, \qquad k_{\mathrm{c}}^2 = \frac{1}{1-\mathrm{i}\Gamma_0}k_0^2, \qquad k_0 = \frac{\omega}{c_0}. \tag{2.9}$$

Here, k_{c} is the complex-valued compressional wave number with the real part k_0. The velocity field $\boldsymbol{v}_1$ is most conveniently represented as the following Helmholtz decomposition [71, 72, 78, 79],

$$\boldsymbol{v}_1 = \boldsymbol{v}_1^d + \boldsymbol{v}_1^\delta, \qquad \text{with} \quad \boldsymbol{\nabla}\times\boldsymbol{v}_1^d = \boldsymbol{0}, \quad \boldsymbol{\nabla}\cdot\boldsymbol{v}_1^\delta = 0, \tag{2.10}$$

where $\boldsymbol{v}_1^d$ is a compressible potential flow with length scale d to be determined in Chapter 3, and $\boldsymbol{v}_1^\delta$ is an incompressible solenoidal flow with length scale δ. Inserting Eq. (2.10) into Eq. (2.7) and requiring solenoidal and irrationally parts to cancel separately leads to the following equations for the velocity fields $\boldsymbol{v}_1^\delta$ and $\boldsymbol{v}_1^d$,

$$\nabla^2\boldsymbol{v}_1^\delta + k_{\mathrm{s}}^2\boldsymbol{v}_1^\delta = \boldsymbol{0}, \qquad k_{\mathrm{s}}^2 = \frac{2\mathrm{i}}{\delta^2}, \qquad \delta = \sqrt{\frac{2\eta_0}{\rho_0\omega}}, \tag{2.11a}$$

$$\nabla^2\boldsymbol{v}_1^d + k_{\mathrm{c}}^2\boldsymbol{v}_1^d = \boldsymbol{0}, \qquad \boldsymbol{v}_1^d = \frac{-\mathrm{i}(1-\mathrm{i}\Gamma_0)}{\omega\rho_0}\boldsymbol{\nabla}p_1, \tag{2.11b}$$

with the shear wave number k_s and the boundary-layer width δ. The incompressible velocity field $\boldsymbol{v}_1^\delta$ that satisfy Eq. (2.11a) describes a heavily damped shear velocity field which is confined to the narrow boundary-layer region of width $\delta \sim 0.5$ µm from the wall, see Table 2.1. Note that no approximations where made in obtaining Eqs. (2.9) and (2.11) from Eqs. (2.7a) and (2.7b).

This thesis: Pressure acoustics with viscous boundary layers

A major contribution of this thesis is the derivation of a boundary condition on the acoustic pressure p_1 that take into account all the effects from the viscous boundary layer, as described in Chapter 3.

2.5 Time-averaged physical quantities of the acoustic fields

The oscillating acoustic pressure $\tilde{p}_1$ and velocity $\tilde{\boldsymbol{v}}_1$ are usually not observed directly in experiments but indirectly through time-averaged effects. The relevant time-averaged quantities are defined in this section.

Energy of the acoustic fields

The local acoustic energy density $E_{\text{ac}}(\boldsymbol{r})$ is the sum of the local kinetic energy density $E_{\text{kin}}(\boldsymbol{r})$ and the local potential energy density $E_{\text{pot}}(\boldsymbol{r})$,

$$E_{\text{ac}}(\boldsymbol{r}) = E_{\text{kin}}(\boldsymbol{r}) + E_{\text{pot}}(\boldsymbol{r}), \qquad E_{\text{kin}}(\boldsymbol{r}) = \frac{1}{4}\rho_0|\boldsymbol{v}_1(\boldsymbol{r})|^2, \qquad E_{\text{pot}}(\boldsymbol{r}) = \frac{1}{4}\kappa_0|p_1(\boldsymbol{r})|^2. \tag{2.12a}$$

The strength of the acoustic fields in a cavity Ω of volume $\mathcal{V}$ and fluid/solid surface area $\mathcal{A}$ is often described through the space(-and-time)-averaged acoustic energy density $\bar{E}_{\text{ac}}$, denoted by an overbar,

$$\bar{E}_{\text{ac}} = \frac{1}{\mathcal{V}}\int_\Omega E_{\text{ac}}\,\mathrm{d}V. \tag{2.12b}$$

At steady state, the total stored energy $\mathcal{V}\bar{E}_{\text{ac}}$ in a cavity is maintained because the total input power $\mathcal{A}\bar{P}_{\text{wall}}$ delivered by the wall with velocity $\tilde{\boldsymbol{V}}_1^0$ is equal to the total viscous dissipation power $\mathcal{V}\bar{P}_{\text{diss}}$ lost in the fluid. In Appendix B these quantities are shown to be [80],

$$\bar{P}_{\text{wall}} = \frac{1}{\mathcal{A}}\int_{\partial\Omega}\left\langle \tilde{\boldsymbol{V}}_1^0 \cdot \tilde{\boldsymbol{\sigma}}_1 \right\rangle \cdot \boldsymbol{n}\,\mathrm{d}A, \qquad \bar{P}_{\text{diss}} = \frac{1}{\mathcal{V}}\int_\Omega \left\langle \tilde{\boldsymbol{\tau}}_1 : (\boldsymbol{\nabla}\tilde{\boldsymbol{v}}_1)^{\mathrm{T}} \right\rangle \mathrm{d}V. \tag{2.13}$$

A high acoustic energy density is obtained by actuating the system at a resonance with frequency $\omega = \omega_{\text{res}}$ and a high quality factor Q which is defined as the ratio between the total stored energy $\mathcal{V}\bar{E}_{\text{ac}}$ and the total energy $\frac{1}{\omega_{\text{res}}}\mathcal{V}\bar{P}_{\text{diss}}$ dissipated per radian,

$$Q = \frac{\omega_{\text{res}}\bar{E}_{\text{ac}}}{\bar{P}_{\text{diss}}}, \qquad \text{at } \omega = \omega_{\text{res}}. \tag{2.14}$$

For systems with acoustically hard walls, which is approximately the case for silicon/glass channels, it is possible to excite a fluid resonance and approximately measure the Q-factor of the fluid cavity [81], and the resonance frequency in this case will be very close to the eigenfrequency of the fluid cavity. In contrast, for systems with acoustically soft walls, such as polymer channels, it is more meaningful to consider the resonator properties of the full device [82], and the resonance frequency of the full device is often very different from the eigenfrequency of the fluid cavity alone.

Time-averaged vector quantities of the acoustic fields

The time-averaged energy flux density $\boldsymbol{S}_{\mathrm{ac}}$, and the acoustic angular momentum density $\boldsymbol{\mathcal{L}}_{\mathrm{ac}}$ with respect to the unperturbed fluid position $\boldsymbol{r}$ are deffined as,

$$\boldsymbol{S}_{\mathrm{ac}} = \langle \tilde{p}_1 \tilde{\boldsymbol{v}}_1 \rangle, \qquad \boldsymbol{\mathcal{L}}_{\mathrm{ac}} = \langle \tilde{\boldsymbol{d}}_1 \times (\rho_0 \tilde{\boldsymbol{v}}_1) \rangle, \tag{2.15a}$$

where $\tilde{\boldsymbol{d}}_1(\boldsymbol{r}) = \mathrm{Re}\big[\frac{\mathrm{i}}{\omega}\boldsymbol{v}_1(\boldsymbol{r})\mathrm{e}^{-\mathrm{i}\omega t}\big]$ is the fluid displacement at the position $\boldsymbol{r}$. Outside the viscous boundary layers, these quantities are related as found by using Eq. (2.11b) and $\boldsymbol{\nabla} \times \boldsymbol{v}_1^d = \boldsymbol{0}$,

$$\boldsymbol{\nabla} \times \boldsymbol{S}_{\mathrm{ac}}^d = \omega^2 \boldsymbol{\mathcal{L}}_{\mathrm{ac}}^d, \tag{2.15b}$$

where fields with superscript d are defined as in Eq. (2.15a) with $\boldsymbol{v}_1 \to \boldsymbol{v}_1^d$. This relation becomes important in Chapter 4 and in Paper III [3], since it shows that bulk-driven acosutic streaming is a consequence of rotating acoustics.

The acoustic fields set up the time-averaged momentum flux density tensor $\boldsymbol{\mathcal{T}}_{\mathrm{ac}}$,

$$\boldsymbol{\mathcal{T}}_{\mathrm{ac}} = \rho_0 \langle \tilde{\boldsymbol{v}}_1 \tilde{\boldsymbol{v}}_1 \rangle. \tag{2.16a}$$

By taking the negative divergence of this tensor and using Eqs. (2.10) and (2.11b) yields the acoustic body force $\boldsymbol{f}_{\mathrm{ac}} = \boldsymbol{f}_{\mathrm{ac}}^d + \boldsymbol{f}_{\mathrm{ac}}^\delta$ acting on the fluid (see also Eq. (36b) and (50) in Paper I [1]),

$$-\boldsymbol{\nabla} \cdot \boldsymbol{\mathcal{T}}_{\mathrm{ac}}^d = \boldsymbol{\nabla}\big(E_{\mathrm{pot}}^d - E_{\mathrm{kin}}^d\big) + \boldsymbol{f}_{\mathrm{ac}}^d, \qquad \boldsymbol{f}_{\mathrm{ac}}^d = \frac{\Gamma_0 \omega}{c_0^2} \boldsymbol{S}_{\mathrm{ac}}^d, \tag{2.16b}$$

$$-\boldsymbol{\nabla} \cdot \boldsymbol{\mathcal{T}}_{\mathrm{ac}}^\delta = -\rho_0 \boldsymbol{\nabla} \cdot \langle \tilde{\boldsymbol{v}}_1^\delta \tilde{\boldsymbol{v}}_1^\delta + \tilde{\boldsymbol{v}}_1^\delta \tilde{\boldsymbol{v}}_1^d + \tilde{\boldsymbol{v}}_1^d \tilde{\boldsymbol{v}}_1^\delta \rangle = \boldsymbol{f}_{\mathrm{ac}}^\delta. \tag{2.16c}$$

Here, the body force $\boldsymbol{f}_{\mathrm{ac}}^d$ drives the so-called bulk-driven acoustic streaming outside the viscous boundary layers, and $\boldsymbol{f}_{\mathrm{ac}}^\delta$ drives the so-called boundary-driven acoustic streaming. These phenomena, are discussed in Section 2.6 below.

The acoustic radiation force

The acoustic radiation force is a key phenomenon in the field of acoustofluidics and describes the time-averaged force on a particle due to the acoustic fields. For a spherical particle of radius a_{p} in the long-wave-length limit $a_{\mathrm{p}} \ll \lambda$ and far away from any obstacle, such as walls or other particles, the general expression for the radiation force is [83],

$$\boldsymbol{F}_{\mathrm{rad}} = -\pi a_{\mathrm{p}}^3 \left[\frac{2\kappa_0}{3} \mathrm{Re}\big(f_0^* p_1^* \boldsymbol{\nabla} p_1\big) - \rho_0 \mathrm{Re}\big(f_1^* \boldsymbol{v}_1^* \cdot \boldsymbol{\nabla} \boldsymbol{v}_1\big) \right], \tag{2.17}$$

where f_0 and f_1 are the dimensionless complex-valued monopole and dipole scattering coefficients, respectively. Note that since Eq. (2.17) is only correct far from the walls, it is implied that $\boldsymbol{v}_1 = \boldsymbol{v}_1^d$ and the superscript "d" is omitted in expressions for the acoustic radiation force. Equation (2.17) may be written in terms of the acoustic radiation potential, or Gorkov potential U_{rad} [84], by writing f_0 and f_1 in real and imaginary parts as $f_0 = f_0^{\text{r}} + \text{i}f_0^{\text{i}}$ and $f_1 = f_1^{\text{r}} + \text{i}f_1^{\text{i}}$, and using that $\boldsymbol{\nabla} \times \boldsymbol{v}_1 = \boldsymbol{0}$ outside the viscous boundary layer,

$$\boldsymbol{F}_{\text{rad}} = -\boldsymbol{\nabla} U_{\text{rad}} - \pi a_{\text{p}}^3 \left[\frac{2\kappa_0}{3} f_0^{\text{i}} \text{Im}\big(p_1^* \boldsymbol{\nabla} p_1\big) - \rho_0 f_1^{\text{i}} \text{Im}\big(\boldsymbol{v}_1^* \cdot \boldsymbol{\nabla} \boldsymbol{v}\big) \right], \tag{2.18a}$$

$$U_{\text{rad}} = \frac{4}{3}\pi a_{\text{p}}^3 \left[f_0^{\text{r}} E_{\text{pot}} - \frac{3}{2} f_1^{\text{r}} E_{\text{kin}} \right]. \tag{2.18b}$$

In many cases, the square parenthesis in Eq. (2.18a) is neglected either because f_0^{i} and f_1^{i} are small (see Table 2.2) or because a standing wave is assumed for which $\text{Im}\big(p_1^* \boldsymbol{\nabla} p_1\big)$ and $\text{Im}\big(\boldsymbol{v}_1^* \cdot \boldsymbol{\nabla} \boldsymbol{v}\big)$ vanish. In that case, the acoustic radiation force is a conservative force towards the minima in the radiation potential U_{rad}, thereby facilitating the focusing of particles which is exploited in acoustofluidics.

The expression for the scattering coefficients f_0 and f_1 may take into account increasingly detailed physics [79, 83, 84, 88–92]. Here, the scattering coefficients derived by Settnes and Bruus [83] are used, which are valid for a spherical particle of radius a_{p}, compressibility κ_{p}, and density ρ_{p} in a viscous fluid with viscous boundary-layer width δ,

$$f_0 = 1 - \frac{\kappa_{\text{p}}}{\kappa_0}, \qquad f_1 = \frac{2\big(\frac{\rho_{\text{p}}}{\rho_0} - 1\big)\big(1-\gamma\big)}{2\frac{\rho_{\text{p}}}{\rho_0} + 1 - 3\gamma}, \qquad \gamma = -\frac{3}{2}\left[1 + \text{i}\left(1 + \frac{\delta}{a_{\text{p}}}\right)\right]\frac{\delta}{a_{\text{p}}}. \tag{2.19}$$

Table 2.2 gives the material parameters and scattering coefficients for polystyrene particles which are often used to test the performance of microfluidic devices in the development process.

Table 2.2: Material parameters for polystyrene particles. The compressibility is calculated as $\kappa_{\text{ps}} = \frac{3(1-\sigma_{\text{ps}})}{1+\sigma_{\text{ps}}} \frac{1}{\rho_{\text{p}} c_{\text{ps}}^2}$ [66]. The values below the line are for a spherical particle of diameter $2a_{\text{p}} = 10\delta$ in water (*e.g.* radius $a_{\text{p}} = 1.9$ µm and frequency $f = 2$ MHz). The contrast factor Φ_{ps} is correct within 0.26 % for all particle sizes in a viscous fluid.

Parameter	Symbol	Value	Unit
Mass density [85]	ρ_{ps}	1050	kg m^{-3}
Compressibility	κ_{ps}	249	TPa^{-1}
Sound speed [86]	c_{ps}	2350	m/s
Poison's ratio [87]	σ_{ps}	0.35	–
Monopole coefficient [83]	$f_{0,\text{ps}}$	0.443	–
Dipole coefficient, Eq. (2.19)	$f_{1,\text{ps}}$	$0.034(1 + \text{i}\,0.005)$	–
Contrast factor, Eq. (2.20)	Φ_{ps}	0.165	–
F_{rad} in a rectangle, Eq. (2.20)	$\max\lvert\boldsymbol{F}_{\text{rad}}^{\text{rect}}\rvert$	0.017	pN

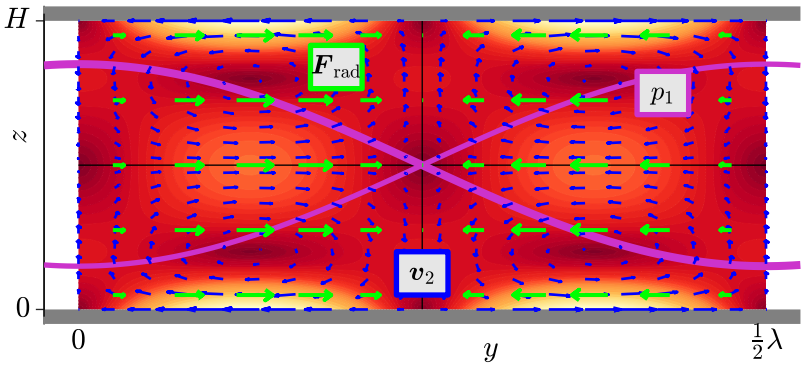

Figure 2.2: A standing pressure wave $p_1 = p_a \cos(k_0 y)$ (magenta lines) with wavelength $\lambda = \frac{2\pi}{k_0}$ parallel to two infinite walls at $z = 0$ and $z = H$. The green arrows show the radiation force $\boldsymbol{F}_{\text{rad}}$ from Eq. (2.20) for positive contrast factor Φ. The blue arrows show the boundary-driven acoustic streaming $\boldsymbol{v}_2$ (blue arrows) with the magnitude 0 (dark red) to $\frac{3}{8\rho_0^2 c_0^3}|p_a|^2$ of Eq. (2.21) (light yellow). Analytical solution of $\boldsymbol{v}_2$ is from Muller *et al.* [93] with the aspect ratio $\frac{H}{\frac{1}{2}\lambda}$ chosen to $\frac{180}{380}$.

A relevant example is a standing wave of the form $p_1 = p_a \cos(k_0 y)$ as shown in Fig. 2.2, for which $\boldsymbol{\nabla} E_{\text{kin}} = -\boldsymbol{\nabla} E_{\text{pot}} = \bar{E}_{\text{ac}} k_0 \sin(2k_0 y)\ \boldsymbol{e}_y$ with $\bar{E}_{\text{ac}} = \frac{1}{4}\kappa_0 p_a^2$ giving the radiation force from Eq. (2.18),

$$\boldsymbol{F}_{\text{rad}}^{\text{rect}} = 4\pi a_{\text{p}}^3 \Phi \bar{E}_{\text{ac}} k_0 \sin(2k_0 y)\ \boldsymbol{e}_y, \qquad \Phi = \frac{1}{3} f_0^{\text{r}} + \frac{1}{2} f_1^{\text{r}}. \tag{2.20}$$

This example introduces the acoustic contrast factor Φ [79, 83, 89]. For hard ($\kappa_{\text{p}} < \kappa_0$) and heavy ($\rho_{\text{p}} > \rho_0$) particles Φ is positive and the radiation force is towards the pressure nodes as shown in Fig. 2.2.

2.6 Acoustic streaming

Acoustic streaming is a steady flow that adds to the oscillatory motion of a sound wave and it has been known for more than 200 years. Some of the first studies of the phenomenon were the thorough observations of the motion of fine grains over a Chladni plate by Chladni [94], Ørsted [95], and Savart [96] in the early 1800. It was here noted, that whereas large grains found rest at the nodal lines of smallest plate vibration, finer grains gathered at the anti nodes having the largest vibration. This phenomenon was explained by M. Faraday [97] to be caused by steady currents in the air above the plate. A thorough theoretical treatment was provided by Lord Rayleigh [70], who explained the acoustic streaming observed in resonating Kundts tubes [98] to be driven by non-linear effects in the viscous boundary layer forming close to the walls. By integrating over the viscous boundary layer, he derived the so-called *limiting velocity* as a matching condition between the inner flow in the boundary layer and the outer streaming rolls. For the standing wave

shown in Fig. 2.2 with pressure $p_1 = p_a \cos(k_0 y)$ and velocity $\boldsymbol{v}_1^d(y) = v_a^d \sin(k_0 y)\, \boldsymbol{e}_y$, this seminal limiting velocity is,

$$\boldsymbol{v}_2^{\text{Rayleigh}} = -\frac{3}{8\omega}\partial_y \left|\boldsymbol{v}_1^d\right|^2 \boldsymbol{e}_y = -\frac{3}{8}\frac{\left|v_a^d\right|^2}{c_0}\cos(2k_0 y)\,\boldsymbol{e}_y = -\frac{3}{8}\frac{\left|p_a\right|^2}{\rho_0^2 c_0^3}\cos(2k_0 y)\,\boldsymbol{e}_y. \tag{2.21}$$

In Fig. 2.2 is shown the acoustic streaming obtained by imposing the boundary condition $\boldsymbol{v}_2 = \boldsymbol{v}_2^{\text{Rayleigh}}$ at the parallel walls [93]. The matching approach by Lord Rayleigh was later generalized by Nyborg [71] who formulated the limiting-velocity theory for standing waves close to weakly curved walls having a curvature radius much larger than the viscous boundary-layer width δ, and oscillating in the normal direction. Further generalizations of the limiting-velocity theory are listed in Table 2.3 and cover the inclusion of travelling waves by Lee and Wang [73], thermoviscous contributions by Rednikov and Sadhal [75], and wall velocities in any direction for a flat wall by Vanneste and Bühler [74].

Table 2.3: Overview of different contributions to the slip-velocity theory. "Field type" refers to the type of the amplitude p_1 of the pressure $\tilde{p}_1 = \mathrm{Re}\big(p_1 \mathrm{e}^{-\mathrm{i}\omega t}\big)$.

Year	Author(s)	Field type	Wall motion	Shape	Viscous model
1884	Lord Rayleigh [70]	Real	Motionless	Flat	Viscous
1958	Nyborg [71]	Real	Perpendicular	Curved	Viscous
1990	Lee & Wang [73]	Complex	Perpendicular	Curved	Viscous
2011	Rednikov & Sadhal [75]	Complex	Motionless	Curved	Thermoviscous
2011	Vanneste & Bühler [74]	Complex	Any direction	Flat	Viscous
2018	Bach & Bruus [1]	Complex	Any direction	Curved	Viscous

This thesis: The slip velocity for curved elastic walls

This thesis contributes to the development of the slip-velocity theory by allowing for both curved walls and wall motion in any direction. Furthermore, the boundary-layer theory is formulated in coordinate-free form without reference to any particular coordinate system which facilitates implementation in general systems, see Chapter 3 for further details.

Governing equations for acoustic streaming

The steady streaming velocity $\boldsymbol{v}_2$ in a homogeneous fluid is described by the second-order time-averaged part of Eq. (2.1) and the boundary condition (2.6c) [1],

$$0 = \rho_0 \boldsymbol{\nabla}\cdot \boldsymbol{v}_2 + \boldsymbol{\nabla}\cdot \langle \tilde{\rho}_1 \tilde{\boldsymbol{v}}_1 \rangle, \qquad \text{for } \boldsymbol{r} \in \Omega, \tag{2.22a}$$

$$\boldsymbol{0} = -\boldsymbol{\nabla} p_2 + \boldsymbol{\nabla}\cdot \boldsymbol{\tau}_2 - \rho_0 \boldsymbol{\nabla}\cdot \langle \tilde{\boldsymbol{v}}_1 \tilde{\boldsymbol{v}}_1 \rangle, \qquad \text{for } \boldsymbol{r} \in \Omega, \tag{2.22b}$$

$$\boldsymbol{0} = \boldsymbol{v}_2 + \langle (\tilde{\boldsymbol{s}}_1 \cdot \boldsymbol{\nabla}) \tilde{\boldsymbol{v}}_1 \rangle, \qquad \text{for } \boldsymbol{r} \in \partial\Omega. \tag{2.22c}$$

From Eq. (2.22b), it is seen that the driving mechanism for the steady acoustic streaming is the convergence of the time-averaged momentum flux density tensor $\rho_0 \langle \tilde{\boldsymbol{v}}_1 \tilde{\boldsymbol{v}}_1 \rangle$ which

gives rise to the time-averaged body force $\boldsymbol{f}_{\text{ac}}$ evaluated in Eqs. (2.16). Acoustic streaming is often classified into three types listed below together with the corresponding driving mechanism:

Boundary-layer streaming, also called "*Schlichting streaming*" [99], or "*inner streaming*" [73], is the short-range acoustic streaming rolls inside the viscous boundary layer, that are driven by the boundary-layer body force,

$$\boldsymbol{f}_{\text{ac}}^{\delta} = -\rho_0 \boldsymbol{\nabla} \cdot \langle \tilde{\boldsymbol{v}}_1^{\delta} \tilde{\boldsymbol{v}}_1^{\delta} + \tilde{\boldsymbol{v}}_1^{\delta} \tilde{\boldsymbol{v}}_1^{d} + \tilde{\boldsymbol{v}}_1^{d} \tilde{\boldsymbol{v}}_1^{\delta} \rangle, \qquad \text{for } \boldsymbol{r} \in \Omega. \tag{2.23a}$$

This streaming decays away from the wall with the boundary-layer length scale δ.

Boundary-driven streaming, also called "*Rayleigh streaming*" [70], or "*outer streaming*" [73] is the long-range acoustic streaming that results from the boundary-layer streaming but varies on a length scale d much longer than the boundary-layer length scale δ. For $d \gg \delta$, this streaming may be thought of as driven by a slip boundary condition,

$$\boldsymbol{v}_2^{d} = \boldsymbol{v}_2^{\text{slip}}, \qquad \text{for } \boldsymbol{r} \in \partial\Omega. \tag{2.23b}$$

Here, the slip boundary condition $\boldsymbol{v}_2^{\text{slip}}$ can be approximated by $\boldsymbol{v}_2^{\text{Rayleigh}}$ from Eq. (2.21) in the special case of a standing 1D wave over a flat wall, but take a more complicated form in the general case of a curved oscillating wall as described in Chapter 3. The slip velocity also takes into account the Lagrangian no-slip condition (2.22c), although streaming driven by this effect is not caused by the body force $\boldsymbol{f}_{\text{ac}}^{\delta}$ of Eq. (2.23a) in boundary layer. Acoustic streaming caused by the Lagrangian no-slip condition is sometimes referred to as "*McIntyre streaming*" [75, 100], but here, it is classified as "*boundary-driven streaming*".

Bulk-driven streaming, also called "*Eckart streaming*" or "*Quartz wind*" [101], is the long-range acoustic streaming outside the viscous boundary layer driven by the body force derived in Eq. (2.16b),

$$\boldsymbol{f}_{\text{ac}}^{d} = \frac{\Gamma_0 \omega}{c_0^2} \boldsymbol{S}_{\text{ac}}^{d}, \qquad \text{for } \boldsymbol{r} \in \Omega. \tag{2.23c}$$

Whereas this expression applies for the homogeneous fluids considered in this thesis, it should be noted that recent studies by Karlsen and Bruus [102, 103] shows that inhomogeneities in the fluid compressibility κ_0 and density ρ_0 induce the non-dissipative body force $-\frac{1}{4}|p_1|^2 \boldsymbol{\nabla}\kappa_0 - \frac{1}{4}|\boldsymbol{v}_1^{d}|^2 \boldsymbol{\nabla}\rho_0$ which should be added on the right-hand side of Eq. (2.23c) in the case of inhomogeneous fluids.

This thesis: Bulk-driven streaming at the wavelength scale

Bulk-driven acoustic streaming is often ignored in microfluidic devices of length scale much smaller than the attenuation length scale, which is *e.g.* the case for a single standing-half-wave resonance. It is however shown in Chapter 4 and in Paper III [3], that the body force $\boldsymbol{f}_{\text{ac}}^{d}$ in Eq. (2.23c) is significant in such systems if the acoustic resonance is rotating.

2.7 Acoustophoresis in microsystems

Acoustophoresis is the migration of particles due to sound waves and the applications of this phenomenon are numerous as described in Chapter 1. One great advantage in microfluidics is the smallness of the channel dimension leading to a laminar flow. This is often also the case for the acoustic streaming, since the streaming Reynolds number $\mathrm{Re}_{\mathrm{str}} = \frac{\rho_0 L_{\mathrm{str}}}{\eta_0}|\boldsymbol{v}_2|$ in water (see Table 2.1) with speed $|\boldsymbol{v}_2| \lesssim 1$ mm/s and streaming length scale $L_{\mathrm{str}} \lesssim 1$ mm is around unity or smaller. In acoustofluidics, the main forces on a suspended spherical particle of radius a_{p}, volume $V_{\mathrm{p}} = \frac{4}{3}\pi a_{\mathrm{p}}^3$, mass m_{p}, and velocity $\boldsymbol{v}_{\mathrm{p}}$, are the Stokes drag force $\boldsymbol{F}_{\mathrm{drag}} = 6\pi\eta_0 a_{\mathrm{p}}(\boldsymbol{v}_2 - \boldsymbol{v}_{\mathrm{p}})$ and the radiation force $\boldsymbol{F}_{\mathrm{rad}}$ from Eq. (2.18), resulting in the following equation of motion for the particle,

$$\left(m_{\mathrm{p}} + \frac{1}{2}\rho_0 V_{\mathrm{p}}\right)\frac{\mathrm{d}\boldsymbol{v}_{\mathrm{p}}}{\mathrm{d}t} = 6\pi\eta_0 a_{\mathrm{p}}(\boldsymbol{v}_2 - \boldsymbol{v}_{\mathrm{p}}) + \boldsymbol{F}_{\mathrm{rad}}, \tag{2.24a}$$

where other forces, such as the gravitational body force $\boldsymbol{F}_g = m_{\mathrm{p}}\boldsymbol{g}$, are omitted for simplicity. In Eq. (2.24a), $\frac{1}{2}\rho_0 V_{\mathrm{p}}$ on the left-hand side is the added mass which is dragged along with the particle [104]. Inertial forces are neglected since their size are $\sim (\rho_0 a_{\mathrm{p}}^3)|\boldsymbol{v}_2|^2/L_{\mathrm{str}}$, which is smaller than the viscous forces of size $\sim \eta_0|\boldsymbol{v}_2|a_{\mathrm{p}}$ by a factor $(\frac{a_{\mathrm{p}}}{L_{\mathrm{str}}})^2\mathrm{Re}_{\mathrm{str}} \ll 1$, see *e.g.* Maxey and Riley [104] for further details. Typical additions of the right-hand side of Eq. (2.24a) include the Oseen correction $\frac{3}{8}\mathrm{Re}_{\mathrm{p}}\, 6\pi\eta_0 a_{\mathrm{p}}(\boldsymbol{v}_2 - \boldsymbol{v}_{\mathrm{p}})$ to account for higher particle Reynolds number $\mathrm{Re}_{\mathrm{p}} = \frac{\rho_0 a_{\mathrm{p}}}{\eta_0}|\boldsymbol{v}_2 - \boldsymbol{v}_{\mathrm{p}}|$ [104, 105], or the Faxén correction $\pi\eta_0 a_{\mathrm{p}}^3\nabla^2\boldsymbol{v}_2$ [104, 106] to account for curvature in the streaming flow. These corrections are neglected in this work.

It is noted from Eq. (2.24a) that the particle will reach a terminal velocity on the time scale $\frac{m_{\mathrm{p}} + \frac{1}{2}\rho_0 V_{\mathrm{p}}}{6\pi\eta_0 a_{\mathrm{p}}}$, which is around 9 µs for a neutrally buoyant particle with $m_{\mathrm{p}} = \rho_0 V_{\mathrm{p}}$ of radius $a_{\mathrm{p}} = 5$ µm in water. With a typical particle velocity of $|\boldsymbol{v}_{\mathrm{p}}| \lesssim 1$ mm/s, the distance travelled in this time is less than 9 nm and a good approximation for the particle velocity in microfluidic acoustophoresis is therefore to use the terminal velocity,

$$\boldsymbol{v}_{\mathrm{p}} \approx \boldsymbol{v}_2 + \frac{1}{6\pi\eta_0 a_{\mathrm{p}}}\boldsymbol{F}_{\mathrm{rad}}. \tag{2.24b}$$

In the simple case of a 1D standing wave shown in Fig. 2.2 this equation may be used with Eq. (2.20) for $\boldsymbol{F}_{\mathrm{rad}}$ and Eq. (2.21) for the slip velocity $\boldsymbol{v}_2^{\mathrm{Rayleigh}}$ to estimate the maximum particle speeds $v_{\mathrm{p}}^{\mathrm{rad}}$ and $v_{\mathrm{p}}^{\mathrm{drag}}$, resulting from the radiation force and from the drag force, respectively,

$$v_{\mathrm{p}}^{\mathrm{rad}} \sim \frac{8\Phi}{9}\frac{a_{\mathrm{p}}^2}{\delta^2}\frac{3}{2\rho_0 c_0}\bar{E}_{\mathrm{ac}}. \qquad v_{\mathrm{p}}^{\mathrm{drag}} \sim \frac{3}{2\rho_0 c_0}\bar{E}_{\mathrm{ac}}, \tag{2.25}$$

where $\bar{E}_{\mathrm{ac}} = \frac{1}{4}\kappa_0|p_a|^2$ is the average acoustic energy density. For an average energy density of $\bar{E}_{\mathrm{ac}} = 1$ Pa in water, we obtain $\frac{3}{2\rho_0 c_0}\bar{E}_{\mathrm{ac}} \approx 1\ \frac{\mu\mathrm{m}}{\mathrm{s}}$, and thus the rule thump about the typical streaming speed, "1 $\frac{\mu\mathrm{m}}{\mathrm{s}}$ per Pa". In experiments, the acoustic energy density $\bar{E}_{\mathrm{ac}}$ may be obtained by balancing the radiation force on a single particle with either gravitational [107] or electrical [108] forces, or by tracing the particle motion and fitting to Eq. (2.24b) [109, 110].

Focusing of small particles using acoustophoresis

As seen from Eq. (2.25), the particle motion of sufficiently small particles will be dominated by the acoustic streaming. The theoretical cross-over radius $a_{\mathrm{p}}^{\mathrm{crit}}$ where the drag force and radiation force are equal is found by equating the two expressions in Eq. (2.25) giving [66, 67],

$$a_{\mathrm{p}}^{\mathrm{crit}} = \sqrt{\frac{9}{8\Phi}}\delta \qquad \Rightarrow \quad a_{\mathrm{p}}^{\mathrm{crit}} \approx 1\ \mu\mathrm{m} \quad \text{for polystyrene particles in water at 2 MHz,} \tag{2.26}$$

where the numerical value is obtained by using Eqs. (2.19) and (2.20) for Φ (note that Φ depends on a_{p}) and the parameters for polystyrene particles listed in Table 2.2. This limit can be reduced by increasing the frequency since $\delta = \sqrt{\frac{2\eta_0}{\rho_0\omega}}$ as done by Collins *et al.* [111] and Wu *et al.* [53] who used surface-acoustic waves (SAW) at a high frequency of around 30-50 MHz to separate polystyrene particles of diameters 0.5 µm and 0.3 µm. Another successful method to handle small particles is developed by Hammarström *et al.* [42] who used a larger seed particle trapped acoustically in a capillary tube to attract smaller particles yielding an up-concentration of particles of diameter 0.1 µm at 4 MHz. Antfolk *et al.* [54] and Mao *et al.* [112] used a rotating acoustic field in a square capillary tube to change the streaming pattern allowing for focusing of particles of diameter 0.6 µm at 3 MHz. Also pulsed ultrasound has been investigated [113, 114] in order to suppress the acoustic streaming. A recent development which is promising for future focusing of nanoparticles is the observation by Karlsen, Qui, Augustsson, and Bruus [102, 103, 115] that acoustic streaming can be suppressed in inhomogeneous fluids.

This thesis: Shape-optimization for suppression of streaming

This thesis contributes to the above development towards handling of sub-micron particles. In Paper V [5] we demonstrate numerically that the acoustic streaming can be suppressed by two orders of magnitude by optimizing the shape of the resonating cavity. It is theoretically shown that this approach allows for focusing of particles with diameter down to 0.3 µm in a standing wave at 3 MHz.

Chapter 3

The viscous boundary layer at a curved oscillating surface

This chapter is devoted to the starting point of the research done in this PhD project, namely the theoretical analysis of the viscous boundary layer at a curved oscillating surface as shown in Fig. 3.1. I will not give the full details of the analysis, which can be found in Paper I [1], but instead provide some of the key steps and results. There will be some overlap with my Master Thesis [116], but the results and derivations are significantly improved. The analysis leads to effective boundary conditions on the long-range acoustic pressure and streaming, which analytically take into account all the physical effects from the viscous boundary layer.

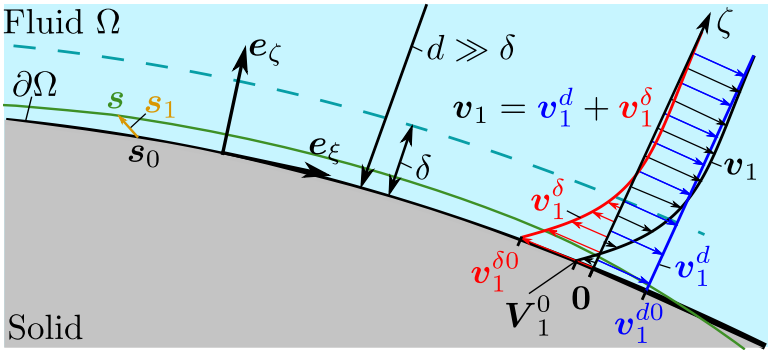

Figure 3.1: Sketch of the fluid-solid interface as in Fig. 2.1 but with the viscous boundary layer added. The local curvilinear coordinate system on the interface is given by the tangent vectors $\boldsymbol{e}_\xi$ and $\boldsymbol{e}_\eta$ and the normal vector $\boldsymbol{e}_\zeta$. By the Helmholtz decomposition in Eq. (2.10), the first-order acoustic fluid velocity $\boldsymbol{v}_1 = \boldsymbol{v}_1^d + \boldsymbol{v}_1^\delta$ is written as the sum of a long-range compressible part $\boldsymbol{v}_1^d$ (blue) extending into the bulk and a short-range incompressible part $\boldsymbol{v}_1^\delta$ (red) with a decay length equal to the boundary-layer width δ. At $\zeta = 0$, Eq. (2.6c) dictates that $\boldsymbol{v}_1^{\delta 0} + \boldsymbol{v}_1^{d0} = \boldsymbol{V}_1^0$. Adapted from Fig. 1 in Paper I [1].

3.1 Length scales of acoustic fields in microsystems

There are several length scales involved in the boundary-layer analysis of the acoustic fields close to a curved oscillating boundary as sketched in Fig. 3.1. Some of these length scales are plotted against frequency in Fig. 3.2 and will be referred to throughout this chapter and Chapter 4.

For a
nm [117],
in Fig. 3
Eq. (2.6b

The varia
the small
the variat
$\mathcal{L}$ which
central as
δ is much

As seen i

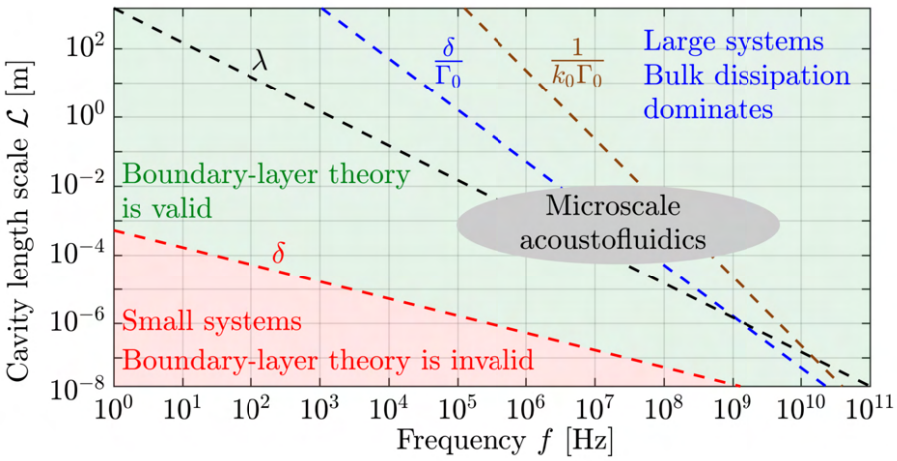

Figure 3.2: Phase diagram of the region of validity of the boundary-layer theory for water with parameters given in Table 2.1. The dashed lines are the boundary-layer length scale $\delta = \sqrt{\frac{2\eta_0}{\rho\omega}}$ (red), the acoustic wavelength $\lambda = \frac{c_0}{f}$ (black), the length scale $\frac{\delta}{\Gamma_0}$,where bulk-dissipation and boundary-dissipation are equal (blue, see Eq. (3.9)), and the bulk dissipation length scale $\frac{1}{k_0\Gamma_0}$ (brown). Microscale acoustofluidics typically spans length scales from 50 µm to 1 cm and frequencies from 0.1 MHz up to several GHz.

cavity length scale $\mathcal{L}$ that may violate condition (3.1b). In the green region of Fig. 3.2, Eq. (3.1b) is satisfied and the boundary-layer theory is valid.

If the conditions (3.1) are satisfied, it is possible to significantly simplify the vector equations for the acoustic fields and streaming in the boundary layer. The reason is that the boundary-layer velocity $\boldsymbol{v}^\delta$, denoted by superscript "δ" varies on the length scale δ in the perpendicular ζ-direction (see Fig. 3.1) but on the length scale d in the parallel directions. One central example is the Laplacian ∇^2 of a boundary-layer field, which simplifies to,

$$\nabla^2 \boldsymbol{v}^\delta = \partial_\zeta^2 \boldsymbol{v}^\delta + \mathcal{O}(\epsilon). \tag{3.2}$$

3.2 The first-order boundary layer and the boundary condition on the acoustic pressure

The viscous boundary layer of the first-order acoustic fields is sketched in Fig. 3.1, and is described by the shear velocity field $\boldsymbol{v}_1^\delta$, satisfying the Helmholtz equation $\nabla^2 \boldsymbol{v}_1^\delta + k_\mathrm{s}^2 \boldsymbol{v}_1^\delta = \boldsymbol{0}$ in Eq. (2.11a), and the incompressibility condition $0 = \boldsymbol{\nabla}\cdot\boldsymbol{v}_1^\delta$ in Eq. (2.10). With the approximation of the Laplacian in Eq. (3.2), the solution that decays away from the boundary $\zeta \to \infty$ is,

$$\boldsymbol{v}_1^\delta \approx \boldsymbol{v}_1^{\delta 0} \mathrm{e}^{\mathrm{i}k_\mathrm{s}\zeta}, \qquad \boldsymbol{v}_1^{\delta 0} = \boldsymbol{V}_1^0 - \boldsymbol{v}_1^{d0}, \tag{3.3}$$

where the superscript "0" denote evaluation at the surface equilibrium position $\boldsymbol{s}_0$ where $\zeta = 0$. Here, $\boldsymbol{v}_1^{\delta 0}$ is chosen to satisfy the boundary condition (2.6c), namely $\boldsymbol{v}_1^{\delta 0} + \boldsymbol{v}_1^{d0} = \boldsymbol{V}_1^0$ at $\zeta = 0$. The incompressibility condition $0 = \boldsymbol{\nabla}\cdot\boldsymbol{v}_1^\delta$ from Eq. (2.10) gives a relation between the perpendicular component $v_{1\zeta}^{\delta 0}$ and the divergence $\boldsymbol{\nabla}\cdot\boldsymbol{v}_1^{\delta 0}$ of the surface field $\boldsymbol{v}_1^{\delta 0}$,

$$0 = \boldsymbol{\nabla}\cdot\boldsymbol{v}_1^\delta = \boldsymbol{\nabla}\cdot\left(\boldsymbol{v}_1^{\delta 0}\mathrm{e}^{\mathrm{i}k_\mathrm{s}\zeta}\right) = \left(\mathrm{i}k_\mathrm{s} v_{1\zeta}^{\delta 0} + \boldsymbol{\nabla}\cdot\boldsymbol{v}_1^{\delta 0}\right)\mathrm{e}^{\mathrm{i}k_\mathrm{s}\zeta} \tag{3.4a}$$

$$\Rightarrow v_{1\zeta}^{\delta 0} = \frac{\mathrm{i}}{k_\mathrm{s}}\boldsymbol{\nabla}\cdot\boldsymbol{v}_1^{\delta 0}. \tag{3.4b}$$

The standard procedure in pressure-acoustics calculations [71, 72, 75] is to insist that the perpendicular component $V_{1\zeta}^0$ of the wall velocity acts directly on the perpendicular component $v_{1\zeta}^{d0}$ of the pressure-related velocity giving the condition $v_{1\zeta}^{d0} = V_{1\zeta}^0$ at the wall. Here, it is found that the perpendicular pressure-related velocity $v_{1\zeta}^{d0}$ depends on both the wall velocity $V_{1\zeta}^0$ and the boundary-layer velocity $v_{1\perp}^{\delta 0}$, giving instead $v_{1\zeta}^{d0} = V_{1\zeta}^0 - v_{1\zeta}^{\delta 0}$. Therefore, by use of Eq. (3.3), the boundary condition on the pressure-induced velocity $v_{1\zeta}^d$ is,

$$v_{1\zeta}^{d0} = V_{1\zeta}^0 - v_{1\zeta}^{\delta 0} = V_{1\zeta}^0 - \frac{\mathrm{i}}{k_\mathrm{s}}\boldsymbol{\nabla}\cdot\left(\boldsymbol{V}_1^0 - \boldsymbol{v}_1^{d0}\right). \tag{3.5}$$

Hence, a parallel compression of the fluid close to the boundary induces a perpendicular velocity due to the viscous incompressible boundary layer. Using that $\boldsymbol{v}_1^d = \frac{-\mathrm{i}(1-\mathrm{i}\Gamma_0)}{\omega\rho_0}\boldsymbol{\nabla}p_1$,

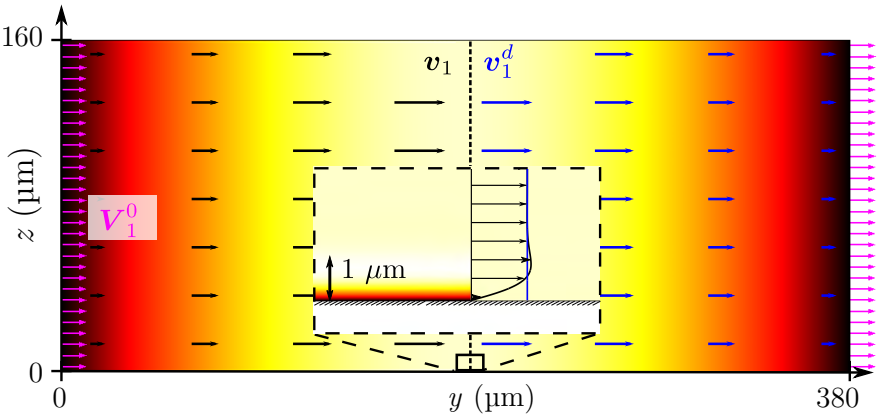

Figure 3.3: Comparison between the acoustic velocity obtained numerically by using the full boundary-layer resolved model (left, black arrows, $\boldsymbol{v}_1$) and the effective model without the boundary layers resolved (right, blue arrows, $\boldsymbol{v}_1^d$) in a rectangular cavity at the resonance frequency $f = 1.9481$ MHz and side-wall actuation $\boldsymbol{V}_1^0 = -\mathrm{i}\omega d_0 \boldsymbol{e}_y$ (magenta arrows) with $d_0 = 0.1$ nm. The color plot ranges from from 0 (black) to 0.68 m/s (light yellow).

Eq. (2.11b), this may be expressed as a boundary condition on the acoustic pressure,

$$\partial_\zeta p_1 + \frac{\mathrm{i}}{k_\mathrm{s}}\left[k_\mathrm{c}^2 p_1 + \partial_\zeta^2 p_1\right] = \frac{\mathrm{i}\omega\rho_0}{1-\mathrm{i}\Gamma_0}\left[V_{1\zeta}^0 - \frac{\mathrm{i}}{k_\mathrm{s}}\boldsymbol{\nabla}\cdot\boldsymbol{V}_1^0\right]. \tag{3.6}$$

As thoroughly verified in Paper I [1] this boundary condition for p_1 takes into account all the effects of the viscous boundary layer analytically. Since this approach avoids the numerical resolving of the boundary layer, it is called an "*effective model*". In Fig. 3.3 is shown a comparison between the acoustic velocity obtained from the full boundary-layer resolved model, Eq. (2.7), and obtained by calculating p_1 with the boundary condition (3.6) and then using $\boldsymbol{v}_1^d = \frac{-\mathrm{i}(1-\mathrm{i}\Gamma_0)}{\omega\rho_0}\boldsymbol{\nabla}p_1$.

Input and power loss for acoustic fields with boundary layers

When calculating the acoustic pressure p_1 with the effective boundary-layer boundary condition (3.6) it is relevant to ask how the viscous energy loss in the boundary layer is taken into account. Physically, the energy dissipates due to velocity gradients which are particularly large in the boundary layer, as calculated from $\bar{P}_\mathrm{diss}$ in Eq. (2.13). In the effective model, this energy loss is taken into account through an energy flux at the boundary. To see this, consider the local energy balance of the long-range fields $\boldsymbol{v}_1^d$ and p_1, which is obtained in Section B.2 of Appendix B,

$$-\boldsymbol{\nabla}\cdot\langle\tilde{p}_1\tilde{\boldsymbol{v}}_1^d\rangle = \frac{1}{2}\Gamma_0\omega\rho_0\left|\boldsymbol{v}_1^d\right|^2, \tag{3.7}$$

expressing the balance between the convergence of energy flux $\langle\tilde{p}_1\tilde{\boldsymbol{v}}_1^d\rangle$ and the power loss $\frac{1}{2}\Gamma_0\omega\rho_0\left|\boldsymbol{v}_1^d\right|^2$ due to both viscous energy transport and dissipation. The global energy

balance is found by integrating this equation over the entire domain Ω and using Gauss's law. In conventional pressure acoustics, the energy flux $\langle \tilde{p}_1 \tilde{v}^d_{1\zeta} \rangle$ at the boundary is given purely by the power $\langle \tilde{p}_1 \tilde{V}^0_{1\zeta} \rangle$ delivered by the wall. When the boundary layer is included, Eq. (3.5) gives the additional contribution $-\langle \tilde{p}_1 \tilde{v}^{\delta 0}_{1\zeta} \rangle$ to this boundary energy flux, leading to the global energy balance between input and loss, see Appendix B for details,

$$\oint_{\partial\Omega} \frac{1}{2} \mathrm{Re}\Big[p_1^* \Big(V^0_{1\zeta} - \frac{\mathrm{i}}{k_\mathrm{s}} \boldsymbol{\nabla}_\parallel \cdot \boldsymbol{V}^0_{1\parallel} \Big) \Big] \,\mathrm{d}A = \int_\Omega \frac{1}{2} \Gamma_0 \rho_0 \omega \big| \boldsymbol{v}^d_1 \big|^2 \,\mathrm{d}V + \oint_{\partial\Omega} \frac{1}{4} \delta \rho_0 \omega \big| \boldsymbol{v}^{d0}_{1\parallel} \big|^2 \,\mathrm{d}A. \tag{3.8}$$

Here, the inclusion of the viscous boundary layer is represented by the second term on each side. Note that the additional power $\oint_{\partial\Omega} -\frac{1}{2}\mathrm{Re}\big[p_1^* \frac{\mathrm{i}}{k_\mathrm{s}} \boldsymbol{\nabla}_\parallel \cdot \boldsymbol{V}^0_{1\parallel}\big] \,\mathrm{d}A$ delivered by the wall is usually negligible since $\frac{1}{k_\mathrm{s}} \boldsymbol{\nabla}_\parallel \cdot \boldsymbol{V}^0_{1\parallel} \sim \frac{\delta}{d} |\boldsymbol{V}^0_{1\parallel}|$ which is usually much smaller than the perpendicular velocity $|V^0_{1\zeta}|$. In contrast, the power-loss term $\oint_{\partial\Omega} \frac{1}{4} \delta \rho_0 \omega \big| \boldsymbol{v}^{d0}_{1\parallel} \big|^2 \,\mathrm{d}A$ on the right-hand side due to the viscous boundary layer is usually much larger than the conventional bulk power-loss term $\int_\Omega \frac{1}{2} \Gamma_0 \rho_0 \omega \big| \boldsymbol{v}^d_1 \big|^2 \,\mathrm{d}V$. For a fluid cavity of length scale $\mathcal{L}$, fluid-solid interface area $\mathcal{L}^2$, and fluid volume $\mathcal{L}^3$, the ratio between the boundary-layer power loss and the bulk power loss is,

$$\frac{\oint_{\partial\Omega} \frac{1}{4} \delta \rho_0 \omega \big| \boldsymbol{v}^{d0}_{1\parallel} \big|^2 \,\mathrm{d}A}{\int_\Omega \frac{1}{2} \Gamma_0 \rho_0 \omega \big| \boldsymbol{v}^d_1 \big|^2 \,\mathrm{d}V} \sim \frac{\delta}{\Gamma_0 \mathcal{L}}. \tag{3.9}$$

Hence, the boundary layer is important for the loss calculations in systems of length scale $\mathcal{L} \lesssim \frac{\delta}{\Gamma_0}$ which is plotted with blue dashed line in Fig. 3.2. For water at 2 MHz frequency, this length is 4.7 cm or 62 λ. For systems much larger than this size, the bulk dissipation dominates and the boundary layer may be ignored in the calculation of the acoustic pressure.

Effective stress on the wall

The presence of the shear field in the boundary layer introduces a viscous stress on the wall in addition to the acoustic pressure. The dominating part of the shear stress tensor $\boldsymbol{\tau}_1$ at the wall is $\eta_0 \partial_\zeta \boldsymbol{v}^\delta_1 = \eta_0 \mathrm{i} k_\mathrm{s} \boldsymbol{v}^{\delta 0}_1$, and the total stress on the wall is approximately,

$$\boldsymbol{\sigma}_1 \cdot \boldsymbol{e}_\zeta \approx -p_1 \boldsymbol{e}_\zeta + \mathrm{i} k_\mathrm{s} \eta_0 \boldsymbol{v}^{\delta 0}_1. \tag{3.10}$$

Note that the second term is usually ϵ smaller than the pressure term, but may be significant for a large parallel wall motion.

3.3 The second-order streaming and the slip boundary condition

The steady acoustic streaming is governed by Eq. (2.22), which contain the two driving mechanisms: (1) the body force $\boldsymbol{f}_\mathrm{ac} = -\boldsymbol{\nabla} \cdot \langle \rho_0 \tilde{\boldsymbol{v}}_1 \tilde{\boldsymbol{v}}_1 \rangle$ and (2) the Lagrangian no-slip

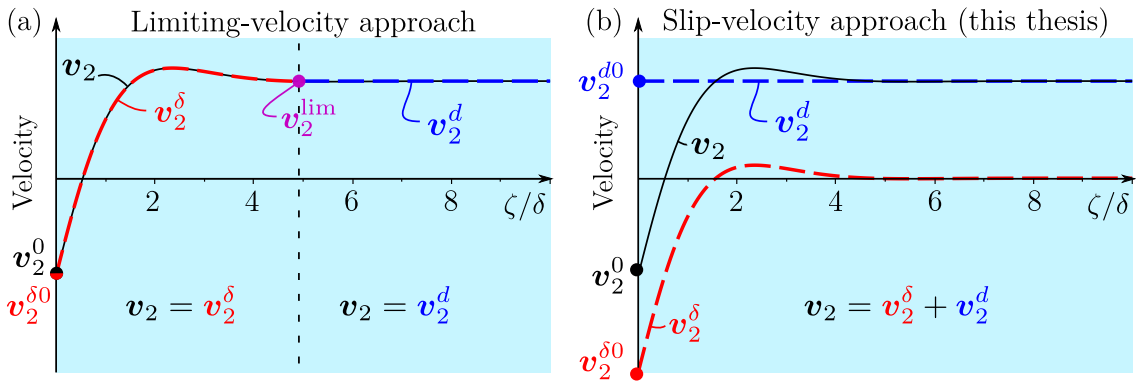

Figure 3.4: Sketch of two different approaches to the second-order boundary-layer analysis. The boundary condition on the fluid velocity is $\boldsymbol{v}_2 = \boldsymbol{v}_2^0$ at the boundary equilibrium position $\zeta = 0$ with $\boldsymbol{v}_2^0 = \boldsymbol{0}$ in Refs. [70–72, 75] and $\boldsymbol{v}_2^0 = -\langle(\tilde{\boldsymbol{s}}_1 \cdot \boldsymbol{\nabla})\tilde{\boldsymbol{v}}_1\rangle$ in Ref. [74] and in this work. (a) In the limiting-velocity approach [70–72, 74, 75], the fluid domain is divided into the boundary-layer region where $\boldsymbol{v}_2 = \boldsymbol{v}_2^\delta$ (red) and the bulk region where $\boldsymbol{v}_2 = \boldsymbol{v}_2^d$ (blue), and the streaming velocity is matched by the limiting velocity $\boldsymbol{v}_2^{\mathrm{lim}}$ (purple) at the edge of the boundary layer. (b) In the slip-velocity approach used in this thesis, the boundary-layer field $\boldsymbol{v}_2^\delta$ (red) and the bulk field $\boldsymbol{v}_2^d$ (blue) coexist in the entire fluid domain and their sum $\boldsymbol{v}_2 = \boldsymbol{v}_2^\delta + \boldsymbol{v}_2^d$ (black) satisfy the boundary condition $\boldsymbol{v}_2^0$ at $\zeta = 0$.

boundary condition $\boldsymbol{0} = \boldsymbol{v}_2 + \langle\tilde{\boldsymbol{s}}_1 \cdot \boldsymbol{\nabla}\tilde{\boldsymbol{v}}_1\rangle$. For the first-order fields, the boundary-layer velocity $\boldsymbol{v}_1^\delta$ was conveniently extracted by a Helmholtz decomposition. For the second-order fields, it is less clear how to extract the boundary-layer streaming. The classical "*limiting-velocity*" approach often used in the literature [70–72, 74, 75] is sketched in Fig. 3.4(a). Here, the inner streaming is first calculated to obtain the so-called "limiting velocity" in the limit $\zeta \to \infty$, which become the boundary condition on the outer streaming. However, this approach makes it inconvenient to implement the no-slip boundary condition, $\boldsymbol{v}_2 = -\langle(\tilde{\boldsymbol{s}}_1 \cdot \boldsymbol{\nabla})\tilde{\boldsymbol{v}}_1\rangle$ at the wall[1]. In this thesis, a slightly different approach is used, called the "*slip-velocity*" approach as sketched in Fig. 3.4(b). Here, the streaming velocity $\boldsymbol{v}_2$ is decomposed into a short-range streaming velocity $\boldsymbol{v}_2^\delta$ and a long-range streaming velocity $\boldsymbol{v}_2^d$ which coexist inside the boundary layer, such that their sum is the total streaming,

$$\boldsymbol{v}_2 = \boldsymbol{v}_2^\delta + \boldsymbol{v}_2^d. \tag{3.11}$$

It is emphasized, that this decomposition is not a mathematical Helmholtz decomposition but rather a physical separation of length scales. Choosing the short-range velocity to decay outside the boundary layer, the long-range velocity $\boldsymbol{v}_2^d$ must ensure the boundary condition,

$$\boldsymbol{v}_2^\delta \to \boldsymbol{0}, \qquad \text{for } \zeta \to \infty, \tag{3.12a}$$

$$\boldsymbol{v}_2^{d0} = -\boldsymbol{v}_2^{\delta 0} - \langle\tilde{\boldsymbol{s}}_1 \cdot \boldsymbol{\nabla}\tilde{\boldsymbol{v}}_1\rangle, \qquad \text{for } \zeta = 0, \tag{3.12b}$$

[1] Vanneste and Bühler [74] did this by solving for the Lagrangian mean flow in their Eq. (4.8).

where it is recalled that the superscript "0" denote evaluation of a velocity field at the surface equilibrium position. The velocity $\boldsymbol{v}_2^{d0}$ in Eq. (3.12b) is the slip velocity on the long-range acoustic streaming at the wall equilibrium position $\zeta = 0$[2]. The following section outlines how to obtain the short-range boundary-layer streaming $\boldsymbol{v}_2^{\delta 0}$ used to calculate the boundary condition (3.12b).

The short-range boundary-layer streaming

The role of the short-range velocity $\boldsymbol{v}_2^{\delta}$ is to set up a shear stress that balances the short-range part $\boldsymbol{f}_{\text{ac}}^{\delta} = -\rho_0 \boldsymbol{\nabla}\cdot\langle \tilde{\boldsymbol{v}}_1^{\delta}\tilde{\boldsymbol{v}}_1^{d} + \tilde{\boldsymbol{v}}_1^{d}\tilde{\boldsymbol{v}}_1^{\delta} + \tilde{\boldsymbol{v}}_1^{\delta}\tilde{\boldsymbol{v}}_1^{\delta}\rangle$ of the body force $\boldsymbol{f}_{\text{ac}}$, see Eq. (2.23a). Exploiting the thin-boundary-layer approximation (3.2) of the Laplacian yields the governing equation for the parallel boundary-layer streaming,

$$\boldsymbol{0} \approx \eta_0 \partial_\zeta^2 \boldsymbol{v}_{2\parallel}^{\delta} - \rho_0 \Big[\boldsymbol{\nabla}\cdot\langle \tilde{\boldsymbol{v}}_1^{\delta}\tilde{\boldsymbol{v}}_1^{d} + \tilde{\boldsymbol{v}}_1^{d}\tilde{\boldsymbol{v}}_1^{\delta} + \tilde{\boldsymbol{v}}_1^{\delta}\tilde{\boldsymbol{v}}_1^{\delta}\rangle\Big]_{\parallel}. \tag{3.13}$$

Here, the parallel part "$\parallel$" of any vector $\boldsymbol{A}$ at a surface with local unit tangent vectors $\boldsymbol{e}_\xi$ and $\boldsymbol{e}_\eta$ is $\boldsymbol{A}_\parallel = (\boldsymbol{A}\cdot\boldsymbol{e}_\xi)\boldsymbol{e}_\xi + (\boldsymbol{A}\cdot\boldsymbol{e}_\eta)\boldsymbol{e}_\eta$. The great advantage of taking the parallel part "$\parallel$" *outside* the divergence is to keep all derivatives in coordinate free form, thus avoiding the curvilinear Christoffel symbols T_{kji} (see Eq. (11) in Paper I [1]). The perpendicular part $v_{2\zeta}^{\delta 0}$ of the short-range streaming is chosen to satisfy the short-range continuity equation (2.22a). In summary, the short-range velocity is obtained by the straight-forward but cumbersome integrals,

$$\boldsymbol{v}_{2\parallel}^{\delta}(\zeta) = \frac{\rho_0}{\eta_0}\left[\int_0^{\zeta}\int_0^{\zeta'} \boldsymbol{\nabla}\cdot\langle \tilde{\boldsymbol{v}}_1^{\delta}\tilde{\boldsymbol{v}}_1^{d} + \tilde{\boldsymbol{v}}_1^{d}\tilde{\boldsymbol{v}}_1^{\delta} + \tilde{\boldsymbol{v}}_1^{\delta}\tilde{\boldsymbol{v}}_1^{\delta}\rangle \,\mathrm{d}\zeta''\mathrm{d}\zeta'\right]_{\parallel}, \tag{3.14a}$$

$$v_{2\zeta}^{\delta}(\zeta) = -\int_0^{\zeta}\left[\boldsymbol{\nabla}_\parallel\cdot\boldsymbol{v}_{2\parallel}^{\delta} + \frac{1}{\rho_0}\boldsymbol{\nabla}\cdot\langle\tilde{\rho}_1\tilde{\boldsymbol{v}}_1^{\delta}\rangle\right]\mathrm{d}\zeta', \tag{3.14b}$$

where all integration constants are chosen to vanish to ensure the condition (3.12a).

The slip boundary condition on the long-range acoustic streaming

The slip velocity $\boldsymbol{v}_2^{d0}$ on the long-range streaming $\boldsymbol{v}_2^{d}$ is defined in Eq. (3.12b) and is obtained simply by evaluating $\boldsymbol{v}_{2\parallel}^{\delta}$ in Eq. (3.14) at the wall $\zeta = 0$. This integration is carried out in Section V A in Paper I [1]. The final result is expressed without reference to any coordinate system but only to the local tangent vectors $\boldsymbol{e}_\xi$, $\boldsymbol{e}_\eta$, and the normal

[2]The slip velocity is also denoted $\boldsymbol{v}_2^{\text{bc}}$ in Paper II [2] and $\boldsymbol{v}_2^{\text{slip}}$ in Paper III [3] and V [5]

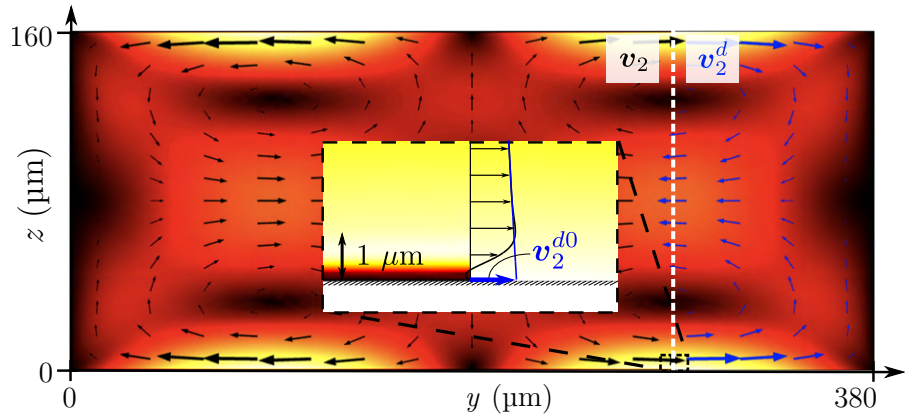

Figure 3.5: The second-order streaming from 0 (black) to 0.12 mm/s (yellow) from the acoustic fields shown in Fig. 3.3 obtained from a the full boundary-layer resolved model of Eq. (2.22) (left, black arrows, $\boldsymbol{v}_2$), and by the effective model of Eq. (3.16) (right, blue arrows, $\boldsymbol{v}_2^d$).

vector $\boldsymbol{e}_\zeta$[3],

$$\boldsymbol{v}_2^{d0} = (\boldsymbol{A}\cdot\boldsymbol{e}_\xi)\,\boldsymbol{e}_\xi + (\boldsymbol{A}\cdot\boldsymbol{e}_\eta)\,\boldsymbol{e}_\eta + (\boldsymbol{B}\cdot\boldsymbol{e}_\zeta)\,\boldsymbol{e}_\zeta, \tag{3.15}$$

$$\boldsymbol{A} = -\frac{1}{2\omega}\mathrm{Re}\Big\{\boldsymbol{v}_1^{\delta 0*}\cdot\boldsymbol{\nabla}\Big(\frac{1}{2}\boldsymbol{v}_1^{\delta 0} - \mathrm{i}\boldsymbol{V}_1^0\Big) - \mathrm{i}\boldsymbol{V}_1^{0*}\cdot\boldsymbol{\nabla}\boldsymbol{v}_1^d + \Big[\frac{2-\mathrm{i}}{2}\boldsymbol{\nabla}\cdot\boldsymbol{v}_1^{\delta 0*} + \mathrm{i}\Big(\boldsymbol{\nabla}\cdot\boldsymbol{V}_1^{0*} - \partial_\zeta v_{1\zeta}^{d*}\Big)\Big]\boldsymbol{v}_1^{\delta 0}\Big\},$$

$$\boldsymbol{B} = \frac{1}{2\omega}\mathrm{Re}\Big\{\mathrm{i}\boldsymbol{v}_1^{d0*}\cdot\boldsymbol{\nabla}\boldsymbol{v}_1^d\Big\}.$$

Here, the vectors $\boldsymbol{A}$ and $\boldsymbol{B}$ may be calculated in any coordinate system not necessarily having coordinate surfaces coinciding with the wall surface. Eq. (3.15) is the slip velocity in the general case of a curved oscillating wall which is valid for thin boundary layers, Eq. (3.1b), and small wall displacements, Eq. (3.1a). This boundary condition constitutes the *effective model* for the long-range acoustic streaming $\boldsymbol{v}_2^d$. It is to be used with the second-order Navier Stokes equation (2.22), which can be written in the simpler form outside the boundary layer as, (see Section V B of Paper I [1]),

$$0 = \boldsymbol{\nabla}\cdot\boldsymbol{v}_2^d \qquad \text{for } \boldsymbol{r}\in\Omega, \tag{3.16a}$$

$$\boldsymbol{0} = -\boldsymbol{\nabla}p_2^d + \eta_0\nabla^2\boldsymbol{v}_2^d + \boldsymbol{f}_{\mathrm{ac}}^d, \qquad \boldsymbol{f}_{\mathrm{ac}}^d = \frac{\Gamma_0\omega}{c_0^2}\boldsymbol{S}_{\mathrm{ac}}^d, \qquad \text{for } \boldsymbol{r}\in\Omega, \tag{3.16b}$$

$$\boldsymbol{v}_2^d = \boldsymbol{v}_2^{d0}, \qquad \text{for } \boldsymbol{r}\in\partial\Omega, \tag{3.16c}$$

In Fig. 3.5 is shown a comparison between the acoustic streaming calculated by the full boundary-layer resolved model, Eq. (2.22), and by this effective model, Eq. (3.16). For a

[3]Strictly, $\boldsymbol{e}_\zeta$ should point towards the fluid and $\boldsymbol{e}_\xi\times\boldsymbol{e}_\eta = \boldsymbol{e}_\zeta$. But in this result, the sign of these vectors is irrelevant, which makes the numerical implementation more tolerant.

more quantitative comparison, see Fig. 4 of Paper I [1]. In the following is listed three limits where the general slip velocity simplifies significantly.

Small wall velocity
The wall velocity $\boldsymbol{V}_1^0$ may be ignored if it is much smaller than the fluid velocity $\boldsymbol{v}_1^d$, which is *e.g.* the case for a fluid resonance with a high Q factor. Ignoring $\boldsymbol{V}_1^0$ in Eq. (3.15) leads to $\boldsymbol{v}_1^{\delta 0} \approx -\boldsymbol{v}_1^{d0}$, and the slip velocity simplifies to,[4]

$$\boldsymbol{v}_{2\parallel}^{d0} = -\frac{1}{8\omega}\boldsymbol{\nabla}_\parallel \left|\boldsymbol{v}_{1\parallel}^{d0}\right|^2 - \frac{1}{2\omega}\mathrm{Re}\Big[\Big(\boldsymbol{\nabla}_\parallel \cdot \boldsymbol{v}_{1\parallel}^{d0}\Big)\boldsymbol{v}_{1\parallel}^{d0*}\Big] + \frac{1}{4\omega}\mathrm{Re}\Big[\mathrm{i}\Big(2\partial_\zeta v_{1\perp}^{d0} - \boldsymbol{\nabla}_\parallel \cdot \boldsymbol{v}_{1\parallel}^{d0}\Big)\boldsymbol{v}_{1\parallel}^{d0*}\Big], \tag{3.17a}$$

$$v_{2\perp}^{d0} = 0. \tag{3.17b}$$

2D standing wave and small wall velocity
For a standing wave, only the two first terms in Eq. (3.17) contribute. For a 2-dimensional (2D) standing wave, say in the cross section of a long straight channel, there is only a single tangential direction and the result simplifies drastically since $(\boldsymbol{\nabla}_\parallel \cdot \boldsymbol{v}_{1\parallel}^{d0})\boldsymbol{v}_{1\parallel}^{d0*} = \frac{1}{2}\boldsymbol{\nabla}_\parallel \left|\boldsymbol{v}_{1\parallel}^{d0}\right|^2$, leading to.

$$\boldsymbol{v}_{2\parallel}^{d0} = -\frac{3}{8\omega}\boldsymbol{\nabla}_\parallel \left|\boldsymbol{v}_{1\parallel}^{d0}\right|^2. \tag{3.18}$$

Note that this is a generalized version of Rayleigh's slip velocity stated in Eq. (2.21).

No boundary layer
In situations where there is no boundary layer, $\boldsymbol{v}_1^\delta = \boldsymbol{0}$ and thus $\boldsymbol{v}_1^{d0} = \boldsymbol{V}_1^0$, the slip velocity reduces to the Stokes drift,

$$\boldsymbol{v}_2^{d0} = -\langle \boldsymbol{s}_1 \cdot \boldsymbol{\nabla} \boldsymbol{v}_1^d \rangle, \qquad \text{for } \boldsymbol{r} \in \boldsymbol{s}_0, \tag{3.19}$$

as required to fulfil the Lagrangian no-slip boundary condition (2.6c). This situation is relevant for a soft wall (a liquid-gas interface) where both the normal stress and the shear stress on the wall in Eq. (3.10) is set to zero implying $\boldsymbol{v}_1^\delta = \boldsymbol{0}$. Another situation where this is a good approximation is for a large flat wall oscillating in the normal direction.

[4] see also Eq. (61a) of Paper I [1], and Eq. (7e) in Paper III [3] where there is a mistake in the last term which should be $(3\mathrm{i} + 2)$ instead of 3i

Chapter 4

Bulk-driven streaming on the wavelength scale

Bulk-driven acoustic streaming is a phenomenon that is often overlooked or ignored in the field of microscale acoustofluidics [23, 43, 69, 118, 119] with the incorrect length-scale argument, that it is only significant in devices of length scale comparable to or longer than the attenuation length scale $(\Gamma_0 k_0)^{-1}$ which is much larger than the acoustic wavelength λ, see Fig. 3.2. However, it is found in Paper III [3] of this thesis that bulk-driven acoustic streaming can be important even for devices of length scale comparable to the acoustic wavelength. In this chapter, bulk-driven acoustic streaming is briefly described and a length-scale condition for ignoring bulk-driven streaming is provided. Furthermore, the theory of Paper III [3] is set into perspective by considering three experimental observations of acoustic streaming reported in the literature.

4.1 The governing equation for bulk-driven streaming

As described in Section 2.6 and in Eq. (2.16b), bulk-driven acoustic streaming is driven by the body force $\boldsymbol{f}_{\mathrm{ac}}^{d}$ which describe the convergence of momentum flux due to attenuation of acoustic waves [69, 74, 100, 120]. Hence, the governing equations for the bulk-driven streaming $\boldsymbol{v}_2^{\mathrm{blk}}$ are (see also Eq. (7) of Paper III [3]),

$$0 = \boldsymbol{\nabla}\cdot\boldsymbol{v}_2^{\mathrm{blk}}, \qquad \text{for } \boldsymbol{r}\in\Omega, \tag{4.1a}$$

$$\boldsymbol{0} = -\boldsymbol{\nabla}p_2^{\mathrm{blk}} + \eta_0\nabla^2\boldsymbol{v}_2^{\mathrm{blk}} + \boldsymbol{f}_{\mathrm{ac}}^{d}, \qquad \boldsymbol{f}_{\mathrm{ac}}^{d} = \frac{\Gamma_0\omega}{c_0^2}\boldsymbol{S}_{\mathrm{ac}}^{d}, \qquad \text{for } \boldsymbol{r}\in\Omega, \tag{4.1b}$$

$$\boldsymbol{v}_2^{\mathrm{blk}} = \boldsymbol{0}, \qquad \text{for } \boldsymbol{r}\in\partial\Omega, \tag{4.1c}$$

As argued in Paper III [3], the body force $\boldsymbol{f}_{\mathrm{ac}}^{d}$ can only create acoustic streaming in a closed system, if it is not a gradient force, or equivalently if the curl of the force is nonzero. Since it was found in Eq. (2.15b) that $\boldsymbol{\nabla}\times\boldsymbol{S}_{\mathrm{ac}}^{d} = \omega^2\boldsymbol{\mathcal{L}}_{\mathrm{ac}}^{d}$ with the acoustic angular momentum $\boldsymbol{\mathcal{L}}_{\mathrm{ac}}^{d}$, it is concluded that the body force can only drive acoustic streaming if the acoustic fields are *rotating*. In Paper III [3] two mechanisms are pointed out to cause rotating acoustics:

Wall-induced rotation where the wall itself is rotating, and *geometry-induced* rotation where the geometry deviates slightly from a perfect symmetry causing two resonances to oscillate at the same frequency but out of phase. For further details, see section V of Paper III [3].

4.2 Bulk-driven versus boundary driven streaming

It is relevant to ask for the condition where bulk-driven streaming is significant relative to the boundary-driven streaming and this question is answered here based on scaling arguments. As bulk-driven streaming is strongly dependent on the phases and the shape of the acoustic fields, each situation requires in principle a special treatment. For the most optimal rotation of the acoustic fields, the energy flux density scales as $\boldsymbol{S}_{\mathrm{ac}}^{d} \sim \frac{1}{2}\rho_0 c_0 (v_1^d)^2$, where v_1^d is the magnitude of the acoustic velocity field $\boldsymbol{v}_1^d$. Using that in Eq. (4.1b), and the scaling $\nabla^2 \boldsymbol{v}_2^{\mathrm{blk}} \sim v_2^{\mathrm{blk}} L_{\mathrm{visc}}^{-2}$ with the shear length scale L_{visc} of the bulk-driven streaming, the following scaling is obtained,

$$v_2^{\mathrm{blk}} \sim \frac{1}{2}\left(\frac{4}{3} + \frac{\eta_0^{\mathrm{b}}}{\eta_0}\right)(k_0 L_{\mathrm{visc}})^2 \frac{(v_1^d)^2}{c_0}. \tag{4.2}$$

This result reveals the well-known observation that bulk-driven streaming is only dependent on the viscosity through the ratio $\frac{\eta_0^{\mathrm{b}}}{\eta_0}$ [100]. The typical scaling of the boundary-driven streaming speed is $v_2^{\mathrm{bdr}} \sim \frac{3}{8}\frac{(v_1^d)^2}{c_0}$ given by the Rayleigh slip velocity in Eq. (2.21). Hence, the ratio between bulk-driven and boundary-driven streaming is,

$$\frac{v_2^{\mathrm{blk}}}{v_2^{\mathrm{bdr}}} \sim \frac{4}{3}\left(\frac{4}{3} + \frac{\eta_0^{\mathrm{b}}}{\eta_0}\right)(k_0 L_{\mathrm{visc}})^2. \tag{4.3}$$

The critical viscous length scale $L_{\mathrm{visc}}^{\mathrm{crit}}$ where v_2^{blk} and v_2^{bdr} are similar is then given in terms of the acoustic wave length λ as,

$$L_{\mathrm{visc}}^{\mathrm{crit}} = \frac{1}{2\pi}\left[\frac{4}{3}\left(\frac{4}{3} + \frac{\eta_0^{\mathrm{b}}}{\eta_0}\right)\right]^{-\frac{1}{2}} \lambda = 0.11\ \lambda, \qquad \text{for water.} \tag{4.4}$$

For the special case of two perpendicular resonance modes in the xy plane of a square-box-shaped cavity of height L_z, a more thorough analysis is given in Eq. (40) Paper III [3], concluding that $L_{\mathrm{visc}}^{\mathrm{crit}} = 0.09\ \lambda$ for water,[1] in good agreement with Eq. (4.4). From Eq. (4.4), the following condition and consequence is extracted,

$$L_{\mathrm{visc}} \ll L_{\mathrm{visc}}^{\mathrm{crit}}: \qquad \text{Bulk-driven streaming can be ignored.} \tag{4.5}$$

In conclusion, the length-scale argument for ignoring bulk-driven streaming in micro-cavities is that the streaming shear length L_{visc} is much smaller than $L_{\mathrm{visc}}^{\mathrm{crit}}$, which is rarely

[1] Eq. (40) of Paper III [3] defines $B^{\mathrm{crit}} = \frac{lL_z}{L^*} = \frac{2L_z}{\lambda} = 0.35$ for water. Using $L_{\mathrm{visc}} = \frac{1}{2}L_z$ yields $L_{\mathrm{visc}}^{\mathrm{crit}} = 0.09\ \lambda$.

satisfied in acoustofluidic devices. The reason why bulk-driven streaming is in many cases not important is that the acoustic fields are not rotating. Remarkably however, as shown in the following section, acoustic rotation may be induced in experiments even though it is not intended.

4.3 Observed examples of bulk-driven streaming on the wavelength scale in rectangular microcavities

This section shows three examples of acoustic streaming on the wavelength scale observed in rectangular-box-shaped cavities. In such cavities, the pressure resonance modes p_1^{lmn} are of the form [3],

$$p_1^{lmn} \propto \cos\left(\frac{l\pi}{L_x}x\right)\cos\left(\frac{m\pi}{L_y}y\right)\cos\left(\frac{n\pi}{L_z}z\right), \tag{4.6}$$

where L_x, L_y, and L_z are the cavity side lengths in the x, y and z direction, respectively, and l, m, and n are integers. For an excitation of a single of these pressure modes, it is found in Paper III [3] that the body force $\boldsymbol{f}_{\rm ac}^{lmn}$ created from the resonance p_1^{lmn} does not generate significant bulk-driven streaming. However, as shown in the three examples below, it is often possible to excite *two* resonance modes at the same frequency, called a double-mode resonance and denoted $p_{lmn}^{l'm'n'} = p_1^{lmn} + p_1^{l'm'n'}$. The corresponding body force $\boldsymbol{f}_{lmn}^{l'm'n'}$ induced by that double mode is (see Eq. (16) of Paper III [3]),

$$\boldsymbol{f}_{lmn}^{l'm'n'} = \frac{\Gamma_0\omega}{c_0^2}\langle p_1^{lmn}\boldsymbol{v}_1^{l'm'n'} + p_1^{l'm'n'}\boldsymbol{v}_1^{lmn}\rangle. \tag{4.7}$$

For each of the following three examples, this body force $\boldsymbol{f}_{lmn}^{l'm'n'}$ is plotted with suitable mode numbers lmn and $l'm'n'$ and compared to the observed streaming. Furthermore, the viscous length scale $L_{\rm visc}$, Eq. (4.4), of the acoustic streaming is estimated in each case and it is found that the condition $L_{\rm visc} \ll L_{\rm visc}^{\rm crit}$ in Eq. (4.5) for ignoring bulk-driven streaming is not satisfied in any of the examples.

Example 1: Cross-section streaming in a square channel

The first example is from Antfolk *et al.* [54], who used a long straight quadratic silicon/glass channel of side length 230 µm, actuated at the frequency $f = 3.19$ MHz that excites a half-wave resonance in both cross-section directions y and z, see Fig. 4.1(a1-a2). In this situation, the viscous length scale used in Section 4.2 above is the half channel width $L_{\rm visc} = 115$µm and the wave length is $\lambda = \frac{c_0}{f} = 479$ µm, and thus,

$$L_{\rm visc} \approx 0.24\lambda. \tag{4.8}$$

Since this is not much smaller than $L_{\rm visc}^{\rm crit} = 0.11\lambda$, see (4.5), the bulk-driven streaming cannot be ignored. The excited pressure double mode was presumably $p_1 = p_{010}^{001} =$

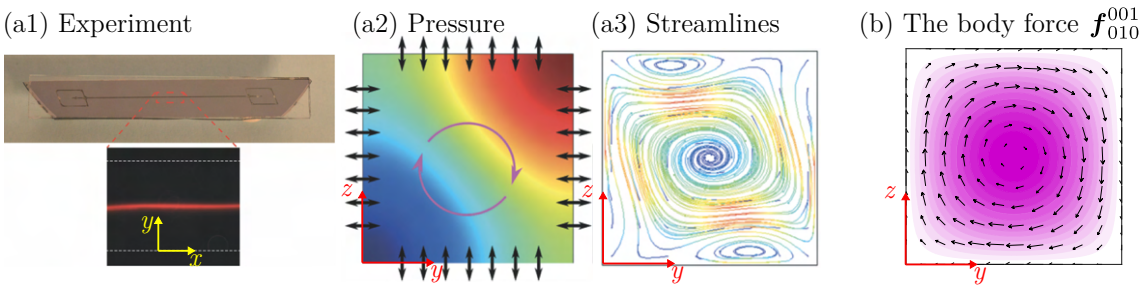

Figure 4.1: An acoustic resonance measured by Antfolk *et al.* [54] in a quadratic channel at $f = 3.19$ MHz. (a) Results from the paper: (a1) Experimental setup and top-view florescent image of focused 0.5-µm polystyrene particles (red). (a2) Simulated pressure obtained by oscillating the side walls with a phase difference of $\frac{1}{2}\pi$. (a3) Result from a direct simulation of the particle streamlines for 0.5-µm polystyrene particles. (b) The body force $\boldsymbol{f}_{010}^{001}$ (arrows) proposed in this thesis to cause the observed streaming shown in (a3), and colorplot of the acoustic angular momentum $\boldsymbol{\mathcal{L}}_{\mathrm{ac}}^{d} \propto \boldsymbol{\nabla} \times \boldsymbol{f}_{010}^{001}$.

$p_1^{010} + p_1^{001}$, see Eq. (4.6), which induces the double-mode body force $\boldsymbol{f}_{010}^{001}$ as shown in Fig. 4.1(b). In the paper, this rotating streaming pattern was obtained numerically by a full boundary-layer resolved simulation where the side walls was actuated with a phase difference of $\frac{1}{2}\pi$ as shown in Fig. 4.1(a2).

Example 2: Transducer-plane streaming in a square cavity

This example has been studied numerically and analytically in Paper II [2] and III [3]. The experiment is from Hagsäter *et al.* [76] who did particle image velocimetry (PIV) on 1 µm polystyrene particles in a square cavity of side lengths 2000 µm and height 200 µm, see Fig. 4.2(a)-(b). The acoustic resonance was excited by a transducer placed below the square cavity at the frequency $f = 2.17$MHz exciting 6 standing half waves in the two horizontal directions x and y. For the acoustic streaming pattern shown in Fig. 4.2(b), the viscous length scale used in Section 4.2 above is the half height $L_{\mathrm{visc}} \approx 100$ µm of the cavity, and the wave length is $\lambda = \frac{c_0}{f} = 690$ µm, and hence,

$$L_{\mathrm{visc}} \approx 0.15\ \lambda. \tag{4.9}$$

Since this is not much smaller than $L_{\mathrm{visc}}^{\mathrm{crit}} = 0.11\lambda$, see (4.5), the bulk-driven streaming cannot be ignored. Note that if only a single half wave was excited in each direction, the wavelength would instead be $\lambda \approx 4000$ µm giving $L_{\mathrm{visc}} \approx 0.025\ \lambda$ and the bulk-driven streaming could safely be ignored (see Fig. 8 of Paper III [3]). The total pressure mode in the experiment was presumably $p_1 = p_{600}^{060} = p_1^{600} + p_1^{060}$, see Eq. (4.6), which induces the double-mode body force $\boldsymbol{f}_{600}^{060}$, see Eq. (4.7), as shown in Fig. 4.2(c). Paper II [2] provides a full-device simulation of the experimental setup, where the body force $\boldsymbol{f}_{\mathrm{ac}}^{d}$ in Eq. (4.1b) is implemented, and the resulting streaming pattern is shown in Fig. 4.2(d), reproducing the observed particle motion in Fig. 4.2(b) remarkably well. In this case, since the transducer

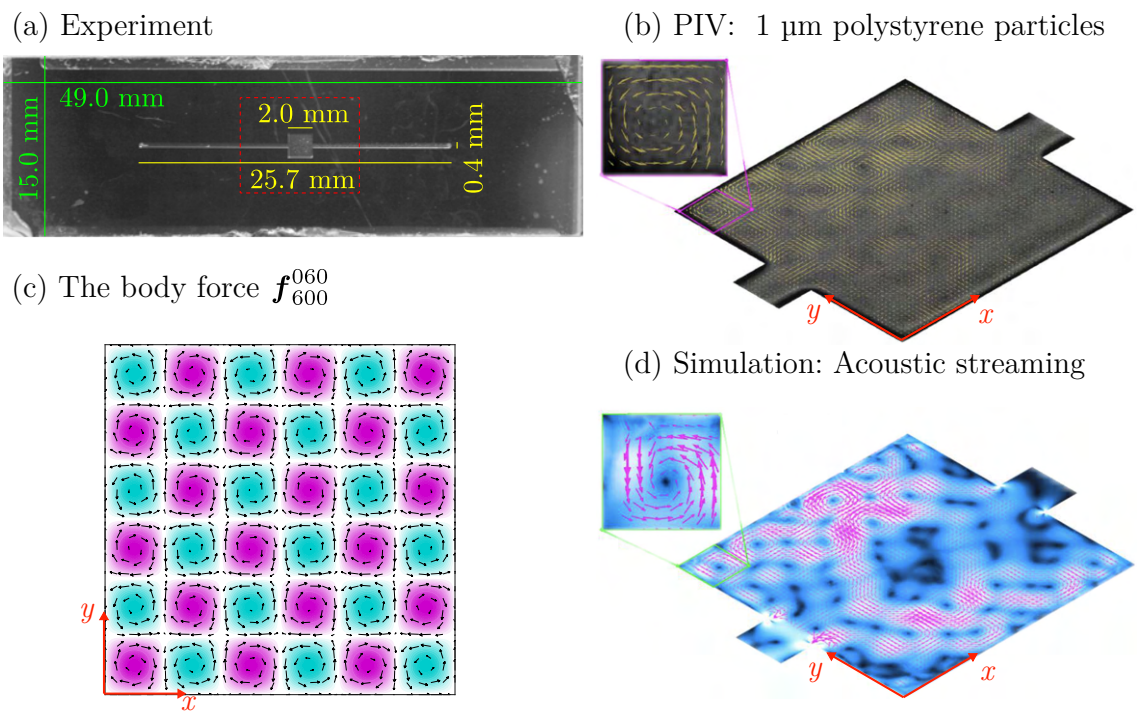

Figure 4.2: Acoustic streaming observed by Hagsäter *et al.* [76] in a square cavity at the resonance $f = 2.17$ MHz. (a) Top-view of the microchip. (b) PIV results for 1 µm polysterene particles mapping out the acoustic streaming. (c) The body force $\boldsymbol{f}_{060}^{006}$ (arrows) proposed in this thesis to cause the observed streaming shown in (b), and colorplot of the acoustic angular momentum $\boldsymbol{\mathcal{L}}_{\mathrm{ac}}^{d} \propto \boldsymbol{\nabla} \times \boldsymbol{f}_{060}^{006}$. (d) Simulation results from Paper III [3] of the acoustic streaming where the body force $\boldsymbol{f}_{\mathrm{ac}}$ is included.

is placed below the cavity, the acoustic rotation in the experiment is most likely caused by a small asymmetry in the geometry *e.g.* due to the side channels. See Paper III [3] for a further analytical treatment of the bulk-driven streaming in this device.

Example 3: Transducer-plane streaming in a long channel

The third example is another experiment from Hagsäter *et al.* [121] where they used a silicon/glass channel of length $L_x = 18.35$ mm, width $L_y = 400$ µm, height $L_z = 150$ µm, and the actuation frequency $f = 1.96$ MHz corresponding to the wavelength $\lambda = \frac{c_0}{f} = 764$ µm. In Fig. 4.3 is shown a PIV measurement of large 5 µm polyamide particles in a section of the long channel. These particles follow the acoustic radiation force and their motion reveal a clear example of a resonance mode which is not just a single standing half wave across the channel. In this figure, the green lines mark the short axial periodicity, and the yellow lines mark the long axial periodicity as well as the width L_y. These length scales suggest that this resonance may be described by the two modes shown in Fig. 4.3(b): $p_1^{14,0,0}$ having 14 half waves along the shown axial length, and $p_1^{5,1,0}$

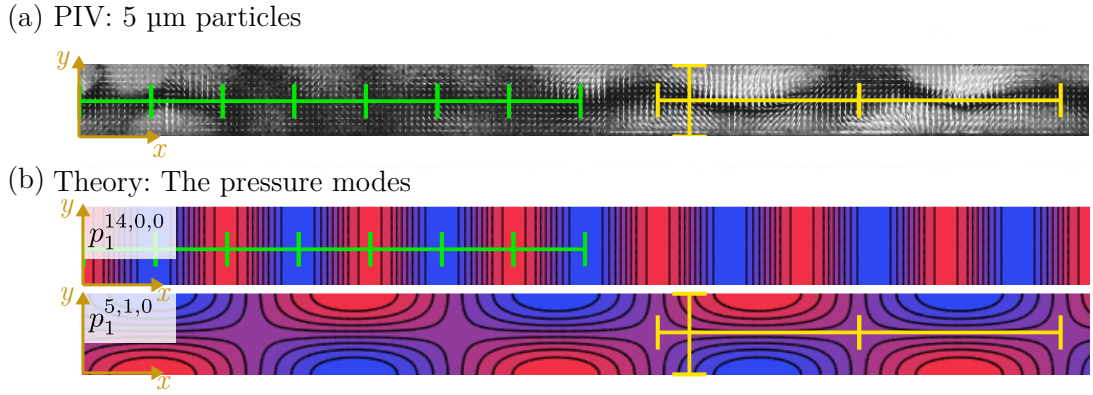

Figure 4.3: An acoustic resonance measured by Hagsäter *et al.* [121] in a long straight silicon/glass channel of width 400 µm at the frequency 1.96 MHz. (a) Top-view PIV meassurement of 5 µm polyamide particles in a section of the long channel. The green and yellow bars show the observed length scales of the resonance. Adapted from Fig. 5(b) of Ref. [121]. (b) The suggested combination of pressure eigenmodes based on the length scales marked with green and yellow in (a).

having 5 half waves along the x directions and 1 half wave across the y direction.

The acoustic streaming pattern for the resonance mode in Fig. 4.3(a) was mapped out in the experiment by using 1 µm polystyrene particles, and the resulting PIV measurement is shown in Fig. 4.4(a). In this case, the viscous length scale used in Section 4.2 above is the half height of the channel leading $L_{\text{visc}} \approx 75$ µm and $\lambda = 764$ µm, leading to

$$L_{\text{visc}} \approx 0.1\ \lambda. \tag{4.10}$$

Since this is not much smaller than $L_{\text{visc}}^{\text{crit}} = 0.11\lambda$, see (4.5), the bulk-driven streaming cannot be ignored. In Fig. 4.4(b) is shown the body force $\boldsymbol{f}_{14,0,0}^{5,1,0}$ which is induced by the pressure modes $p_1^{14,0,0}$ and $p_1^{5,1,0}$ displayed in Fig. 4.3(b). Remarkably, this very irregular

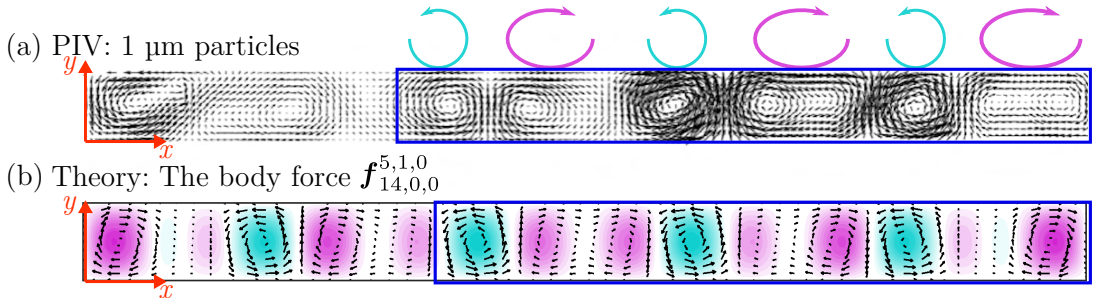

Figure 4.4: Same channel and frequency as in Fig. 4.3. (a) PIV meassurement of 1 µm polystyrene particles in a section of the channel. Adapted from Fig. 7(b) of Ref. [121]. (b) The body force $\boldsymbol{f}_{14,0,0}^{5,1,0}$ (arrows) proposed in this thesis to cause the observed streaming shown in (a), and colorplot of the acoustic angular momentum $\boldsymbol{\mathcal{L}}_{\text{ac}}^{d} \propto \boldsymbol{\nabla} \times \boldsymbol{f}_{14,0,0}^{5,1,0}$.

streaming pattern is well explained by the suggested body force. This observed acoustic streaming is therefore likely to be classified as *bulk-driven streaming*.

4.4 Concluding remarks

In this chapter, it is argued that bulk-driven acoustic streaming should be given more attention both in the understanding and in calculations of most acoustofluidic devices. It is shown in Eq. (4.4) that for devices of length scale comparable to or larger than the critical viscous length scale $L_{\mathrm{visc}}^{\mathrm{crit}} = 0.11\ \lambda$ for water, bulk driven streaming may be important. Bulk-driven streaming is created if the acoustic fields are rotating and as shown in the three experimental examples above, acoustic rotation may occur unexpectedly due to the simultaneous excitation of two pressure resonance modes at the same frequency.

Chapter 5

FEM modelling in COMSOL and validation

In this PhD project, numerical modelling has been used for simulations of experimental observations, for validations of analytical theories, for parametric studies, and for shape optimizations. These simulations were carried out using the commercial softwares COMSOL Multiphysics [122] and MATLAB [123]. This chapter gives a brief introduction to the Finite Element Method (FEM), see Fig. 5.1, which is used internally in COMSOL, and the modelled equations and boundary conditions are summarized. Furthermore, the validation of the numerical and analytical results is discussed.

5.1 The Finite Element Method

The governing equations (2.7), (2.9), and (2.22) considered in this PhD project are all time-independent conservation equations of the form,

$$\boldsymbol{\nabla} \cdot \boldsymbol{J}\big[g(\boldsymbol{r})\big] + F\big[g(\boldsymbol{r})\big] = 0, \tag{5.1}$$

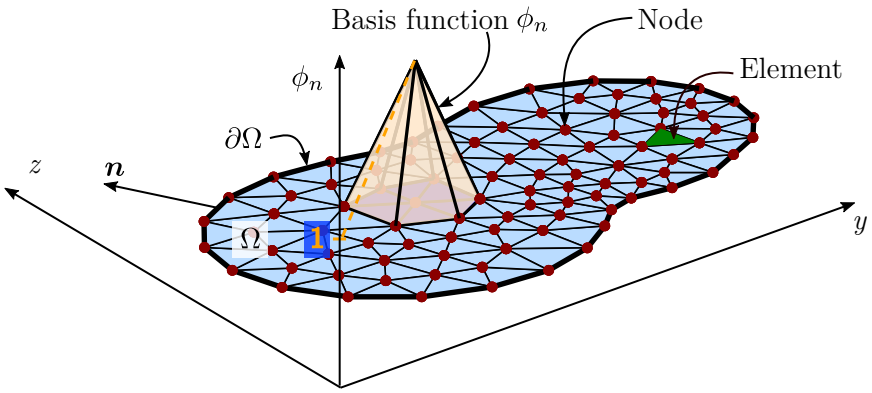

Figure 5.1: Sketch of a 2D domain Ω equipped with nodes, elements, and normal vector $\boldsymbol{n}$. A single (linear) basis function $\phi_n(\boldsymbol{r})$ is shown. Adapted from Ref. [124].

where $g(\boldsymbol{r})$ is a generalized dependent field, $\boldsymbol{J}$ is a generalized current, and F is a generalized forcing term. The solution $g(\boldsymbol{r})$ that satisfy Eq. (5.1) is the so-called strong solution. A weak formulation of Eq. (5.1) is constructed by multiplying it by a test function $\psi(\boldsymbol{r})$ and integrating over the domain Ω with boundary $\partial\Omega$ and using integration by parts,

$$\oint_{\partial\Omega} \psi(\boldsymbol{r})\boldsymbol{J}\big[g(\boldsymbol{r})\big]\cdot\boldsymbol{n}\,\mathrm{d}A + \int_{\Omega}\Big\{-\boldsymbol{\nabla}\psi(\boldsymbol{r})\cdot\boldsymbol{J}\big[g(\boldsymbol{r})\big] + \psi(\boldsymbol{r})F\big[g(\boldsymbol{r})\big]\Big\}\,\mathrm{d}V = 0. \tag{5.2}$$

In the FEM, the numerical discritization is done by choosing a finite number of nodes leading to a finite number of domain elements between the nodes, see Fig. 5.1. For each node n, a basis function $\phi_n(\boldsymbol{r})$ is defined to be unity at the node, smooth inside the elements next to the node, and zero in all other elements. The solution $g(\boldsymbol{r})$ is approximated by a linear combination of these basis functions,

$$g(\boldsymbol{r}) \approx \sum_n c_n\phi_n(\boldsymbol{r}), \tag{5.3}$$

where the coefficients c_n are to be found numerically. To obtain equations for these coefficients, Eq. (5.3) is inserted into Eq. (5.2). Furthermore, since Eq. (5.2) is required to hold for any test function ψ, a usual convenient choice is to chose $\psi(\boldsymbol{r}) = \phi_m(\boldsymbol{r})$, giving,

$$\sum_n\left\{\oint_{\partial\Omega}\phi_m(\boldsymbol{r})\boldsymbol{J}\big[\phi_n(\boldsymbol{r})\big]\cdot\boldsymbol{n}\,\mathrm{d}A + \int_{\Omega}\Big\{-\boldsymbol{\nabla}\phi_m(\boldsymbol{r})\cdot\boldsymbol{J}\big[\phi_n(\boldsymbol{r})\big] + \phi_m(\boldsymbol{r})F\big[\phi_n(\boldsymbol{r})\big]\Big\}\,\mathrm{d}V\right\}c_n = 0. \tag{5.4}$$

These equations form the matrix equation $\sum_n K_{mn}c_n = 0$ for all m, where K_{mn} is known and c_n is unknown. To obtain a non-trivial solution, boundary conditions need to be specified. In COMSOL, the module "Weak Form PDE" is used, where the integrand of the weak formulation (5.2) is given as input, as well as boundary conditions in the form of either "*Weak contributions*" or "*Dirichlet boundary contributions*". Table 5.1 gives an overview of the equations and corresponding boundary conditions simulated in this

Table 5.1: An overview of the effective and full model used in this PhD project, with corresponding mesh size and order of the polynomial basis function ϕ_n.

Field	Governing equation	Boundary condition	
Effective model. Mesh size: d.			
p_1 (4'th order)	Eq. (2.9)	Eq. (3.6)	Neumann
$\boldsymbol{v}_2^d$ (3'rd order)	Eq. (3.16b)	Eq. (3.15)	Dirichlet
p_2^d (2'nd order)	Eq. (3.16a)	$\int_\Omega p_2^d\,\mathrm{d}V = 0$	Global constraint
Full model. Mesh size: δ at the boundaries and k_0^{-1} in the bulk.			
$\boldsymbol{v}_1$ (3'rd order)	Eq. (2.7b)	Eq. (2.7c)	Dirichlet
p_1 (2'nd order)	Eq. (2.7a)	–	–
$\boldsymbol{v}_2$ (3'rd order)	Eq. (2.22b)	Eq. (2.22c)	Dirichlet
p_2 (2'nd order)	Eq. (2.22a)	$\int_\Omega p_2\,\mathrm{d}V = 0$	Global constraint

PhD project, as well as the chosen mesh size (see Fig. 5.2 (a1) below), and order of the polynomial basis functions ϕ_n. In the following, each of the relevant boundary conditions are briefly described.

The Neumann Boundary Condition (weak contribution)

To implement a Neumann boundary condition, *i.e.* a prescribed *flux* at the boundary of the form $\boldsymbol{J}\cdot\boldsymbol{n} = N(\boldsymbol{r})$, the feature "*Weak Contribution*" in COMSOL is used. Here, the integrand of the left surface integral in Eq. (5.4) is changed by replacing $\boldsymbol{J}\big[g(\boldsymbol{r})\big]\cdot\boldsymbol{n}$ by $\phi_m(\boldsymbol{r})N(\boldsymbol{r})$, giving

$$\sum_n \left\{ \int_\Omega \Big\{ -\boldsymbol{\nabla}\phi_m(\boldsymbol{r})\cdot\boldsymbol{J}\big[\phi_n(\boldsymbol{r})\big] + \phi_m(\boldsymbol{r})F\big[\phi_n(\boldsymbol{r})\big] \Big\}\,\mathrm{d}V \right\} c_n = -\oint_{\partial\Omega} \phi_m(\boldsymbol{r})N(\boldsymbol{r})\,\mathrm{d}A, \quad (5.5)$$

which form a solvable system of equations of the form $\sum_n K_{mn}c_n = b_m$. A simple example is the inviscid Helmholtz equation for the acoustic pressure, $\nabla^2 p_1 + k_0^2 p_1 = 0$ which is formulated as Eq. (5.1) by choosing the current $\boldsymbol{J}[p_1(\boldsymbol{r})] = \boldsymbol{\nabla}p_1(\boldsymbol{r})$ and the forcing term $F[p_1(\boldsymbol{r})] = k_0^2 p_1(\boldsymbol{r})$. A prescribed wall motion is implemented as $\boldsymbol{n}\cdot\boldsymbol{\nabla}p_1 = \mathrm{i}\omega\rho_0\boldsymbol{n}\cdot\boldsymbol{V}_1^0$ and hence $N(\boldsymbol{r}) = \mathrm{i}\omega\rho_0\boldsymbol{n}\cdot\boldsymbol{V}_1^0$.

The Dirichlet Boundary Condition

To implement a Direchlet boundary condition, *i.e.* a prescribed *value* at the boundary of the form $g(\boldsymbol{r}) = D(\boldsymbol{r})$, the feature "*Dirichlet Boundary Condtion*" in COMSOL is used. Since the fields are represented as the sum (5.3) and $\phi_n(\boldsymbol{r})$ is unity at the nodes, this condition can be implemented by setting the coefficients $c_n = D(\boldsymbol{r}_n)$ for the nodes n at the boundary $n \in \{n_{\partial_\Omega}\}$ with position $\boldsymbol{r}_n$. Hence, the matrix equation obtained from Eq. (5.4) changes to $\sum_{n\notin\{n_{\partial\Omega}\}} K_{mn}c_n = -\sum_{n\in\{n_{\partial\Omega}\}} K_{mn}D(\boldsymbol{r}_n) = b_m$.

Global Constraint

In the time-averaged equations (2.22) and (3.16) for the acoustic streaming, the acoustic pressure p_2 only enters though its gradient and therefore there is an arbitrary constant base level that has to be fixed. To do that, the feature "*Global Contraint*" in COMSOL is used to impose $\int_\Omega p_2\,\mathrm{d}V = 0$.

5.2 Validation of results

The numerical and analytical results obtained in this PhD project are substantiated by comparison between different methods as summarized in Table 5.2. In Paper I [1], the acoustic fields and streaming are calculated without resolving the boundary layer by using effective boundary conditions. This method is validated against a full boundary-layer resolved model, which has previously been tested against experiments [93], and against analytic solutions. An example of comparison between full, effective, and analytical solutions is shown in Fig. 5.2. In Paper II [2], a full acoustofluidic device is simulated using

Table 5.2: Overview of the research methods used in the published papers I-V. "Reduced simulations" reefer to a simulation method, where analytical results are used to obtain better efficiency or higher simplicity. "Full simulations" reefer to a simulation method without the simplifications used in "Reduced simulations". (✓) denote a method that has been used without publication.

	Paper I	Paper II	Paper III	Paper IV	Paper V
Reduced simulations	✓	✓	✓	✓	✓
Full simulations	✓			✓	(✓)
Analytical results	✓		✓	✓	✓
Convergence tests	(✓)	(✓)	(✓)	(✓)	(✓)
Experiments		✓	(✓)		

the effective boundary conditions, and the results are substantiated since they reproduce the experimental observations. In Paper III [3], an analytical theory is made for the conditions where bulk-driven acoustic streaming is strongest. The theory is validated against a 3-dimensional (3D) simulation with effective boundary conditions at the walls. In Paper IV [4], an analytical theory is made for the axial dependency of the acoustic fields in long straight capillary tubes, which, as shown, can be obtained from a reduced 2D calculation. The theory is validated against a full 3D simulation with effective boundary conditions at the walls. In Paper V [5], the effective boundary conditions are used to efficiently calculate the acoustic fields and streaming for many cavity shapes, in order to optimize the shape of the cavity for suppression of acoustic streaming. The streaming in the optimized shape has also been calculated by using a full boundary-layer with agreeing results. Furthermore, an analytical explanation of the suppression of the acoustic streaming is provided. Finally, for all published numerical simulations, a numerical convergence test was done similar to that in Ref. [66] by Muller *et al.*, but not shown in the papers.

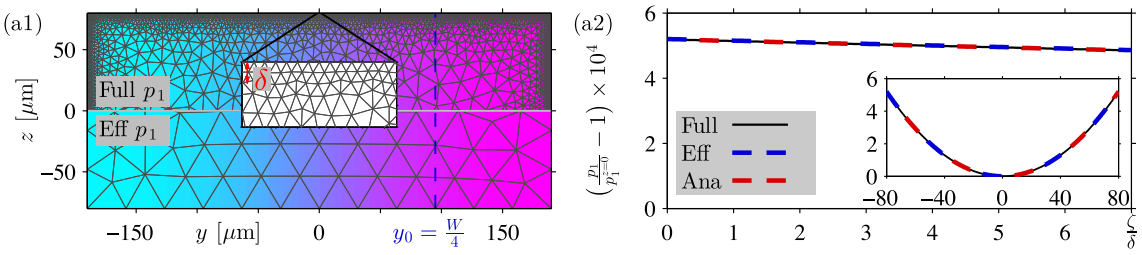

Figure 5.2: Example of validation of results by comparison between full simulation "Full", effective simulation "Eff", and analytical results "Ana" for the acoustic pressure p_1 at resonance $f_{\text{res}} = 1.967$ MHz in a microcavity. (a1) Color plot of p_1 from -1 MPa (purple) to 1 MPa (cyan) and the used FEM mesh for the full simulation (upper half) and for the effective simulation (lower half). (a2) Line plot of p_1 along the dashed blue cut line in (a1) at $y = \frac{1}{4}W$ for the full model (black solid line), the effective model (blue dashed line), and the analytical results (red dashed line). Adapted from Fig. 1 in Paper I [1].

Chapter 6

Summary of results

In this chapter, the research published in the papers I-V [1–5] is summarized with the purpose of giving the reader an overview of the work done in the PhD project, a motivation for each paper, as well as the most significant contributions provided by each paper.

6.1 Paper I: Theory of pressure acoustics with viscous boundary layers and streaming in curved elastic cavities

The acoustic fields and streaming in a fluid are strongly dependent on the viscous boundary layer forming close to a solid wall, where the fluid motion adapts to the wall motion. In numerical simulations, the narrow width of this boundary layer requires an extremely fine numerical resolution. As described in Chapter 3, current boundary-layer theories [70–72, 74, 75] offer a solution to this problem by formulating an effective slip velocity for the acoustic streaming. The motivation for this paper was to generalize the slip-velocity theory to apply for a curved wall that oscillates in any direction. In the process, it was discovered that even though the acoustic pressure p_1 does not vary on the boundary-layer length scale δ, it is possible to formulate a boundary condition on p_1 that takes into account all the effects from the viscous boundary layer. This boundary-layer boundary condition on p_1 is one of the most important contributions of the thesis. It is given in Eq. (25) of Paper I [1] and here,

$$\partial_\zeta p_1 + \frac{\mathrm{i}}{k_\mathrm{s}}\Big[k_c^2 p_1 + \partial_\zeta^2 p_1\Big] = \frac{\mathrm{i}\omega\rho_0}{1-\mathrm{i}\Gamma_0}\Big[V_{1\zeta}^0 - \frac{\mathrm{i}}{k_\mathrm{s}}\boldsymbol{\nabla}\cdot\boldsymbol{V}_1^0\Big]. \tag{6.1}$$

Another key result of the thesis is the generalization of the streaming slip velocity, that has been extended to apply for a curved surface that oscillates in any direction. It is

written in Eq. (55) of Paper I [1] and restated here,

$$\begin{aligned}
\boldsymbol{v}_2^{d0} &= \left(\boldsymbol{A}\cdot\boldsymbol{e}_\xi\right)\boldsymbol{e}_\xi + \left(\boldsymbol{A}\cdot\boldsymbol{e}_\eta\right)\boldsymbol{e}_\eta + \left(\boldsymbol{B}\cdot\boldsymbol{e}_\zeta\right)\boldsymbol{e}_\zeta, \\
\boldsymbol{A} &= -\frac{1}{2\omega}\mathrm{Re}\Big\{\boldsymbol{v}_1^{\delta 0*}\cdot\boldsymbol{\nabla}\Big(\frac{1}{2}\boldsymbol{v}_1^{\delta 0} - \mathrm{i}\boldsymbol{V}_1^0\Big) - \mathrm{i}\boldsymbol{V}_1^{0*}\cdot\boldsymbol{\nabla}\boldsymbol{v}_1^d \\
&\qquad + \left[\frac{2-\mathrm{i}}{2}\boldsymbol{\nabla}\cdot\boldsymbol{v}_1^{\delta 0*} + \mathrm{i}\Big(\boldsymbol{\nabla}\cdot\boldsymbol{V}_1^{0*} - \partial_\perp v_{1\perp}^{d*}\Big)\right]\boldsymbol{v}_1^{\delta 0}\Big\}, \\
\boldsymbol{B} &= \frac{1}{2\omega}\mathrm{Re}\Big\{\mathrm{i}\boldsymbol{v}_1^{d0*}\cdot\boldsymbol{\nabla}\boldsymbol{v}_1^d\Big\}.
\end{aligned} \tag{6.2}$$

Note that this slip velocity is formulated in terms of the local tangent vectors $\boldsymbol{e}_\xi$ and $\boldsymbol{e}_\eta$ and normal vector $\boldsymbol{e}_\eta$, but with no reference to any coordinate system and therefore, it is straight-forward (but cumbersome) to implement in general geometries with no need of calculating any curvilinear quantities of the surface.

6.2 Paper II: 3D modeling of acoustofluidics in a liquid-filled cavity including streaming, viscous boundary layers, surrounding solids, and a piezoelectric transducer

The effective boundary conditions developed in Paper I [1]for the first-order pressure p_1 and for the acoustic streaming $\boldsymbol{v}_2$, lead to drastic reductions in the computer memory required for simulations. They were used in Paper II [2], to simulate a full experimental setup by Hagsäter *et al.* [76] including the water domain, the Pyrex-glass lid, the surrounding silicon, and the actuating piezoelectric transducer. The simulation reproduced the characteristic 6-by-6 streaming pattern which was observed in the experiment, and it was found numerically, that this streaming pattern is not driven by the slip velocity, but instead by the body force $\boldsymbol{f}_{\mathrm{ac}}^d$ in the bulk of the fluid as described in Chapter 4. This was further analyzed theoretically in Paper III [3]. The developed full-device simulation allows for detailed studies of full acoustofluidic devices, and this paper demonstrates and communicates how it can be done.

6.3 Paper III: Bulk-driven acoustic streaming at resonance in closed microcavities

Bulk driven acoustic streaming, or Eckart streaming, is driven by the body force $\boldsymbol{f}_{\mathrm{ac}}$ which represent the convergence of time-averaged momentum flux from the acoustic fields. It is derived in Eq. (50) of Paper I [1] in agreement with Eckart [101],

$$\boldsymbol{f}_{\mathrm{ac}}^d = \frac{\Gamma_0\omega}{c_0^2}\boldsymbol{S}_{\mathrm{ac}}^d, \tag{6.3}$$

where $\boldsymbol{S}_{\mathrm{ac}}^d = \langle\tilde{p}_1\tilde{\boldsymbol{v}}_1^d\rangle$ is the acoustic energy flux density. Bulk-driven acoustic streaming is usually observed in the context of a propagating acoustic beam over the length scale

of many wave lengths, and it is often ignored in resonating microfluidic cavities of size comparable with the acoustic wave length [69, 118]. However, Hagsäter *et al.* [76] observed a rotating streaming pattern at resonance which is very likely to be classified as bulk-driven streaming as also found numerically in Paper II [2]. The motivation for Paper III [3] was to understand the creation of this kind of streaming in resonating devices theoretically.

It was found, that when two standing waves oscillate out of phase and in perpendicular directions, they create a rotating resonance which gives rise to a significant rotating body force $\boldsymbol{f}_{\mathrm{ac}}^{d}$ on the fluid. The two key messages of this paper is that (1) the body force $\boldsymbol{f}_{\mathrm{ac}}^{d}$ of Eq. (6.3) should in general not be ignored in calculations of microfluidic devices, and (2) the bulk-driven streaming at resonance is very sensitive to small deviations in the cavity geometry and it may occur unexpectedly even though the actuation is not itself rotating. To reproduce bulk driven streaming in simulations, it is therefore important to check the sensitivity to small changes in the geometry.

6.4 Paper IV: Theory of acoustic trapping of microparticles in capillary tubes

Acoustic trapping in capillary tubes is facilitated by placing a piezoelectric transducer under the tube and actuating at a cross-section resonance [39–41, 45]. Suspended particles are then focused in the cross section and attracted axially towards the maximum acoustic energy above the transducer. The motivation for this paper was to a obtain general understanding of the axial dependency of the acoustic fields and radiation force in the acoustic trap. This was done by calculating the acoustic pressure analytcally by using the boundary-layer boundary condition (6.1) derived in Paper I [1].

It was found that for any tube cross section, the 3D axial dependency of the acoustic fields can be determined from a reduced 2D calculation in the cross section of the capillary tube, combined with the axial dependency of the actuation. This finding allows for general statements about the axial dependency of the acoustic fields and radiation force in capillary tubes. A significant conclusion is that there exists an optimal axial actuation length for acoustic trapping in capillary tubes, which for typical devices is found to be a few times the cross-section wavelength. The analytical results pave the way for further analysis in long straight channels, *e.g.* of acoustic streaming.

6.5 Paper V: Suppression of acoustic streaming in shape-optimized channels

Acoustic streaming is a key obstacle in the field of acoustofluidics for controlled handling of sub-micron particles. For a standing-half-wave resonance in a 380 µm-wide channel, spherical polystyrene particles of diameter smaller than around 1.8 µm cannot be focused because of the acoustic streaming [66, 67]. The overall motivation for the theoretical studies on acoustic streaming done in this PhD project, is to obtain insight that can be used to overcome this obstacle. Paper V [5] presents the discovery, that acoustic streaming

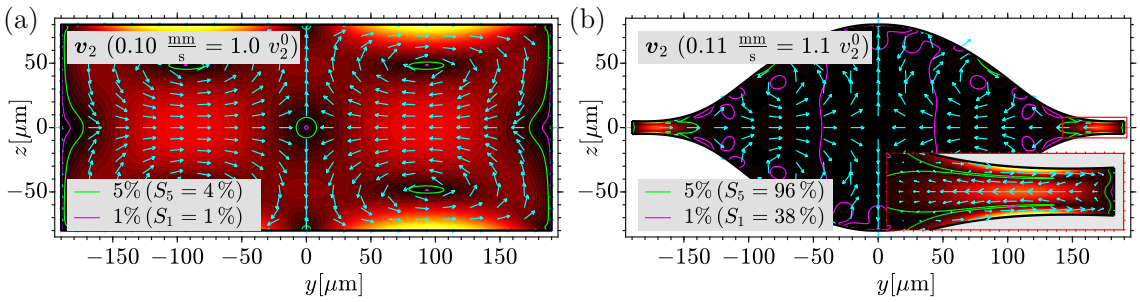

Figure 6.1: Comparison between the acoustic streaming (normalized cyan arrows) in a rectangular cross section and the optimized cross section from 0 (black) to 0.11 mm/s (yellow). The green and magenta contours mark the regions where the streaming is suppressed to respectively 5 % and 1 % of the characteristic streaming velocity v_2^0 which is 0.10 $\frac{\text{mm}}{\text{s}}$ in this case. Adapted from Fig. 1 in Paper V [5].

can be suppressed significantly by optimising the shape of the resonance cavity as shown in Fig. 6.1(b). Quantitatively, the acoustic streaming speed is here suppressed to less than 5 % of that in the rectangle [Fig. 6.1(a)] in around 96 % of the cross-section area. The shape was obtained by an iterative shape-optimization algorithm with an efficiency ensured by the effective boundary conditions derived in Paper I [1]. This result considered to be among the most important contributions of this thesis.

Chapter 7

Papers of the PhD project

7.1 Paper I: J. Acoust. Soc. Am. 144(2), 766-784 (2018)

Theory of pressure acoustics with viscous boundary layers and streaming in curved elastic cavities

DOI: 10.1121/1.5049579

Authors: J. S. Bach and H. Bruus.
Journal: J. Acoust. Soc. Am. **144**(2), 766-784 (2018)

Remarks: This paper has some overlap with work presented in my MSc thesis [116], however, the analysis and the results have been significantly extended.

Theory of pressure acoustics with viscous boundary layers and streaming in curved elastic cavities

Jacob S. Bach and Henrik Bruus[a)]
Department of Physics, Technical University of Denmark, DTU Physics Building 309, DK-2800 Kongens Lyngby, Denmark

(Received 22 April 2018; revised 6 July 2018; accepted 20 July 2018; published online 17 August 2018)

The acoustic fields and streaming in a confined fluid depend strongly on the viscous boundary layer forming near the wall. The width of this layer is typically much smaller than the bulk length scale set by the geometry or the acoustic wavelength, which makes direct numerical simulations challenging. Based on this separation in length scales, the classical theory of pressure acoustics is extended by deriving a boundary condition for the acoustic pressure that takes viscous boundary-layer effects fully into account. Using the same length-scale separation for the steady second-order streaming, and combining it with time-averaged short-range products of first-order fields, the usual limiting-velocity theory is replaced with an analytical slip-velocity condition on the long-range streaming field at the wall. The derived boundary conditions are valid for oscillating cavities of arbitrary shape and wall motion, as long as both the wall curvature and displacement amplitude are sufficiently small. Finally, the theory is validated by comparison with direct numerical simulation in two examples of two-dimensional water-filled cavities: The well-studied rectangular cavity with prescribed wall actuation, and a more generic elliptical cavity embedded in an externally actuated rectangular elastic glass block.
https://doi.org/10.1121/1.5049579

[PLM] Pages: 766–784

I. INTRODUCTION

The study of ultrasound effects in fluids in sub-millimeter cavities and channels has intensified the past decade, as microscale acoustofluidic devices are used increasingly in biology, environmental and forensic sciences, and clinical diagnostics.[1,2] Examples include cell synchronization,[3] enrichment of prostate cancer cells in blood,[4] size-independent sorting of cells,[5] manipulation of *C. elegans*,[6] and single-cell patterning.[7] Acoustics can also be used for non-contact microfluidic trapping and particle enrichment[8–10] as well as acoustic tweezing.[11–14]

The two fundamental physical phenomena that enable these microscale acoustofluidic applications are rooted in nonlinear acoustics. One fundamental phenomenon is the acoustic radiation force, which tends to focus suspended particles in the pressure nodes based on their acoustic contrast to the surrounding fluid.[15–21] The second fundamental phenomenon is the acoustic streaming appearing as steady flow rolls which tend to defocus suspended particles due to the Stokes drag.[22–27] Because the acoustic radiation force scales with the volume of the suspended particle, and the Stokes drag with its radius, the former dominates for large particles and the latter for small. For water at room temperature and 1 MHz ultrasound, the critical particle radius for the crossover between these two regimes has been determined to be around 2 μm.[28,29]

So far, the vast majority of successful microscale acoustofluidics applications has been for large (above 2 μm) particles, such as cells, whose dynamics is dominated by the well-characterized, robust acoustic radiation force, which depends on the bulk properties of the acoustic field and material parameters of the particles and the surrounding fluid. However, there is a strong motivation to handle also sub-micrometer particles such as bacteria, exosomes, and viruses, for use in contemporary lab-on-a-chip-based diagnostics and biomedical research.[9,30–32] In contrast to large particles, the dynamics of small (sub-micrometer) particles is dominated by the drag force from the ill-characterized acoustic streaming. To control the handling of such nanoparticle suspensions, a deeper understanding of the often complicated acoustic streaming is called for.

One important aspect of ultrasound acoustics is the large velocity gradients in the sub-micrometer-thin viscous boundary layer near rigid boundaries.[22] The shear stress and the Reynolds stress that build up in this region are responsible for the viscous damping of the acoustic fields and for the acoustic streaming, respectively. In water with kinematic viscosity $\nu_0 \approx 10^{-6}\,\mathrm{m^2/s}$ at the frequency $f = (1/2\pi)\omega \approx 1$ MHz, the thickness $\delta = \sqrt{2\nu_0/\omega}$ of this boundary layer is on the order of 500 nm, while the acoustic wavelength is around 1.5 mm. This three-orders-of-magnitude separation of physically relevant length scales poses a severe challenge for numerical simulations. To circumvent the problem of resolving the thin boundary layer, we develop a theory were analytical solutions for the boundary layers are used to formulate boundary conditions for the pressure field and bulk streaming field, which both varies on the much longer length scale $d \gg \delta$.

First, we extend the classical pressure acoustics theory by formulating a boundary condition for the acoustic pressure that includes the presence of the boundary layer, which

a)Electronic mail: bruus@fysik.dtu.dk

is otherwise neglected. Thus, our extended boundary condition takes into account important effect of the boundary layer, such as increased viscous damping, shifts in resonance frequencies, and shear stresses on the surrounding walls.

Second, we formulate a generalized slip-velocity boundary condition for bulk acoustic streaming over curved oscillating surfaces. An important step in this direction was the development of the limiting-velocity theory by Nyborg in 1958 for perpendicularly oscillating curved walls.[33] Later modifications of this theory comprise modifications to the analysis in curvilinear coordinates by Lee and Wang in 1989,[34] and the treatment of oscillations in any direction for flat walls by Vanneste and Bühler in 2011.[35] Here, we extend these theories to harmonic oscillations in any direction of an arbitrarily shaped elastic wall, provided that both the radius of curvature and the acoustic wavelength are much larger than the boundary layer length-scale δ, and that also the amplitude of the perpendicular surface vibration is much smaller than δ.

Notably, the theoretical description developed here allows us to perform numerical simulations of the linear and nonlinear acoustics in arbitrarily shaped liquid-filled cavities embedded in oscillating elastic solids. Examples and validation of such simulations for two-dimensional (2D) systems are presented in the final sections of this paper, while a study of three-dimensional (3D) systems is work in progress to be presented later.

II. WALL MOTION AND PERTURBATION THEORY

We consider a fluid domain Ω bounded by an elastic, oscillating solid, see Fig. 1. All acoustic effects in the fluid are generated by the fluid-solid interface that oscillates harmonically around its equilibrium position, denoted $\boldsymbol{s}_0$ or $\partial\Omega$, with an angular frequency ω. The instantaneous position $\boldsymbol{s}(\boldsymbol{s}_0, t)$ at time t of this interface (the wall), is described by the small complex displacement $\boldsymbol{s}_1(\boldsymbol{s}_0)\mathrm{e}^{-\mathrm{i}\omega t}$,

$$\boldsymbol{s}(\boldsymbol{s}_0, t) = \boldsymbol{s}_0 + \boldsymbol{s}_1(\boldsymbol{s}_0)\,\mathrm{e}^{-\mathrm{i}\omega t}. \tag{1}$$

In contrast to Muller and Bruus,[36] we do not study the transient phase leading to this steady oscillatory motion.

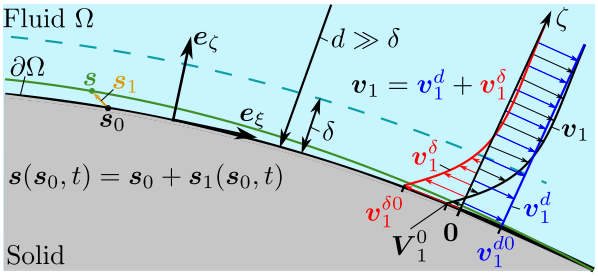

FIG. 1. (Color online) Sketch of the interface between a fluid (light blue, Ω) and a curved, oscillating solid (dark gray) with instantaneous position $\boldsymbol{s}$ (dark green line) and equilibrium position $\boldsymbol{s}_0$ (black line, $\partial\Omega$). The local curvilinear coordinate system on the interface is given by the tangent vectors $\boldsymbol{e}_\xi$ and $\boldsymbol{e}_\eta$ and the normal vector $\boldsymbol{e}_\zeta$. By a Helmholtz decomposition, the first-order acoustic fluid velocity $\boldsymbol{v}_1 = \boldsymbol{v}_1^d + \boldsymbol{v}_1^\delta$ is written as the sum of a long-range compressible part $\boldsymbol{v}_1^d$ (dark blue) extending into the bulk and a short-range incompressible part $\boldsymbol{v}_1^\delta$ (light red) with a decay length equal to the boundary-layer width δ. $\boldsymbol{V}_1^0 = \boldsymbol{v}_1^{d0} + \boldsymbol{v}_1^{\delta 0}$ is the Lagrangian velocity of the interface (the wall).

A. Fundamental conservation laws in acoustofluidics

The theory of acoustofluidics in Ω is derived from the conservation of the fluid mass and momentum density,

$$\partial_t \rho = -\boldsymbol{\nabla}\cdot(\rho\boldsymbol{v}), \tag{2a}$$

$$\partial_t(\rho\boldsymbol{v}) = -\boldsymbol{\nabla}\cdot[(\rho\boldsymbol{v})\boldsymbol{v}] + \boldsymbol{\nabla}\cdot\boldsymbol{\sigma}, \tag{2b}$$

where ρ is the mass density, $\boldsymbol{v}$ is the Eulerian fluid velocity, and $\boldsymbol{\sigma}$ is the viscous stress tensor, given by

$$\boldsymbol{\sigma} = -p\,\mathbf{I} + \boldsymbol{\tau}, \tag{2c}$$

$$\boldsymbol{\tau} = \eta_0^{\mathrm{b}}(\boldsymbol{\nabla}\cdot\boldsymbol{v})\mathbf{I} + \eta_0\left[\boldsymbol{\nabla}\boldsymbol{v} + (\boldsymbol{\nabla}\boldsymbol{v})^{\mathrm{T}} - \frac{2}{3}(\boldsymbol{\nabla}\cdot\boldsymbol{v})\mathbf{I}\right]. \tag{2d}$$

Here, p is the pressure and $\boldsymbol{\tau}$ is the viscous part of the stress tensor given in terms of the bulk viscosity η_0^{b}, the dynamic viscosity η_0, the identity matrix $\mathbf{I}$, and the superscript "T" denoting matrix transpose. Thermal dissipation is neglected throughout this work. We introduce the isentropic compressibility κ_0 and speed of sound c_0,

$$\kappa_0 = \frac{1}{\rho_0}\left(\frac{\partial\rho}{\partial p}\right)_S = \frac{1}{\rho_0 c_0^2}, \tag{3}$$

as well as the small dimensionless damping coefficient Γ in terms of the viscosity ratio β,

$$\Gamma = (\beta+1)\eta_0\omega\kappa_0, \quad \beta = \frac{\eta_0^{\mathrm{b}}}{\eta_0} + \frac{1}{3}. \tag{4}$$

B. Perturbation expansion

The linear acoustic response of the system is proportional to the displacement stimulus $\boldsymbol{s}_1(\boldsymbol{s}_0)\mathrm{e}^{-\mathrm{i}\omega t}$, and the resulting complex-valued quantities $Q_1(\boldsymbol{r})\,\mathrm{e}^{-\mathrm{i}\omega t}$ are called first-order fields with subscript "1". The physical time-dependent quantity $Q_1^{\mathrm{phys}}(\boldsymbol{r}, t)$ corresponding to Q_1 is given by the real part $Q_1^{\mathrm{phys}}(\boldsymbol{r}, t) = \mathrm{Re}[Q_1(\boldsymbol{r})\,\mathrm{e}^{-\mathrm{i}\omega t}]$.

As the governing equations are nonlinear, we also encounter higher-order terms, and in the present work, we include terms to second order in the stimulus. Moreover, since we are only interested in the steady part of these second-order fields, we let in the following the subscript "2" denote a time-averaged quantity, written as $Q_2(\boldsymbol{r}) = \langle Q_2(\boldsymbol{r}, t)\rangle = (\omega/2\pi)\int_0^{2\pi/\omega} Q_2(\boldsymbol{r}, t)\,\mathrm{d}t$. Time-averages of products of time-harmonic complex-valued first-order fields A_1 and B_1 are also of second order, and for those we have $\langle A_1 B_1\rangle = \frac{1}{2}\mathrm{Re}[A_1(\boldsymbol{r})B_1^*(\boldsymbol{r})]$, where the asterisk denote complex conjugation.

Using this notation for the fluid, we expand the mass density ρ, the pressure p, and the velocity $\boldsymbol{v}$ in perturbation series of the form

$$\rho = \rho_0 + \rho_1(\boldsymbol{r})\mathrm{e}^{-\mathrm{i}\omega t} + \rho_2(\boldsymbol{r}), \tag{5a}$$

$$p = p_0 + p_1(\boldsymbol{r})\mathrm{e}^{-\mathrm{i}\omega t} + p_2(\boldsymbol{r}), \tag{5b}$$

$$\boldsymbol{v} = \boldsymbol{0} + \boldsymbol{v}_1(\boldsymbol{r})\mathrm{e}^{-\mathrm{i}\omega t} + \boldsymbol{v}_2(\boldsymbol{r}), \tag{5c}$$

where $\rho_1 \ll \rho_0$, $p_1 = c_0^2\rho_1 \ll c_0^2\rho_0$, and $|\boldsymbol{v}_1| \ll c_0$. The subscripts 1 and 2 denote the order in the small acoustic Mach number $\mathrm{Ma} = (1/c_0)|\boldsymbol{v}_1|$, which itself is proportional to $\boldsymbol{s}_1$.

C. No-slip boundary condition at the wall

To characterize the wall motion, we compute the time derivative of $\boldsymbol{s}(\boldsymbol{s}_0, t)$ in Eq. (1),

$$\partial_t \boldsymbol{s}(\boldsymbol{s}_0, t) = -\mathrm{i}\omega \boldsymbol{s}_1(\boldsymbol{s}_0)\,\mathrm{e}^{-\mathrm{i}\omega t} = \boldsymbol{V}_1^0(\boldsymbol{s}_0)\,\mathrm{e}^{-\mathrm{i}\omega t}, \tag{6}$$

where $\boldsymbol{V}_1^0(\boldsymbol{s}_0) = -\mathrm{i}\omega \boldsymbol{s}_1(\boldsymbol{s}_0)$ is the Lagrangian velocity of the wall surface element with equilibrium position $\boldsymbol{s}_0$ and instantaneous position $\boldsymbol{s}$. The no-slip boundary condition on the Eulerian fluid velocity $\boldsymbol{v}(\boldsymbol{r}, t)$ is imposed at the instantaneous surface position $\boldsymbol{s}(t)$,[35,37]

$$\boldsymbol{v}(\boldsymbol{s}_0 + \boldsymbol{s}_1\mathrm{e}^{-\mathrm{i}\omega t}, t) = \boldsymbol{V}_1^0(\boldsymbol{s}_0)\,\mathrm{e}^{-\mathrm{i}\omega t}, \quad \text{no–slip condition.} \tag{7}$$

Combining Eqs. (5c) and (7) with the Taylor expansion $\boldsymbol{v}_1(\boldsymbol{s}_0 + \boldsymbol{s}_1, t) \approx \boldsymbol{v}_1(\boldsymbol{s}_0)\mathrm{e}^{-\mathrm{i}\omega t} + \langle(\boldsymbol{s}_1 \cdot \boldsymbol{\nabla})\boldsymbol{v}_1\rangle|_{\boldsymbol{s}_0}$, and collecting the terms order by order, gives

$$\boldsymbol{v}_1(\boldsymbol{s}_0) = \boldsymbol{V}_1^0(\boldsymbol{s}_0), \quad \text{1st–order condition,} \tag{8a}$$

$$\boldsymbol{v}_2(\boldsymbol{s}_0) = -\langle(\boldsymbol{s}_1 \cdot \boldsymbol{\nabla})\boldsymbol{v}_1\rangle|_{\boldsymbol{s}_0}, \quad \text{2nd–order condition.} \tag{8b}$$

Note that the expansion, or Stokes drift, in Eq. (8b) is valid, if the length scale over which $\boldsymbol{v}_1$ varies is much larger than $|\boldsymbol{s}_1|$. So we require $|\boldsymbol{s}_{1\parallel}| \ll d$ and $|\boldsymbol{s}_{1\zeta}| \ll \delta$.

D. The limit of weakly curved, thin boundary layers

The crux of our work is the analytical treatment of weakly curved, thin viscous boundary layers. This notion is quantified using the boundary-layer length scale δ and the compressional length scale d,

$$\delta = \sqrt{\frac{2\nu_0}{\omega}}, \quad d = \min\{k_0^{-1}, R\}, \tag{9}$$

where d is the minimum of the wavelength scale $k_0^{-1} = c_0/\omega$ and the length scale R over which the surface curves. We express our subsequent analysis to lowest order in ϵ, defined as the ratio of these length scales,

$$\epsilon = \frac{\delta}{d} \ll 1, \tag{10}$$

where the inequality holds in the limit of weakly curved ($\delta/R \ll 1$), thin boundary layers ($k_0\delta \ll 1$), a condition usually satisfied in microfluidic devices.

E. Local boundary-layer coordinates

The limit $\epsilon \ll 1$ allows for drastic simplifications of the otherwise complex analytical expressions for curvilinear derivatives of fields inside the boundary layers at distances of order δ or smaller from the wall. To see this, we introduce the local, right-handed, orthogonal, curvilinear coordinate system with coordinates ξ, η, and ζ. The latter measures distance away from the surface equilibrium position along the surface unit normal vector $\boldsymbol{e}_\zeta$, while the tangential coordinates ξ and η increase in the respective directions of the unit tangent vectors $\boldsymbol{e}_\xi$ and $\boldsymbol{e}_\eta$, but not necessarily measuring arc length, see Fig. 1. To make the scale R of the curved surface explicit, we use the vectorial notation for curvilinear derivatives and introduce the differential-geometric symbols employed in previous boundary-layer analyses in the literature,[33,34]

$$h_i = |\partial_i \boldsymbol{r}|, \quad T_{kji} = \left(\tilde{\partial}_k \boldsymbol{e}_j\right) \cdot \boldsymbol{e}_i, \quad \text{for } i,j,k = \xi,\eta,\zeta,$$
$$\tilde{\partial}_i = \frac{1}{h_i}\partial_i, \quad \mathcal{H}_k = T_{iki} = \tilde{\partial}_k\left[\sum_{i\neq k} \log h_i\right]. \tag{11}$$

Note that this is not covariant formulation, see Appendix A for details on the differential geometry. Because ζ measures arc length, we have $h_\zeta = 1$ and consequently $\tilde{\partial}_\zeta = \partial_\zeta$. The surface length scale can now be defined as $R \sim \min\{T_{kji}^{-1}, \mathcal{H}_k^{-1}\}$, which in many situations is comparable with the surface curvature radius.

F. Surface fields, boundary-layer fields, and bulk fields

For $\epsilon \ll 1$, we may separate any field $\boldsymbol{A}$ inside the boundary layer in the perpendicular coordinate ζ,

$$\boldsymbol{A}(\xi,\eta,\zeta) = \boldsymbol{A}^0(\xi,\eta)\,a(\zeta), \quad \zeta \lesssim \delta \ll d. \tag{12}$$

Here, superscript "0" defines a surface field $\boldsymbol{A}^0(\xi,\eta) = \boldsymbol{A}(\xi,\eta,0)$, such as the wall velocity $\boldsymbol{V}_1^0$ and the fluid velocity $\boldsymbol{v}^0$ at the equilibrium position $\boldsymbol{s}_0$ of the wall. Note that a surface field does not have a perpendicular derivative, although it does have a perpendicular component. This coordinate separation results in the following expressions in vectorial notation for the divergence (A6) and advective derivative (A8) involving surface fields:

$$\boldsymbol{\nabla} \cdot \boldsymbol{A}^0 = \boldsymbol{\nabla}_\parallel \cdot \boldsymbol{A}_\parallel^0 + \mathcal{H}_\zeta A_\zeta^0, \tag{13a}$$

$$(\boldsymbol{A}^0 \cdot \boldsymbol{\nabla})\boldsymbol{B}^0 = \boldsymbol{A}_\parallel^0 \cdot (\boldsymbol{\nabla}_\parallel B_i^0)\,\boldsymbol{e}_i + A_k^0 B_j^0 T_{kji}\boldsymbol{e}_i, \tag{13b}$$

$$\boldsymbol{A}_\parallel = A_\xi\,\boldsymbol{e}_\xi + A_\eta\,\boldsymbol{e}_\eta, \tag{13c}$$

$$\boldsymbol{\nabla}_\parallel = \boldsymbol{e}_\xi\tilde{\partial}_\xi + \boldsymbol{e}_\eta\tilde{\partial}_\eta, \tag{13d}$$

where subscript "$\parallel$" denotes tangential components. See Appendix A for supplemental details.

Importantly, for fluid fields, we distinguish between bulk fields $\boldsymbol{A}^d$ that extend into the bulk with spatial variation on the compressional length scale d and that are typically found by numerical simulation, and boundary-layer fields $\boldsymbol{A}^\delta$ that decays to zero away from the wall at the boundary-layer length scale δ, as sketched in Fig. 1,

$$\boldsymbol{A}^\delta = \boldsymbol{A}^{\delta 0}(\xi,\eta)\,a^\delta(\zeta), \quad \text{with } a^\delta(\zeta) \to 0 \text{ for } \frac{\zeta}{\delta} \to \infty. \tag{14}$$

This specific property makes it possible to obtain analytical solutions for the boundary-layer fields $\boldsymbol{A}^\delta$, because the

surface-derivative quantities $\nabla_\parallel$, T_{kji}, and $\mathcal{H}_k$, all of size d^{-1}, are a factor of ϵ smaller than the perpendicular derivative ∂_ζ of size δ^{-1}, so they can be neglected. To lowest order in ϵ, as detailed further at the end of Appendix A, the curvilinear derivatives of scalar and vector boundary-layer fields thus simplify to

$$\nabla^2 g^\delta \approx \partial_\zeta^2 g^\delta, \tag{15a}$$

$$\nabla^2 \boldsymbol{A}^\delta \approx \boldsymbol{A}^{\delta 0}\partial_\zeta^2 a(\zeta) = \partial_\zeta^2 \boldsymbol{A}^\delta, \tag{15b}$$

$$\boldsymbol{\nabla}\cdot\boldsymbol{A}^\delta \approx \boldsymbol{\nabla}_\parallel\cdot\boldsymbol{A}_\parallel^\delta + \partial_\zeta A_\zeta^\delta. \tag{15c}$$

With Eqs. (13) and (15), we have established to leading order in ϵ the expressions in vectorial form for the curvilinear derivatives in the boundary layer necessary for the subsequent analytical treatment of the boundary layer. In summary, the length-scale conditions for our theory to be valid, in particular Eqs. (8) and (15), are

$$\delta \ll d, \quad |\boldsymbol{s}_{1\parallel}| \ll d, \quad |s_{1\zeta}| \ll \delta. \tag{16}$$

III. FIRST-ORDER TIME-HARMONIC FIELDS

Returning to the perturbation expansion (5), we write the first-order part of the governing equations (2),

$$p_1 = c_0^2\rho_1, \tag{17a}$$

$$-\mathrm{i}\omega\kappa_0 p_1 = -\boldsymbol{\nabla}\cdot\boldsymbol{v}_1, \tag{17b}$$

$$-\mathrm{i}\omega\rho_0\boldsymbol{v}_1 = -\boldsymbol{\nabla}[p_1 - \beta\eta_0\boldsymbol{\nabla}\cdot\boldsymbol{v}_1] + \eta_0\nabla^2\boldsymbol{v}_1, \tag{17c}$$

we make a standard Helmholtz decomposition of the velocity field $\boldsymbol{v}_1$,[21,33,34,37]

$$\boldsymbol{v}_1 = \boldsymbol{v}_1^d + \boldsymbol{v}_1^\delta, \quad \text{where } \boldsymbol{\nabla}\times\boldsymbol{v}_1^d = \boldsymbol{0} \text{ and } \boldsymbol{\nabla}\cdot\boldsymbol{v}_1^\delta = 0, \tag{18}$$

and insert it into Eq. (17). We separate the equations in solenoidal and irrotational parts and find

$$\mathrm{i}\omega\kappa_0 p_1 = \boldsymbol{\nabla}\cdot\boldsymbol{v}_1^d, \tag{19a}$$

$$-\mathrm{i}\omega\rho_0\boldsymbol{v}_1^d = \boldsymbol{\nabla}\cdot\boldsymbol{\sigma}_1^d = -(1-\mathrm{i}\Gamma)\boldsymbol{\nabla}p_1, \tag{19b}$$

$$-\mathrm{i}\omega\rho_0\boldsymbol{v}_1^\delta = \boldsymbol{\nabla}\cdot\boldsymbol{\sigma}_1^\delta = \eta_0\nabla^2\boldsymbol{v}_1^\delta. \tag{19c}$$

From this, we derive Helmholtz equations for the bulk fields p_1 and $\boldsymbol{v}_1^d$ as well as for the boundary-layer field $\boldsymbol{v}_1^\delta$,

$$\nabla^2 p_1 + k_\mathrm{c}^2 p_1 = 0, \quad \text{where } k_\mathrm{c} = \left(1+\mathrm{i}\frac{\Gamma}{2}\right)k_0, \tag{20a}$$

$$\nabla^2\boldsymbol{v}_1^d + k_\mathrm{c}^2\boldsymbol{v}_1^d = \boldsymbol{0}, \tag{20b}$$

$$\nabla^2\boldsymbol{v}_1^\delta + k_\mathrm{s}^2\boldsymbol{v}_1^\delta = \boldsymbol{0}, \quad \text{where } k_\mathrm{s} = \frac{1+\mathrm{i}}{\delta}. \tag{20c}$$

Here, we have introduced the compressional wavenumber k_c in terms of Γ defined in Eq. (4) and $k_0 = \omega/c_0$, and the shear wave number k_s in terms of δ. Note that Γ is of second order in ϵ,

$$\Gamma = \frac{1+\beta}{2}(k_0\delta)^2 \sim \epsilon^2 \ll 1. \tag{21}$$

From Eq. (19b) follows that the long-range velocity $\boldsymbol{v}_1^d$ is a potential flow proportional to $\boldsymbol{\nabla}p_1$, and as such it is the acoustic velocity of pressure acoustics. The short-range velocity $\boldsymbol{v}_1^\delta$ is confined to the thin boundary layer of width δ close to the surface, and therefore it is typically not observed in experiments and is ignored in classical pressure acoustics. In the following we derive an analytic solution for the boundary-layer field $\boldsymbol{v}_1^\delta$, which is used to determine a boundary condition for p_1. In this way, the viscous effects from the boundary layer are taken into account in computations of the long-range pressure-acoustic fields p_1 and $\boldsymbol{v}_1^d$.

A. Analytical form of the first-order boundary-layer field

By using Eq. (15b), the analytical solution $\boldsymbol{v}_1^\delta$ to Eq. (20c) is found to be

$$\boldsymbol{v}_1^\delta = \boldsymbol{v}_1^{\delta 0}(\xi,\eta)\,\mathrm{e}^{\mathrm{i}k_\mathrm{s}\zeta} + \mathcal{O}(\epsilon), \tag{22a}$$

which describes a shear wave heavily damped over a single wave length, as it travels away from the surface with speed $c_\mathrm{sw} = \omega\delta \ll c_0$. To satisfy the boundary condition (8a), we impose the following condition for $\boldsymbol{v}_1^{\delta 0}$ at the equilibrium position $\boldsymbol{s}_0$ of the wall,

$$\boldsymbol{v}_1^{\delta 0} = \boldsymbol{V}_1^0 - \boldsymbol{v}_1^{d0}, \quad \text{first–order no–slip condition.} \tag{22b}$$

B. Boundary condition for the first-order pressure field

We now derive a boundary condition for the first-order pressure field p_1, which takes the viscous boundary layer effects into account without explicit reference to $\boldsymbol{v}_1$. First, it is important to note that the incompressibility condition $\boldsymbol{\nabla}\cdot\boldsymbol{v}_1^\delta = 0$ used on Eq. (22a) leads to a small perpendicular short-range velocity at $\boldsymbol{s}_0$,

$$v_{1\zeta}^{\delta 0} = \frac{\mathrm{i}}{k_\mathrm{s}}\boldsymbol{\nabla}\cdot\boldsymbol{v}_1^{\delta 0} = \frac{\mathrm{i}}{k_\mathrm{s}}\boldsymbol{\nabla}\cdot\boldsymbol{V}_1^0 - \frac{\mathrm{i}}{k_\mathrm{s}}\boldsymbol{\nabla}\cdot\boldsymbol{v}_1^{d0}. \tag{23}$$

Because $k_\mathrm{s}^{-1} \simeq \delta$ and $\boldsymbol{\nabla}\cdot\boldsymbol{v}_1^{\delta 0} \simeq d^{-1}$, we find that $|v_{1\zeta}^{\delta 0}| \sim \epsilon|v_1| \ll |v_1|$. We repeatedly exploit this relation to neglect terms with $v_{1\zeta}^{\delta 0}$ in the following analyses to lowest order in ϵ. Using the no-slip condition (22b), the boundary condition on the long-range velocity becomes

$$v_{1\zeta}^{d0} = V_{1\zeta}^0 - v_{1\zeta}^{\delta 0} \tag{24a}$$

$$= \left(V_{1\zeta}^0 - \frac{\mathrm{i}}{k_\mathrm{s}}\boldsymbol{\nabla}\cdot\boldsymbol{V}_1^0\right) + \frac{\mathrm{i}}{k_\mathrm{s}}\boldsymbol{\nabla}\cdot\boldsymbol{v}_1^{d0} \tag{24b}$$

$$\approx \left(V_{1\zeta}^0 - \frac{\mathrm{i}}{k_\mathrm{s}}\boldsymbol{\nabla}_\parallel\cdot\boldsymbol{V}_{1\parallel}^0\right) + \frac{\mathrm{i}}{k_\mathrm{s}}\boldsymbol{\nabla}_\parallel\cdot\boldsymbol{v}_{1\parallel}^{d0}, \tag{24c}$$

where the last step is written for later convenience using $(\mathrm{i}/k_\mathrm{s})\boldsymbol{\nabla}\cdot(\boldsymbol{v}_1^{d0}-\boldsymbol{V}_1^0)=(\mathrm{i}/k_\mathrm{s})\boldsymbol{\nabla}_\parallel\cdot(\boldsymbol{v}_{1\parallel}^{d0}-\boldsymbol{V}_{1\parallel}^0)-(\mathrm{i}\mathcal{H}_\zeta/k_\mathrm{s})v_{1\zeta}^{\delta 0}$ from Eqs. (13a) and (22b) and using that $v_{1\zeta}^{\delta 0}\sim\epsilon|v_1|$. This boundary condition involves the usual expression $V_{1\zeta}^0$ used in classical pressure acoustics plus an $\mathcal{O}(\epsilon)$-correction term proportional to k_s^{-1}, due to the parallel divergence of fluid velocity inside the boundary layer that forces a fluid flow perpendicular to the surface to fulfil the incompressibility of the short-range velocity $\boldsymbol{v}_1^\delta$. Note that this correction term is generated partly by the external wall motion $-(\mathrm{i}/k_\mathrm{s})\boldsymbol{\nabla}_\parallel\cdot\boldsymbol{V}_{1\parallel}^0$ and partly by the fluid motion itself $(\mathrm{i}/k_\mathrm{s})\boldsymbol{\nabla}_\parallel\cdot\boldsymbol{v}_{1\parallel}^{d0}$. Hence, the wall can affect the long-range fields either by a perpendicular component $V_{1\zeta}^0$ or by a parallel divergence $\boldsymbol{\nabla}_\parallel\cdot\boldsymbol{V}_{1\parallel}^0$. The correction term $(\mathrm{i}/k_\mathrm{s})\boldsymbol{\nabla}_\parallel\cdot\boldsymbol{v}_{1\parallel}^{d0}$ due to the fluid motion itself gives the boundary-layer damping of the acoustic energy, see Sec. IV.

Finally, we write Eq. (24b) in terms of the pressure p_1 using $\boldsymbol{\nabla}\cdot\boldsymbol{v}_1^{d0}=\boldsymbol{\nabla}\cdot\boldsymbol{v}_1^d-\partial_\zeta v_{1\zeta}^d$ and Eq. (19),

$$\partial_\zeta p_1=\frac{\mathrm{i}\omega\rho_0}{1-\mathrm{i}\Gamma}\left(V_{1\zeta}^0-\frac{\mathrm{i}}{k_\mathrm{s}}\boldsymbol{\nabla}\cdot\boldsymbol{V}_1^0\right)-\frac{\mathrm{i}}{k_\mathrm{s}}(k_\mathrm{c}^2p_1+\partial_\zeta^2p_1),\quad\text{boundary condition at } \boldsymbol{s}_0. \tag{25}$$

C. Boundary condition for the first-order stress

The boundary condition for the first-order stress $\boldsymbol{\sigma}_1\cdot\boldsymbol{e}_\zeta$ on the surrounding wall is found using Eqs. (2c) and (2d). In the viscous stress $\boldsymbol{\tau}_1$, the divergence terms are neglected, because (19a) leads to $|\eta_0\boldsymbol{\nabla}\cdot\boldsymbol{v}_1^d|\approx\eta_0\omega\kappa_0p_1\approx\Gamma p_1\ll p_1$. The remaining part of $\boldsymbol{\tau}_1$ is dominated by the term $\eta_0\partial_\zeta\boldsymbol{v}_1^\delta$, and we obtain $\boldsymbol{\sigma}_1\cdot\boldsymbol{e}_\zeta=-p_1\boldsymbol{e}_\zeta+\eta_0\partial_\zeta\boldsymbol{v}_1^\delta$ at $\boldsymbol{s}_0$. Here, we insert $\partial_\zeta\boldsymbol{v}_1^\delta=\mathrm{i}k_\mathrm{s}\boldsymbol{v}_1^\delta$ from Eq. (22a), and use Eqs. (19b) and (22b) to express $\boldsymbol{\sigma}_1\cdot\boldsymbol{e}_\zeta$ in terms of the long-range pressure p_1 and wall velocity $\boldsymbol{V}_1^0$ to lowest order in $\Gamma\sim(k_0\delta)^2$,

$$\boldsymbol{\sigma}_1\cdot\boldsymbol{e}_\zeta=-p_1\boldsymbol{e}_\zeta+\mathrm{i}k_\mathrm{s}\eta_0\left(\boldsymbol{V}_1^0+\frac{\mathrm{i}}{\omega\rho_0}\boldsymbol{\nabla}p_1\right),\quad\text{boundary condition at } \boldsymbol{s}_0. \tag{26}$$

This is the usual pressure condition plus a correction term of order ϵ due to the viscous shear stress $\eta_0\partial_\zeta\boldsymbol{v}_1^\delta$ from the boundary layer.

Equations (20), (24), (25), and (26) constitute our main theoretical result for the first-order acoustic fields. Remarkably, explicit reference to the curvilinear quantities are absent in these equations, only the notion of perpendicular and tangential directions and components are important. In the numerical implementation of them in Sec. VII, we use Cartesian coordinates.

IV. ACOUSTIC POWER LOSS

From the pressure p_1, we derive an expression for the acoustic power loss solely in terms of long-range fields. We introduce the energy density E_ac^d and the energy-flux density $\boldsymbol{S}_\mathrm{ac}^d$ of the long-range acoustic fields,

$$E_\mathrm{ac}^d(\boldsymbol{r},t)=\frac{\kappa_0}{2}\left[\mathrm{Re}\left(p_1\mathrm{e}^{-\mathrm{i}\omega t}\right)\right]^2+\frac{\rho_0}{2}\left|\mathrm{Re}\left(\boldsymbol{v}_1^d\mathrm{e}^{-\mathrm{i}\omega t}\right)\right|^2, \tag{27a}$$

$$\boldsymbol{S}_\mathrm{ac}^d(\boldsymbol{r},t)=\mathrm{Re}(p_1\mathrm{e}^{-\mathrm{i}\omega t})\,\mathrm{Re}(\boldsymbol{v}_1^d\mathrm{e}^{-\mathrm{i}\omega t}), \tag{27b}$$

with the time averages

$$\langle E_\mathrm{ac}^d\rangle=\frac{1}{4}\kappa_0|p_1|^2+\frac{1}{4}\rho_0|\boldsymbol{v}_1^d|^2, \tag{28a}$$

$$\langle\boldsymbol{S}_\mathrm{ac}^d\rangle=\langle p_1\boldsymbol{v}_1^d\rangle=c_0^2\langle\rho_1\boldsymbol{v}_1^d\rangle. \tag{28b}$$

In terms of real-valued physical quantities, Eqs. (19a) and (19b) become $\kappa_0\partial_t\mathrm{Re}(p_1\mathrm{e}^{-\mathrm{i}\omega t})=-\boldsymbol{\nabla}\cdot\mathrm{Re}(\boldsymbol{v}_1^d\mathrm{e}^{-\mathrm{i}\omega t})$ and $\rho_0\partial_t\mathrm{Re}(\boldsymbol{v}_1^d\mathrm{e}^{-\mathrm{i}\omega t})=-\boldsymbol{\nabla}\cdot\mathrm{Re}[(1-\mathrm{i}\Gamma)p_1\mathrm{e}^{-\mathrm{i}\omega t}]$. Taking the scalar product of $\mathrm{Re}(\boldsymbol{v}_1^d\mathrm{e}^{-\mathrm{i}\omega t})$ with the latter leads to expressions for the time derivative $\partial_tE_\mathrm{ac}^d$ and its time-averaged value $\langle\partial_tE_\mathrm{ac}^d\rangle$, which is zero due to the harmonic time dependence,

$$\partial_tE_\mathrm{ac}^d=-\boldsymbol{\nabla}\cdot\boldsymbol{S}_\mathrm{ac}^d-\Gamma\rho_0\omega|\mathrm{Re}(\boldsymbol{v}_1^d\mathrm{e}^{-\mathrm{i}\omega t})|^2, \tag{29a}$$

$$-\boldsymbol{\nabla}\cdot\langle\boldsymbol{S}_\mathrm{ac}^d\rangle=\frac{1}{2}\Gamma\omega\rho_0|\boldsymbol{v}_1^d|^2. \tag{29b}$$

The latter expression describes the local balance between the convergence of energy-flux density $\langle\boldsymbol{S}_\mathrm{ac}^d\rangle$ and the rate of change of acoustic energy due to the combined effect of viscous dissipation and viscous energy flux. See Appendix B for a more detailed discussion of this point. Integrating Eq. (29b) over the entire fluid domain Ω, and using Gauss's theorem with the ζ-direction pointing into Ω, leads to the global balance of energy rates,

$$\int_{\partial\Omega}\langle p_1v_{1\zeta}^{d0}\rangle\mathrm{d}A=\int_\Omega\frac{1}{2}\Gamma\rho_0\omega|\boldsymbol{v}_1^d|^2\,\mathrm{d}V. \tag{30}$$

This general result reduces to that of classical pressure acoustics only in the special case where $v_{1\zeta}^{d0}=V_{1\zeta}^0$. As seen from Eq. (24c), $v_{1\zeta}^{d0}$ is generated partly externally by the wall motion, and partly internally by the fluid motion. Inserting Eq. (24c) into Eq. (30), and separating wall-velocity terms from fluid-velocity terms gives

$$\oint_{\partial\Omega}\left\langle p_1\left(V_{1\zeta}^0-\frac{\mathrm{i}}{k_\mathrm{s}}\boldsymbol{\nabla}_\parallel\cdot\boldsymbol{V}_{1\parallel}^0\right)\right\rangle\mathrm{d}A=\int_\Omega\frac{1}{2}\Gamma\rho_0\omega|\boldsymbol{v}_1^d|^2\,\mathrm{d}V-\oint_{\partial\Omega}\left\langle p_1\left(\frac{\mathrm{i}}{k_\mathrm{s}}\boldsymbol{\nabla}_\parallel\cdot\boldsymbol{v}_{1\parallel}^{d0}\right)\right\rangle\mathrm{d}A. \tag{31}$$

Here, the left-hand side represents the acoustic power gain due to the wall motion, while the right-hand side represents the acoustic power loss $\langle P_\mathrm{loss}^d\rangle$ due to the fluid motion. Integrating the last term by parts and using that $\oint_{\partial\Omega}\boldsymbol{\nabla}_\parallel\cdot\langle p_1[(\mathrm{i}/k_\mathrm{s})\boldsymbol{v}_{1\parallel}^{d0}]\rangle\mathrm{d}A=0$ for any closed surface, we can by Eq. (19b) rewrite $\langle P_\mathrm{loss}^d\rangle$ to lowest order in Γ as

$$\frac{1}{\omega}\langle P_\mathrm{loss}^d\rangle=\int_\Omega\frac{\Gamma}{2}\rho_0|\boldsymbol{v}_1^d|^2\,\mathrm{d}V+\oint_{\partial\Omega}\frac{\delta}{4}\rho_0|\boldsymbol{v}_{1\parallel}^{d0}|^2\,\mathrm{d}A, \tag{32}$$

which is always positive. The quality factor Q of an acoustic cavity resonator can be calculated from the long-range fields $\langle E_\mathrm{ac}^d\rangle$ in Eq. (28a) and $\langle P_\mathrm{loss}^d\rangle$ in Eq. (32) as

$$Q = \frac{\int_\Omega \langle E^d_{\mathrm{ac}} \rangle \, \mathrm{d}V}{\frac{1}{\omega} \langle P^d_{\mathrm{loss}} \rangle}, \quad \text{at resonance.} \tag{33}$$

We emphasize that in general, $\langle P_{\mathrm{loss}} \rangle$ is not identical to the viscous heat generation $\langle P^{\mathrm{diss}}_{\mathrm{visc}} \rangle = \int_\Omega \langle \nabla \boldsymbol{v}_1 : \boldsymbol{\tau}_1 \rangle \, \mathrm{d}V$, although as discussed in Appendix B, these might be approximately equal in many common situations.[38]

V. SECOND-ORDER STREAMING FIELDS

As specified in Sec. II B, we only consider the time-averaged streaming and not time-dependent streaming as done by Muller and Bruus.[36] For notational simplicity, we therefore drop the angled bracket $\langle \cdot \rangle$ from the time-averaged velocity $\boldsymbol{v}_2$, pressure p_2, and stress $\boldsymbol{\sigma}_2$. The streaming $\boldsymbol{v}_2$ is governed by the time-averaged part of Eq. (2) to second order in $\mathrm{Ma} = (1/c_0)|\boldsymbol{v}_1|$, together with the boundary condition (8b),

$$0 = \boldsymbol{\nabla} \cdot (\rho_0 \boldsymbol{v}_2 + \langle \rho_1 \boldsymbol{v}_1 \rangle), \quad \text{for } \boldsymbol{r} \in \Omega, \tag{34a}$$

$$\boldsymbol{0} = \boldsymbol{\nabla} \cdot \boldsymbol{\sigma}_2 - \rho_0 \boldsymbol{\nabla} \cdot \langle \boldsymbol{v}_1 \boldsymbol{v}_1 \rangle, \quad \text{for } \boldsymbol{r} \in \Omega, \tag{34b}$$

$$\boldsymbol{0} = \boldsymbol{v}_2 + \langle (\boldsymbol{s}_1 \cdot \boldsymbol{\nabla}) \boldsymbol{v}_1 \rangle, \quad \text{at } \boldsymbol{s}_0. \tag{34c}$$

For the given first-order fields ρ_1 and $\boldsymbol{v}_1$, this is a linear Stokes flow problem for $\boldsymbol{v}_2$ and $\boldsymbol{\sigma}_2$. We decompose the problem into one part driven by the long-range source terms, $\boldsymbol{\nabla} \cdot \langle \rho_1 \boldsymbol{v}^d_1 \rangle$ in Eq. (34a) and $\rho_0 \boldsymbol{\nabla} \cdot \langle \boldsymbol{v}^d_1 \boldsymbol{v}^d_1 \rangle$ in Eq. (34b), and another part driven by the short-range source terms $\boldsymbol{\nabla} \cdot \langle \rho_1 \boldsymbol{v}^\delta_1 \rangle$ and $\rho_0 \boldsymbol{\nabla} \cdot \langle \boldsymbol{v}^\delta_1 \boldsymbol{v}^\delta_1 + \boldsymbol{v}^\delta_1 \boldsymbol{v}^d_1 + \boldsymbol{v}^d_1 \boldsymbol{v}^\delta_1 \rangle$. The corresponding responses are long-range bulk fields "d" and short-range boundary-layer fields "δ,"

$$\boldsymbol{v}_2 = \boldsymbol{v}^d_2 + \boldsymbol{v}^\delta_2, \tag{35a}$$

$$p_2 = p^d_2 + p^\delta_2, \tag{35b}$$

$$\boldsymbol{\sigma}_2 = \boldsymbol{\sigma}^d_2 + \boldsymbol{\sigma}^\delta_2, \tag{35c}$$

$$\boldsymbol{v}^{d0}_2 = -\boldsymbol{v}^{\delta 0}_2 - \langle (\boldsymbol{s}_1 \cdot \boldsymbol{\nabla}) \boldsymbol{v}_1 \rangle, \quad \text{at } \boldsymbol{s}_0. \tag{35d}$$

Given the boundary conditions Eqs. (35d) and (36d), this length-scale-based decomposition of the linear Stokes problem is unique, see Eqs. (36) and (48), but in contrast to the first-order decomposition (18), it is not a Helmholtz decomposition. Nevertheless, the computational strategy remains the same: we find analytical solutions to the short-range δ-fields, and from this we derive boundary conditions for the long-range d-fields.

Note that our method to calculate the steady second-order fields differs from the standard method of matching "inner" boundary-layer solutions with "outer" bulk solutions.[33–35] Our short- and long-range fields co-exist in the boundary layer, but are related by imposing boundary conditions at $\boldsymbol{s}_0$.

A. Short-range boundary-layer streaming

The short-range part of Eq. (34) consists of all terms containing at least one short-range δ-field,

$$0 = \boldsymbol{\nabla} \cdot (\rho_0 \boldsymbol{v}^\delta_2 + \langle \rho_1 \boldsymbol{v}^\delta_1 \rangle), \tag{36a}$$

$$\boldsymbol{0} = -\rho_0 \boldsymbol{\nabla} \cdot \langle \boldsymbol{v}^\delta_1 \boldsymbol{v}^\delta_1 + \boldsymbol{v}^\delta_1 \boldsymbol{v}^d_1 + \boldsymbol{v}^d_1 \boldsymbol{v}^\delta_1 \rangle + \boldsymbol{\nabla} \cdot \boldsymbol{\sigma}^\delta_2, \tag{36b}$$

$$\boldsymbol{\nabla} \cdot \boldsymbol{\sigma}^\delta_2 = \boldsymbol{\nabla}(-p^\delta_2 + \beta \eta_0 \boldsymbol{\nabla} \cdot \boldsymbol{v}^\delta_2) + \eta_0 \nabla^2 \boldsymbol{v}^\delta_2, \tag{36c}$$

$$\text{where } \boldsymbol{v}^\delta_2 \to 0 \text{ as } \zeta \to \infty. \tag{36d}$$

Notably, condition (36d) leads to a nonzero short-range streaming velocity $\boldsymbol{v}^{\delta 0}_2$ at the wall, which, due to the full velocity boundary condition (34c), in turn implies a slip condition $\boldsymbol{v}^{d0}_2$ (35d) on the long-range streaming velocity.

First, we investigate the scaling of p^δ_2 by taking the divergence of Eq. (36b) and using Eqs. (36a) and (36c) together with $\boldsymbol{\nabla} \cdot \boldsymbol{v}^\delta_1 = 0$ and Eq. (19),

$$\begin{aligned} \nabla^2 p^\delta_2 &= -\nu_0 (1+\beta) \nabla^2 \langle \boldsymbol{v}^\delta_1 \cdot \boldsymbol{\nabla} \rho_1 \rangle \\ &\quad - \rho_0 \boldsymbol{\nabla} \cdot \Big(\boldsymbol{\nabla} \cdot \langle \boldsymbol{v}^\delta_1 \boldsymbol{v}^\delta_1 + \boldsymbol{v}^\delta_1 \boldsymbol{v}^d_1 + \boldsymbol{v}^d_1 \boldsymbol{v}^\delta_1 \rangle \Big) \end{aligned} \tag{37a}$$

$$\begin{aligned} &= -\rho_0 \Gamma \nabla^2 \langle \boldsymbol{v}^\delta_1 \cdot (\mathrm{i} \boldsymbol{v}^d_1) \rangle + 2 \rho_0 k_0^2 \langle \boldsymbol{v}^\delta_1 \cdot \boldsymbol{v}^d_1 \rangle \\ &\quad - \rho_0 \Big\langle \boldsymbol{\nabla}(2 \boldsymbol{v}^d_1 + \boldsymbol{v}^\delta_1) \, : \, (\boldsymbol{\nabla} \boldsymbol{v}^\delta_1)^{\mathrm{T}} \Big\rangle. \end{aligned} \tag{37b}$$

Recalling from Eq. (23) that $|v^{\delta 0}_{1\zeta}| \sim \delta d^{-1} v_1$, we find $|\rho_0 (\boldsymbol{\nabla} \boldsymbol{v}^d_1) \, : \, (\boldsymbol{\nabla} \boldsymbol{v}^\delta_1)^{\mathrm{T}}| \sim (\delta d)^{-1} \rho_0 v_1^2$ which is the largest possible scaling of the right-hand side. Since by definition p^δ_2 is a boundary-layer field, we have $|\nabla^2 p^\delta_2| \sim \delta^{-2} p^\delta_2$, and the scaling of $|p^\delta_2|$ becomes

$$|p^\delta_2| \lesssim \epsilon \rho_0 v_1^2. \tag{38}$$

Thus, $\boldsymbol{\nabla} p^\delta_2$ can be neglected in the parallel component of Eq. (36b), but not necessarily in the perpendicular one. Similarly, in Eq. (36c) we have $\boldsymbol{\nabla}(\beta \eta_0 \boldsymbol{\nabla} \cdot \boldsymbol{v}^\delta_2) = -\beta \nu_0 \boldsymbol{\nabla} \langle \boldsymbol{v}^\delta_1 \cdot \boldsymbol{\nabla} \rho_1 \rangle$ which scales as $\beta \eta_0 d^{-2} (v_1^2 / c_0)$ and thus much smaller than $|\eta_0 \nabla^2 \boldsymbol{v}^\delta_2| \sim \eta_0 \delta^{-2} (v_1^2 / c_0)$.

Henceforth, using the approximation (15b) for the boundary-layer field $\boldsymbol{v}^\delta_2$ in Eq. (36b), we obtain the parallel equation to lowest order in ϵ,

$$\nu_0 \partial_\zeta^2 \boldsymbol{v}^\delta_{2\parallel} = \Big[\boldsymbol{\nabla} \cdot \langle \boldsymbol{v}^\delta_1 \boldsymbol{v}^d_1 + \boldsymbol{v}^d_1 \boldsymbol{v}^\delta_1 + \boldsymbol{v}^\delta_1 \boldsymbol{v}^\delta_1 \rangle \Big]_\parallel. \tag{39a}$$

Combining this with Eq. (36a), and using Eqs. (15c) and (18), leads to an equation for the perpendicular component $v^{\delta 0}_{2\zeta}$ of the short-range streaming velocity,

$$\partial_\zeta v^{\delta 0}_{2\zeta} = -\boldsymbol{\nabla}_\parallel \cdot \boldsymbol{v}^\delta_{2\parallel} - \frac{1}{\rho_0} \langle \boldsymbol{v}^\delta_1 \cdot \boldsymbol{\nabla} \rho_1 \rangle. \tag{39b}$$

To determine the analytical solution for $\boldsymbol{v}^\delta_{2\parallel}$ in Eq. (39a), we Taylor-expand $\boldsymbol{v}^d_1$ to first order in ζ in the boundary layer, and we use the solution (22a) for $\boldsymbol{v}^\delta_1$,

$$\boldsymbol{v}^d_1 = \boldsymbol{v}^{d0}_1 + (\partial_\zeta \boldsymbol{v}^d_1)^0 \, \zeta, \quad \text{for } \zeta \ll d, \tag{40a}$$

$$\boldsymbol{v}^\delta_1 = \boldsymbol{v}^{\delta 0}_1 \, q(\zeta), \quad \text{with } q(\zeta) = \mathrm{e}^{\mathrm{i} k_s \zeta}. \tag{40b}$$

With these expressions, Eq. (39a) becomes

$$\nu_0\partial_\zeta^2 \boldsymbol{v}_{2\parallel}^{\delta} = \Big\{\boldsymbol{\nabla}\cdot\langle[\boldsymbol{v}_1^{\delta 0}q][\boldsymbol{v}_1^{d0}1] + [\boldsymbol{v}_1^{\delta 0}q][(\partial_\zeta \boldsymbol{v}_1^{d})^0\zeta] + [\boldsymbol{v}_1^{d0}1][\boldsymbol{v}_1^{\delta 0}q] + [(\partial_\zeta \boldsymbol{v}_1^{d})^0\zeta][\boldsymbol{v}_1^{\delta 0}q] + [\boldsymbol{v}_1^{\delta 0}q][\boldsymbol{v}_1^{\delta 0}q]\rangle\Big\}_\parallel. \tag{41}$$

In general, the divergence $\boldsymbol{\nabla}\cdot\langle \boldsymbol{A}_1\boldsymbol{B}_1\rangle$ of the time-averaged outer product of two first-order fields of the form $\boldsymbol{A}_1 = \boldsymbol{A}_1^0(\xi,\eta)\,a(\zeta)$ and $\boldsymbol{B}_1 = \boldsymbol{B}_1^0(\xi,\eta)\,b(\zeta)$, is

$$\boldsymbol{\nabla}\cdot\big\langle [\boldsymbol{A}_1^0 a]\,[\boldsymbol{B}_1^0 b]\big\rangle = \frac{1}{2}\mathrm{Re}\Big\{\boldsymbol{\nabla}\cdot\Big[(\boldsymbol{A}_1^0 a)(\boldsymbol{B}_1^0 b)^*\Big]\Big\} \tag{42a}$$

$$= \frac{1}{2}\mathrm{Re}\big\{\boldsymbol{\nabla}\cdot\big[(ab^*)(\boldsymbol{A}_1^0\boldsymbol{B}_1^{0*})\big]\big\} \tag{42b}$$

$$= \frac{1}{2}\mathrm{Re}\big\{ab^*\boldsymbol{\nabla}\cdot(\boldsymbol{A}_1^0\boldsymbol{B}_1^{0*}) + \boldsymbol{A}_1^0(\boldsymbol{B}_1^{0*}\cdot\boldsymbol{\nabla})(ab^*)\big\} \tag{42c}$$

$$= \frac{1}{2}\mathrm{Re}\Big\{ab^*\boldsymbol{\nabla}\cdot(\boldsymbol{A}_1^0\boldsymbol{B}_1^{0*}) + \boldsymbol{A}_1^0 B_{1\zeta}^{0*}\partial_\zeta(ab^*)\Big\}. \tag{42d}$$

When solving for $\boldsymbol{v}_{2\parallel}^{\delta 0}$ in Eq. (41), we must integrate such divergences twice and then evaluate the result at the surface $\zeta = 0$. The result is

$$\int^{\zeta}\mathrm{d}\zeta_2\int^{\zeta_2}\mathrm{d}\zeta_1\,\boldsymbol{\nabla}\cdot\Big[(\boldsymbol{A}_1^0 a(\zeta_1))(\boldsymbol{B}_1^0 b(\zeta_1))^*\Big]\Big|_{\zeta=0} = \frac{1}{2}\mathrm{Re}\Big\{I_{ab}^{(2)}\boldsymbol{\nabla}\cdot(\boldsymbol{A}_1^0\boldsymbol{B}_1^{0*}) + I_{ab}^{(1)}\boldsymbol{A}_1^0 B_{1\zeta}^{0*}\Big\}, \tag{43a}$$

where we have defined the integrals $I_{ab}^{(n)}$ as

$$I_{ab}^{(1)} = \int^{\zeta}\mathrm{d}\zeta_1\,a(\zeta_1)\,b(\zeta_1)^*|_{\zeta=0}, \tag{43b}$$

$$I_{ab}^{(2)} = \int^{\zeta}\mathrm{d}\zeta_2\int^{\zeta_2}\mathrm{d}\zeta_1\,a(\zeta_1)\,b(\zeta_1)^*|_{\zeta=0}, \tag{43c}$$

$$I_{ab}^{(3)} = \int^{\zeta}\mathrm{d}\zeta_3\int^{\zeta_3}\mathrm{d}\zeta_2\int^{\zeta_2}\mathrm{d}\zeta_1\,a(\zeta_1)\,b(\zeta_1)^*|_{\zeta=0}. \tag{43d}$$

We choose all integration constants to be zero to fulfil the condition (36d) at infinity. From Eq. (41) we see that the functions $a(\zeta)$ and $b(\zeta)$ in our case are either $q(\zeta)$, ζ, or unity. By straightforward integration, we find in increasing order of δ,

$$I_{qq}^{(1)} = -\frac{1}{2}\delta,\quad I_{q1}^{(1)} = -\frac{1+\mathrm{i}}{2}\delta,$$
$$I_{qq}^{(2)} = \frac{1}{4}\delta^2,\quad I_{q1}^{(2)} = \frac{\mathrm{i}}{2}\delta^2,\quad I_{q\zeta}^{(1)} = -\frac{\mathrm{i}}{2}\delta^2,$$
$$I_{qq}^{(3)} = -\frac{1}{8}\delta^3,\quad I_{q1}^{(3)} = \frac{1-\mathrm{i}}{4}\delta^3,\quad I_{q\zeta}^{(2)} = -\frac{1-\mathrm{i}}{2}\delta^3. \tag{43e}$$

Using Eq. (43) we find $\boldsymbol{v}_{2\parallel}^{\delta 0}$ by integration of Eq. (41) to leading order in ϵ,

$$\boldsymbol{v}_{2\parallel}^{\delta 0} = \frac{1}{2\nu_0}\mathrm{Re}\Big\{I_{qq}^{(2)}\boldsymbol{\nabla}\cdot\big(\boldsymbol{v}_1^{\delta 0}\boldsymbol{v}_1^{\delta 0*}\big) + I_{q1}^{(2)}\boldsymbol{\nabla}\cdot\big(\boldsymbol{v}_1^{\delta 0}\boldsymbol{v}_1^{d0*}\big) + I_{1q}^{(2)}\boldsymbol{\nabla}\cdot\big(\boldsymbol{v}_1^{d0}\boldsymbol{v}_1^{\delta 0*}\big) + I_{qq}^{(1)}\boldsymbol{v}_1^{\delta 0}v_{1\zeta}^{\delta 0*} + I_{1q}^{(1)}\boldsymbol{v}_1^{d0}v_{1\zeta}^{\delta 0*} + I_{q1}^{(1)}\boldsymbol{v}_1^{\delta 0}v_{1\zeta}^{d0*} + I_{q\zeta}^{(1)}\boldsymbol{v}_1^{\delta 0}\partial_\zeta v_{1\zeta}^{d*}\Big\}_\parallel. \tag{44}$$

We have neglected the term $(1/2\nu_0)\mathrm{Re}\{I_{\zeta q}^{(1)}(\partial_\zeta \boldsymbol{v}_1^d)^0 v_{1\zeta}^{\delta 0*}\}$, as $v_{1\zeta}^{\delta 0} \sim \epsilon|\boldsymbol{v}_{1\parallel}^{\delta 0}|$ due to Eq. (23), and the two terms proportional to $I_{\zeta q}^{(2)}$ and $I_{q\zeta}^{(2)}$, as these are $\sim\delta^3$. Remarkably, the term $I_{q1}^{(1)}\boldsymbol{v}_1^{\delta 0}v_{1\zeta}^{d0*}$ may scale with an extra factor ϵ^{-1} compared to all other terms, and thus may dominate the boundary-layer velocity. However, in the computation of the long-range slip velocity $\boldsymbol{v}_{2\parallel}^{d0}$ in Sec. V B, its contribution is canceled by the Stokes drift $\langle \boldsymbol{s}_1\cdot\boldsymbol{\nabla}\boldsymbol{v}_1\rangle$, as also noted in Ref. 35. Using $\boldsymbol{v}_1^{d0} = \boldsymbol{V}_1^0 - \boldsymbol{v}_1^{\delta 0}$, the property $(I_{ab}^{(n)})^* = I_{ba}^{(n)}$, and rearranging terms, we arrive at

$$\boldsymbol{v}_{2\parallel}^{\delta 0} = \frac{1}{2\nu_0}\mathrm{Re}\Big\{\Big(I_{qq}^{(2)} - 2\mathrm{Re}I_{q1}^{(2)}\Big)\boldsymbol{\nabla}\cdot\big(\boldsymbol{v}_1^{\delta 0}\boldsymbol{v}_1^{\delta 0*}\big) + I_{q1}^{(2)}\boldsymbol{\nabla}\cdot\big(\boldsymbol{v}_1^{\delta 0}\boldsymbol{V}_1^{0*}\big) + I_{1q}^{(2)}\boldsymbol{\nabla}\cdot\big(\boldsymbol{V}_1^{0}\boldsymbol{v}_1^{\delta 0*}\big) + \Big(I_{qq}^{(1)} - 2\mathrm{Re}I_{q1}^{(1)}\Big)\boldsymbol{v}_1^{\delta 0}v_{1\zeta}^{\delta 0*} + I_{1q}^{(1)}\boldsymbol{V}_1^{0}v_{1\zeta}^{\delta 0*} + I_{q1}^{(1)}\boldsymbol{v}_1^{\delta 0}V_{1\zeta}^{0*} + I_{q\zeta}^{(1)}\boldsymbol{v}_1^{\delta 0}\partial_\zeta v_{1\zeta}^{d*}\Big\}_\parallel. \tag{45}$$

The perpendicular short-range velocity component $v_{2\zeta}^{\delta 0}$ is found by integrating Eq. (39b) with respect to ζ. The integration of the $\boldsymbol{\nabla}_\parallel\cdot\boldsymbol{v}_{2\parallel}^{\delta}$-term is carried out by simply increasing the superscript of the $I_{ab}^{(n)}$-integrals in Eq. (45) from "(n)" to "$(n+1)$," while the integration of the $\boldsymbol{\nabla}\rho_1$-term is carried out by using Eq. (19b) to substitute $(1/\rho_0)\boldsymbol{\nabla}\rho_1$ by $\mathrm{i}\omega c_0^{-2}\boldsymbol{v}_1^d$ and introducing the suitable $I_{ab}^{(n)}$-integral for the factor $q(\zeta)\,\mathrm{i}$, namely, $I_{qi}^{(1)} = -\mathrm{i}I_{q1}^{(1)}$,

$$v_{2\zeta}^{\delta 0} = -\frac{1}{2\nu_0}\boldsymbol{\nabla}_\parallel\cdot\mathrm{Re}\Big\{\Big(I_{qq}^{(3)} - 2\mathrm{Re}I_{q1}^{(3)}\Big)\boldsymbol{\nabla}\cdot\big(\boldsymbol{v}_1^{\delta 0}\boldsymbol{v}_1^{\delta 0*}\big) + I_{q1}^{(3)}\boldsymbol{\nabla}\cdot\big(\boldsymbol{v}_1^{\delta 0}\boldsymbol{V}_1^{0*}\big) + I_{1q}^{(3)}\boldsymbol{\nabla}\cdot\big(\boldsymbol{V}_1^{0}\boldsymbol{v}_1^{\delta 0*}\big) + \Big(I_{qq}^{(2)} - 2\mathrm{Re}I_{q1}^{(2)}\Big)\boldsymbol{v}_1^{\delta 0}v_{1\zeta}^{\delta 0*} + I_{1q}^{(2)}\boldsymbol{V}_1^{0}v_{1\zeta}^{\delta 0*} + I_{q1}^{(2)}\boldsymbol{v}_1^{\delta 0}V_{1\zeta}^{0*} + I_{q\zeta}^{(2)}\boldsymbol{v}_1^{\delta 0}\partial_\zeta v_{1\zeta}^{d*}\Big\}_\parallel + \frac{k_0}{2c_0}\mathrm{Re}\Big\{\mathrm{i}I_{q1}^{(1)}\boldsymbol{v}_1^{\delta 0}\cdot\boldsymbol{v}_1^{d0*}\Big\}. \tag{46}$$

Using Eq. (43e), expressions (45) and (46) for the short-range streaming at the surface $\zeta = 0$ become

$$\boldsymbol{v}_{2\parallel}^{\delta 0} = \frac{1}{2\omega}\mathrm{Re}\Big\{\frac{1}{2}\boldsymbol{\nabla}\cdot\big(\boldsymbol{v}_1^{\delta 0}\boldsymbol{v}_1^{\delta 0*}\big) + \mathrm{i}\boldsymbol{\nabla}\cdot\big(\boldsymbol{v}_1^{\delta 0}\boldsymbol{V}_1^{0*}\big) - \mathrm{i}\boldsymbol{\nabla}\cdot\big(\boldsymbol{V}_1^{0}\boldsymbol{v}_1^{\delta 0*}\big) + \frac{1}{\delta}\boldsymbol{v}_1^{\delta 0}v_{1\zeta}^{\delta 0*} - \mathrm{i}\boldsymbol{v}_1^{\delta 0}\partial_\zeta v_{1\zeta}^{d*} - \frac{1-\mathrm{i}}{\delta}\boldsymbol{V}_1^{0}v_{1\zeta}^{\delta 0*} - \frac{1+\mathrm{i}}{\delta}\boldsymbol{v}_1^{\delta 0}V_{1\zeta}^{0*}\Big\}_\parallel \tag{47a}$$

and

$$v_{2\zeta}^{\delta 0} = -\frac{\delta}{2\omega}\mathrm{Re}\Big[\boldsymbol{\nabla}_\parallel \cdot \Big\{-\frac{5}{4}\boldsymbol{\nabla}\cdot\Big(\boldsymbol{v}_1^{\delta 0}\boldsymbol{v}_1^{\delta 0*}\Big) + \frac{1-\mathrm{i}}{2}\boldsymbol{\nabla}\cdot\Big(\boldsymbol{v}_1^{\delta 0}\boldsymbol{V}_1^{0*}\Big) + \frac{1+\mathrm{i}}{2}\boldsymbol{\nabla}\cdot\Big(\boldsymbol{V}_1^{0}\boldsymbol{v}_1^{\delta 0*}\Big) + \frac{1}{2\delta}\boldsymbol{v}_1^{\delta 0}v_{1\zeta}^{\delta 0*} - \frac{\mathrm{i}}{\delta}\boldsymbol{V}_1^0 v_{1\zeta}^{\delta 0*} + \frac{\mathrm{i}}{\delta}\boldsymbol{v}_1^{\delta 0}V_{1\zeta}^{0*} - (1-\mathrm{i})\boldsymbol{v}_1^{\delta 0}\partial_\zeta v_{1\zeta}^{d*}\Big\}_\parallel - k_0^2(1-\mathrm{i})\boldsymbol{v}_1^{\delta 0}\cdot\boldsymbol{v}_1^{d0*}\Big] \tag{47b}$$

$$= -\frac{1}{2\omega}\mathrm{Re}\Big[\boldsymbol{\nabla}_\parallel\cdot\Big(\mathrm{i}\boldsymbol{v}_{1\parallel}^{\delta 0}V_{1\zeta}^{0*}\Big)\Big] + \mathcal{O}(\epsilon). \tag{47c}$$

B. Long-range bulk streaming

The long-range part of Eq. (34) is

$$0 = \boldsymbol{\nabla}\cdot\big[\rho_0\boldsymbol{v}_2^d + \langle\rho_1\boldsymbol{v}_1^d\rangle\big], \tag{48a}$$

$$\boldsymbol{0} = -\rho_0\boldsymbol{\nabla}\cdot\langle\boldsymbol{v}_1^d\boldsymbol{v}_1^d\rangle + \boldsymbol{\nabla}\cdot\boldsymbol{\sigma}_2^d, \tag{48b}$$

$$\boldsymbol{\nabla}\cdot\boldsymbol{\sigma}_2^d = -\boldsymbol{\nabla}(p_2^d - \beta\eta_0\boldsymbol{\nabla}\cdot\boldsymbol{v}_2^d) + \eta_0\nabla^2\boldsymbol{v}_2^d, \tag{48c}$$

$$\boldsymbol{v}_2^{d0} = -\boldsymbol{v}_2^{\delta 0} - \langle(\boldsymbol{s}_1\cdot\boldsymbol{\nabla})\boldsymbol{v}_1\rangle, \text{ at } \boldsymbol{s}_0. \tag{48d}$$

In contrast to the limiting-velocity matching at the outer edge of the boundary layer done by Nyborg,[33] we define the boundary condition (48d) on the long-range streaming $\boldsymbol{v}_2^d$ at the equilibrium position $\boldsymbol{s}_0$.

To simplify Eq. (48), we investigate the products of first-order fields. In Eq. (48a), we use Eq. (29b) and find

$$\boldsymbol{\nabla}\cdot\boldsymbol{v}_2^d = -\frac{\boldsymbol{\nabla}\cdot\langle\rho_1\boldsymbol{v}_1^d\rangle}{\rho_0} = -\frac{\boldsymbol{\nabla}\cdot\langle\boldsymbol{S}_{\mathrm{ac}}^d\rangle}{\rho_0 c_0^2} = \Gamma\frac{k_0|\boldsymbol{v}_1^d|^2}{2c_0}. \tag{49}$$

Since each term in $\boldsymbol{\nabla}\cdot\boldsymbol{v}_2^d$ scales as $(k_0/c_0)|\boldsymbol{v}_1^d|^2 \gg (\Gamma/2)(k_0/c_0)\,|\boldsymbol{v}_1^d|^2$, we conclude that $\boldsymbol{\nabla}\cdot\boldsymbol{v}_2^d \approx 0$ is a good approximation, corresponding to ignoring the small viscous dissipation in the energy balance expressed by Eq. (29b). In Eq. (48b), the divergence of momentum flux can be rewritten using Eq. (19b),

$$\rho_0\boldsymbol{\nabla}\cdot\langle\boldsymbol{v}_1^d\boldsymbol{v}_1^d\rangle = -\boldsymbol{\nabla}\langle\mathcal{L}_{\mathrm{ac}}^d\rangle - \frac{\Gamma\omega}{c_0^2}\langle\boldsymbol{S}_{\mathrm{ac}}^d\rangle, \tag{50}$$

where we introduced the long-range time-averaged acoustic Lagrangian density,

$$\langle\mathcal{L}_{\mathrm{ac}}^d\rangle = \frac{1}{4}\kappa_0|p_1|^2 - \frac{1}{4}\rho_0|\boldsymbol{v}_1^d|^2. \tag{51}$$

Note that $|\boldsymbol{\nabla}\langle\mathcal{L}_{\mathrm{ac}}^d\rangle| \sim \omega p_1^2/\rho_0 c_0^3$, whereas $|(\Gamma\omega/c_0^2)\langle\boldsymbol{S}_{\mathrm{ac}}^d\rangle| \sim \Gamma\omega p_1^2/(\rho_0 c_0^3)$, so the first term in Eq. (50) is much larger than the second term. However, as also noted by Riaud *et al.*,[39] since the first term is a gradient, it cannot drive any rotating streaming. In practice, it is therefore advantageous to work with the excess pressure $p_2^d - \langle\mathcal{L}_{\mathrm{ac}}^d\rangle$. Finally, in Eq. (48c), we again use $\boldsymbol{\nabla}\cdot\boldsymbol{v}_2^d \approx 0$. With these considerations, Eqs. (48) become those of an incompressible Stokes flow driven by the body force $(\Gamma\omega/c_0^2)\langle\boldsymbol{S}_{\mathrm{ac}}^d\rangle$ and the slip velocity $\boldsymbol{v}_2^{d0}$ at the boundary,

$$0 = \boldsymbol{\nabla}\cdot\boldsymbol{v}_2^d, \tag{52a}$$

$$\boldsymbol{0} = -\boldsymbol{\nabla}\Big[p_2^d - \langle\mathcal{L}_{\mathrm{ac}}^d\rangle\Big] + \eta_0\nabla^2\boldsymbol{v}_2^d + \frac{\Gamma\omega}{c_0^2}\langle\boldsymbol{S}_{\mathrm{ac}}^d\rangle, \tag{52b}$$

$$\boldsymbol{v}_2^{d0} = -\boldsymbol{v}_2^{\delta 0} - \langle(\boldsymbol{s}_1\cdot\boldsymbol{\nabla})\boldsymbol{v}_1\rangle|_{\zeta=0}. \tag{52c}$$

These equations describe acoustic streaming in general. The classical Eckart streaming[40] originates from the body force $(\Gamma\omega/c_0^2)\langle\boldsymbol{S}_{\mathrm{ac}}^d\rangle$, while the classical Rayleigh streaming[22] is due to the boundary condition (52c).

The Stokes drift $\langle\boldsymbol{s}_1\cdot\boldsymbol{\nabla}\boldsymbol{v}_1\rangle|_{\zeta=0}$, induced by the oscillating wall, is computed from Eqs. (6), (18), and (22a),

$$\begin{aligned}\langle\boldsymbol{s}_1\cdot\boldsymbol{\nabla}\boldsymbol{v}_1\rangle|_{\zeta=0} &= -\frac{1}{2\omega}\mathrm{Re}\Big[\mathrm{i}\boldsymbol{V}_1^{0*}\cdot\boldsymbol{\nabla}\Big(\boldsymbol{v}_1^d + \boldsymbol{v}_1^{\delta 0}q\Big)\Big]_{\zeta=0}\\ &= -\frac{1}{2\omega}\mathrm{Re}\Big[\mathrm{i}\boldsymbol{V}_1^{0*}\cdot\boldsymbol{\nabla}\Big(\boldsymbol{v}_1^d + \boldsymbol{v}_1^{\delta 0}\Big) - \frac{1+\mathrm{i}}{\delta}V_{1\zeta}^{0*}\boldsymbol{v}_1^{\delta 0}\Big].\end{aligned} \tag{53}$$

From this, combined with Eqs. (47) and (52c), follows the boundary condition $\boldsymbol{v}_2^{d0}$ for the long-range streaming velocity $\boldsymbol{v}_2^d$ expressed in terms of the short-range velocity $\boldsymbol{v}_2^{\delta 0}$ and the wall velocity $\boldsymbol{V}_1^0$. The parallel component is

$$\boldsymbol{v}_{2\parallel}^{d0} = -\frac{1}{2\omega}\mathrm{Re}\Big\{\boldsymbol{\nabla}\cdot\Big(\frac{1}{2}\boldsymbol{v}_1^{\delta 0}\boldsymbol{v}_1^{\delta 0*} + \mathrm{i}\boldsymbol{v}_1^{\delta 0}\boldsymbol{V}_1^{0*} - \mathrm{i}\boldsymbol{V}_1^0\boldsymbol{v}_1^{\delta 0*}\Big) + \frac{1}{\delta}\boldsymbol{v}_1^{\delta 0}v_{1\zeta}^{\delta 0*} - \mathrm{i}\boldsymbol{v}_1^{\delta 0}\partial_\zeta v_{1\zeta}^{d*} - \frac{1-\mathrm{i}}{\delta}\boldsymbol{V}_1^0 v_{1\zeta}^{\delta 0*} - \mathrm{i}\boldsymbol{V}_1^{0*}\cdot\boldsymbol{\nabla}\Big(\boldsymbol{v}_1^d + \boldsymbol{v}_1^{\delta 0}\Big)\Big\}_\parallel, \tag{54a}$$

where the large terms proportional to $[(1+\mathrm{i})/\delta]V_{1\zeta}^{0*}\boldsymbol{v}_{1\parallel}^{\delta 0}$ canceled out, as also noted by Vanneste and Bühler.[35] Similarly, the perpendicular component becomes

$$\begin{aligned}v_{2\zeta}^{d0} = \frac{\delta}{2\omega}\mathrm{Re}\Big[&-k_0^2(1-\mathrm{i})\boldsymbol{v}_1^{\delta 0}\cdot\boldsymbol{v}_1^{d0*} + \boldsymbol{\nabla}_\parallel\\ &\cdot\Big\{\boldsymbol{\nabla}\cdot\Big[-\frac{5}{4}\boldsymbol{v}_1^{\delta 0}\boldsymbol{v}_1^{\delta 0*} + \frac{1+\mathrm{i}}{2}\Big(\boldsymbol{V}_1^0\boldsymbol{v}_1^{\delta 0*} + \boldsymbol{v}_1^{\delta 0*}\boldsymbol{V}_1^0\Big)\Big]\\ &+\Big[\frac{1}{2\delta}v_{1\zeta}^{\delta 0*} + \frac{\mathrm{i}}{\delta}V_{1\zeta}^{0*} - (1-\mathrm{i})\partial_\zeta v_{1\zeta}^{d*}\Big]\boldsymbol{v}_1^{\delta 0}\\ &-\frac{\mathrm{i}}{\delta}v_{1\zeta}^{\delta 0*}\boldsymbol{V}_1^0\Big\}_\parallel\Big] + \frac{1}{2\omega}\mathrm{Re}\Big[\mathrm{i}\boldsymbol{V}_1^{0*}\cdot\boldsymbol{\nabla}\Big(\boldsymbol{v}_1^d + \boldsymbol{v}_1^{\delta 0}\Big)\\ &-\frac{1+\mathrm{i}}{\delta}V_{1\zeta}^{0*}\boldsymbol{v}_1^{\delta 0}\Big]_\zeta\end{aligned} \tag{54b}$$

$$= \frac{1}{2\omega}\mathrm{Re}\Big[\boldsymbol{\nabla}_\parallel\cdot\Big(\mathrm{i}\boldsymbol{v}_{1\parallel}^{\delta 0}V_{1\zeta}^{0*}\Big) - \frac{1+\mathrm{i}}{\delta}V_{1\zeta}^{0*}v_{1\zeta}^{\delta 0} + \Big\{\mathrm{i}\boldsymbol{V}_1^{0*}\cdot\boldsymbol{\nabla}\Big(\boldsymbol{v}_1^d + \boldsymbol{v}_1^{\delta 0}\Big)\Big\}_\zeta\Big] + \mathcal{O}(\epsilon). \tag{54c}$$

Taking the divergences in Eq. (54a) and using Eq. (23), as well as computing Eq. (54c) to lowest order in ϵ, leads to the final expression for the slip velocity at $\zeta = 0$,

$$\begin{aligned}
\boldsymbol{v}_2^{d0} &= (\boldsymbol{A}\cdot\boldsymbol{e}_\xi)\boldsymbol{e}_\xi + (\boldsymbol{A}\cdot\boldsymbol{e}_\eta)\boldsymbol{e}_\eta + (\boldsymbol{B}\cdot\boldsymbol{e}_\zeta)\boldsymbol{e}_\zeta,\\
\boldsymbol{A} &= -\frac{1}{2\omega}\mathrm{Re}\Big\{\boldsymbol{v}_1^{\delta 0*}\cdot\boldsymbol{\nabla}\Big(\frac{1}{2}\boldsymbol{v}_1^{\delta 0} - \mathrm{i}\boldsymbol{V}_1^0\Big) - \mathrm{i}\boldsymbol{V}_1^{0*}\cdot\boldsymbol{\nabla}\boldsymbol{v}_1^d\\
&\quad + \Big[\frac{2-\mathrm{i}}{2}\boldsymbol{\nabla}\cdot\boldsymbol{v}_1^{\delta 0*} + \mathrm{i}\Big(\boldsymbol{\nabla}\cdot\boldsymbol{V}_1^{0*} - \partial_\zeta v_{1\zeta}^{d*}\Big)\Big]\boldsymbol{v}_1^{\delta 0}\Big\},\\
\boldsymbol{B} &= \frac{1}{2\omega}\mathrm{Re}\big\{\mathrm{i}\boldsymbol{v}_1^{d0*}\cdot\boldsymbol{\nabla}\boldsymbol{v}_1^d\big\},
\end{aligned} \tag{55}$$

where $\boldsymbol{A}$ and $\boldsymbol{B}$ are associated with the parallel and perpendicular components $\boldsymbol{v}_{2\parallel}^{d0}$ and $\boldsymbol{v}_{2\zeta}^{d0}$, respectively, and where to simplify we used $(\boldsymbol{v}_{1\parallel}^{\delta 0}\cdot\boldsymbol{\nabla}_\parallel)V_{1\zeta}^{0*} = (\boldsymbol{v}_1^{\delta 0}\cdot\boldsymbol{\nabla})V_{1\zeta}^{0*}$ and the relations $T_{\zeta ji} = 0$, $T_{kjj} = 0$, and $T_{kji} = T_{jki}$ for the curvilinear quantities, see Eq. (A3) in Appendix A.

Equations (52) and (55) constitute our main theoretical result for the second-order acoustic streaming.

VI. SPECIAL CASES

In the following, we study some special cases of our main results (20a) and (25) for the acoustic pressure p_1 and Eqs. (52) and (55) for the streaming velocity $\boldsymbol{v}_2^d$, and relate them to previous studies in the literature.

A. Wall oscillations restricted to the perpendicular direction

The case of a weakly curved wall oscillating only in the perpendicular direction was studied by Nyborg[33] and later refined by Lee and Wang.[34] Using our notation, the boundary conditions used in these studies were

$$\boldsymbol{v}_1^{d0} + \boldsymbol{v}_1^{\delta 0} = \boldsymbol{V}_1^0 = V_{1\zeta}^0\,\boldsymbol{e}_\zeta, \tag{56}$$

whereby $\boldsymbol{\nabla}\cdot\boldsymbol{V}_1^0 = \mathcal{H}_\zeta V_{1\zeta}^0$, so that our boundary condition (25) for p_1 to lowest order in Γ becomes

$$\partial_\zeta p_1 = \mathrm{i}\omega\rho_0\Big(1 - \frac{\mathrm{i}}{k_\mathrm{s}}\mathcal{H}_\zeta\Big)V_{1\zeta}^0 - \frac{\mathrm{i}}{k_\mathrm{s}}\Big(k_\mathrm{c}^2 p_1 + \partial_\zeta^2 p_1\Big). \tag{57}$$

Similarly, for the steady streaming $\boldsymbol{v}_2^d$, Eq. (56) gives $\boldsymbol{\nabla}\cdot\boldsymbol{v}_1^{\delta 0} \approx -\boldsymbol{\nabla}_\parallel\cdot\boldsymbol{v}_{1\parallel}^{d0} = -(\boldsymbol{\nabla}\cdot\boldsymbol{v}_1^d - \partial_\zeta v_{1\zeta}^d - \mathcal{H}_\zeta V_{1\zeta}^0)$ evaluated at $\zeta = 0$. Combining this expression with the derivative rule (13b) and the index notation $\bar{\xi} = \eta$ and $\bar{\eta} = \xi$, as well as $\alpha, \beta = \xi, \eta$, the boundary condition (55) gives to lowest order in ϵ the tangential components

$$\begin{aligned}
v_{2\beta}^{d0} &= -\frac{1}{4\omega}\mathrm{Re}\Big\{v_{1\alpha}^{d0*}\Big(\tilde{\partial}_\alpha v_{1\beta}^{d0}\Big) + v_{1\alpha}^{d0*}v_{1\bar{\beta}}^{d0}T_{\alpha\bar{\beta}\beta}\\
&\quad + 2\mathrm{i}V_{1\zeta}^0\Big(\partial_\zeta v_{1\beta}^{d*} + v_{1\alpha}^{d0*}T_{\alpha\zeta\beta}\Big) + \Big[(2-\mathrm{i})\boldsymbol{\nabla}\cdot\boldsymbol{v}_1^{d*}\\
&\quad -(2-3\mathrm{i})\partial_\zeta v_{1\zeta}^{d*} - (2+\mathrm{i})\mathcal{H}_\zeta V_{1\zeta}^{0*}\Big]v_{1\beta}^d\Big\}.
\end{aligned} \tag{58a}$$

and the perpendicular component

$$v_{2\zeta}^{d0} = \frac{1}{2\omega}\mathrm{Re}\Big\{\mathrm{i}v_{1k}^{d0*}\,\tilde{\partial}_k v_{1\zeta}^d\Big\}. \tag{58b}$$

When comparing our expressions with the results of Lee and Wang,[34] denoted by a superscript "LW" below, we note the following. Neither the pressure p_1 nor the steady perpendicular streaming velocity $v_{2\zeta}^d$ were studied by Lee and Wang, so our results Eqs. (57) and (58b) for these fields represent an extension of their work. The slip condition (58a) for the parallel streaming velocity $v_{2\beta}^d$ with $\beta = \xi, \eta$ is presented in Eqs. $(19)^{\mathrm{LW}}$ and $(20)^{\mathrm{LW}}$ as the limiting values u_L and v_L for the two parallel components of $\boldsymbol{v}_2^d$ outside the boundary layer. A direct comparison is obtained by (1) identifying our $\boldsymbol{v}_1^d$ with the acoustic velocity $(u_{a0}, v_{a0}, w_{a0})^{\mathrm{LW}}$, and our T_{kji} with T_{ijk}^{LW}; (2) taking the complex conjugate of the argument of the real value in Eq. (58a), and (3) noting that q_x and q_y defined in Eqs. $(3)^{\mathrm{LW}}$ and $(4)^{\mathrm{LW}}$ equal the first two terms of Eq. (58a). By inspection we find agreement, except that Lee and Wang are missing the terms $2\mathrm{i}V_{1\zeta}^0(\partial_\zeta v_{1\beta}^{d*} + v_{1\alpha}^{d0*}T_{\alpha\zeta\beta})$, which in our calculation partly arise from the Lagrangian velocity boundary condition (34c), where Lee and Wang have used the no slip condition $\boldsymbol{v}_2 = \boldsymbol{0}$. For more details see Appendix C 1.

B. A flat wall oscillating in any direction

The case of a flat wall oscillating in any direction was studied by Vanneste and Bühler.[35] In this case, we adapt Cartesian coordinates $(\xi, \eta, \zeta) = (x, y, z)$, for which all scale factors h_i are unity, $\tilde{\partial}_i = \partial_i$, and all curvilinear quantities T_{kji} and $\mathcal{H}_k$ are zero. The resulting boundary conditions (25) and (55) for the pressure p_1 and for the long-range streaming $\boldsymbol{v}_2^d$, then simplify to

$$\partial_\zeta p_1 = \mathrm{i}\omega\rho_0 V_{1\zeta}^0 - \frac{1+\mathrm{i}}{2}\delta\Big(\mathrm{i}\omega\rho_0\boldsymbol{\nabla}_\parallel\cdot\boldsymbol{V}_{1\parallel}^0 + k_\mathrm{c}^2 p_1 + \partial_\zeta^2 p_1\Big), \tag{59a}$$

$$\begin{aligned}
v_{2\beta}^{d0} &= -\frac{1}{4\omega}\mathrm{Re}\Big\{(1-2\mathrm{i})v_{1\alpha}^{\delta 0*}\partial_\alpha v_{1\beta}^{\delta 0} - 4\mathrm{i}v_{1\alpha}^{\delta 0*}\partial_\alpha v_{1\beta}^{d0}\\
&\quad + \Big[(2+\mathrm{i})\partial_\alpha v_{1\alpha}^{\delta 0*} + 2\mathrm{i}\Big(\partial_\alpha v_{1\alpha}^{d0*} - \partial_\zeta v_{1\zeta}^{d*}\Big)\Big]\\
&\quad \times v_{1\beta}^{\delta 0} - 2\mathrm{i}\,v_{1k}^{d*}\partial_k v_{1\beta}^d\Big\},
\end{aligned} \tag{59b}$$

$$v_{2\zeta}^{d0} = -\frac{1}{4\omega}\mathrm{Re}\Big\{-2\mathrm{i}\,v_{1k}^{d*}\partial_k v_{1\zeta}^d\Big\}. \tag{59c}$$

The pressure condition (59a) was not studied in Ref. 35, so it represents an extension of the existing theory. On the other hand, Eqs. (59b) and (59c) are in full agreement with Eq. (4.14) in Vanneste and Bühler.[35] To see this, we identify our first-order symbols with those used in Ref. 35 as $\boldsymbol{v}_1^d = 2\boldsymbol{\nabla}\hat{\phi}$ and $\boldsymbol{v}_{1\parallel}^{\delta 0} = -2\hat{U}\boldsymbol{e}_x - 2\hat{V}\boldsymbol{e}_y$, and we relate our steady Eulerian second-order long-range velocity $\boldsymbol{v}_2^d$ with their Lagrangian mean flow $\bar{\boldsymbol{u}}^{\mathrm{L}}$ using the Stokes drift expression (34c) as $\boldsymbol{v}_2^d + (1/\omega)\langle\mathrm{i}\boldsymbol{v}_1^d\cdot\boldsymbol{\nabla}\boldsymbol{v}_1^d\rangle = \bar{\boldsymbol{u}}^{\mathrm{L}}$ at the interface $z = 0$. For more details see Appendix C 2.

C. Small surface velocity compared to the bulk velocity

At resonance in acoustic devices with a large resonator quality factor $Q \gg 1$, the wall velocity $\boldsymbol{V}_1^0$ is typically a

factor Q smaller than the bulk fluid velocity $\boldsymbol{v}_1^d$,[25,36] which is written as $V_1^0 \sim Q^{-1} v_1^d \ll v_1^d$. In this case, as well as for rigid walls, we use $\boldsymbol{V}_1^0 = \boldsymbol{0}$ in Eq. (55), so that $\boldsymbol{v}_1^{\delta 0} = -\boldsymbol{v}_1^{d0}$ and

$$\langle \boldsymbol{v}_1^{\delta 0} \cdot \boldsymbol{\nabla} \boldsymbol{v}_1^{\delta 0} \rangle = \langle \boldsymbol{v}_1^{d0} \cdot \boldsymbol{\nabla} \boldsymbol{v}_1^{d0} \rangle \approx \frac{1}{4} \boldsymbol{\nabla}_\parallel |\boldsymbol{v}_{1\parallel}^{d0}|^2. \tag{60}$$

Here, $v_{1\zeta}^{d0}$ is neglected because $|v_{1\zeta}^{d0}| \approx |V_{1\zeta}^0| \ll |\boldsymbol{v}_{1\parallel}^{d0}|$, and we have used that $\boldsymbol{\nabla} \times \boldsymbol{v}_1^d = 0$ from Eq. (18). Hence, for devices with rigid walls $\boldsymbol{V}_1^0 = \boldsymbol{0}$, or resonant devices with $|\boldsymbol{v}_1^{d0}| \gg |\boldsymbol{V}_1^0|$, the slip-velocity $\boldsymbol{v}_2^{d0}$ becomes

$$\boldsymbol{v}_{2\parallel}^{d0} = \frac{-1}{8\omega} \boldsymbol{\nabla}_\parallel |\boldsymbol{v}_{1\parallel}^{d0}|^2 - \mathrm{Re}\left\{ \left(\frac{2-\mathrm{i}}{4\omega} \boldsymbol{\nabla}_\parallel \cdot \boldsymbol{v}_{1\parallel}^{d0*} + \frac{\mathrm{i}}{2\omega} \partial_\zeta v_{1\zeta}^{d*} \right) \boldsymbol{v}_{1\parallel}^{d0} \right\}, \tag{61a}$$

$$v_{2\zeta}^{d0} = 0. \tag{61b}$$

Two important limits are parallel acoustics, where $|\partial_\zeta v_{1\zeta}^d| \ll |\boldsymbol{\nabla}_\parallel \cdot \boldsymbol{v}_{1\parallel}^{d0}|$, and perpendicular acoustics, where $|\partial_\zeta v_{1\zeta}^d| \gg |\boldsymbol{\nabla}_\parallel \cdot \boldsymbol{v}_{1\parallel}^{d0}|$. In the first limit, the pressure is mainly related to the parallel velocity variations, and from Eqs. (19a) and (19b) we have $\boldsymbol{\nabla}_\parallel \cdot \boldsymbol{v}_{1\parallel}^{d0} = \mathrm{i}\omega\kappa_0 p_1$ and $\boldsymbol{v}_{1\parallel}^{d0} = -(\mathrm{i}/\rho_0\omega)\boldsymbol{\nabla}_\parallel p_1$. For parallel acoustics we can therefore write Eq. (61a) as,

$$\boldsymbol{v}_{2\parallel}^{d0} = \frac{1}{8\omega\rho_0} \boldsymbol{\nabla}_\parallel \left(2\kappa_0 |p_1|^2 - \rho_0 |\boldsymbol{v}_{1\parallel}^{d0}|^2 \right) + \frac{\kappa_0}{2} \langle \boldsymbol{S}_{\mathrm{ac}\parallel}^d \rangle, \quad \text{for parallel acoustics, } |\partial_\zeta v_{1\zeta}^d| \ll |\boldsymbol{\nabla}_\parallel \cdot \boldsymbol{v}_{1\parallel}^{d0}|. \tag{62a}$$

The classical period-doubled Rayleigh streaming,[22] which arises from a one-dimensional parallel standing wave, results from the gradient-term in Eq. (62a). This is seen by considering a rigid wall in the x-y plane with a standing wave above it in the x direction of the form $\boldsymbol{v}_1^d = v_{1a} \cos(k_0 x)\, \boldsymbol{e}_x$, where v_{1a} is a velocity amplitude. Inserting this into Eq. (62a) yields Rayleigh's seminal boundary velocity $\boldsymbol{v}_{2\parallel}^{d0} = (3/8)(v_{1a}^2/c_0) \sin(2k_0 x)\, \boldsymbol{e}_x$. Another equally simple example of parallel acoustics is the boundary condition generated by a planar travelling wave of the form $\boldsymbol{v}_1^d = v_{1a} \mathrm{e}^{\mathrm{i}k_0 x} \boldsymbol{e}_x$. Here, only the energy-flux density $\langle \boldsymbol{S}_{\mathrm{ac}\parallel}^d \rangle$ in Eq. (62a) contributes to the streaming velocity which becomes the constant value $\boldsymbol{v}_{2\parallel}^{d0} = (1/4)(v_{1a}^2/c_0)\, \boldsymbol{e}_x$.

The opposite limit is perpendicular acoustics, where the pressure is mainly related to the perpendicular velocity variations $\partial_\zeta v_{1\zeta}^d = \mathrm{i}\omega\kappa_0 p_1$. In this limit, Eq. (61a) is given by a single term

$$\boldsymbol{v}_{2\parallel}^{d0} = -\kappa_0 \langle \boldsymbol{S}_{\mathrm{ac}\parallel}^d \rangle, \quad \text{for perpendicular acoustics, } |\partial_\zeta v_{1\zeta}^d| \gg |\boldsymbol{\nabla}_\parallel \cdot \boldsymbol{v}_{1\parallel}^{d0}|. \tag{62b}$$

We emphasize that in these two limits, the only mechanism that can induce a streaming slip velocity, which rotates parallel to the surface, is the energy-flux density $\langle \boldsymbol{S}_{\mathrm{ac}}^d \rangle$. As seen from Eq. (52b), this mechanism also governs the force density driving streaming in the bulk. In general, $\langle \boldsymbol{S}_{\mathrm{ac}}^d \rangle$ can drive rotating streaming, if it has a nonzero curl. This we compute to lowest order in Γ using Eq. (19b) and $\boldsymbol{\nabla} \times \boldsymbol{v}_1^d = \boldsymbol{0}$, and find it to be proportional to the acoustic angular momentum density,

$$\boldsymbol{\nabla} \times \langle \boldsymbol{S}_{\mathrm{ac}}^d \rangle = \omega^2 \langle \boldsymbol{r}_1^d \times (\rho_0 \boldsymbol{v}_1^d) \rangle, \quad \boldsymbol{r}_1^d = \frac{\mathrm{i}}{\omega} \boldsymbol{v}_1^d. \tag{63}$$

VII. NUMERICAL MODELING IN COMSOL

In the following we implement our extended acoustic pressure theory, Eqs. (20a) and (25) for p_1, and streaming theory, Eqs. (52) and (55) for $\boldsymbol{v}_2^d$ and p_2, in the commercial finite-element-method (FEM) software COMSOL MULTIPHYSICS.[41] We compare these simulations with a full boundary-layer-resolved model for the acoustics, Eqs. (17) and (8a) for $\boldsymbol{v}_1$ and p_1, and for the streaming, Eqs. (34) and (8b) for $\boldsymbol{v}_2$ and p_2. The full model is based on our previous acoustofluidic modeling of fluids-only systems[28,36,42] and solid-fluid systems.[43]

Remarkably, our extended (effective) acoustic pressure model makes it possible to simulate acoustofluidic systems not accessible to the brute-force method of the full model for three reasons: (1) In the full model, the thin boundary layers need to be resolved with a fine FEM mesh. This is not needed in our effective model. (2) For the first-order acoustics, the full model is based on the vector field $\boldsymbol{v}_1$ and the scalar field p_1, whereas our effective model is only based on the scalar field p_1. (3) For the second-order streaming, the full equations (34) contain large canceling terms, which have been removed in the equations (52) used in the effective model. Therefore, also in the bulk, the effective model can be computed on a much coarser FEM mesh than the full model.

In Sec. VIII, we model a fluid domain Ω_{fl} driven by boundary conditions applied directly on $\partial\Omega_{\mathrm{fl}}$, and in Sec. IX, we model a fluid domain Ω_{fl} embedded in an elastic solid domain Ω_{sl} driven by boundary conditions applied on the outer part of the solid boundary $\partial\Omega_{\mathrm{sl}}$.

In COMSOL, we specify user-defined equations and boundary conditions in weak form using the PDE mathematics module, and we express all vector fields in Cartesian coordinates (x, y, z). At the boundary $\partial\Omega_{\mathrm{fl}}$, the local right-handed orthonormal basis $\{\boldsymbol{e}_\xi, \boldsymbol{e}_\eta, \boldsymbol{e}_\zeta\}$ is implemented using the built-in COMSOL tangent vectors `t1` and `t2` as well as the normal vector `n`, all given in Cartesian coordinates. Boundary-layer fields (superscript "0"), such as $\boldsymbol{V}_1^0$, $\boldsymbol{v}_1^{d0}$, and $\boldsymbol{v}_1^{\delta 0}$, are defined on the boundary $\partial\Omega_{\mathrm{fl}}$ only, and their spatial derivatives are computed using the built-in tangent-plane derivative operator `dtang`. For example, in COMSOL we call the Cartesian components of $\boldsymbol{v}_1^{\delta 0}$ for `vdX`, `vdY`, and `vdZ` and compute $\boldsymbol{\nabla} \cdot \boldsymbol{v}_1^{\delta 0}$ as `dtang(vdX,x)+dtang(vdY,y)+dtang(vdZ,z)`. The models are implemented in COMSOL using the following two-step procedure.[36]

Step (1), first-order fields:[42,43] For a given frequency ω, the driving first-order boundary conditions for the system are specified; the wall velocity $\boldsymbol{V}_1^0$ on $\partial\Omega_{\mathrm{fl}}$ for the fluid-only model, and the outer wall displacement $\boldsymbol{u}_1$ on $\partial\Omega_{\mathrm{sl}}$ for the solid-fluid model. Then, the first-order fields are solved; the pressure p_1 in Ω_{fl} using Eqs. (20a) and (25), and, if included in the model, the solid displacement $\boldsymbol{u}_1$ in the solid domain Ω_{sl}.

In particular, in COMSOL we implement $\partial_\zeta^2 p_1 = (\boldsymbol{e}_\zeta \cdot \boldsymbol{\nabla})^2 p_1$ in Eq. (25) as $\mathtt{nx}*\mathtt{nx}*\mathtt{p1xx} + 2*\mathtt{nx}*\mathtt{ny}*\mathtt{p1xy} + \cdots$.

Step (2), second-order fields:[36,42] Time averages $\frac{1}{2}\mathrm{Re}\{f^* g\}$ are implemented using the built-in COMSOL operator `realdot` as $0.5*\mathtt{realdot}(\mathtt{f},\mathtt{g})$. Moreover, in the boundary condition (55), the normal derivative of $v_{1\zeta}^d$ in $\boldsymbol{A}$ is rewritten as $\partial_\zeta v_{1\zeta}^d = \boldsymbol{\nabla}\cdot\boldsymbol{v}_1^d - \boldsymbol{\nabla}\cdot\boldsymbol{v}_1^{d0} = \mathrm{i}\kappa_0\omega p_1^0 - \boldsymbol{\nabla}\cdot\boldsymbol{v}_1^{d0}$ for computational ease, and the advective derivatives in $\boldsymbol{A}$ and $\boldsymbol{B}$, such as the term $\mathrm{Re}\{\boldsymbol{v}_1^{\delta 0*}\cdot\boldsymbol{\nabla}\boldsymbol{v}_1^{\delta 0}\}\cdot\boldsymbol{e}_x$ in $\boldsymbol{A}\cdot\boldsymbol{e}_x$, are computed as $\mathtt{realdot}(\mathtt{vdX},\ \mathtt{dtang}(\mathtt{vdX},\mathtt{x})) + \mathtt{realdot}(\mathtt{vdY},\mathtt{dtang}(\mathtt{vdX},\mathtt{y})) + \mathtt{realdot}(\mathtt{vdZ},\mathtt{dtang}(\mathtt{vdX},\mathtt{z}))$.

All numerics were carried out on a workstation, Dell Inc Precision T3610 Intel Xeon CPU E5–1650 v2 at 3.50 GHz with 128 GB RAM and 6 CPU cores.

VIII. EXAMPLE I: A RECTANGULAR CAVITY

We apply our theory to a long, straight channel along the x axis with a rectangular cross section in the vertical y-z plane, a system intensively studied in the literature both theoretically[28,36,42] and experimentally.[25,45–47] We consider the 2D rectangular fluid domain Ω_{fl} with $-\frac{1}{2}W < y < \frac{1}{2}W$ and $-\frac{1}{2}H < z < \frac{1}{2}H$, where the top and bottom walls at $z = \pm\frac{1}{2}H$ are stationary and the vertical side walls at $y = \pm\frac{1}{2}W$ oscillate with a given velocity $V_{1y}^0 w(z)\mathrm{e}^{-\mathrm{i}\omega t}\boldsymbol{e}_y$ and frequency $f = \omega/2\pi$ close to $c_0/2W$, thus exciting a half-wave resonance in the y-direction. In the simulations we choose the wall velocity to be $V_{1y}^0 = d_0\omega$ with a displacement amplitude $d_0 = 0.1$ nm. The material parameters used in the model are shown in Table I.

We compare the results from the effective theory with the full boundary-layer-resolved simulation developed by Muller *et al.*[28] Moreover, we derive analytical expressions for the acoustic fields, using pressure acoustics and our extended boundary condition (25), and for the streaming boundary condition using Eq. (55).

A. First-order pressure

To leading order in ϵ and assuming small variations in z, Eqs. (20a) and (25) in the fluid domain Ω_{fl} become

$$\nabla^2 p_1 + k_0^2 p_1 = 0, \quad \boldsymbol{r}\in\Omega_{\mathrm{fl}}, \tag{64a}$$

TABLE I. Material parameters at 25 °C used in the numerical modeling presented in Secs. VIII and IX.

Water (Ref. 42)			
Mass density	ρ_0	997.05	kg m^{-3}
Compressibility	κ_0	452	TPa^{-1}
Speed of sound	c_0	1496.7	m s^{-1}
Dynamic viscosity	η_0	0.890	mPa s
Bulk viscosity	η_0^{b}	2.485	mPa s
Pyrex glass (Ref. 44)			
Mass density	ρ_{sl}	2230	kg m^{-3}
Speed of sound, longitudinal	c_{lo}	5592	m s^{-1}
Speed of sound, transverse	c_{tr}	3424	m s^{-1}
Solid damping coefficient	Γ_{sl}	0.001	

$$\partial_y p_1 = \mathrm{i}\omega\rho_0 V_{1y}^0 w(z), \quad y = \pm\frac{1}{2}W, \tag{64b}$$

$$\mp\partial_z p_1 = -\frac{\mathrm{i}}{k_{\mathrm{s}}}k_0^2 p_1, \quad z = \pm\frac{1}{2}H. \tag{64c}$$

This problem is solved analytically by separation of variables, introducing k_y and k_z with $k_y^2 + k_z^2 = k_0^2$ and choosing a symmetric velocity envelope function $w(z) = \cos(k_z z)$. The solution is the pressure $p_1 = A\sin(k_y y)\cos(k_z z)$, where A is found from Eq. (64b),

$$p_1(y,z) = \frac{\mathrm{i}\omega\rho_0 V_{1y}^0}{k_y\cos\left(k_y\frac{W}{2}\right)}\sin(k_y y)\cos(k_z z). \tag{65}$$

According to Eq. (64c), k_z must satisfy

$$k_0^2 = \mathrm{i}k_{\mathrm{s}}k_z\tan\left(k_z\frac{H}{2}\right), \tag{66}$$

and using $\tan(k_z H/2)\approx k_z H/2$ for $k_z H \ll 1$, we obtain

$$k_z^2 = -(1+\mathrm{i})\frac{\delta}{H}k_0^2, \quad k_y^2 = \left[1+(1+\mathrm{i})\frac{\delta}{H}\right]k_0^2. \tag{67}$$

Note that the real part of k_y becomes slightly larger than k_0 since the presence of the boundary layers introduces a small variation in the z direction. The half-wave resonance that maximizes the amplitude of p_1 in Eq. (65) is therefore found at a frequency f_{res} slightly lower than $f_{\mathrm{res}}^0 = c_0/2W$,

$$f_{\mathrm{res}} = \left(1-\frac{1}{2}\Gamma_{\mathrm{bl}}\right)f_{\mathrm{res}}^0, \quad \text{with } \Gamma_{\mathrm{bl}} = \frac{\delta}{H}. \tag{68}$$

Here, we introduced the boundary-layer damping coefficient Γ_{bl} that shifts f_{res} away from f_{res}^0. This resonance shift arises from the extended boundary condition (25) and is thus beyond classical pressure acoustics.

Using $f = f_{\mathrm{res}}$ in Eq. (65) and expanding to leading order in Γ_{bl}, gives the resonance pressure and velocity,

$$\frac{p_1^{\mathrm{res}}}{\rho_0 c_0} = -\frac{4V_{1y}^0}{\pi\Gamma_{\mathrm{bl}}}\Big\{\sin(\tilde{y}) + \frac{\Gamma_{\mathrm{bl}}}{2}[\mathrm{i}\tilde{y}\cos(\tilde{y}) - (1+\mathrm{i})\sin(\tilde{y})]\Big\}Z^{\mathrm{res}}(\tilde{z}), \tag{69a}$$

$$v_{1y}^{d,\mathrm{res}} = \frac{4\mathrm{i}V_{1y}^0}{\pi\Gamma_{\mathrm{bl}}}\left\{\cos(\tilde{y}) - \frac{\Gamma_{\mathrm{bl}}}{2}\mathrm{i}\tilde{y}\sin(\tilde{y})\right\}Z^{\mathrm{res}}(\tilde{z}), \tag{69b}$$

$$v_{1z}^{d,\mathrm{res}} = \frac{4\mathrm{i}V_{1y}^0}{\pi}(1+\mathrm{i})\sin(\tilde{y})\,\tilde{z}, \tag{69c}$$

where $\tilde{y} = \pi(y/W)$, $\tilde{z} = \pi(z/W)$, and $Z_{\mathrm{res}}(\tilde{z}) = 1 + \frac{1}{2}\Gamma_{\mathrm{bl}}(1+\mathrm{i})\tilde{z}^2$. Note that at resonance, the horizontal velocity component is amplified by a factor $\Gamma_{\mathrm{bl}}^{-1}$ relative to the

wall velocity, $v_{1y}^{d,\mathrm{res}} \sim \Gamma_{\mathrm{bl}}^{-1} v_{1z}^{d,\mathrm{res}} \sim \Gamma_{\mathrm{bl}}^{-1} V_{1y}^{0}$, while the horizontal component is not.

In Fig. 2, we compare an effective ("Eff") pressure-acoustics simulation of p_1 solving Eqs. (20a) and (25), with a full pressure-velocity simulation of p_1 and $\boldsymbol{v}_1$ from Eq. (17) as in Muller and Bruus.[28] The analytical results ("Ana") for p_1^{res}, $v_{1y}^{d,\mathrm{res}}$, and $v_{1z}^{d,\mathrm{res}}$ in Eq. (69) are also plotted along the line $y = \frac{1}{4}W$ in Figs. 2(a2), 2(b2), and 2(c2), respectively. The relative deviation between the full and effective fields outside the boundary layer are less than 0.1% even though the latter was obtained using only 5000 degrees of freedom (DoF) on the coarse mesh compared to the 600 000 DoF on the fine mesh for the former. The effective model $\boldsymbol{v}_{1,\mathrm{Eff}}^{d}$ gives the boundary-layer velocity $\boldsymbol{v}_1^{\delta}$ by Eq. (22), and thus by Eq. (18) the complete velocity $\boldsymbol{v}_1 = \boldsymbol{v}_{1,\mathrm{Eff}}^{d} + \boldsymbol{v}_1^{\delta}$ (blue dots in Fig. 2).

To study the resonance behaviour of the acoustic resonator further, we compute the space- and time-averaged energy density $\langle \bar{E}_{\mathrm{ac}}^{d} \rangle$ stored in the acoustic field for frequencies f close to the resonance frequency f_{res}. Inserting $k_y = (\pi/W)(1 + (\mathrm{i}/2)\Gamma_{\mathrm{bl}}) + (2\pi/c_0)(f - f_{\mathrm{res}})$ into Eq. (65), results in the Lorentzian line-shape for $\langle \bar{E}_{\mathrm{ac}}^{d} \rangle$,

$$\left\langle \bar{E}_{\mathrm{ac}}^{d} \right\rangle = \left\langle \bar{E}_{\mathrm{ac}}^{d,\mathrm{kin}} \right\rangle + \left\langle \bar{E}_{\mathrm{ac}}^{d,\mathrm{pot}} \right\rangle = 2\left\langle \bar{E}_{\mathrm{ac}}^{d,\mathrm{pot}} \right\rangle = \frac{2}{HW} \int\int_{\Omega_{\mathrm{fl}}} \frac{1}{2} \kappa_0 \langle p_1 p_1 \rangle \, \mathrm{d}y\mathrm{d}z \tag{70a}$$

$$\approx \frac{\frac{1}{\pi^2}\rho_0 \left(V_{1y}^{0}\right)^2}{\left(\frac{f}{f_{\mathrm{res}}} - 1\right)^2 + \left(\frac{1}{2}\Gamma_{\mathrm{bl}}\right)^2}, \quad \text{for } f \approx f_{\mathrm{res}}. \tag{70b}$$

As shown in the graph of $\langle \bar{E}_{\mathrm{ac}}^{d} \rangle$ in Fig. 3, there is full agreement between the effective pressure-acoustics model, the full pressure-velocity model, and the analytical model. In this figure we also show the result obtained using classical pressure acoustics (CPA, gray curves) with $\partial_\zeta p_1 = \mathrm{i}\omega\rho_0 V_{1\zeta}^{0}$ where we see that the boundary layer introduces both damping and shift of the resonance frequency. From the resonance curve follows the maximum energy density at resonance, $\langle \bar{E}_{\mathrm{ac}}^{d,\mathrm{res}} \rangle = \langle \bar{E}_{\mathrm{ac}}^{d}(f_{\mathrm{res}}) \rangle$, and the quality factor Q,

$$\langle \bar{E}_{\mathrm{ac}}^{d,\mathrm{res}} \rangle = \frac{1}{4}\rho_0 \left(\frac{4V_{1y}^{0}}{\pi\Gamma_{\mathrm{bl}}}\right)^2, \quad Q = \frac{1}{\Gamma_{\mathrm{bl}}} = \frac{H}{\delta}. \tag{71}$$

This is also in agreement with the Q-factor in Eq. (33),

$$Q = \frac{2\int\int_{\Omega_{\mathrm{fl}}} \frac{1}{4}\rho_0 |v_{1y}^{\mathrm{res}}|^2 \, \mathrm{d}y\mathrm{d}z}{2\int_{-W/2}^{+W/2} \frac{1}{4}\delta\rho_0 |v_{1y}^{\mathrm{res}}|^2 \, \mathrm{d}y} = \frac{H}{\delta}, \tag{72}$$

which was previously derived by Muller and Bruus[36] and by Hahn *et al.*[38] using the approximation $P_{\mathrm{loss}} \approx P_{\mathrm{visc}}^{\mathrm{diss}}$ in Eq. (33).

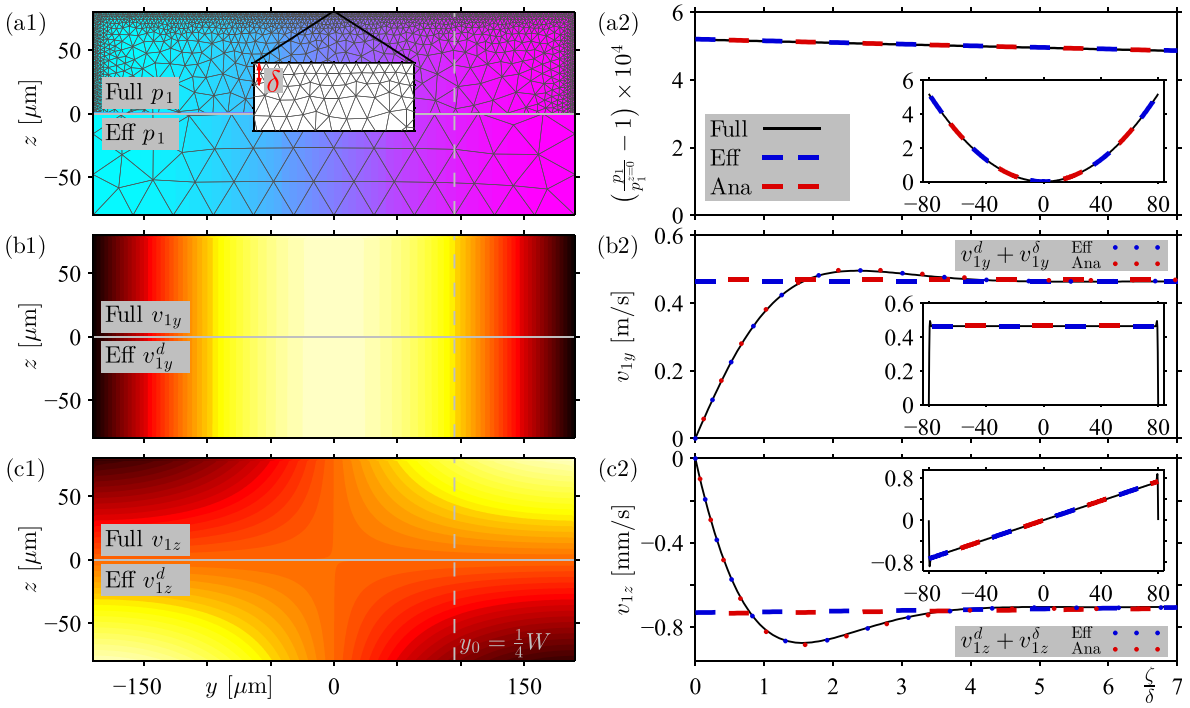

FIG. 2. (Color online) First-order pressure and velocity fields in the vertical rectangular cross section of a long, straight channel of width $W = 380\,\mu$m and height $H = 160\,\mu$m at resonance $f_{\mathrm{res}} = 1.967$ MHz and actuation velocity $V_{1y}^{0} = 2\pi f_{\mathrm{res}} \times 0.1$ nm. Color plots of the full (upper half) and effective (lower half) model fields: (a1) the pressure p_1 from -1 MPa (dark purple) to 1 MPa (light cyan) and the finite element mesh (gray), (b1) the horizontal velocity v_{1y} from 0 m/s (black) to 0.7 m/s (white), and (c1) the vertical velocity v_{1z} from -1 mm/s (black) to 1 mm/s (white). Line plots [Full, Eff, and Ana = analytics from Eq. (69)] at $y_0 = \frac{1}{4}W$ for $-\frac{1}{2}H < z < -\frac{1}{2}H + 7\delta$ (light gray dashed lines) of (a2) the relative pressure deviation $p_1(y_0, z)/p_1(y_0, 0) - 1$, (b2) the horizontal velocity v_{1y}, and (c2) the vertical velocity v_{1z}. Dots are the full velocity (18) $\boldsymbol{v}_1 = \boldsymbol{v}_1^d + \boldsymbol{v}_1^\delta$ with $\boldsymbol{v}_1^\delta$ from Eq. (22) and $\boldsymbol{v}_1^d$ from either "Eff" (dark blue dots) or "Ana" (light red dots). The insets are the corresponding plots along the entire line $-\frac{1}{2}H < z < \frac{1}{2}H$.

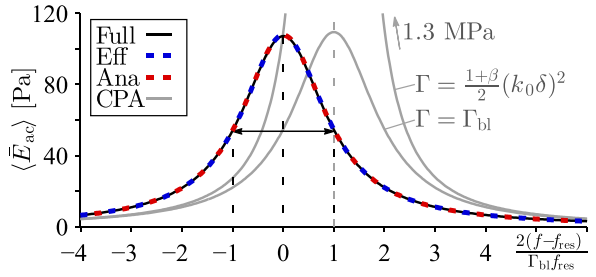

FIG. 3. (Color online) Resonance curves for the rectangular channel. "Ana" refers to the analytical result from Eq. (70b) and "CPA" refers to simulations using classical pressure acoustics with the boundary condition $\partial_\zeta p_1 = i\omega V^0_{1\zeta}$ at $\boldsymbol{r} \in \partial\Omega$ with different choices of bulk damping coefficient Γ.

B. Second-order streaming solution

For the full model at resonance $f_{\rm res}$, we solve Eq. (34), while for the effective model we solve Eq. (52) with the boundary condition on $\boldsymbol{v}_2^d$ obtained by inserting the velocity fields from Eq. (69) into Eq. (54). At the surfaces $z = \pm\frac{1}{2}H$, we find to lowest order in ϵ,

$$v_{2y}^{d0} = \frac{3}{8c_0}\left(\frac{4V_{1y}^0}{\pi\Gamma_{\rm bl}}\right)^2 \sin(2\tilde{y}), \tag{73a}$$

$$v_{2z}^{d0} = \mp(k_0\delta)\frac{1}{8c_0}\left(\frac{4V_{1y}^0}{\pi\Gamma_{\rm bl}}\right)^2 [1 + 10\cos(2\tilde{y})]. \tag{73b}$$

The resulting fields of the two models are shown in Fig. 4. Again, we have good quantitative agreement between the two numerical models, now better than 1% or $3k_0\delta$, for 9000 DoF and 600 000 DoF, respectively.

Analytically, Eq. (73a) is the usual parallel-direction boundary condition for the classical Rayleigh streaming,[22] while Eq. (73b) is beyond that, being the perpendicular-direction boundary condition on the streaming, which is a factor $k_0\delta \approx 3\times10^{-3}$ smaller than the parallel one. This is confirmed in Fig. 4(b) showing the streaming velocity close to $z = -\frac{1}{2}H$ at $y = \frac{1}{4}W$.

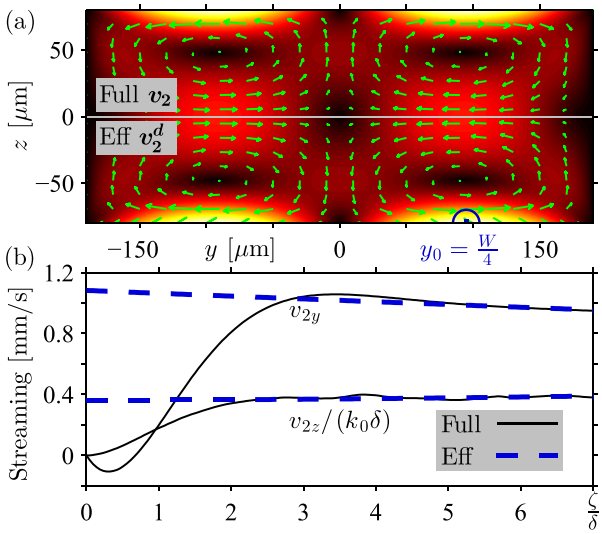

FIG. 4. (Color online) Simulated second-order velocity for the rectangular channel. (a) The full-model $\boldsymbol{v}_2$ (above) and the effictive-model $\boldsymbol{v}_2^d$ (below). (b) Line plots near the center of the dark blue half circle in (a) at $y_0 = \frac{1}{4}W$ for $-\frac{1}{2}H < z < -\frac{1}{2}H + 7\delta$.

IX. EXAMPLE II: A CURVED OSCILLATING CAVITY

Next, we implement in COMSOL our boundary conditions (25) and (55) in a system with a curved solid-fluid interface that oscillates in any direction, as described in Sec. VII. We consider an ellipsoidal fluid domain (water) of horizontal major axis $W = 380\,\mu$m and vertical minor axis $H = 160\,\mu$m surrounded by a rectangular solid domain (Pyrex) of width $W_{\rm sl} = 680\,\mu$m and height $H_{\rm sl} = 460\,\mu$m, see Fig. 5. We actuate the solid at its bottom surface using a vertical velocity amplitude $V_z^{\rm act} = d_0\omega\sin(\pi y/W_{\rm sl})$ with $d_0 = 0.1$ nm and at the resonance frequency $f_{\rm res} = 2.222$ MHz, which has

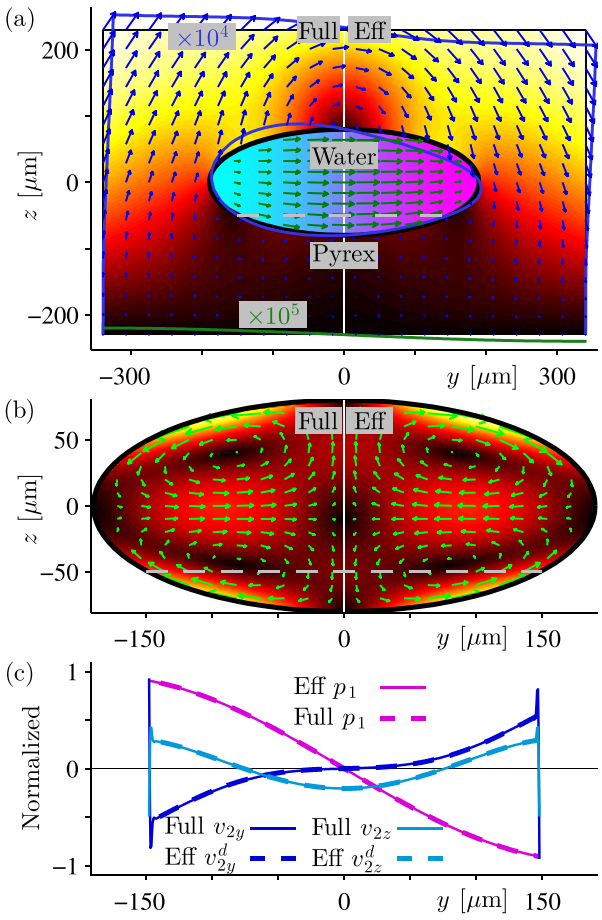

FIG. 5. (Color online) Full (left) and effective (right) simulations for a curved channel with fluid-solid coupling. (a) An elliptic fluid domain with the acoustic pressure p_1 from −0.35 MPa (dark purple) to +0.35 MPa (light cyan) and fluid velocity (green arrows, max 0.2 m/s) surrounded by solid Pyrex with a displacement field $\boldsymbol{u}_{\rm sl}$ (dark blue arrows) and displacement magnitude $|\boldsymbol{u}_{\rm sl}|$ from 0 nm (black) to 2.7 nm (yellow). To be visible, the displacement (dark blue line and dark blue arrows, max 2.7 nm) is enhanced 10^4 times, except at the bottom (green line, max 0.1 nm) where it is enhanced 10^5 times. (b) Streaming velocity $\boldsymbol{v}_2$ (light green arrows) and magnitude from 0 μm/s (black) to 7.8 μm/s (light yellow). (c) Line plots along the light ray dashed line in (a) and (b) of p_1 normalized by 0.35 MPa and $\boldsymbol{v}_2$ by 7.8 μm/s.

been determined numerically as in Fig. 3. The linear governing equations for the displacement field $\boldsymbol{u}_{\mathrm{sl}}$ of the solid are those used by Ley and Bruus,[48]

$$\boldsymbol{\nabla}\cdot\boldsymbol{\sigma}_{\mathrm{sl}} = -\rho_{\mathrm{sl}}\omega^2(1+\mathrm{i}\Gamma_{\mathrm{sl}})\boldsymbol{u}, \quad \text{solid domain}, \tag{74a}$$

$$-\mathrm{i}\omega\boldsymbol{u}_{\mathrm{sl}} = V_z^{\mathrm{act}}(y)\,\boldsymbol{e}_z, \quad \text{actuation at } z=-\frac{1}{2}H_{\mathrm{sl}}, \tag{74b}$$

$$\boldsymbol{n}_{\mathrm{sl}}\cdot\boldsymbol{\sigma}_{\mathrm{sl}} = \boldsymbol{0}, \quad \text{at solid–air interfaces}, \tag{74c}$$

$$\boldsymbol{n}_{\mathrm{sl}}\cdot\boldsymbol{\sigma}_{\mathrm{sl}} = \boldsymbol{n}_{\mathrm{sl}}\cdot\boldsymbol{\sigma}_1, \quad \text{at solid–fluid interfaces}, \tag{74d}$$

where $\boldsymbol{\sigma}_{\mathrm{sl}} = \rho_{\mathrm{sl}}c_{\mathrm{tr}}^2[\boldsymbol{\nabla}\boldsymbol{u}_{\mathrm{sl}} + (\boldsymbol{\nabla}\boldsymbol{u}_{\mathrm{sl}})^T] + \rho_{\mathrm{sl}}(c_{\mathrm{lo}}^2 - 2c_{\mathrm{tr}}^2)(\boldsymbol{\nabla}\cdot\boldsymbol{u}_{\mathrm{sl}})\mathbf{I}$ is the stress tensor of the solid with mass density ρ_{sl}, transverse velocity c_{tr}, longitudinal velocity c_{lo}, and damping coefficient Γ_{sl}, while $\boldsymbol{n}_{\mathrm{sl}}$ is the solid surface normal, and $\boldsymbol{n}_{\mathrm{sl}}\cdot\boldsymbol{\sigma}_1 = \boldsymbol{e}_\zeta\cdot\boldsymbol{\sigma}_1$ is the fluid stress on the solid, Eq. (26). The material parameter values are listed in Table I.

We solve numerically Eqs. (20a) and (25) in first order and Eqs. (52) and (55) in second order. The results are shown in Fig. 5, where we compare the simulation results from the full boundary-layer resolved simulation of Eq. (34) with the effective model. Even for this more complex and realistic system consisting of an elastic solid with a curved oscillating interface coupled to a viscous fluid, we obtain good quantitative agreement between the two numerical models, better than 1% for 600 000 DoF and 9000 DoF, respectively.

X. CONCLUSION

We have studied acoustic pressure and streaming in curved elastic cavities having time-harmonic wall oscillations in any direction. Our analysis relies on the condition that both the surface curvature and wall displacement are sufficiently small as quantified in Eq. (16).

We have developed an extension of the conventional theory of first-order pressure acoustics by including the viscous effects of the thin viscous boundary layer. Based on this theory, we have also derived a slip-velocity boundary condition for the steady second-order acoustic streaming, which allows for efficient computations of the resulting incompressible Stokes flow.

The core of our theory is the decomposition of the first- and second-order fields into long- and short-range fields varying on the large bulk length scale d and the small boundary-layer length scale δ, respectively, see Eqs. (19) and (35). In the physically relevant limits, this velocity decomposition allows for analytical solutions of the boundary-layer fields. We emphasize that in contrast to the conventional second-order matching theory of inner solutions in the boundary layer and outer solutions in the bulk, our long- and short-range, second-order, time-averaged fields co-exist in the boundary layer, but the latter die out exponentially beyond the boundary layer leaving only the former in the bulk.

The main theoretical results of the extended pressure acoustics in Sec. III are the boundary conditions (25) and (26) for the pressure p_1 and the stress $\boldsymbol{\sigma}_1\cdot\boldsymbol{e}_\zeta$ expressed in terms of the pressure p_1 and the velocity $\boldsymbol{V}_1^0$ of the wall. These boundary conditions are to be applied to the governing Helmholtz equation (20a) for p_1, and the gradient form (19b) of the compressional acoustic velocity field $\boldsymbol{v}_1^d$. Furthermore, in Sec. IV, we have used the extended pressure boundary condition to derive an expression for the acoustic power loss P_{loss}, Eq. (32), and the quality factor Q, Eq. (33), for acoustic resonances in terms of boundary-layer and bulk loss mechanisms. The main results of the streaming theory in Sec. V are the governing incompressible Stokes equation (52) for the streaming velocity $\boldsymbol{v}_2^d$ and the corresponding extended boundary condition (55) for the streaming slip velocity $\boldsymbol{v}_2^{d0}$. In this context, we have developed a compact formalism based on the $I_{ab}^{(n)}$-integrals of Eq. (43) to carry out with relative ease the integrations that lead to the analytical expression for $\boldsymbol{v}_2^{d0}$. Last, in Sec. VI, we have applied our extended pressure-acoustics theory to several special cases. We have shown how it leads to predictions that goes beyond previous theoretical results in the literature by Lord Rayleigh,[22] Nyborg,[33] Lee and Wang,[34] and Vanneste and Bühler,[35] while it does agree in the appropriate limits with these results.

The physical interpretation of our extended pressure acoustics theory may be summarized as follows: The fluid velocity $\boldsymbol{v}_1$ is the sum of a compressible velocity $\boldsymbol{v}_1^d$ and an incompressible velocity $\boldsymbol{v}_1^\delta$, where the latter dies out beyond the boundary layer. In general, the tangential component $\boldsymbol{V}_{1\parallel}^0 = \boldsymbol{v}_{1\parallel}^{d0} + \boldsymbol{v}_{1\parallel}^{\delta 0}$ of the no-slip condition at the wall induces a tangential compression of $\boldsymbol{v}_1^\delta$ due to the tangential compression of $\boldsymbol{v}_1^d$ and $\boldsymbol{V}_1^0$. This in turn induces a perpendicular velocity component $v_{1\zeta}^{\delta 0}$ due to the incompressibility of $\boldsymbol{v}_1^\delta$. To fulfil the perpendicular no-slip condition $V_{1\zeta}^0 = v_{1\zeta}^{d0} + v_{1\zeta}^{\delta 0}$, the perpendicular component $v_{1\zeta}^{d0}$ of the acoustic velocity must therefore match not just the wall velocity $V_{1\zeta}^0$, as in classical pressure acoustics, but the velocity difference $V_{1\zeta}^0 - v_{1\zeta}^{\delta 0}$. The inclusion of $v_{1\zeta}^{\delta 0}$ takes into account the power delivered to the acoustic fields by the tangential wall motion, and the power lost from the acoustic fields due to tangential fluid motion. Consequently, by incorporating into the boundary condition an analytical solution of $\boldsymbol{v}_1^\delta$, our theory leads to the correct acoustic fields, resonance frequencies, resonance Q-factors, and acoustic streaming.

In Secs. VII–IX we have demonstrated the implementation of our extended acoustic pressure theory in numerical finite-element COMSOL models, and we have presented the results of two specific models in 2D: a water domain with a rectangular cross section and a given velocity actuation on the domain boundary, and a water domain with an elliptic cross section embedded in a rectangular glass domain that is actuated on the outer boundary. By restricting our examples to 2D, we have been able to perform direct numerical simulations of the full boundary-layer-resolved model, and to use these results for validation of our extended acoustic pressure and streaming theory. Remarkably, we have found that even in 2D, our approach makes it possible to simulate acousto-fluidic systems with a drastic nearly 100-fold reduction in the necessary degrees of freedom, while achieving the same quantitative accuracy, typically of order $k_0\delta$, compared to direct numerical simulations of the full boundary-layer resolved model. We have identified three reasons for this

reduction: (1) Neither our first-order nor our second-order method involve the fine-mesh resolution of the boundary layer. (2) Our first-order equations (20a) and (25) requires only the scalar pressure p_1 as an independent variable, while the vector velocity $\boldsymbol{v}_1$ is subsequently computed from p_1, Eq. (19b). (3) Our second-order equations (52) and (55) avoid the numerically demanding evaluation in the entire fluid domain of large terms that nearly cancel, and therefore our method requires a coarser mesh compared to the full model, also in the bulk.

The results from the numerical examples in Secs. VIII and IX show that the extended pressure acoustics theory has the potential of becoming a versatile and very useful tool in the field of acoustofluidics. For the fluid-only rectangular domain in Sec. VIII, we showed how the theory not only leads to accurate numerical results for the acoustic fields and streaming, but also allows for analytical solutions, which correctly predict crucial details related to viscosity of the first-order acoustic resonance, and which open up for a deeper analysis of the physical mechanisms that lead to acoustic streaming. For the coupled fluid-solid system in 2D of an elliptical water domain embedded in a rectangular glass block, we showed in Sec. IX an important example of a more complete and realistic model of an actuated acoustofluidic system. The extended pressure acoustics theory allowed for calculations of acoustic fields and streaming with a relative accuracy lower than 1%. Based on preliminary work in progress in our group, it appears that the extended pressure acoustic theory makes 3D simulations feasible within reasonable memory consumptions for a wide range of microscale acoustofluidic systems such as fluid-filled cavities and channels driven by attached piezoelectric crystals as well as droplets in two-phase systems and on vibrating substrates.

Currently, we have neglected thermal dissipation. It would of course be an obvious and interesting study, to extend the presented theory to include thermoviscous effects. Previous studies[42,49] on acoustofluidic systems with flat walls oscillating only in the perpendicular direction, have shown that the acoustic streaming is unaffected for channels with a height larger than 250 $\delta \approx 100\,\mu$m. We thus expect the predictions of this work to hold for such "high" channels. However, for more flat channels, a significant reduction of the acoustic streaming is predicted, for example a reduction factor of 2 for a channel of height $25\delta \approx 10\ \mu$m.[42] For such "flat" channels, the thermal boundary-layer must be included in our model to ensure reliable predictions. Such an extension of our model seems feasible, as the thermal boundary-layer width is about 3 times smaller than the viscous boundary-layer width for water at 2 MHz and 25 °C. Thus the basic idea of a weakly curved, thin boundary-layer model can be maintained, but of course at the expense of analytical complications arising from including the heat transport equation together with temperature dependence of the material parameters in the presented first- and second-order perturbation theory.

Although we have developed the extended pressure-acoustics theory and corresponding streaming theory within the narrow scope of microscale acoustofluidics, our theories are of general nature and may likely find a much wider use in other branches of acoustics.

APPENDIX A: DIFFERENTIAL GEOMETRY

In the following we present the basic differential geometry used in this work. Because our analysis is carried out in the limit of weakly curved, thin boundary layers, defined by $\epsilon \ll 1$ of Eq. (10) as discussed in Sec. II D, simplifications arise so that we do not need to unfold the full notation of differential geometry based on co- and contravariant derivatives, the metric tensor, and the full Christoffel symbols.[50,51] Instead, we follow the tradition in the field set by Nyborg[33] and by Lee and Wang,[34] and use the vectorial notation based on the unit tangent vectors $\boldsymbol{e}_i$ and the scale factors h_i at position $\boldsymbol{r}$ in the thin boundary layer,

$$\boldsymbol{e}_i = \frac{1}{h_i}\,\partial_i \boldsymbol{r}, \quad \text{with } h_i = |\partial_i \boldsymbol{r}| \quad \text{for } i = \xi, \eta, \zeta, \tag{A1a}$$

$$\boldsymbol{e}_k \cdot \boldsymbol{e}_i = \delta_{ki}, \quad \text{orthonormality by construction.} \tag{A1b}$$

It is natural to introduce the scaled derivatives $\tilde{\partial}_i$ and the curvilinear quantities T_{kji} and $\mathcal{H}_k$,

$$\tilde{\partial}_i = h_i^{-1}\,\partial_i, \quad \text{so that } \boldsymbol{e}_i = \tilde{\partial}_i \boldsymbol{r}, \tag{A2a}$$

$$T_{kji} = (\tilde{\partial}_k \boldsymbol{e}_j) \cdot \boldsymbol{e}_i, \ \text{for } k, j, i = \xi, \eta, \zeta, \tag{A2b}$$

$$\mathcal{H}_k = T_{iki}, \quad \text{sum over repeated index } i. \tag{A2c}$$

T_{kji} is related to, but not identical with, the celebrated Christoffel symbols of differential geometry. The following relations for T_{kji} are useful in the analysis:

$$T_{kji} = T_{jki}, \quad \text{for } i \neq j, \tag{A3a}$$

$$T_{k\xi\xi} = T_{k\eta\eta} = T_{k\zeta\zeta} = 0, \tag{A3b}$$

$$T_{\zeta ji} = 0. \tag{A3c}$$

Equation (A3a) follows from $T_{kji} = (1/h_k)\partial_k((1/h_j)\partial_j \boldsymbol{r}) \cdot \boldsymbol{e}_i = (\partial_k \partial_j \boldsymbol{r}/h_k h_j) \cdot \boldsymbol{e}_i - (\partial_k h_j/h_k h_j)\boldsymbol{e}_j \cdot \boldsymbol{e}_i$, which is symmetric in k and j as the last term is zero for $j \neq i$, Eq. (A3b) is proven by observing $T_{k\xi\xi} = (\tilde{\partial}_k \boldsymbol{e}_\xi) \cdot \boldsymbol{e}_\xi = \frac{1}{2}\tilde{\partial}_k(\boldsymbol{e}_\xi \cdot \boldsymbol{e}_\xi) = 0$ as $\boldsymbol{e}_\xi \cdot \boldsymbol{e}_\xi = 1$, and Eq. (A3c) arises because ζ is defined as the normal direction, and as a consequence T_{kji} is only nonzero for the tangential derivatives $T_{\xi ji}$ and $T_{\eta ji}$, and $\mathcal{H}_k = T_{\xi k\xi} + T_{\eta k\eta}$. It is in this sense that the surface length scale is set by $R \sim \min\{T_{kji}^{-1}, \mathcal{H}_k^{-1}\}$ as stated in Sec. II E.

From now on, we use the index notation, where, as in Eq. (A2c), a repeated index implies a summation. In curvilinear coordinates, the $\boldsymbol{\nabla}$ operator and vector fields are written as

$$\boldsymbol{\nabla} = \boldsymbol{e}_i \tilde{\partial}_i, \quad \boldsymbol{A} = A_i\,\boldsymbol{e}_i, \tag{A4}$$

and from this all other differential operators are calculated. The first example is the Laplacian of a scalar,

$$\begin{aligned}\nabla^2 g = \boldsymbol{\nabla} \cdot \boldsymbol{\nabla} g &= (\boldsymbol{e}_j \tilde{\partial}_j) \cdot \boldsymbol{e}_i \tilde{\partial}_i g \\ &= \left[\boldsymbol{e}_j \cdot \boldsymbol{e}_i \tilde{\partial}_j + \boldsymbol{e}_j \cdot (\tilde{\partial}_j \boldsymbol{e}_i)\right] \tilde{\partial}_i g \\ &= (\tilde{\partial}_i + T_{jij})\tilde{\partial}_i g = (\tilde{\partial}_i \tilde{\partial}_i + \mathcal{H}_i \tilde{\partial}_i) g.\end{aligned} \tag{A5}$$

The divergence of a vector field $\boldsymbol{A}$ takes the form

$$\begin{aligned}\boldsymbol{\nabla}\cdot\boldsymbol{A} &= \boldsymbol{e}_i\cdot\tilde{\partial}_i(A_k\boldsymbol{e}_k) = \Big[(\tilde{\partial}_i A_k)\boldsymbol{e}_k + A_k\tilde{\partial}_i\boldsymbol{e}_k\Big]\cdot\boldsymbol{e}_i \\ &= (\tilde{\partial}_i A_k)\delta_{ik} + A_k T_{iki} = (\tilde{\partial}_k + \mathcal{H}_k)A_k, \end{aligned} \tag{A6}$$

while the gradient of a vector field $\boldsymbol{B}$ is

$$\begin{aligned}\boldsymbol{\nabla}\boldsymbol{B} &= \boldsymbol{e}_k\tilde{\partial}_k(B_j\boldsymbol{e}_j) = \boldsymbol{e}_k\Big[(\tilde{\partial}_k B_i)\boldsymbol{e}_i + B_j\tilde{\partial}_k\boldsymbol{e}_j\Big] \\ &= \boldsymbol{e}_k(\tilde{\partial}_k B_i + T_{kji}B_j)\boldsymbol{e}_i. \end{aligned} \tag{A7}$$

From this follows the advective derivative $(\boldsymbol{A}\cdot\boldsymbol{\nabla})\boldsymbol{B}$ of a vector $\boldsymbol{B}$ with respect to a vector $\boldsymbol{A}$,

$$(\boldsymbol{A}\cdot\boldsymbol{\nabla})\boldsymbol{B} = A_k(\tilde{\partial}_k B_i + T_{kji}B_j)\boldsymbol{e}_i, \tag{A8}$$

and the Laplacian of a vector $\boldsymbol{B}$,

$$\begin{aligned}\nabla^2 B = \boldsymbol{\nabla}\cdot\boldsymbol{\nabla}B &= e_n\tilde{\partial}_n\Big[e_k(\tilde{\partial}_k B_i + T_{kji}B_j)e_i\Big] \\ &= \mathcal{H}_k(\tilde{\partial}_k B_i + T_{kji}B_j)e_i \\ &\quad + \Big[\tilde{\partial}_k\tilde{\partial}_k B_i + B_j\tilde{\partial}_k T_{kji} + T_{kji}\tilde{\partial}_k B_j\Big]e_i \\ &\quad + (\tilde{\partial}_k B_i + T_{kji}B_j)T_{kim}e_m. \end{aligned} \tag{A9}$$

In the analysis of fields in the weakly curved, thin boundary layer, it is useful to decompose a given vector $\boldsymbol{A}$ into parallel and perpendicular components,

$$\boldsymbol{A} = \boldsymbol{A}_\parallel + A_\zeta\,\boldsymbol{e}_\zeta, \tag{A10a}$$

$$\boldsymbol{A}_\parallel = A_\xi\,\boldsymbol{e}_\xi + A_\eta\,\boldsymbol{e}_\eta = A_\alpha\,\boldsymbol{e}_\alpha, \tag{A10b}$$

where here and in the following, repeated Greek index α only sums over the tangential indices ξ and η. Likewise, the parallel components of the $\boldsymbol{\nabla}$ operator (A4), the divergence (A6), and the advective derivative (A8) are

$$\boldsymbol{\nabla}_\parallel = \boldsymbol{e}_\alpha\tilde{\partial}_\alpha, \tag{A11a}$$

$$\boldsymbol{\nabla}_\parallel\cdot\boldsymbol{A}_\parallel = (\tilde{\partial}_\alpha + \mathcal{H}_\alpha)A_\alpha, \tag{A11b}$$

$$(\boldsymbol{A}\cdot\boldsymbol{\nabla}_\parallel)\boldsymbol{B} = A_\alpha(\tilde{\partial}_\alpha B_i + T_{\alpha ji}B_j)\boldsymbol{e}_i, \tag{A11c}$$

For the short-ranged boundary-layer vector field $\boldsymbol{A}^\delta = \boldsymbol{A}^{\delta 0}(\xi,\eta)\,a^\delta(\zeta)$ introduced in Eq. (14), and the analogous scalar field $g^\delta = g^{\delta 0}(\xi,\eta)\,a^\delta(\zeta)$, the derivative expressions simplifies in the weakly curved thin boundary-layer limit $\epsilon \ll 1$. The reason is that terms containing surface-derivative quantities $\boldsymbol{\nabla}_\parallel$, T_{kji}, and $\mathcal{H}_k$, all of size d^{-1}, are a factor of ϵ smaller than terms with the perpendicular derivative $\tilde{\partial}_\zeta = \partial_\zeta$, which picks up a factor of δ^{-1} due to the factor $a^\delta(\zeta)$ that decays on the length scale δ.

For $\nabla^2 g^\delta$ in Eq. (A5), the first term $\tilde{\partial}_i\tilde{\partial}_i g^\delta = \partial_\zeta^2 g^\delta \sim \delta^{-2}g^\delta$ is ϵ^{-1} larger than the second term $\mathcal{H}_i\tilde{\partial}_i g^\delta \sim R^{-1}\delta^{-1}g^\delta$, so that $\nabla^2 g^\delta \approx \partial_\zeta^2 g^\delta$ as stated in Eq. (15a).

Similarly, for $\nabla^2\boldsymbol{A}^\delta$ in Eq. (A9), the only term that does not contain at least one factor $\mathcal{H}_k$ or T_{kji} is $(\tilde{\partial}_k\tilde{\partial}_k A_i^\delta)\,\boldsymbol{e}_i \approx (\partial_\zeta^2 A_i^\delta)\,\boldsymbol{e}_i = \partial_\zeta^2\boldsymbol{A}^\delta$ as stated in Eq. (15b).

Finally, for Eq. (A6), $\tilde{\boldsymbol{\nabla}}\cdot\boldsymbol{A}^\delta = \boldsymbol{\nabla}_\parallel\cdot\boldsymbol{A}_\parallel^\delta + (\tilde{\partial}_\zeta + \mathcal{H}_\zeta)A_\zeta^\delta \approx \boldsymbol{\nabla}_\parallel\cdot\boldsymbol{A}_\parallel^\delta + \partial_\zeta A_\zeta^\delta$ as stated in Eq. (15c).

APPENDIX B: ACOUSTIC POWER BALANCE

The time averages $\langle E_{\mathrm{ac}}^{\mathrm{kin}}\rangle$, $\langle E_{\mathrm{ac}}^{\mathrm{pot}}\rangle$, and $\langle E_{\mathrm{ac}}\rangle$ of the kinetic, the potential, and the total acoustic energy density, respectively, are given by

$$\langle E_{\mathrm{ac}}^{\mathrm{kin}}\rangle = \frac{1}{2}\rho_0\langle\boldsymbol{v}_1\cdot\boldsymbol{v}_1\rangle, \tag{B1a}$$

$$\langle E_{\mathrm{ac}}^{\mathrm{pot}}\rangle = \frac{1}{2}\kappa_0\langle p_1 p_1\rangle, \tag{B1b}$$

$$\langle E_{\mathrm{ac}}\rangle = \langle E_{\mathrm{ac}}^{\mathrm{kin}}\rangle + \langle E_{\mathrm{ac}}^{\mathrm{pot}}\rangle. \tag{B1c}$$

Using Gauss's theorem and $\rho_0\partial_t\boldsymbol{v}_1 = \boldsymbol{\nabla}\cdot\boldsymbol{\sigma}_1$, the time-averaged total power delivered by the surrounding wall is written as the sum of the time-averaged rate of change of the acoustic energy and total power dissipated into heat,

$$\oint_{\partial\Omega}\langle\boldsymbol{V}_1^0\cdot\boldsymbol{\sigma}_1\rangle\cdot\boldsymbol{n}\,\mathrm{d}A = \int_\Omega\boldsymbol{\nabla}\cdot\langle\boldsymbol{v}_1\cdot\boldsymbol{\sigma}_1\rangle\,\mathrm{d}V \tag{B2a}$$

$$= \int_\Omega[\langle\boldsymbol{v}_1\cdot(\boldsymbol{\nabla}\cdot\boldsymbol{\sigma}_1)\rangle + \langle(\boldsymbol{\nabla}\boldsymbol{v}_1)\,:\boldsymbol{\sigma}_1\rangle]\mathrm{d}V \tag{B2b}$$

$$= \int_\Omega[\langle\partial_t E_{\mathrm{ac}}\rangle + \langle(\boldsymbol{\nabla}\boldsymbol{v}_1)\,:\,\boldsymbol{\tau}_1\rangle]\mathrm{d}V. \tag{B2c}$$

Solving for the time-averaged change in acoustic energy $\int_\Omega\langle\partial_t E_{\mathrm{ac}}\rangle\mathrm{d}V$ in Eq. (B2c) gives

$$\int_\Omega\langle\partial_t E_{\mathrm{ac}}\rangle\,\mathrm{d}V = \oint_{\partial\Omega}\langle\boldsymbol{V}_1^0\cdot\boldsymbol{\sigma}_1\rangle\cdot\boldsymbol{n}\,\mathrm{d}A - \int_\Omega\langle(\boldsymbol{\nabla}\boldsymbol{v}_1)\,:\,\boldsymbol{\tau}_1\rangle\,\mathrm{d}V \tag{B3a}$$

$$= \oint_{\partial\Omega}\langle\boldsymbol{V}_1^0(-p_1)\rangle\cdot\boldsymbol{n}\,\mathrm{d}A + \int_\Omega\langle\boldsymbol{v}_1\cdot(\boldsymbol{\nabla}\cdot\boldsymbol{\tau}_1)\rangle\,\mathrm{d}V, \tag{B3b}$$

where Gauss's theorem transforms $\int_{\partial\Omega}\langle\boldsymbol{V}_1^0\cdot\boldsymbol{\tau}_1\rangle\cdot\boldsymbol{n}\,\mathrm{d}A$ into a volume integral, and $\boldsymbol{n} = -\boldsymbol{e}_\zeta$ is the normal vector of the fluid domain Ω. We may interpret the last term in Eq. (B3b) as the rate of change of stored energy due to the viscosity-induced power $\langle P_{\mathrm{visc}}\rangle$,

$$\langle P_{\mathrm{visc}}\rangle = \langle P_{\mathrm{visc}}^{\mathrm{diss}}\rangle + \langle P_{\mathrm{visc}}^{\mathrm{wall}}\rangle. \tag{B4}$$

Here, $\langle P_{\mathrm{visc}}^{\mathrm{diss}}\rangle$ is the viscous power dissipation into heat and $\langle P_{\mathrm{visc}}^{\mathrm{wall}}\rangle$ is the power from the viscous part of the work performed by the wall on the fluid,

$$\langle P_{\mathrm{visc}}\rangle = \int_\Omega\langle\boldsymbol{v}_1\cdot(\boldsymbol{\nabla}\cdot\boldsymbol{\tau}_1)\rangle\mathrm{d}V, \tag{B5a}$$

$$\langle P_{\mathrm{visc}}^{\mathrm{diss}}\rangle = -\int_\Omega \langle(\boldsymbol{\nabla}\cdot\boldsymbol{v}_1)\,:\,\boldsymbol{\tau}_1\rangle\,\mathrm{d}V, \tag{B5b}$$

$$\langle P_{\mathrm{visc}}^{\mathrm{wall}}\rangle = \oint_{\partial\Omega}\langle \boldsymbol{v}_1\cdot\boldsymbol{\tau}_1\rangle\cdot\boldsymbol{n}\,\mathrm{d}A. \tag{B5c}$$

Using Eqs. (18) and (19) we evaluate $\langle P_{\mathrm{visc}}\rangle$,

$$\langle P_{\mathrm{visc}}\rangle = \int_\Omega \langle \boldsymbol{v}_1\cdot(\boldsymbol{\nabla}\cdot\boldsymbol{\tau}_1)\rangle\,\mathrm{d}V \tag{B6a}$$

$$= \int_\Omega \langle \boldsymbol{v}_1\cdot(\mathrm{i}\Gamma\boldsymbol{\nabla}p_1 - \mathrm{i}\omega\rho_0\boldsymbol{v}_1^{\delta})\rangle\,\mathrm{d}V \tag{B6b}$$

$$= \int_\Omega\left[-\frac{\Gamma\omega\rho_0}{2}|\boldsymbol{v}_1^d|^2 + \langle\partial_t E_{\mathrm{ac}}^{\mathrm{kin},\delta}\rangle\right]\mathrm{d}V - \oint_{\partial\Omega}\langle p_1\boldsymbol{v}_1^{\delta 0}\rangle\cdot\boldsymbol{n}\,\mathrm{d}A, \tag{B6c}$$

where we used Eq. (19) and Gauss's theorem. Inserting Eq. (B6c) into Eq. (B3b) leads to Eq. (30). Comparing with Eq. (32), we can relate $\langle P_{\mathrm{loss}}\rangle = \langle P_{\mathrm{loss}}^d\rangle$ and $\langle P_{\mathrm{visc}}\rangle$,

$$\langle P_{\mathrm{loss}}\rangle = \langle P_{\mathrm{visc}}\rangle - \oint_{\partial\Omega}\left\langle p_1\left[\frac{\mathrm{i}}{k_{\mathrm{s}}}\boldsymbol{\nabla}_\parallel\cdot\boldsymbol{V}_{1\parallel}^0\right]\right\rangle\cdot\boldsymbol{n}\,\mathrm{d}A \tag{B7a}$$

$$= \langle P_{\mathrm{visc}}^{\mathrm{diss}}\rangle + \langle P_{\mathrm{visc}}^{\mathrm{wall}}\rangle - \oint_{\partial\Omega}\left\langle p_1\left[\frac{\mathrm{i}}{k_{\mathrm{s}}}\boldsymbol{\nabla}_\parallel\cdot\boldsymbol{V}_{1\parallel}^0\right]\right\rangle\cdot\boldsymbol{n}\,\mathrm{d}A. \tag{B7b}$$

Note that $\langle P_{\mathrm{loss}}\rangle$ is not in general the same as the power $\langle P_{\mathrm{visc}}^{\mathrm{diss}}\rangle$ dissipated into heat. These might, however, be approximately equal if the power

$$\oint_{\partial\Omega} -\langle p_1\boldsymbol{V}_1^0\rangle\cdot\boldsymbol{n}\,\mathrm{d}A$$

delivered by the pressure is approximately balanced by dissipation $\langle P_{\mathrm{visc}}^{\mathrm{diss}}\rangle$. This happens, if

$$\oint_{\partial\Omega} -\langle p_1\boldsymbol{V}_1^0\rangle\cdot\boldsymbol{n}\,\mathrm{d}A$$

is much larger than $\langle P_{\mathrm{visc}}^{\mathrm{wall}}\rangle$ and

$$\oint_{\partial\Omega}\left\langle p_1\left[\frac{\mathrm{i}}{k_{\mathrm{s}}}\boldsymbol{\nabla}_\parallel\cdot\boldsymbol{V}_{1\parallel}^0\right]\right\rangle\cdot\boldsymbol{n}\,\mathrm{d}A,$$

which is usually satisfied.

APPENDIX C: COMPARISON WITH PREVIOUS RESULTS IN THE LITERATURE

1. Comparison with Lee and Wang (1989)

In the following we rewrite the ξ-component $v_{2\xi}^{d0}$ of the streaming velocity in Eq. (58a) using the notation of Lee and Wang[34] to compare it directly with u_L given in their Eq. $(19)^{\mathrm{LW}}$. First, we take the complex conjugate of the argument of the real value, set $\beta=\xi$, and write explicitly the sum over the repeated index $\alpha=\xi,\eta$,

$$\begin{aligned} v_{2\xi}^{d0} = -\frac{1}{4\omega}\mathrm{Re}\Big\{ & v_{1\xi}^{d0}\left(\tilde\partial_\xi v_{1\xi}^{d0*}\right) + v_{1\xi}^{d0}v_{1\eta}^{d0*}T_{\xi\eta\xi} \\ & + v_{1\eta}^{d0}\left(\tilde\partial_\eta v_{1\xi}^{d0*}\right) + v_{1\eta}^{d0}v_{1\eta}^{d0*}T_{\eta\eta\xi} + \left[(2+\mathrm{i})\boldsymbol{\nabla}\cdot\boldsymbol{v}_1^d\right. \\ & - (2+3\mathrm{i})\partial_\zeta v_{1\zeta}^d - (2-\mathrm{i})\mathcal{H}_\zeta V_{1\zeta}^{0*}]v_{1\xi}^{d*} \\ & -2\mathrm{i}V_{1\zeta}^{0*}\left(\partial_\zeta v_{1\xi}^d + v_{1\xi}^{d0}T_{\xi\zeta\xi} + v_{1\eta}^{d0}T_{\eta\zeta\xi}\right)\Big\}. \end{aligned} \tag{C1}$$

This expression is rewritten using the notation of Lee and Wang, $\boldsymbol{v}_1^d=\boldsymbol{u}_{a0}$, $(v_{1\xi}^{d0},v_{1\eta}^{d0},v_{1\zeta}^{d0})=(u_{a0},v_{a0},w_{a0})$, $(\xi,\eta,\zeta)=(x,y,z)$, $\mathcal{H}_\zeta=H$, $(\tilde\partial_\xi,\tilde\partial_\eta,\tilde\partial_\zeta)=(\partial_{x_1},\partial_{x_2},\partial_{x_3})$, $T_{kji}=T_{ijk}^{\mathrm{LW}}$, and $V_{1\zeta}^0=w_{a0}+\mathcal{O}(\epsilon)$,

$$\begin{aligned} v_{2\xi}^{d0} &= -\frac{1}{4\omega}\mathrm{Re}\big\{u_{a0}\left[\partial_{x_1}u_{a0}^* + v_{a0}^*T_{121}^{\mathrm{LW}}\right] \\ &\quad + v_{a0}\left[\partial_{x_2}u_{a0}^* + v_{a0}^*T_{122}^{\mathrm{LW}} + u_{a0}^*[(2+\mathrm{i})\boldsymbol{\nabla}\cdot\boldsymbol{u}_{a0}\right. \\ &\quad \left. - (2+3\mathrm{i})\partial_z w_{a0} - (2-\mathrm{i})Hw_{a0}]\right] \\ &\quad - 2\mathrm{i}w_{a0}^*\left(\partial_z u_{a0} + u_{a0}T_{131}^{\mathrm{LW}} + v_{a0}T_{132}^{\mathrm{LW}}\right)\big\} \\ &= -\frac{1}{4\omega}\mathrm{Re}\big\{q_x + u_{a0}^*[(2+\mathrm{i})\boldsymbol{\nabla}\cdot\boldsymbol{u}_{a0} \\ &\quad - (2+3\mathrm{i})\partial_z w_{a0} - (2-\mathrm{i})Hw_{a0}] \\ &\quad - 2\mathrm{i}w_{a0}^*\left(\partial_z u_{a0} + u_{a0}T_{131}^{\mathrm{LW}} + v_{a0}T_{132}^{\mathrm{LW}}\right)\big\} \\ &= u_L + \frac{1}{2\omega}\mathrm{Re}\left\{\mathrm{i}w_{a0}^*\left(\partial_z u_{a0} + u_{a0}T_{131}^{\mathrm{LW}} + v_{a0}T_{132}^{\mathrm{LW}}\right)\right\}. \end{aligned} \tag{C2}$$

Here, we have used the definition of q_x in Eq. $(3)^{\mathrm{LW}}$ and the result in Eq. $(19)^{\mathrm{LW}}$ for the x-component u_L of the streaming velocity just outside the boundary layer.

Similarly, we obtain for the η-component $v_{2\eta}^{d0}$ in Eq. (58a),

$$v_{2\eta}^{d0} = v_L + \frac{1}{2\omega}\mathrm{Re}\left\{\mathrm{i}w_{a0}^*\left(\partial_z v_{a0} + u_{a0}T_{231}^{\mathrm{LW}} + v_{a0}T_{232}^{\mathrm{LW}}\right)\right\}, \tag{C3}$$

where we have used the definition in Eq. $(4)^{\mathrm{LW}}$ for q_y and the result in Eq. $(20)^{\mathrm{LW}}$ for the y-component v_L of the streaming velocity. The comparison obtained in Eqs. (C2) and (C3) is discussed in Sec. VI A.

2. Comparison with Vanneste and Bühler (2011)

In the following we rewrite the ξ-component $v_{2\xi}^{d0}$ of the Eulerian streaming velocity in Eq. (59b) using the notation of Vanneste and Bühler[35] to compare it directly with the Lagrangian streaming velocity $\bar u_{\mathrm{slip}}^{\mathrm{L}}$ given in their Eq. $(4.10)^{\mathrm{VB}}$. First, given the flat wall, $(\xi,\eta,\zeta)=(x,y,z)$ and for all i,j,k we have $h_i=1$, $\mathcal{H}_i=0$, and $T_{ijk}=0$. Then, we identify our first-order velocity fields with theirs: From Eqs. $(2.6)^{\mathrm{VB}}$ and $(3.1)^{\mathrm{VB}}$ follows $\boldsymbol{v}_1^d=2\boldsymbol{\nabla}\hat\phi$, and from Eqs. $(3.9)^{\mathrm{VB}}$ and $(3.10)^{\mathrm{VB}}$ we read that $\boldsymbol{v}_{1\parallel}^{\delta 0}=-2\hat U\boldsymbol{e}_x-2\hat V\boldsymbol{e}_y$. Next, we relate our steady Eulerian second-order velocity $\boldsymbol{v}_2^d$ with their Lagrangian mean flow $\bar u_{\mathrm{slip}}^{\mathrm{L}}$ Eq. $(4.10)^{\mathrm{VB}}$. Using $\mathrm{Re}Z=\frac{1}{2}Z+\mathrm{c.c.}=\frac{1}{2}Z^*+\mathrm{c.c.}$, we obtain

$$
\begin{aligned}
v_{2\xi}^{d0} &= -\frac{1}{4\omega}\mathrm{Re}\Big\{(1-2\mathrm{i})v_{1\alpha}^{\delta 0*}\partial_\alpha v_{1\xi}^{\delta 0} - 4\mathrm{i}v_{1\alpha}^{\delta 0*}\partial_\alpha v_{1\xi}^{d0} + \Big[(2+\mathrm{i})\partial_\alpha v_{1\alpha}^{\delta 0*} + 2\mathrm{i}\Big(\partial_\alpha v_{1\alpha}^{d0*} - \partial_\zeta v_{1\zeta}^{d*}\Big)\Big]v_{1\xi}^{\delta 0} - 2\mathrm{i}\,v_{1k}^{d*}\partial_k v_{1\xi}^{d}\Big\} \\
&= -\frac{1}{2\omega}\Big\{(1+2\mathrm{i})\hat{U}\partial_x\hat{U}^* + (1+2\mathrm{i})\hat{V}\partial_y\hat{U}^* + 4\mathrm{i}\hat{U}^*\partial_x^2\hat{\phi} + 4\mathrm{i}\hat{V}^*\partial_x\partial_y\hat{\phi} \\
&\quad + \Big[(2+\mathrm{i})\partial_x\hat{U}^* + (2+\mathrm{i})\partial_y\hat{V}^* + 2\mathrm{i}\Big(\partial_x^2\hat{\phi} + \partial_y^2\hat{\phi} - \partial_z^2\hat{\phi}\Big)\Big]\hat{U}^*\Big\} + \mathrm{c.c.} - \frac{1}{\omega}\langle \mathrm{i}\boldsymbol{v}_1^{\mathrm{d}}\cdot\boldsymbol{\nabla}\boldsymbol{v}_1^{\mathrm{d}}\rangle \\
&= -\frac{1}{2\omega}\Big\{3(1+\mathrm{i})\hat{U}\partial_x\hat{U}^* + (1+2\mathrm{i})\hat{V}\partial_y\hat{U}^* + (2+\mathrm{i})\hat{U}\partial_y\hat{V}^*\Big\} - \frac{\mathrm{i}}{\omega}\Big\{2\partial_x\partial_y\hat{\phi}\hat{V}^* + \Big(\partial_x^2\hat{\phi} + \partial_y^2\hat{\phi} - \partial_z^2\hat{\phi}\Big)\hat{U}^*\Big\} + \mathrm{c.c.} - \hat{\mathrm{u}}^{\mathrm{S}} \\
&= u_{\mathrm{slip}}^{\mathrm{L}} - \hat{u}^{\mathrm{S}} = u_{\mathrm{slip}}^{\mathrm{E}}.
\end{aligned}
\tag{C4}
$$

Here, we have used that the Lagrangian velocity $u_{\mathrm{slip}}^{\mathrm{L}}$, calculated by Vanneste and Bühler in their Eq. (4.10)$^{\mathrm{VB}}$, is related to the Eulerian velocity $u_{\mathrm{slip}}^{\mathrm{E}}$ through the Stokes drift velocity $\hat{u}^{\mathrm{S}} = (1/\omega)\langle \mathrm{i}\boldsymbol{v}_1^d\cdot\boldsymbol{\nabla}\boldsymbol{v}_1^d\rangle$ of Eq. (34c).

Similarly, for the y component $v_{2\eta}^{d0}$ of the streaming,

$$
v_{2\eta}^{d0} = v_{\mathrm{slip}}^{\mathrm{L}} - \hat{v}^{\mathrm{S}} = v_{\mathrm{slip}}^{\mathrm{E}}. \tag{C5}
$$

The comparison obtained in Eqs. (C4) and (C5) is discussed in Sec. VI B.

[1]H. Bruus, J. Dual, J. Hawkes, M. Hill, T. Laurell, J. Nilsson, S. Radel, S. Sadhal, and M. Wiklund, "Forthcoming lab on a chip tutorial series on acoustofluidics: Acoustofluidics-exploiting ultrasonic standing wave forces and acoustic streaming in microfluidic systems for cell and particle manipulation," Lab Chip **11**(21), 3579–3580 (2011).

[2]T. Laurell and A. Lenshof, *Microscale Acoustofluidics* (Royal Society of Chemistry, Cambridge, 2015).

[3]P. Thevoz, J. D. Adams, H. Shea, H. Bruus, and H. T. Soh, "Acoustophoretic synchronization of mammalian cells in microchannels," Anal. Chem. **82**(7), 3094–3098 (2010).

[4]P. Augustsson, C. Magnusson, M. Nordin, H. Lilja, and T. Laurell, "Microfluidic, label-free enrichment of prostate cancer cells in blood based on acoustophoresis," Anal. Chem. **84**(18), 7954–7962 (2012).

[5]P. Augustsson, J. T. Karlsen, H.-W. Su, H. Bruus, and J. Voldman, "Iso-acoustic focusing of cells for size-insensitive acousto-mechanical phenotyping," Nat. Commun. **7**, 11556 (2016).

[6]X. Ding, S.-C. S. Lin, B. Kiraly, H. Yue, S. Li, I.-K. Chiang, J. Shi, S. J. Benkovic, and T. J. Huang, "On-chip manipulation of single microparticles, cells, and organisms using surface acoustic waves," Proc. Natl. Acad. Sci. U.S.A. **109**(28), 11105–11109 (2012).

[7]D. J. Collins, B. Morahan, J. Garcia-Bustos, C. Doerig, M. Plebanski, and A. Neild, "Two-dimensional single-cell patterning with one cell per well driven by surface acoustic waves," Nat. Commun. **6**, 8686 (2015).

[8]B. Hammarström, M. Evander, H. Barbeau, M. Bruzelius, J. Larsson, T. Laurell, and J. Nillsson, "Non-contact acoustic cell trapping in disposable glass capillaries," Lab Chip **10**(17), 2251–2257 (2010).

[9]B. Hammarström, T. Laurell, and J. Nilsson, "Seed particle enabled acoustic trapping of bacteria and nanoparticles in continuous flow systems," Lab Chip **12**, 4296–4304 (2012).

[10]B. Hammarström, M. Evander, J. Wahlström, and J. Nilsson, "Frequency tracking in acoustic trapping for improved performance stability and system surveillance," Lab Chip **14**, 1005–1013 (2014).

[11]B. W. Drinkwater, "Dynamic-field devices for the ultrasonic manipulation of microparticles," Lab Chip **16**, 2360–2375 (2016).

[12]D. J. Collins, C. Devendran, Z. Ma, J. W. Ng, A. Neild, and Y. Ai, "Acoustic tweezers via sub-time-of-flight regime surface acoustic waves," Sci. Adv. **2**(7), e1600089 (2016).

[13]H. G. Lim, Y. Li, M.-Y. Lin, C. Yoon, C. Lee, H. Jung, R. H. Chow, and K. K. Shung, "Calibration of trapping force on cell-size objects from ultrahigh-frequency single-beam acoustic tweezer," IEEE Trans. Ultrason. Ferroelectr. Freq. Control **63**(11), 1988–1995 (2016).

[14]D. Baresch, J.-L. Thomas, and R. Marchiano, "Observation of a single-beam gradient force acoustical trap for elastic particles: Acoustical tweezers," Phys. Rev. Lett. **116**, 024301 (2016).

[15]L. V. King, "On the acoustic radiation pressure on spheres," Proc. R. Soc. London, Ser. A **147**(861), 212–240 (1934).

[16]K. Yosioka and Y. Kawasima, "Acoustic radiation pressure on a compressible sphere," Acustica **5**, 167–173 (1955).

[17]A. A. Doinikov, "Acoustic radiation force on a spherical particle in a viscous heat-conducting fluid. I. General formula," J. Acoust. Soc. Am. **101**(2), 713–721 (1997).

[18]A. A. Doinikov, "Acoustic radiation force on a spherical particle in a viscous heat-conducting fluid. II. Force on a rigid sphere," J. Acoust. Soc. Am. **101**(2), 722–730 (1997).

[19]A. A. Doinikov, "Acoustic radiation force on a spherical particle in a viscous heat-conducting fluid. III. Force on a liquid drop," J. Acoust. Soc. Am. **101**(2), 731–740 (1997).

[20]M. Settnes and H. Bruus, "Forces acting on a small particle in an acoustical field in a viscous fluid," Phys. Rev. E **85**, 016327 (2012).

[21]J. T. Karlsen and H. Bruus, "Forces acting on a small particle in an acoustical field in a thermoviscous fluid," Phys. Rev. E **92**, 043010 (2015).

[22]Lord Rayleigh, "On the circulation of air observed in Kundt's tubes, and on some allied acoustical problems," Philos. Trans. R. Soc. London **175**, 1–21 (1884).

[23]H. Schlichting, "Berechnung ebener periodischer grenzeschichtströmungen," Phys. Z. **33**, 327–335 (1932).

[24]M. Wiklund, R. Green, and M. Ohlin, "Acoustofluidics 14: Applications of acoustic streaming in microfluidic devices," Lab Chip **12**, 2438–2451 (2012).

[25]P. B. Muller, M. Rossi, A. G. Marin, R. Barnkob, P. Augustsson, T. Laurell, C. J. Kähler, and H. Bruus, "Ultrasound-induced acoustophoretic motion of microparticles in three dimensions," Phys. Rev. E **88**(2), 023006 (2013).

[26]J. Lei, P. Glynne-Jones, and M. Hill, "Modal Rayleigh-like streaming in layered acoustofluidic devices," Phys. Fluids **28**, 012004 (2016).

[27]A. Riaud, M. Baudoin, O. Bou Matar, L. Becerra, and J.-L. Thomas, "Selective manipulation of microscopic particles with precursor swirling Rayleigh waves," Phys. Rev. Appl. **7**, 024007 (2017).

[28]P. B. Muller, R. Barnkob, M. J. H. Jensen, and H. Bruus, "A numerical study of microparticle acoustophoresis driven by acoustic radiation forces and streaming-induced drag forces," Lab Chip **12**, 4617–4627 (2012).

[29]R. Barnkob, P. Augustsson, T. Laurell, and H. Bruus, "Acoustic radiation- and streaming-induced microparticle velocities determined by microparticle image velocimetry in an ultrasound symmetry plane," Phys. Rev. E **86**, 056307 (2012).

[30]M. Antfolk, P. B. Muller, P. Augustsson, H. Bruus, and T. Laurell, "Focusing of sub-micrometer particles and bacteria enabled by two-dimensional acoustophoresis," Lab Chip **14**, 2791–2799 (2014).

[31]Z. Mao, P. Li, M. Wu, H. Bachman, N. Mesyngier, X. Guo, S. Liu, F. Costanzo, and T. J. Huang, "Enriching nanoparticles via acoustofluidics," ACS Nano **11**(1), 603–612 (2017).

[32]M. Wu, Z. Mao, K. Chen, H. Bachman, Y. Chen, J. Rufo, L. Ren, P. Li, L. Wang, and T. J. Huang, "Acoustic separation of nanoparticles in continuous flow," Adv. Funct. Mater. **27**(14), 1606039 (2017).

[33]W. L. Nyborg, "Acoustic streaming near a boundary," J. Acoust. Soc. Am. **30**(4), 329–339 (1958).

[34]C. Lee and T. Wang, "Near-boundary streaming around a small sphere due to 2 orthogonal standing waves," J. Acoust. Soc. Am. **85**(3), 1081–1088 (1989).

[35]J. Vanneste and O. Bühler, "Streaming by leaky surface acoustic waves," Proc. R. Soc. London, Ser. A **467**(2130), 1779–1800 (2011).

[36]P. B. Muller and H. Bruus, "Theoretical study of time-dependent, ultrasound-induced acoustic streaming in microchannels," Phys. Rev. E **92**, 063018 (2015).
[37]C. E. Bradley, "Acoustic streaming field structure: The influence of the radiator," J. Acoust. Soc. Am. **100**(3), 1399–1408 (1996).
[38]P. Hahn and J. Dual, "A numerically efficient damping model for acoustic resonances in microfluidic cavities," Phys. Fluids **27**, 062005 (2015).
[39]A. Riaud, M. Baudoin, O. Bou Matar, J.-L. Thomas, and P. Brunet, "On the influence of viscosity and caustics on acoustic streaming in sessile droplets: An experimental and a numerical study with a cost-effective method," J. Fluid Mech. **821**, 384–420 (2017).
[40]C. Eckart, "Vortices and streams caused by sound waves," Phys. Rev. **73**, 68–76 (1948).
[41]COMSOL Multiphysics 5.3a (2017), www.comsol.com (Last viewed 3 August 2018).
[42]P. B. Muller and H. Bruus, "Numerical study of thermoviscous effects in ultrasound-induced acoustic streaming in microchannels," Phys. Rev. E **90**(4), 043016 (2014).
[43]M. W. H. Ley and H. Bruus, "Continuum modeling of hydrodynamic particle-particle interactions in microfluidic high-concentration suspensions," Lab Chip **16**(7), 1178–1188 (2016).
[44]CORNING, Houghton Park C-8, Corning, NY 14831, USA, *Glass Silicon Constraint Substrates*, http://www.valleydesign.com/Datasheets/Corning%20Pyrex%207740.pdf (Last viewed April 18, 2018).
[45]R. Barnkob, P. Augustsson, T. Laurell, and H. Bruus, "Measuring the local pressure amplitude in microchannel acoustophoresis," Lab Chip **10**(5), 563–570 (2010).
[46]P. Augustsson, R. Barnkob, S. T. Wereley, H. Bruus, and T. Laurell, "Automated and temperature-controlled micro-PIV measurements enabling long-term-stable microchannel acoustophoresis characterization," Lab Chip **11**(24), 4152–4164 (2011).
[47]R. Barnkob, I. Iranmanesh, M. Wiklund, and H. Bruus, "Measuring acoustic energy density in microchannel acoustophoresis using a simple and rapid light-intensity method," Lab Chip **12**, 2337–2344 (2012).
[48]M. W. H. Ley and H. Bruus, "Three-dimensional numerical modeling of acoustic trapping in glass capillaries," Phys. Rev. Appl. **8**, 024020 (2017).
[49]A. Y. Rednikov and S. S. Sadhal, "Acoustic/steady streaming from a motionless boundary and related phenomena: Generalized treatment of the inner streaming and examples," J. Fluid. Mech. **667**, 426–462 (2011).
[50]E. Kreyszig, *Differential Geometry* (Dover Publications, New York, 1991).
[51]L. D. Landau and E. M. Lifshitz, *The Classical Theory of Fields*, 4th ed. (Butterworth-Heinemann, Oxford, 1980), Vol. 4.

7.2 Paper II: AIMS Math 4, 99-111 (2019)

3D modeling of acoustofluidics in a liquid-filled cavity including streaming, viscous boundary layers, surrounding solids, and a piezoelectric transducer

DOI: 10.3934/Math.2019.1.99

Authors: N.R. Skov, J. S. Bach, B.G. Winckelmann, and H. Bruus.
Journal: AIMS Math **4**, 99-111 (2019)

AIMS Mathematics

http://www.aimspress.com/journal/Math

AIMS Mathematics, 4(1): 99–111.
DOI:10.3934/Math.2019.1.99
Received: 14 November 2018
Accepted: 20 January 2019
Published: 30 January 2019

Research article

3D modeling of acoustofluidics in a liquid-filled cavity including streaming, viscous boundary layers, surrounding solids, and a piezoelectric transducer

Nils R. Skov, Jacob S. Bach, Bjørn G. Winckelmann and Henrik Bruus*

Department of Physics, Technical University of Denmark, DTU Physics Building 309, DK-2800 Kongens Lyngby, Denmark

* **Correspondence:** Email: bruus@fysik.dtu.dk; Tel: +4545253307.

Abstract: We present a full 3D numerical simulation of the acoustic streaming observed in full-image micro-particle velocimetry by Hagsäter *et al.*, Lab Chip **7**, 1336 (2007) in a 2 mm by 2 mm by 0.2 mm microcavity embedded in a 49 mm by 15 mm by 2 mm chip excited by 2-MHz ultrasound. The model takes into account the piezo-electric transducer, the silicon base with the water-filled cavity, the viscous boundary layers in the water, and the Pyrex lid. The model predicts well the experimental results.

Keywords: microscale acoustofluidics; acoustic streaming; numerical simulation; 3D modeling
Mathematics Subject Classification: 42B37, 65M60, 70J35, 74F10

1. Introduction and definition of the model system

For the past 15 years, ultrasound-based microscale acoustofluidic devices have successfully and in increasing numbers been used in the fields of biology, environmental and forensic sciences, and clinical diagnostics [1–5]. However, it remains a challenge to model and optimize a given device including all relevant acoustofluidic aspects. Steadily, good progress is being made towards this goal. Examples of recent advances in modeling include work in two dimensions (2D) by Muller and Bruus [6, 7] on thermoviscous and transient effects of acoustic pressure, radiation force, and streaming in the fluid domain, and work by Nama *et al.* [8] on acoustophoresis induced by a given surface acoustic wave in a fluid domain capped by a PDMS lid. Examples of 3D modeling include work by Lei *et al.* [9, 10] on boundary-layer induced streaming in fluid domains with hard wall and outgoing plane-wave boundary conditions, work by Gralinski *et al.* [11] on the acoustic pressure fields in circular capillaries including the fluid and glass domains and excited by a given wall vibration, a model later extended by Ley and Bruus [12] to take into account absorption and outgoing waves, and work by Hahn and Dual [13] on the acoustic pressure and acoustic radiation force in the fluid domain including the surrounding transducer, silicon and glass domains, as well as bulk, boundary-layer, and thermal dissipation.

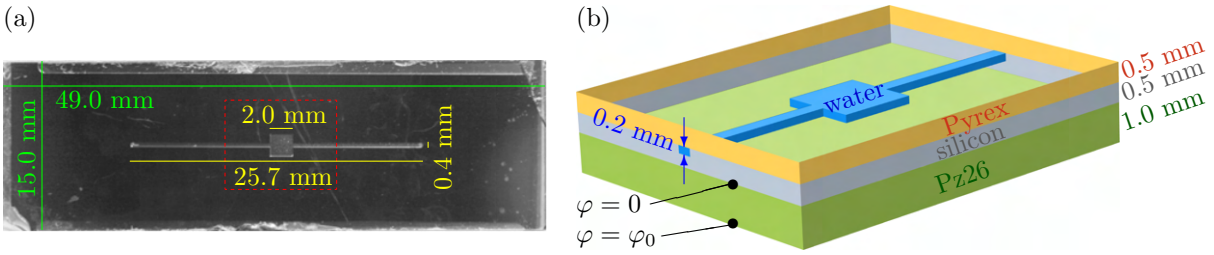

Figure 1. (a) Top-view photograph of the original transducer-silicon-glass device studied in 2007 by Hagsäter *et al.* [16]. (b) A cut-open 3D sketch of the device in the red-dashed area of panel (a) showing the Pz26 piezo-electric transducer (green), the silicon base (gray), the water-filled cavity (blue) in the top of the silicon base, and the Pyrex lid (orange).

Table 1. The length, width, and height $L \times W \times H$ (in mm) of the six rectangular elements in the acoustofluidic device model of Figure 1(b): The piezoelectric transducer (pz), the silicon base (si), the Pyrex lid (py), the main cavity (ca), and the two inlet channels (c1) and (c2).

Pz26	Silicon	Pyrex	Cavity	Channel 1	Channel 2
$L_{pz} \times W_{pz} \times H_{pz}$	$L_{si} \times W_{si} \times H_{si}$	$L_{py} \times W_{py} \times H_{py}$	$L_{ca} \times W_{ca} \times H_{ca}$	$L_{c1} \times W_{c1} \times H_{c1}$	$L_{c2} \times W_{c2} \times H_{c2}$
$49 \times 15 \times 1.0$	$49 \times 15 \times 0.5$	$49 \times 15 \times 0.5$	$2.02 \times 2 \times 0.2$	$11.3 \times 0.4 \times 0.2$	$12.4 \times 0.4 \times 0.2$

In this paper, we present a 3D model and its implementation in the commercial software COMSOL Multiphysics [14] of a prototypical acoustofluidic silicon-glass-based device that takes into account the following physical aspects: the piezo-electric transducer driving the system, the silicon base that contains the acoustic cavity, the fluid with bulk- and boundary-layer-driven streaming, the Pyrex lid, and a dilute microparticle suspension filling the cavity. This work represents a synthesis of our previous modeling of streaming in 2D [6], acoustic fields in 3D [12], and boundary-layer analysis [15] enabling effective-model computation of streaming in 3D, and it combines and extends the 3D streaming study in the fluid domain by Lei *et al.* [10] and the 3D study of acoustics in the coupled transducer-sold-fluid system by Hahn and Dual [13]. To test the presented coupled 3D model, we have, as Lei *et al.* [10], chosen to model the system studied experimentally by Hagsäter *et al.* in 2007 [16] and shown in Figure 1. It consists of a rectangular 0.5-mm high silicon base, into the surface of which is etched a shallow square-shaped cavity with two inlet channels attached. The cavity is sealed with a 0.5-mm high Pyrex lid that exactly covers the silicon base. At the bottom of the silicon base is attached a 1-mm high rectangular Pz26 piezo-electric transducer. All three solid layers are 49 mm long and 15 mm wide. The nearly-square cavity is 2.02 mm long and 2 mm wide and has attached two inlet channels both 0.4 mm wide, but of unequal lengths 11.3 mm and 12.4 mm, respectively. The channels and cavity are 0.2 mm deep. A sketch of the model device is shown in Figure 1, and its geometrical parameters are summarized in Table 1. The transducer is grounded at the top and driven by an ac voltage $\tilde{\varphi}$ of amplitude $\varphi_0 = 1$ V and a frequency around 2.2 MHz applied to its bottom surface.

2. Theoretical background

We summarize the coupled equations of motion for a system driven by a time-harmonic electric potential, $\tilde{\varphi} = \varphi_0\, \mathrm{e}^{-\mathrm{i}\omega t}$ applied to selected boundaries of a piezo-electric Pz26 ceramic. Here, tilde denotes a field with harmonic time dependency, ω is the angular frequency in the low MHz range, and "i" is the imaginary unit. This harmonic boundary condition excites the time-harmonic fields: the electric potential $\tilde{\varphi}(\boldsymbol{r}, t)$ in the Pz26 ceramic, the displacement $\tilde{\boldsymbol{u}}(\boldsymbol{r}, t)$ in the solids, and the acoustic pressure $\tilde{p}_1(\boldsymbol{r}, t)$ in the water,

$$\tilde{\varphi}(\boldsymbol{r}, t) = \varphi(\boldsymbol{r})\, \mathrm{e}^{-\mathrm{i}\omega t}, \qquad \tilde{\boldsymbol{u}}(\boldsymbol{r}, t) = \boldsymbol{u}(\boldsymbol{r})\, \mathrm{e}^{-\mathrm{i}\omega t}, \qquad \tilde{p}_1(\boldsymbol{r}, t) = p_1(\boldsymbol{r})\, \mathrm{e}^{-\mathrm{i}\omega t}. \tag{2.1}$$

In our simulation, we first solve the linear equations of the amplitude fields $\varphi(\boldsymbol{r})$, $\boldsymbol{u}(\boldsymbol{r})$, and $p_1(\boldsymbol{r})$. Then, based on time-averaged products (over one oscillation period) of these fields, we compute the nonlinear acoustic radiation force $\boldsymbol{F}^{\mathrm{rad}}$ and the steady-state acoustic streaming velocity $\boldsymbol{v}_2(\boldsymbol{r})$.

2.1. Linear acoustics in the fluid

In the fluid (water) of density ρ_{fl}, sound speed c_{fl}, dynamic viscosity η_{fl}, and bulk viscosity $\eta_{\mathrm{fl}}^{\mathrm{b}}$, we model the acoustic pressure p_1 as in Ref. [12],

$$\nabla^2 p_1 = -\frac{\omega^2}{c_{\mathrm{fl}}^2}(1 + \mathrm{i}\Gamma_{\mathrm{fl}})\, p_1, \qquad \boldsymbol{v}_1 = -\mathrm{i}\, \frac{1 - \mathrm{i}\Gamma_{\mathrm{fl}}}{\omega\rho_{\mathrm{fl}}}\, \boldsymbol{\nabla} p_1, \qquad \Gamma_{\mathrm{fl}} = \left(\frac{4}{3}\eta_{\mathrm{fl}} + \eta_{\mathrm{fl}}^{\mathrm{b}}\right)\omega\kappa_{\mathrm{fl}}. \tag{2.2}$$

Here, $\boldsymbol{v}_1$ is the acoustic velocity which is proportional to the pressure gradient $\boldsymbol{\nabla} p_1$, while $\Gamma_{\mathrm{fl}} \ll 1$ is a weak absorption coefficient, and $\kappa_{\mathrm{fl}} = (\rho_{\mathrm{fl}} c_{\mathrm{fl}}^2)^{-1}$ is the isentropic compressibility of the fluid, see Table 2 for parameter values. The time-averaged acoustic energy density $E_{\mathrm{ac}}^{\mathrm{fl}}$ in the fluid domain is the sum of the time-averaged (over one oscillation period) kinetic and compressional energy densities,

$$E_{\mathrm{ac}}^{\mathrm{fl}} = \frac{1}{4}\rho_{\mathrm{fl}}\left|\boldsymbol{v}_1\right|^2 + \frac{1}{4}\kappa_{\mathrm{fl}}\left|p_1\right|^2. \tag{2.3}$$

Table 2. Material parameters at 25 °C for isotropic Pyrex borosilicate glass [17], cubic-symmetric silicon [18], and water [6]. Note that $c_{12} = c_{11} - 2c_{44}$ for isotropic solids.

Parameter		Pyrex	Si	Unit	Parameter		Water	Unit
Mass density	ρ_{sl}	2230	2329	kg m^{-3}	Mass density	ρ_{fl}	997.05	kg m^{-3}
Elastic modulus	c_{11}	69.72	165.7	GPa	Sound speed	c_{fl}	1496.7	m s^{-1}
Elastic modulus	c_{44}	26.15	79.6	GPa	Dyn. viscosity	η_{fl}	2.485	mPa s
Elastic modulus	c_{12}	17.43	63.9	GPa	Bulk viscosity	$\eta_{\mathrm{fl}}^{\mathrm{b}}$	0.890	mPa s
Damping coeff.	Γ_{sl}	0.0004	0.0000	1	Damping coeff.	Γ_{fl}	0.00002	1
–	–	–	–	–	Compressibility	κ_{fl}	452	TPa^{-1}

2.2. Linear elastic motion of the solids

In the solid materials, each with a given density ρ_{sl}, we model the displacement field $\boldsymbol{u}$ using the equation of motion given by [12]

$$-\rho_{\mathrm{sl}}\omega^2(1 + \mathrm{i}\Gamma_{\mathrm{sl}})\, \boldsymbol{u} = \boldsymbol{\nabla} \cdot \boldsymbol{\sigma}, \tag{2.4}$$

where $\Gamma_{\text{sl}} \ll 1$ is a weak damping coefficient. Here, $\boldsymbol{\sigma}$ is the stress tensor, which is coupled to $\boldsymbol{u}$ through a stress-strain relation depending on the material-dependent elastic moduli. The time-averaged acoustic energy density in the solids is given by the sum of kinetic and elastic contributions,

$$E_{\text{ac}}^{\text{sl}} = \frac{1}{4}\rho_{\text{sl}}\omega^2|u|^2 + \frac{1}{4}\text{Re}[(\boldsymbol{\nabla}\boldsymbol{u}) : \boldsymbol{\sigma}^*], \tag{2.5}$$

where "Re" denotes the real value and "*" the complex conjugate of a complex number, respectively.

2.3. Stress-strain coupling in elastic solids

For a crystal with either cubic or isotropic symmetry, the relation between the stress tensor σ_{ij} and strain components $\frac{1}{2}(\partial_i u_j + \partial_j u_i)$ is given in the compact Voigt representation as [19]

$$\left(\begin{array}{c} \sigma_{xx} \\ \sigma_{yy} \\ \sigma_{zz} \\ \hline \sigma_{yz} \\ \sigma_{xz} \\ \sigma_{xy} \end{array}\right) = \left(\begin{array}{ccc|ccc} c_{11} & c_{12} & c_{12} & 0 & 0 & 0 \\ c_{12} & c_{11} & c_{12} & 0 & 0 & 0 \\ c_{12} & c_{12} & c_{11} & 0 & 0 & 0 \\ \hline 0 & 0 & 0 & c_{44} & 0 & 0 \\ 0 & 0 & 0 & 0 & c_{44} & 0 \\ 0 & 0 & 0 & 0 & 0 & c_{44} \end{array}\right) \left(\begin{array}{c} \partial_x u_x \\ \partial_y u_y \\ \partial_z u_z \\ \hline \partial_y u_z + \partial_z u_y \\ \partial_x u_z + \partial_z u_x \\ \partial_x u_y + \partial_y u_x \end{array}\right), \quad \text{for Pyrex and silicon.} \tag{2.6}$$

Here, c_{ij} are the elastic moduli which are listed for Pyrex and silicon in Table 2.

2.4. Stress-strain coupling in piezoelectric ceramics

Lead-zirconate-titanate (PZT) ceramics are piezoelectric below their Curie temperature, which typically is $200 - 400$ °C. Using Cartesian coordinates and the Voigt notation for a PZT ceramic, the mechanical stress tensor σ_{ij} and electric displacement field D_i are coupled to the mechanical strain components $\frac{1}{2}(\partial_i u_j + \partial_j u_i)$ and the electrical potential φ through the relation [19]

$$\left(\begin{array}{c} \sigma_{xx} \\ \sigma_{yy} \\ \sigma_{zz} \\ \hline \sigma_{yz} \\ \sigma_{xz} \\ \sigma_{xy} \\ \hline D_x \\ D_y \\ D_z \end{array}\right) = \left(\begin{array}{ccc|ccc|ccc} c_{11} & c_{12} & c_{13} & 0 & 0 & 0 & 0 & 0 & -e_{31} \\ c_{12} & c_{11} & c_{13} & 0 & 0 & 0 & 0 & 0 & -e_{31} \\ c_{13} & c_{13} & c_{33} & 0 & 0 & 0 & 0 & 0 & -e_{33} \\ \hline 0 & 0 & 0 & c_{44} & 0 & 0 & 0 & -e_{15} & 0 \\ 0 & 0 & 0 & 0 & c_{44} & 0 & -e_{15} & 0 & 0 \\ 0 & 0 & 0 & 0 & 0 & c_{66} & 0 & 0 & 0 \\ \hline 0 & 0 & 0 & 0 & e_{15} & 0 & \varepsilon_{11} & 0 & 0 \\ 0 & 0 & 0 & e_{15} & 0 & 0 & 0 & \varepsilon_{11} & 0 \\ e_{31} & e_{31} & e_{33} & 0 & 0 & 0 & 0 & 0 & \varepsilon_{33} \end{array}\right) \left(\begin{array}{c} \partial_x u_x \\ \partial_y u_y \\ \partial_z u_z \\ \hline \partial_y u_z + \partial_z u_y \\ \partial_x u_z + \partial_z u_x \\ \partial_x u_y + \partial_y u_x \\ \hline -\partial_x \varphi \\ -\partial_y \varphi \\ -\partial_z \varphi \end{array}\right), \quad \text{for Pz26.} \tag{2.7}$$

The values of the material parameters for the PZT ceramic Pz26 are listed in Table 3. Due to the high electric permittivity of Pz26, we only model the electric potential φ in the transducer, and since we assume no free charges here and only low-MHz frequencies, φ must satisfy the quasi-static equation,

$$\boldsymbol{\nabla} \cdot \boldsymbol{D} = 0, \quad \text{for Pz26.} \tag{2.8}$$

Table 3. Material parameters of Ferroperm Ceramic Pz26 from Meggitt A/S [20]. Isotropy in the x-y plane implies $c_{66} = \frac{1}{2}(c_{11} - c_{12})$. The damping coefficient is $\Gamma_{\mathrm{sl}} = 0.02$ [13].

Parameter	Value	Parameter	Value	Parameter	Value
ρ_{sl}	7700 kg/m^3	ε_{11}	828 ε_0	ε_{33}	700 ε_0
c_{11}	168 GPa	c_{33}	123 GPa	e_{31}	-2.8 C/m^2
c_{12}	110 GPa	c_{44}	30.1 GPa	e_{33}	14.7 C/m^2
c_{13}	99.9 GPa	c_{66}	29.0 GPa	e_{15}	9.86 C/m^2

2.5. Boundary conditions and boundary layers in the fluid at the fluid-solid interfaces

The applied boundary conditions are the usual ones, namely that (1) the stress and the velocity fields are continuous across all fluid-solid and solid-solid interfaces, (2) the stress is zero on all outer boundaries facing the air, (3) the piezoelectric ceramic is driven by a given electric potential at specified surfaces that represent the presence of infinitely thin, massless electrodes, and (4) there are no free charges on the surface of the ceramic. The influence ($A \leftarrow B$) on domain A from domain B with the surface normal $\boldsymbol{n}$ pointing away from A, is given by

$$\text{Pz26 domain} \leftarrow \text{ground electrode, top:} \qquad \varphi = 0, \tag{2.9a}$$

$$\text{Pz26 domain} \leftarrow \text{phase electrode, bottom:} \qquad \varphi = \varphi_0, \tag{2.9b}$$

$$\text{Pz26 and solid domain} \leftarrow \text{air:} \qquad \boldsymbol{\sigma}\cdot\boldsymbol{n} = \boldsymbol{0} \quad \text{and} \quad \boldsymbol{n}\cdot\boldsymbol{D} = 0, \tag{2.9c}$$

$$\text{Solid domain} \leftarrow \text{fluid:} \qquad \boldsymbol{\sigma}\cdot\boldsymbol{n} = -p_1\,\boldsymbol{n} + \mathrm{i}k_{\mathrm{s}}\eta_{\mathrm{fl}}(\boldsymbol{v}_{\mathrm{sl}} - \boldsymbol{v}_1), \tag{2.9d}$$

$$\text{Fluid domain} \leftarrow \text{solid:} \qquad \boldsymbol{v}_1\cdot\boldsymbol{n} = \boldsymbol{v}_{\mathrm{sl}}\cdot\boldsymbol{n} + \frac{\mathrm{i}}{k_{\mathrm{s}}}\boldsymbol{\nabla}_{\parallel}\cdot(\boldsymbol{v}_{\mathrm{sl}} - \boldsymbol{v}_1)_{\parallel}. \tag{2.9e}$$

While the overall structure of these boundary conditions is the usual continuity in stress and velocity, the details of Eqs. (2.9d) and (2.9e) are not conventional. They are the boundary conditions for the surface stress $\boldsymbol{\sigma}\cdot\boldsymbol{n}$ of Eq. (2.4) and the acoustic velocity $\boldsymbol{v}_1$ of Eq. (2.2) (proportional to the gradient of the acoustic pressure p_1) derived by Bach and Bruus using their recent effective pressure-acoustics theory [15]. In this theory, the viscous boundary layer of thickness $\delta = \sqrt{2\eta_{\mathrm{fl}}/(\rho_{\mathrm{fl}}\omega)}$ (≈ 0.35 μm at 2.3 MHz) has been taken into account analytically. As a result, terms appear in Eqs. (2.9d) and (2.9e) that involve the shear-wave number $k_{\mathrm{s}} = (1+\mathrm{i})\,\delta^{-1}$ as well as the tangential divergence of the tangential component of the difference between the solid-wall velocity $\boldsymbol{v}_{\mathrm{sl}} = -\mathrm{i}\omega\boldsymbol{u}$ and the acoustic velocity $\boldsymbol{v}_1$ at the fluid-solid interface. This boundary condition also takes into account the large dissipation in the boundary layers, which leads to an effective damping coefficient $\Gamma_{\mathrm{fl}}^{\mathrm{eff}} \approx \frac{\delta}{H} \approx 0.002$, the ratio of the boundary layer width δ to the device height H [6, 13, 15]. Remarkably, this boundary-layer dissipation dominates dissipation in the fluid domain, because $\Gamma_{\mathrm{fl}} \ll \Gamma_{\mathrm{fl}}^{\mathrm{eff}} \ll 1$.

2.6. The acoustic streaming

The acoustic streaming is the time-averaged (over one oscillation period), steady fluid velocity $\boldsymbol{v}_2$ that is induced by the acosutic fields. In our recent analysis [15], we have shown that the governing equation of $\boldsymbol{v}_2$ corresponds to a steady-state, incompressible Stokes flow with a body force in the bulk due to the time-averaged acoustic dissipation proportional to Γ_{fl}. Further, at fluid-solid interfaces, the slip velocity $\boldsymbol{v}_2^{\mathrm{bc}}$ takes into account both the motion of the surrounding elastic solid and the Reynolds

stress induced in viscous boundary layer in the fluid,

$$\boldsymbol{\nabla}\cdot\boldsymbol{v}_2 = 0, \qquad \eta_{\mathrm{fl}}\nabla^2\boldsymbol{v}_2 = \boldsymbol{\nabla}p_2 - \frac{\Gamma_{\mathrm{fl}}\omega}{2c_{\mathrm{fl}}^2}\,\mathrm{Re}\big[p_1^*\boldsymbol{v}_1\big], \qquad \boldsymbol{v}_2 = \boldsymbol{v}_2^{\mathrm{bc}}, \ \text{ at fluid-solid interfaces,} \tag{2.10a}$$

$$\boldsymbol{n}\cdot\boldsymbol{v}_2^{\mathrm{bc}} = 0, \qquad (\mathbf{1}-\boldsymbol{n}\boldsymbol{n})\cdot\boldsymbol{v}_2^{\mathrm{bc}} = -\frac{1}{8\omega}\boldsymbol{\nabla}_{\parallel}\big|\boldsymbol{v}_{1\parallel}\big|^2 - \mathrm{Re}\left[\left(\frac{2-\mathrm{i}}{4\omega}\boldsymbol{\nabla}_{\parallel}\cdot\boldsymbol{v}_{1\parallel}^* + \frac{\mathrm{i}}{2\omega}\partial_{\perp}v_{1\perp}^*\right)\boldsymbol{v}_{1\parallel}\right]. \tag{2.10b}$$

Here, we have used a special case of the slip velocity $\boldsymbol{v}_2^{\mathrm{bc}}$, which is only valid near acoustic resonance, where the magnitude $|\boldsymbol{v}_1|$ of the acoustic velocity in the bulk is much larger than $\omega\,|\boldsymbol{u}_{\mathrm{sl}}^{\mathrm{bc}}|$ of the walls.

2.7. The acoustic radiation force and streaming drag force on suspended microparticles

The response of primary interest in acoustofluidic applications, is the acoustic radiation force $\boldsymbol{F}^{\mathrm{rad}}$ and the Stokes drag from the acoustic streaming $\boldsymbol{v}_2$ acting on suspended microparticles. In this work, we consider 1- and 5-μm-diameter spherical polystyrene "Styron 666" (ps) particles with density ρ_{ps} and compressibility κ_{ps}. For such large microparticle suspended in water of density ρ_{fl} and compressibility κ_{fl}, thermoviscous boundary layers can be neglected, and the monopole and dipole acoustic scattering coefficients f_0 and f_1 are real numbers given by [21],

$$f_0 = 1 - \frac{\kappa_{\mathrm{ps}}}{\kappa_{\mathrm{fl}}} = 0.468, \qquad f_1 = \frac{2(\rho_{\mathrm{ps}}-\rho_{\mathrm{fl}})}{2\rho_{\mathrm{ps}}+\rho_{\mathrm{fl}}} = 0.034. \tag{2.11a}$$

Given an acoustic pressure p_1 and velocity $\boldsymbol{v}_1$, a single suspended microparticle of radius a, experience an acoustic radiation force $\boldsymbol{F}^{\mathrm{rad}}$, which, since f_0 and f_1 are real, is given by the potential U^{rad} [22],

$$\boldsymbol{F}^{\mathrm{rad}} = -\boldsymbol{\nabla}U^{\mathrm{rad}}, \qquad \text{where} \qquad U^{\mathrm{rad}} = \frac{4\pi}{3}a^3\left(f_0\,\frac{1}{4}\kappa_{\mathrm{fl}}|p_1|^2 - f_1\,\frac{3}{8}\rho_{\mathrm{fl}}|\boldsymbol{v}_1|^2\right). \tag{2.11b}$$

The microparticle is also influenced by a Stokes drag force $\boldsymbol{F}^{\mathrm{drag}} = 6\pi\eta_{\mathrm{fl}}a(\boldsymbol{v}_2-\boldsymbol{v}_{\mathrm{ps}})$, where $\boldsymbol{v}_2$ and $\boldsymbol{v}_{\mathrm{ps}}$ is the streaming velocity and the polystyrene particle velocity at the particle position $\boldsymbol{r}_{\mathrm{ps}}(t)$, respectively. In the experiments, the streaming and particle velocities are smaller than $v_0 = 1$ mm/s, which for a 5-μm-diameter particle corresponds to a small particle-Reynolds number $\frac{1}{\rho_{\mathrm{fl}}}\eta_{\mathrm{fl}}av_0 = 0.6$. Consequently, we can ignore the inertial effects and express the particle velocity for a particle at position $\boldsymbol{r}$ from the force balance $\boldsymbol{F}^{\mathrm{rad}} + \boldsymbol{F}^{\mathrm{drag}} = \mathbf{0}$, between the acoustic radiation force and streaming drag force,

$$\boldsymbol{v}_{\mathrm{ps}}(\boldsymbol{r}) = \boldsymbol{v}_2(\boldsymbol{r}) + \frac{1}{6\pi\eta_{\mathrm{fl}}a}\,\boldsymbol{F}^{\mathrm{rad}}(\boldsymbol{r}). \tag{2.12}$$

The particle trajectory $\boldsymbol{r}_{\mathrm{ps}}(t)$ is then determined by straightforward time integration of $\frac{\mathrm{d}}{\mathrm{d}t}\boldsymbol{r}_{\mathrm{ps}} = \boldsymbol{v}_{\mathrm{ps}}(\boldsymbol{r}_{\mathrm{ps}})$.

2.8. Numerical implementation

Following the procedure described in Ref. [12], including mesh convergence tests, the coupled field equations (2.2) and (2.4) for the fluid pressure p_1 and elastic-solid displacement $\boldsymbol{u}$ are implemented directly in the finite-element-method software Comsol Multiphysics 5.3a [14] using the weak form interface "*PDE Weak Form*". A COMSOL script with a PDE-weak-form implementation

of acoustofluidics is available as supplemental material in Ref. [7]. Here, we extend the model of Ref. [12] by including the transducer with the piezoelectric stress-strain coupling Eq. (2.6) and implementing the governing equation (2.8) for the electric potential φ in weak form. Similarly, the boundary conditions Eq. (2.9) are implemented in weak form. Specifically, the effective-model boundary conditions are implemented as "*Weak Contributions*" as follows. The stress condition Eq. (2.9d) is given by the weak contribution

$$\begin{aligned} &\texttt{test(uX)} * (-\texttt{p1} * \texttt{nX} + \texttt{i} * \texttt{ks} * \texttt{etafl} * (\texttt{vslX} - \texttt{v1X})) \\ &+ \texttt{test(uY)} * (-\texttt{p1} * \texttt{nY} + \texttt{i} * \texttt{ks} * \texttt{etafl} * (\texttt{vslY} - \texttt{v1Y})) \\ &+ \texttt{test(uZ)} * (-\texttt{p1} * \texttt{nZ} + \texttt{i} * \texttt{ks} * \texttt{etafl} * (\texttt{vslZ} - \texttt{v1Z})), \end{aligned} \tag{2.13}$$

where $\boldsymbol{n} = (\texttt{nX}, \texttt{nY}, \texttt{nZ})$ is the normal vector away from the solid domain, and $\texttt{test(uX)}$ is the finite-element test function corresponding to the x-component u_x of the solid displacement field $\boldsymbol{u}$, and similar for y and z. The velocity condition Eq. (2.9e) is given by the weak contribution

$$\begin{aligned} &\texttt{i} * \texttt{omega} * \texttt{rhofl}/(1 - \texttt{i} * \texttt{Gammafl}) * \texttt{test(p1)} * (\texttt{vslX} * \texttt{nX} + \texttt{vslY} * \texttt{nY} + \texttt{vslZ} * \texttt{nZ} \\ &\quad + \texttt{i}/\texttt{ks} * (\texttt{dtang}(\texttt{vslX} - \texttt{v1X}, \texttt{x}) + \texttt{dtang}(\texttt{vslY} - \texttt{v1Y}, \texttt{y}) + \texttt{dtang}(\texttt{vslZ} - \texttt{v1Z}, \texttt{z})), \end{aligned} \tag{2.14}$$

where $\boldsymbol{n} = (\texttt{nX}, \texttt{nY}, \texttt{nZ})$ now is the normal vector away from the fluid, $\texttt{test(p1)}$ is the test function for p_1, and $\texttt{dtang}$ is the tangent-plane derivative operator available in COMSOL, see Ref. [15].

In a second step, we implement Eq. (2.10) for the acoustic streaming $\boldsymbol{v}_2$ in weak form. Specifically, the effective-model slip velocity condition are implemented as a "*Dirichlet Boundary Condition*" as follows. We use the outward normal vector $(\texttt{nX}, \texttt{nY}, \texttt{nZ})$ as before and also the two perpendicular tangent vectors $(\texttt{t1X}, \texttt{t1Y}, \texttt{t1Z})$ and $(\texttt{t2X}, \texttt{t2Y}, \texttt{t2Z})$, and write the x-component $\texttt{v2bcX}$ of $\boldsymbol{v}_2^{\text{bc}}$ as,

$$\texttt{v2bcX} = (\texttt{t1X} * \texttt{AX} + \texttt{t1Y} * \texttt{AY} + \texttt{t1Z} * \texttt{AZ}) * \texttt{t1X} + (\texttt{t2X} * \texttt{AX} + \texttt{t2Y} * \texttt{AY} + \texttt{t2Z} * \texttt{AZ}) * \texttt{t2X}, \tag{2.15}$$

and similarly for the y and z components. Here, $(\texttt{AX}, \texttt{AY}, \texttt{AZ})$ is a vector defined in terms of the tangent-plane derivative $\boldsymbol{\nabla}_{\parallel}$ and the parallel velocity $\boldsymbol{v}_{1\parallel} = (\texttt{v1parX}, \texttt{v1parY}, \texttt{v1parZ})$ with the x-component $\texttt{v1parX} = (\boldsymbol{v}_1 \cdot \boldsymbol{t}_1)\, t_{1x} + (\boldsymbol{v}_1 \cdot \boldsymbol{t}_2)\, t_{2x}$, as follows,

$$\texttt{AX} = -1/8/\texttt{omega} * (\texttt{dtang}(\texttt{S1}, \texttt{x}) + \texttt{realdot}((4 + 2 * \texttt{i})/4 * \texttt{S2} - 4 * \texttt{i} * \texttt{S3}, \texttt{v1parX}), \tag{2.16a}$$

$$\texttt{AY} = -1/8/\texttt{omega} * (\texttt{dtang}(\texttt{S1}, \texttt{y}) + \texttt{realdot}((4 + 2 * \texttt{i})/4 * \texttt{S2} - 4 * \texttt{i} * \texttt{S3}, \texttt{v1parY}), \tag{2.16b}$$

$$\texttt{AZ} = -1/8/\texttt{omega} * (\texttt{dtang}(\texttt{S1}, \texttt{z}) + \texttt{realdot}((4 + 2 * \texttt{i})/4 * \texttt{S2} - 4 * \texttt{i} * \texttt{S3}, \texttt{v1parZ}), \tag{2.16c}$$

$$\texttt{S1} = \texttt{abs(v1parX)\^{}2} + \texttt{abs(v1parY)\^{}2} + \texttt{abs(v1parZ)\^{}2}, \tag{2.16d}$$

$$\texttt{S2} = \texttt{dtang(v1parX, x)} + \texttt{dtang(v1parY, y)} + \texttt{dtang(v1parZ, z)}, \tag{2.16e}$$

$$\texttt{S3} = \texttt{i} * \texttt{omega/rhofl/cfl\^{}2} * \texttt{p1} - \texttt{S2}. \tag{2.16f}$$

Finally, the acoustic radiation force $\boldsymbol{F}^{\text{rad}}$ acting on the particles is calculated from Eq. (2.11) using the acoustic pressure p_1 and velocity $\boldsymbol{v}_1$, and subsequently in a third step, following Ref. [23], we compute the particle trajectories $\boldsymbol{r}_{\text{ps}}(t)$ from the time-integration of Eq. (2.12).

We optimize the mesh to obtain higher resolution in the water-filled cavity, where we need to calculate numerical derivatives of the resulting fields to compute the streaming and radiation forces, and less in the surrounding solids and in the transducer. We ensure having at least six nodal points per

wave length in all domains, which for the second-order test function we use, corresponds to maximum mesh sizes of 0.52 mm, 0.59 mm, 0.50 mm, and 0.22 mm in the domains of Pz26, silicon, Pyrex, and water, respectively. The final implementation of the model contains 1.1 and 0.4 million degrees of freedom for the first- and second-order fields, repsectively. On our workstation, a Dell Inc Precision T7500 Intel Xeon CPU X5690 at 3.47 GHz with 128 GB RAM and 2 CPU cores, the model requires 45 GB RAM and takes 18 min per frequency. When running frequency sweeps of up to 70 frequency values, we used the DTU high-performance computer cluster requiring 464 GB RAM and 11 min per frequency.

3. Results for the transducer-glass-silicon acoustofluidic device

We apply the 3D model of Section 2 to the transducer-glass-silicon acoustofluidic device by Hagsäter *et al.* [16], shown in Figure 1 and using the parameter values listed in Tables 1, 2, and 3. In Figure 2 we compare the experimental results from Ref. [16] with our model simulations.

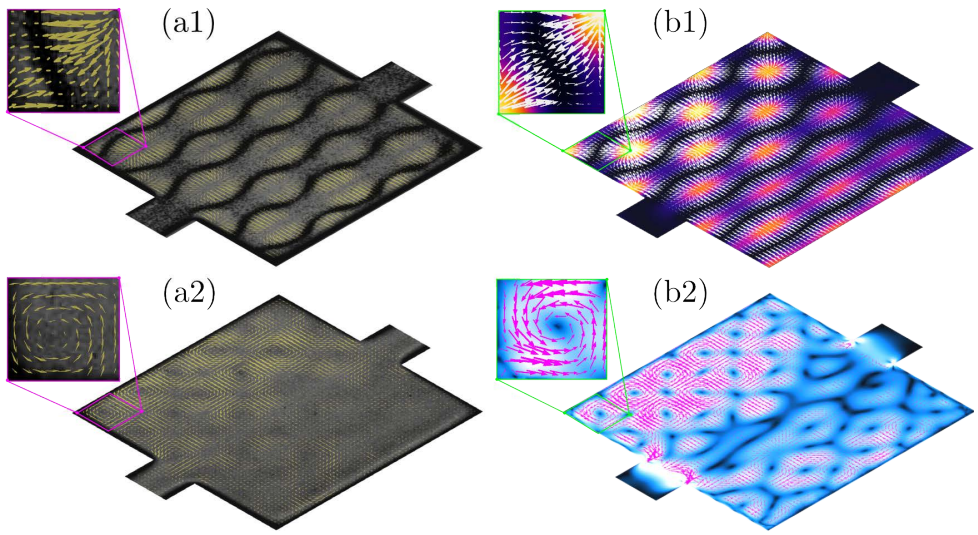

Figure 2. (a1) Micro-PIV measurements adapted from Ref. [16] of the particle velocity $\boldsymbol{v}_{\mathrm{ps}}$ after 1 ms (yellow arrows, maximum 200 μm/s) superimposed on a micrograph of the final positions (black curved bands) of 5-μm-diameter polystyrene particles in water with a standing ultrasound wave at 2.17 MHz. (a2) Same as panel (a1), but for 1-μm-diameter polystyrene particles moving in a 6-by-6 flow-roll pattern without specific final positions. (b1) Numerical 3D COMSOL modeling with actuation voltage $\varphi_0 = 1$ V of the acoustic potential U^{rad} from 0 fJ (black) to 7 fJ (orange) and the velocity (yellow arrows, maximum 170 μm/s) after 1 ms of 5-μm-diameter polystyrene particles in the horizontal center plane of the water-filled cavity at the resonance $f = 2.166$ MHz. (b2) Numerical modeling at the same conditions as in panel (b1), but at the slightly lower frequency 2.163 MHz, of the particle velocity $\boldsymbol{v}_{\mathrm{ps}}$ (magenta vectors) and its magnitude v_{ps} from 0 (black) to 200 μm/s (white) of 1-μm-diameter polystyrene particles.

In Figure 2(a1) we show the measured micro-particle image velocimetry (micro-PIV) results obtained on a large number of 5-μm-diameter tracer particles at an excitation frequency of 2.17 MHz. The yellow arrows indicate the velocity of the tracer particles 1 ms after the ultrasound has been turned on, and the black bands are the tracer particles focused at the minimum of the acoustic potential $U^{\rm rad}$ after a couple of seconds of ultrasound actuation. A clear pattern of 3 wavelengths in each direction is observed. Similarly, in Figure 2(a2) is shown the micro-PIV results for the smaller 1-μm-diameter tracer particles. It is seen that these particles, in contrast to the larger particles, are not focused but keep moving in a 6-by-6 flow-roll pattern. This result from Ref. [16] is remarkable, as the conventional Rayleigh streaming pattern [6, 7, 23] has four streaming rolls per wavelength oriented in the vertical plane, but here is only seen two rolls per wavelength, and they are oriented in the horizontal plane.

In Figure 2(b1) and (b2) we see that our model predicts the observed acoustofluidics response qualitatively for both the larger and the smaller tracer particles at a resonance frequency slightly below 2.17 MHz. Even the uneven local amplitudes of the particle velocity $\boldsymbol{v}_{\rm ps}$ in the 6-by-6 flow-roll pattern, which shifts around as the frequency is changed a few kHz, is in accordance with the observations. In Ref. [16] it is mentioned that "*If the frequency is shifted slightly in the vicinity of 2.17 MHz, the same vortex pattern will still be visible, but the strength distribution between the vortices will be altered.*". We have chosen the 3-kHz lower frequency in Figure 2(b2) compared to (b1) to obtain a streaming pattern similar to the observed one for the small 5-μm-diameter particles.

Quantitatively, we find the following. The acoustic resonance is located at 2.166 MHz, only 0.2 % lower than the experimental value of 2.17 MHz. This good agreement should not be over emphasized, as we had to assume a certain length and width of the Pz26 transducer, because its actual size was not reported in Ref. [16]. Another source of error is that we have not modeled the coupling gel used in the experiment between the Pz26 transducer and the silicon base. The actual actuation voltage in the experiment has not been reported, so we have chosen $\varphi_0 = 1$ V, well within the range of the 20 V peak-to-peak function generator mentioned in Ref. [16], as it results in velocities $v_{\rm ps} \approx 170$ μm/s for the large 5-μm-diameter, in agreement with the 200 μm/s reported in the experiment.

In Figure 3 we show another result that is in agreement with the experimental observations, namely the particle trajectories $\boldsymbol{r}_{\rm ps}(t)$ for suspensions of tracer particles of different size. The larger 5-μm-diameter particles are focused along the bottom of the troughs in the acoustic potential $U^{\rm rad}$, shown in Figure 2(b1), after a short time $\frac{1}{12}(2\text{ mm})/(170\ \mu\text{m/s}) \approx 1$ s, forming the red wavy bands in Figure 3(a) very similar to the observed black bands in Figure 2(a1). In contrast, the smaller 1-μm-diameter particles are caught by the 6-by-6 streaming vortex pattern and swirl around without being focused, at least within the first 1.5 s as shown in Figure 3(b), in full agreement with the experimental observation shown in Figure 2(a2).

4. Discussion

Our full 3D numerical model, which takes into account the piezo-electric transducer, the silicon base with the water-filled cavity, the viscous boundary layers in the water, and the Pyrex lid, has been tested qualitatively and quantitatively by comparing the results for the acoustic radiation force, for the streaming velocity, and for the trajectories of tracer particles of two different sizes with the decade-old experimental results presented by Hagsäter *et al.* [16]. Remarkably, as predicted by Bach

and Bruus [15], we find that the characteristic horizontal 6-by-6 flow-roll pattern of the small 1-μm-diameter particles is caused by the so-called Eckart bulk force, the term in (2.10a) proportional to the acoustic energy flux density or intensity $\boldsymbol{S}_{\mathrm{ac}} = \frac{1}{2}\mathrm{Re}[p_1^* \boldsymbol{v}_1]$. In our simulations this pattern occupies 80 % of the cavity volume stretching from 0.1 to 0.9 in units of the channel height H_{ca} and looks as the one in the midplane at 0.5 H_{ca} shown in Figs. 2(b2) and 3(b). Lei *et al.* [10] also pointed out that $\boldsymbol{S}_{\mathrm{ac}}$ could lead to the horizontal 6-by-6 flow-roll pattern in their 3D-fluid-domain model with hard-wall and outgoing-plane-wave boundary conditions of the same device. In their model, the Eckart bulk force was neglected, and the horizontal-flow-roll producing term $\boldsymbol{S}_{\mathrm{ac}}$ appears only as part of their limiting-velocity boundary condition. As the remaining curl-free part of the boundary condition is dominating, they found the horizontal 6-by-6 flow-roll pattern to be confined to narrow regions around the two horizontal planes at 0.2 and 0.8 H_{ca} and absent in the center plane at 0.5 H_{ca}, the focal plane in the experimental studies. As our slip-velocity condition (2.10b) also contains $\boldsymbol{S}_{\mathrm{ac}}$, see Eq. (62a) in Ref. [15], we do reproduce their findings, when we suppress the Eckart bulk force in Eq. (2.10b). This is illustrated in Figure 3(c), where we show that the flow-roll behavior is suppressed in the center plane and replaced by a clear divergent behavior.

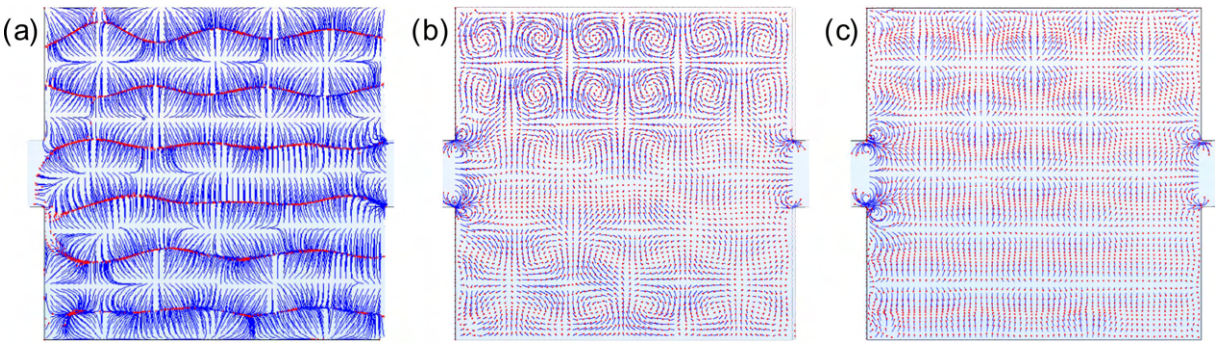

Figure 3. Numerical 3D COMSOL modeling of the trajectories $\boldsymbol{r}_{\mathrm{ps}}(t)$ (blue tracks) of 3600 polystyrene particles of radius a corresponding to the cases shown in Figure 2(b1) and (b2). The particles start from 60×60 regular quadratic grid points in the horizontal center plane of the cavity at $t = 0$ s when the ultrasound field is turned on, and their positions after 1.5 s are represented by red points. (a) $a = 2.5$ μm at $f = 2.166$ MHz. (b) $a = 0.5$ μm at $f = 2.163$ MHz with the Eckart bulk force in Eq. (2.10a) increased by a factor 4. (c) Same as panel (b) but without the Eckart bulk force in Eq. (2.10a).

In agreement with Lei *et al.* [10], we find that although the determination of the first-order pressure p_1 and the acoustic potential U^{rad} is fairly robust, the computation of the streaming velocity $\boldsymbol{v}_2$ from the Stokes equation (2.10a) is sensitive to the exact value of the frequency and of the detailed shape of the fluid solid interface. In Ref. [24] we have shown in a simplified 3D-rectangular-fluid-domain model that the rotation of the acoustic intensity changes an order of magnitude when the aspect ratio $L_{\mathrm{ca}}/W_{\mathrm{ca}}$ changes 1 %. In this study we have increased the Eckart bulk force in Eq. (2.10a) by a factor of 4 in order to make the rotating 6x6 pattern dominate clearly over the Rayleigh streaming in the center plane. This amplification may reflect that the chosen aspect ratio $L_{\mathrm{ca}}/W_{\mathrm{ca}} = 1.01$ was not

exactly the one realized in the experiment, an effect which should be studied further in experiments and simulations.

Our numerical study indicate that although the cavity in the Hagsäter device has a size of only three acoustic wavelengths, the existence of in-plane flow rolls may be controlled by the Eckart bulk force. This conclusion runs contrary to the conventional wisdom that the Eckart bulk force is only important in systems of a size, which greatly exceeds the acoustic wave length. This phenomenon deserves a much closer study in future work.

While our model takes many of the central aspects of acoustofluidics into account, it can still be improved. One possible improvement would be to include the influence of heating on the material parameters as in Ref. [6]. One big challenge in this respect is to determine the material parameters of the solids, which may be temperature and frequency dependent. Another difficult task is to model the coupling between the transducer and the chip, which in experiments typically are coupled using coupling gels or other ill-characterized adhesives. The last point we would like to raise is use of the simple Stokes drag law on the suspended particles in the cavity. Clearly, this model may be improved by including particle-wall effects and particle-particle interactions. However, as direct simulations of both of these effects are very memory consuming their implementation would require effective models.

5. Conclusion

We have described the implementation of a full 3D modeling of an acoustofluidic device taking into account the viscous boundary layers and acoustic streaming in the fluid, the vibrations of the solid material, and the piezoelectricity in the transducer. As such, our simulation is in many ways close to a realistic device, which is also reflected in the agreement between the simulation and the experiment shown in Figs. 2 and 3. Our model has correctly predicted the unusual streaming pattern observed in the device at the 2.17-Mz resonance: a horizontal 6-by-6 flow-roll pattern in 80 % of the cavity volume, a pattern much different form the conventional 12-by-2 Rayleigh streaming pattern in the vertical plane. Moreover, our model has revealed the surprising importance of the Eckart bulk force in an acoustic cavity with a size comparable to the acoustic wavelength. In future work, we must analyze the sensitivity of the streaming velocity and improve our understanding of the amplitude of the Eckart bulk force.

By introducing the model, we have demonstrated that simulations can be used to obtain detailed information about the performance of an acoustofluidic device in 3D. Such simulations are likely to be useful for studies of the basic physics of acoustofluidics as well as for engineering purposes, such as improving existing microscale acoustofluidic devices. However, To fully exploit such modeling, more accurate determination is needed of the acoustic parameters of the actual transducers, elastic walls, and particle suspensions employed in a given experiment.

Acknowledgments

H. Bruus was supported by the *BioWings* project funded by the European Union's Horizon 2020 *Future and Emerging Technologies* (FET) programme, grant No. 801267.

Conflict of interest

All authors declare no conflicts of interest in this paper.

References

1. A. Lenshof, C. Magnusson and T. Laurell, *Acoustofluidics 8: Applications in acoustophoresis in continuous flow microsystems*, Lab Chip, **12** (2012), 1210–1223.
2. M. Gedge and M. Hill, *Acoustofluidics 17: Surface acoustic wave devices for particle manipulation*, Lab Chip, **12** (2012), 2998–3007.
3. E. K. Sackmann, A. L. Fulton and D. J. Beebe, *The present and future role of microfluidics in biomedical research*, Nature, **507** (2014), 181–189.
4. T. Laurell and A. Lenshof, *Microscale Acoustofluidics*, Cambridge: Royal Society of Chemistry, 2015.
5. M. Antfolk and T. Laurell, *Continuous flow microfluidic separation and processing of rare cells and bioparticles found in blood - a review*, Anal. Chim. Acta, **965** (2017), 9–35.
6. P. B. Muller and H. Bruus, *Numerical study of thermoviscous effects in ultrasound-induced acoustic streaming in microchannels*, Phys. Rev. E, **90** (2014), 043016.
7. P. B. Muller and H. Bruus, *Theoretical study of time-dependent, ultrasound-induced acoustic streaming in microchannels*, Phys. Rev. E, **92** (2015), 063018.
8. N. Nama, R. Barnkob, Z. Mao, et al. *Numerical study of acoustophoretic motion of particles in a PDMS microchannel driven by surface acoustic waves*, Lab Chip, **15** (2015), 2700–2709.
9. J. Lei, P. Glynne-Jones and M. Hill, *Acoustic streaming in the transducer plane in ultrasonic particle manipulation devices*, Lab Chip, **13** (2013), 2133–2143.
10. J. Lei, P. Glynne-Jones and M. Hill, *Numerical simulation of 3D boundary-driven acoustic streaming in microfluidic devices*, Lab Chip, **3** (2014), 532–541.
11. I. Gralinski, S. Raymond, T. Alan, et al. *Continuous flow ultrasonic particle trapping in a glass capillary*, J. Appl. Phys., **115** (2014), 054505.
12. M. W. H. Ley and H. Bruus, *Three-dimensional numerical modeling of acoustic trapping in glass capillaries*, Phys. Rev. Appl., **8** (2017), 024020.
13. P. Hahn and J. Dual, *A numerically efficient damping model for acoustic resonances in microfluidic cavities*, Phys. Fluids, **27** (2015), 062005.
14. COMSOL Multiphysics 53a, 2017. Available from: `www.comsol.com`.
15. J. S. Bach and H. Bruus, *Theory of pressure acoustics with viscous boundary layers and streaming in curved elastic cavities*, J. Acoust. Soc. Am., **144** (2018), 766–784.
16. S. M. Hagsäter, T. G. Jensen, H. Bruus, et al. *Acoustic resonances in microfluidic chips: full-image micro-PIV experiments and numerical simulations*, Lab Chip, **7** (2007), 1336–1344.
17. CORNING, *Glass Silicon Constraint Substrates*, Houghton Park C-8, Corning, NY 14831, USA, accessed 23 October 2018. Available from: http://www.valleydesign.com/Datasheets/Corning Pyrex 7740.pdf.

18. M. A. Hopcroft, W. D. Nix and T. W. Kenny, *What is the Young's modulus of silicon*, IEEEASME Journal of Microelectromechanical Systems, **19** (2010), 229–238.

19. J. Dual and D. Möller, *Acoustofluidics 4: Piezoelectricity and Application to the Excitation of Acoustic Fields for Ultrasonic Particle Manipulation*, Lab Chip, **12** (2012), 506–514.

20. Meggit A/S, *Ferroperm Matdat 2017*, Porthusvej 4, DK-3490 Kvistgaard, Denmark, accessed 23 October 2018. Available from: `https://www.meggittferroperm.com/materials/`.

21. J. T. Karlsen and H. Bruus, *Forces acting on a small particle in an acoustical field in a thermoviscous fluid*, Phys. Rev. E, **92** (2015), 043010.

22. M. Settnes and H. Bruus, *Forces acting on a small particle in an acoustical field in a viscous fluid*, Phys. Rev. E, **85** (2012), 016327.

23. P. B. Muller, R. Barnkob, M. J. H. Jensen, et al. *A numerical study of microparticle acoustophoresis driven by acoustic radiation forces and streaming-induced drag forces*, Lab Chip, **12** (2012), 4617–4627.

24. J. S. Bach and H. Bruus, *Different origins of acoustic streaming at resonance*, Proceedings of Meeting on Acoustics 21ISNA, **34** (2018), 022005.

AIMS Press

7.3 Paper III: Phys. Rev. E 100, 023104 1-20 (2019)

Bulk-driven acoustic streaming at resonance in closed microcavities

DOI: 10.1103/PhysRevE.100.023104

Authors: J. S. Bach and H. Bruus.
Journal: Phys. Rev. E **100**, 023104 (2019)

Bulk-driven acoustic streaming at resonance in closed microcavities

Jacob S. Bach* and Henrik Bruus†

Department of Physics, Technical University of Denmark, DTU Physics Building 309, DK-2800 Kongens Lyngby, Denmark

(Received 22 May 2019; published 7 August 2019)

Bulk-driven acoustic (Eckart) streaming is the steady flow resulting from the time-averaged acoustic energy flux density in the bulk of a viscous fluid. In simple cases, like the one-dimensional single standing-wave resonance, this energy flux is negligible, and therefore the bulk-driven streaming is often ignored relative to the boundary-driven (Rayleigh) streaming in the analysis of resonating acoustofluidic devices with length scales comparable to the acoustic wavelength. However, in closed acoustic microcavities with viscous dissipation, two overlapping resonances may be excited at the same frequency as a double mode. In contrast to single modes, the double modes can support a steady rotating acoustic energy flux density and thus a corresponding rotating bulk-driven acoustic streaming. We derive analytical solutions for the double modes in a rectangular-box-shaped cavity including the viscous boundary layers, and use them to map out possible rotating patterns of bulk-driven acoustic streaming. Remarkably, the rotating bulk-driven streaming may be excited by a nonrotating actuation, and we determine the optimal geometry that maximizes this excitation. In the optimal geometry, we finally simulate a horizontal 2×2, 4×4, and 6×6 streaming-roll pattern in a shallow square cavity. We find that the high-frequency 6×6 streaming-roll pattern is dominated by the bulk-driven streaming as opposed to the low-frequency 2×2 streaming pattern, which is dominated by the boundary-driven streaming.

DOI: 10.1103/PhysRevE.100.023104

I. INTRODUCTION

Acoustophoresis, particle migration by ultrasound in a microfluidic setting, is an increasingly popular method for noncontact and label-free handling of microparticles suspended in a fluid. Examples include acoustic separation [1–3], trapping [4,5], and tweezing [6–8], as well as enrichment of cancer cells [9,10] and bacteria [11,12], and size-independent sorting of cells [13].

The acoustic field induces the acoustic radiation force that acts on suspended particles and scales with the particle volume [14–18], as well as the acoustic streaming in the fluid [19–22] that gives rise to a viscous Stokes drag force on the particles which scales with the linear size of the particles [23]. Consequently, the streaming-induced drag force is the dominating acoustic force for particles smaller than a critical size. For example, for an aqueous suspension of spherical polystyrene particles in a 1-MHz ultrasound field, the critical radius has been determined to be around 2 μm [24,25]. To extend the application of acoustophoresis into the regime of submicrometer particles, such as bacteria, viruses, and exosomes, a deep understanding of acoustic streaming is therefore important.

The first theoretical analysis of acoustic streaming dates back to Lord Rayleigh [19], who investigated the streaming generated by the viscous boundary layers close to the walls in planar and cylindrical systems. This analysis was later generalized by Nyborg [22], who formulated a slip velocity condition for the acoustic streaming outside the viscous boundary layers at weakly curved boundaries oscillating in the normal direction. Further extensions to this slip-velocity theory involve curvilinear corrections for curved boundary [26], general motion of a flat boundary [27], and general motion of a curved boundary [28]. This kind of streaming is caused by the velocity mismatch between the boundary and the acoustic wave in the bulk, and we refer to it as boundary-driven acoustic streaming.

Acoustic streaming can also be generated by attenuation of the acoustic wave in the bulk as shown by Eckart [29], who established the basic theory and investigated the steady flow caused by a sound beam. This kind of streaming is generated by a force, which is proportional to the acoustic energy flux density (or intensity) such that, say, a sound beam generates acoustic streaming in its direction of propagation. We refer to this kind of streaming as bulk-driven acoustic streaming.

While bulk-driven streaming is known to have a clear effect in systems much larger than the acoustic wavelength [30], it is often neglected in studies of resonating devices with length scales comparable with the acoustic wavelength. However, the bulk-driven streaming was taken into account implicitly by Antfolk *et al.* in their study of a long straight microchannel with a nearly square cross section [11], as they made a direct numerical simulation of the acoustofluidic properties of the system. They showed numerically that the experimentally observed single-vortex streaming pattern, which remarkably appeared in their microchannel instead of the usual quadrupolar Rayleigh-vortex pattern, could be explained if two orthogonal acoustic resonances with nearly identical resonance frequencies were excited with a quarter-period phase difference at the same frequency.

Such orthogonal phase-shifted acoustic waves have been used in other experiments to generate an acoustic radiation

*jasoba@fysik.dtu.dk
†bruus@fysik.dtu.dk

torque acting on suspended particles [26,31–35]. Also traveling Bessel beams [36,37] as well as arrays of holographic acoustic elements [38] have been used for this purpose, but not for generating specific streaming patterns.

Inspired by the work of Antfolk *et al.* [11], we study in this paper bulk-driven acoustic streaming at resonance in rectangular-box-shaped cavities with acoustically hard walls and side lengths comparable to the acoustic wavelength. The paper is organized as follows: In Sec. II we present the governing equations for the acoustic pressure and the acoustic streaming at resonance, where the viscous boundary layers are taken into account using our recent boundary-layer analysis [28]. We apply these equations in Sec. III to derive analytical solutions for the acoustic single-mode pressure resonances in the rectangular cavity. We also introduce the so-called double-mode resonances, where two overlapping single modes are excited simultaneously at the same frequency. In Sec. IV we establish the so-called overlap and phase conditions for double-mode resonances that lead to a strong acoustic body force, which causes the bulk-driven streaming. A main result is presented in Sec. V, where we show how a weak symmetry breaking of a perfect square cavity can lead to a rotating body force even for a nonrotating actuation. We validate our theory in Sec. VI by direct numerical simulation in the case of a shallow nearly square cavity similar to the geometry studied experimentally by Hagsäter *et al.* [39]. We predict that the bulk-driven streaming in closed microcavities is enhanced by increasing the frequency and the bulk viscosity, just as is the case for Eckart streaming in open systems [29]. We propose to test this prediction by replacing water with pyridine in the microcavity. Finally, we discuss our results in Sec. VII and present our conclusions in Sec. VIII.

II. GOVERNING EQUATIONS

The time-harmonic acoustic fields in the fluid domain Ω are induced by the time-harmonic displacement field $\boldsymbol{u}(\boldsymbol{r},t)$ of the wall at the boundary $\partial\Omega$ of the domain,

$$\boldsymbol{u}(\boldsymbol{r},t) = \mathrm{Re}[\boldsymbol{u}_1(\boldsymbol{r})e^{-i\omega t}], \quad \boldsymbol{r}\in\partial\Omega, \tag{1}$$

where $\boldsymbol{r}$ is position, t is time, $\omega = 2\pi f$ is the angular frequency corresponding to the driving frequency f, and "Re" is the real part of complex-valued fields. In the quiescent and homogeneous fluid of mass density ρ_fl and ambient pressure p_fl, we apply standard perturbation theory in the small Mach number $\mathrm{Ma} = \frac{v_1}{c_\mathrm{fl}} \sim \frac{\rho_1}{\rho_\mathrm{fl}} \ll 1$ (see, e.g., Ref. [18]) to describe the fluid velocity $\boldsymbol{v}(\boldsymbol{r},t)$, pressure $p(\boldsymbol{r},t)$, and mass density $\rho(\boldsymbol{r},t)$:

$$p(\boldsymbol{r},t) = p_\mathrm{fl} + \mathrm{Re}[p_1(\boldsymbol{r})e^{-i\omega t}] + p_2(\boldsymbol{r}), \tag{2a}$$

$$\boldsymbol{v}(\boldsymbol{r},t) = \boldsymbol{0} \ + \mathrm{Re}[\boldsymbol{v}_1(\boldsymbol{r})e^{-i\omega t}] + \boldsymbol{v}_2(\boldsymbol{r}), \tag{2b}$$

$$\rho(\boldsymbol{r},t) = \rho_\mathrm{fl} + \mathrm{Re}[\rho_1(\boldsymbol{r})e^{-i\omega t}] + \rho_2(\boldsymbol{r}). \tag{2c}$$

Here, subscript "1" denotes the first-order, complex-valued, time-harmonic acoustic fields $\propto\mathrm{Ma}^1$, and subscript "2" the second-order, real-valued, time-averaged steady fields $\propto\mathrm{Ma}^2$. We do not compute the oscillating second-order fields containing $e^{\pm i2\omega t}$ as these have zero time average. In contrast, we do compute the oscillating first-order fields because products of these appear as source terms for the time-averaged second-order fields. In Eq. (2), real-valued, physical first-order fields $\tilde{A}_1(\boldsymbol{r},t)$ are written in terms of their complex-valued amplitude $A_1(\boldsymbol{r})$ as $\tilde{A}_1(\boldsymbol{r},t) = \mathrm{Re}[A_1(\boldsymbol{r})e^{-i\omega t}]$. The time average of a product of two real-valued, physical first-order fields $\tilde{A}_1(\boldsymbol{r},t)$ and $\tilde{B}_1(\boldsymbol{r},t)$ is then given in terms of the complex-valued amplitudes $A_1(\boldsymbol{r})$ and $B_1(\boldsymbol{r})$ as $\langle\tilde{A}_1(\boldsymbol{r},t)\tilde{B}_1(\boldsymbol{r},t)\rangle = \frac{1}{2}\,\mathrm{Re}\,[A_1(\boldsymbol{r})B_1^*(\boldsymbol{r})]$.

A. Pressure acoustics with boundary layers

The complex-valued acoustic pressure $p_1(\boldsymbol{r})$ satisfies a Helmholtz equation with a complex-valued compressional wave number k_c having the real part $k_0 = \frac{\omega}{c_\mathrm{fl}}$. We apply the effective boundary condition for $p_1(\boldsymbol{r})$ recently derived by Bach and Bruus [28], which takes the viscous boundary layer into account at the domain boundary $\partial\Omega$. We introduce the *inward* normal derivative $\partial_\perp = -\boldsymbol{n}\cdot\nabla$, $\boldsymbol{n}$ being the outward-pointing surface normal vector, and the effective *inward* normal displacement $U_{1\perp}(\boldsymbol{r})$ of the wall in terms of the actual displacement $\boldsymbol{u}_1(\boldsymbol{r})$:

$$\nabla^2 p_1 + k_\mathrm{c}^2 p_1 = 0, \quad k_\mathrm{c} = \left(1 + i\frac{\Gamma_\mathrm{fl}}{2}\right)k_0, \quad \boldsymbol{r}\in\Omega, \tag{3a}$$

$$\partial_\perp p_1 + \frac{i}{k_\mathrm{s}}\left(k_\mathrm{c}^2 p_1 + \partial_\perp^2 p_1\right) = \frac{k_0^2 U_{1\perp}(\boldsymbol{r})}{\kappa_\mathrm{fl}}, \quad \boldsymbol{r}\in\partial\Omega, \tag{3b}$$

$$U_{1\perp}(\boldsymbol{r}) = \frac{1}{1 - i\Gamma_\mathrm{fl}}\left(-\boldsymbol{n} - \frac{i}{k_\mathrm{s}}\nabla\right)\cdot\boldsymbol{u}_1, \quad \boldsymbol{r}\in\partial\Omega. \tag{3c}$$

Here, $i = \sqrt{-1}$, Γ_fl is the weak bulk damping coefficient, and k_s is the viscous boundary layer wave number, given in terms of the viscous boundary-layer width δ, the dynamic viscosity η_fl, the bulk viscosity $\eta_\mathrm{fl}^\mathrm{b}$, and the isentropic compressibility $\kappa_\mathrm{fl} = \frac{1}{\rho_\mathrm{fl}}(\frac{\partial\rho}{\partial p})_S = \frac{1}{\rho_\mathrm{fl}c_\mathrm{fl}^2}$ of the fluid,

$$\Gamma_\mathrm{fl} = \left(\frac{4}{3} + \frac{\eta_\mathrm{fl}^\mathrm{b}}{\eta_\mathrm{fl}}\right)\eta_\mathrm{fl}\kappa_\mathrm{fl}\omega \ll 1, \quad k_\mathrm{s} = \frac{1+i}{\delta}, \quad \delta = \sqrt{\frac{2\eta_\mathrm{fl}}{\rho_\mathrm{fl}\omega}}. \tag{4}$$

Equation (3) for the acoustic pressure p_1 is valid for boundary-layer widths δ much smaller than both the acoustic length scale k_0^{-1} and the geometry length cavity L_geom, a condition which is usually satisfied.

From the acoustic pressure p_1 we directly obtain the irrotational acoustic velocity $\boldsymbol{v}_1$ and the acoustic mass density ρ_1 in Eq. (2) through the relations [28]

$$\boldsymbol{v}_1 = -\frac{i(1 - i\Gamma_\mathrm{fl})}{\omega\rho_\mathrm{fl}}\nabla p_1, \quad \nabla\times\boldsymbol{v}_1 = \boldsymbol{0}, \tag{5a}$$

$$\rho_1 = \rho_\mathrm{fl}\kappa_\mathrm{fl}p_1. \tag{5b}$$

Further, we define the following relevant time-averaged first-order products: the acoustic energy density E_ac, kinetic energy density E_kin, potential energy density E_pot, energy flux density vector $\boldsymbol{S}_\mathrm{ac}$, as well as the time-averaged acoustic angular

momentum density $\boldsymbol{\mathcal{L}}_{\rm ac}$ with respect to the unperturbed fluid position $\boldsymbol{r}$,[1]

$$E_{\rm ac} = E_{\rm kin} + E_{\rm pot}, \qquad E_{\rm kin} = \tfrac{1}{4}\rho_{\rm fl}|\boldsymbol{v}_1|^2, \tag{6a}$$

$$\boldsymbol{S}_{\rm ac} = \langle \tilde{p}_1 \tilde{\boldsymbol{v}}_1 \rangle, \qquad E_{\rm pot} = \tfrac{1}{4}\kappa_{\rm fl}|p_1|^2, \tag{6b}$$

$$\boldsymbol{\mathcal{L}}_{\rm ac} = \langle \tilde{\boldsymbol{d}}_1 \times (\rho_{\rm fl}\tilde{\boldsymbol{v}}_1)\rangle, \quad \boldsymbol{d}_1(\boldsymbol{r}) = \frac{i}{\omega}\boldsymbol{v}_1(\boldsymbol{r}). \tag{6c}$$

Here, $\boldsymbol{d}_1(\boldsymbol{r})$ is the fluid displacement at position $\boldsymbol{r}$.

B. Acoustic streaming at fluid resonance

Outside the narrow viscous boundary layers of width $\delta \lesssim$ 500 nm (for water at MHz frequencies), the second-order acoustic streaming velocity $\boldsymbol{v}_2$ is described as a Stokes flow driven by the acoustic body force $\boldsymbol{f}_{\rm ac}$ in the domain Ω [see Eq. (8) in Ref. [40] and Eq. (52b) in Ref. [28]], and by the slip velocity $\boldsymbol{v}_2^{\rm slip}$ at the domain boundary $\partial\Omega$ [see Eq. (A19) in Ref. [28]]:

$$0 = \nabla\cdot\boldsymbol{v}_2, \quad \boldsymbol{r}\in\Omega, \tag{7a}$$

$$\boldsymbol{0} = -\nabla p_2 + \eta_{\rm fl}\nabla^2\boldsymbol{v}_2 + \boldsymbol{f}_{\rm ac}, \quad \boldsymbol{r}\in\Omega, \tag{7b}$$

$$\boldsymbol{v}_2 = \boldsymbol{v}_2^{\rm slip}, \quad \boldsymbol{r}\in\partial\Omega. \tag{7c}$$

Here, $\boldsymbol{f}_{\rm ac}$ in Ω and $\boldsymbol{v}_2^{\rm slip}$ at $\partial\Omega$, are given by

$$\boldsymbol{f}_{\rm ac} = \frac{\Gamma_{\rm fl}\omega}{c_{\rm fl}^2}\boldsymbol{S}_{\rm ac}, \tag{7d}$$

$$\boldsymbol{v}_2^{\rm slip} = \frac{1}{2}\kappa_{\rm fl}\boldsymbol{S}_{\rm ac} - \frac{1}{2\rho_{\rm fl}\omega}\nabla_\parallel[E_{\rm kin} - 2E_{\rm pot}] + \frac{3}{4\omega}{\rm Re}[i\partial_\perp v_{1\perp}\boldsymbol{v}_{1\parallel}^*], \tag{7e}$$

where we have used the expression for the slip velocity $\boldsymbol{v}_2^{\rm slip}$ valid near a fluid resonance, in which case the magnitude $|\boldsymbol{v}_1|$ of the acoustic velocity $\boldsymbol{v}_1$ in the bulk is much larger than that of the wall velocity $|\omega\boldsymbol{u}_1| \ll |\boldsymbol{v}_1|$ [see Eq. (55) in Ref. [28] for the slip velocity including the wall motion and Stokes drift]. We use the name *bulk-driven acoustic streaming* for the streaming driven by the acoustic body force $\boldsymbol{f}_{\rm ac}$ in Eq. (7d), and the name *boundary-driven streaming* for the streaming driven by the slip velocity $\boldsymbol{v}_2^{\rm slip}$ in Eq. (7e). Note that $\boldsymbol{f}_{\rm ac}$ increases with the frequency squared, as $\Gamma_{\rm fl}\propto\omega$, whereas $\boldsymbol{v}_2^{\rm slip}$ is independent of the frequency, as $\nabla_\parallel, \partial_\perp \sim k_0 = \frac{1}{c_{\rm fl}}\omega$.

One central quantity in the governing equations (7) for the acoustic streaming is the acoustic energy flux density $\boldsymbol{S}_{\rm ac}$, which enters both in the body force $\boldsymbol{f}_{\rm ac}$ [Eq. (7d)] and in the slip velocity $\boldsymbol{v}_2^{\rm slip}$ [Eq. (7e)]. This quantity is rotating (has a nonzero curl) if the acoustic fields are rotating, as seen by taking the curl of $\boldsymbol{S}_{\rm ac} = \langle\tilde{p}_1\tilde{\boldsymbol{v}}_1\rangle$ and using Eq. (5a) with $\nabla p_1 \approx i\omega\rho_{\rm fl}\boldsymbol{v}_1$ and $\nabla\times\boldsymbol{v}_1 = \boldsymbol{0}$,

$$\nabla\times\boldsymbol{S}_{\rm ac} = \omega^2\boldsymbol{\mathcal{L}}_{\rm ac}, \tag{8a}$$

where $\boldsymbol{\mathcal{L}}_{\rm ac}$ is the time-averaged acoustic angular momentum density defined in Eq. (6c). Using Stokes theorem for any closed loop shows that the energy flux density $\boldsymbol{S}_{\rm ac}$, and therefore the body force $\boldsymbol{f}_{\rm ac}$, points in a direction which rotates around areas with high acoustic angular momentum density

$$\oint \boldsymbol{f}_{\rm ac}\cdot d\boldsymbol{l} = \frac{\Gamma_{\rm fl}\omega}{c_{\rm fl}^2}\oint \boldsymbol{S}_{\rm ac}\cdot d\boldsymbol{l} = \frac{\Gamma_{\rm fl}\omega^3}{c_{\rm fl}^2}\int \boldsymbol{\mathcal{L}}_{\rm ac}\cdot\boldsymbol{n}\,dA. \tag{8b}$$

Hence, bulk-driven streaming is a consequence of acoustic fields with a nonzero acoustic angular momentum density $\boldsymbol{\mathcal{L}}_{\rm ac}$ defined in Eq. (6c). We refer to acoustic fields with nonzero $\boldsymbol{\mathcal{L}}_{\rm ac}$ as "*rotating acoustics*."

III. ACOUSTIC RESONANCE MODES IN A RECTANGULAR BOX WITH VISCOUS BOUNDARY LAYERS

We consider the rectangular-box-shaped cavity of dimensions $L_x\times L_y\times L_z$, where $0\leqslant x\leqslant L_x$, $0\leqslant y\leqslant L_y$, and $0\leqslant z\leqslant L_z$. Below, we give the solutions for the resonance modes of the acoustic pressure p_1 satisfying Eq. (3) in this geometry with viscous boundary layers. We refer the reader to Appendix A for the detailed derivations. The resulting expressions are valid for frequencies close to resonances of a high Q factor $Q\gg 1$ and for narrow boundary layers [see Eq. (A3)]. We then evaluate the second-order quantities $\boldsymbol{S}_{\rm ac}$, $\boldsymbol{f}_{\rm ac}$, and $\boldsymbol{\mathcal{L}}_{\rm ac}$ which vanish for all single-mode resonances but not for double-mode resonances, where two single modes are excited simultaneously by the same frequency.

A. Single-mode resonances

First, neglecting viscosity, the resonance solution for p_1 is proportional to the eigenfunctions $R^{lmn}(\boldsymbol{r})$ of the Helmholtz equation (3a), which are the usual hard-wall standing resonance modes with integer number l, m, and n half-waves in the x, y, and z directions, respectively,

$$p_1^{lmn} \propto R^{lmn}(\boldsymbol{r}) = \cos\left(K_x^l x\right)\cos\left(K_y^m y\right)\cos\left(K_z^n z\right). \tag{9a}$$

Here, the wave numbers K_x^l, K_y^m, and K_z^n are real-valued, purely geometrical quantities that dictate the resonance wave numbers K_0^{lmn}:

$$K_x^l = \frac{l\pi}{L_x}, \quad K_y^m = \frac{m\pi}{L_y}, \quad K_z^n = \frac{n\pi}{L_z}, \tag{9b}$$

$$K_0^{lmn} = \sqrt{\left(K_x^l\right)^2 + \left(K_y^m\right)^2 + \left(K_z^n\right)^2}. \tag{9c}$$

In the presence of viscosity and hence viscous boundary layers, the resonant wave numbers k_0^{lmn} and angular frequencies ω^{lmn} are down-shifted slightly relative to the inviscid values

[1]The standard definition of the full angular momentum density is $\boldsymbol{\mathcal{L}} = \boldsymbol{r}^{\rm L}[t]\times\{\rho[\boldsymbol{r}^{\rm L}(t),t]\boldsymbol{v}[\boldsymbol{r}^{\rm L}(t),t]\}$, defined in terms of the instantaneous Lagrangian fluid position $\boldsymbol{r}^{\rm L}(t) = \boldsymbol{r} + \tilde{\boldsymbol{d}}_1(\boldsymbol{r},t) + \mathcal{O}({\rm Ma}^2)$, where $\boldsymbol{r}$ is the equilibrium position of the fluid. Taylor expanding $\rho[\boldsymbol{r}^{\rm L}(t),t] \approx \rho(\boldsymbol{r},t) + \tilde{\boldsymbol{d}}_1\cdot\nabla\rho$ and $\boldsymbol{v}[\boldsymbol{r}^{\rm L}(t),t] \approx \boldsymbol{v}(\boldsymbol{r},t) + \tilde{\boldsymbol{d}}_1\cdot\nabla\boldsymbol{v}(\boldsymbol{r},t)$, and using the expansion in Eq. (2) we obtain the time-averaged full angular momentum density $\boldsymbol{\mathcal{L}} = \boldsymbol{r}\times\{\rho_{\rm fl}[\boldsymbol{v}_2 + \langle\tilde{\boldsymbol{d}}_1\cdot\nabla\tilde{\boldsymbol{v}}_1\rangle] + \langle\tilde{\rho}_1\tilde{\boldsymbol{v}}_1\rangle\} + \langle\tilde{\boldsymbol{d}}_1\times(\rho_{\rm fl}\tilde{\boldsymbol{v}}_1)\rangle$. Here, the last term is $\boldsymbol{\mathcal{L}}_{\rm ac}$ from Eq. (6c) and expresses the angular momentum density of each fluid particle around its equilibrium position $\boldsymbol{r}$.

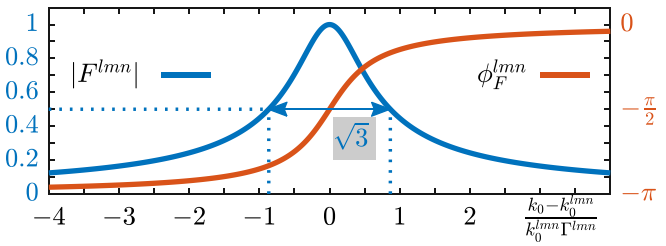

FIG. 1. The modulus $|F^{lmn}|$ (left axis) and phase ϕ_F^{lmn} (right axis) of the frequency-dependent factor F^{lmn} in Eq. (12c). The double arrow marks the full-width-at-half-maximum linewidth $\sqrt{3}k_0^{lmn}\Gamma^{lmn}$ of $|F^{lmn}|$.

due to the boundary-layer damping coefficients $\Gamma_{\mathrm{bl}}^{lmn}$:

$$k_0^{lmn} = \left(1 - \frac{1}{2}\Gamma_{\mathrm{bl}}^{lmn}\right)K_0^{lmn}, \quad \omega^{lmn} = k_0^{lmn}c_{\mathrm{fl}}, \tag{10a}$$

$$\Gamma_{\mathrm{bl}}^{lmn} = \left(\frac{K_x^l}{K_0^{lmn}}\right)^2\left(\frac{\delta}{L_y^m}+\frac{\delta}{L_z^n}\right) + \left(\frac{K_y^m}{K_0^{lmn}}\right)^2\left(\frac{\delta}{L_z^n}+\frac{\delta}{L_x^l}\right) + \left(\frac{K_z^n}{K_0^{lmn}}\right)^2\left(\frac{\delta}{L_x^l}+\frac{\delta}{L_y^m}\right), \tag{10b}$$

where $L_x^l = \int_0^{L_x}\cos^2(K_x^l x)\,dx = \frac{1}{2}(1+\delta_{0l})L_x$ and similarly for L_y^m and L_z^n. As an example, a pure x mode will have $K_0^{l00} = K_x^l$ and $K_y^0 = K_z^0 = 0$ giving $\Gamma_{\mathrm{bl}}^{l00} = \frac{\delta}{L_y}+\frac{\delta}{L_z}$ corresponding to the boundary-layer damping from the four boundaries parallel to the x axis. The total damping coefficient Γ^{lmn} of the resonance mode lmn includes both the boundary-layer-damping coefficients $\Gamma_{\mathrm{bl}}^{lmn}$ and the bulk-damping coefficient $\Gamma_{\mathrm{fl}}^{lmn}$, given in Eq. (4) with $\omega = \omega^{lmn}$,

$$\Gamma^{lmn} = \Gamma_{\mathrm{bl}}^{lmn} + \Gamma_{\mathrm{fl}}^{lmn}. \tag{11}$$

For frequencies close to the resonance frequencies, we have $k_0 \approx k_0^{lmn}$ or $\omega \approx \omega^{lmn}$, and the resonance pressure mode p_1^{lmn} satisfying Eq. (3) is the product of a complex-valued amplitude P_1^{lmn}, an internal frequency dependency $F^{lmn}(k_0)$, and the usual real-valued, hard-wall spatial dependency $R^{lmn}(\boldsymbol{r})$ from Eq. (9a):

$$p_1^{lmn}(k_0,\boldsymbol{r}) = P_1^{lmn}F^{lmn}(k_0)R^{lmn}(\boldsymbol{r}) \ \text{ for } k_0 \approx k_0^{lmn}, \tag{12a}$$

$$P_1^{lmn} = \frac{\rho_{\mathrm{fl}}c_{\mathrm{fl}}^2}{\Gamma^{lmn}}\frac{\int_{\partial\Omega}U_{1\perp}R^{lmn}\,dA}{\int_\Omega (R^{lmn})^2\,dV} = \left|P_1^{lmn}\right|e^{i\phi_{\mathrm{act}}^{lmn}}, \tag{12b}$$

$$F^{lmn}(k_0) = \frac{\frac{1}{2}k_0^{lmn}\Gamma^{lmn}}{\left(k_0-k_0^{lmn}\right)+i\frac{1}{2}k_0^{lmn}\Gamma^{lmn}} = |F^{lmn}|e^{i\phi_F^{lmn}}. \tag{12c}$$

Here, we have also given P_1^{lmn} and F^{lmn} in their polar form and introduced the corresponding external actuation phase $\phi_{\mathrm{act}}^{lmn}$ and internal frequency-dependent phase ϕ_F^{lmn}. The phase ϕ_F^{lmn} is plotted in Fig. 1 together with the modulus $|F^{lmn}|$. The total phase $\phi_{\mathrm{tot}}^{lmn}$ of the mode lmn is the sum of these phases:

$$\phi_{\mathrm{tot}}^{lmn} = \phi_{\mathrm{act}}^{lmn} + \phi_F^{lmn}. \tag{13}$$

B. Double-mode resonances

The bulk-driven acoustic streaming is driven by the body force $\boldsymbol{f}_{\mathrm{ac}}$, defined in Eq. (7d) and restated here solely in terms of the pressure p_1, by using $\boldsymbol{v}_1 \approx \frac{-i}{\omega\rho_{\mathrm{fl}}}\nabla p_1$ as given in Eq. (5a):

$$\boldsymbol{f}_{\mathrm{ac}} = \frac{\Gamma_{\mathrm{fl}}\omega}{c_{\mathrm{fl}}^2}\langle\tilde{p}_1\tilde{\boldsymbol{v}}_1\rangle = \Gamma_{\mathrm{fl}}\kappa_{\mathrm{fl}}\frac{1}{2}\mathrm{Re}[ip_1\nabla p_1^*]. \tag{14}$$

For any single-mode resonance lmn of the form of Eq. (12a), this expression will vanish since ip_1^{lmn} is exactly $\frac{\pi}{2}$ out of phase with ∇p_1^{lmn}. This motivates us to consider double-mode resonances, which occur if two single modes lmn and $l'm'n'$ overlap, such that they can be excited simultaneously at the same frequency $f = \frac{1}{2\pi}k_0c_{\mathrm{fl}}$, with $k_0^{lmn} \approx k_0 \approx k_0^{l'm'n'}$. In that case, the total pressure is the sum of two modes

$$p_1 = p_{l'm'n'}^{lmn} = p_1^{lmn} + p_1^{l'm'n'}, \tag{15}$$

and the body force $\boldsymbol{f}_{\mathrm{ac}}$ in Eq. (14) becomes $\boldsymbol{f}_{l'm'n'}^{lmn}$:

$$\begin{aligned}\boldsymbol{f}_{l'm'n'}^{lmn} &= \tfrac{1}{2}\Gamma_{\mathrm{fl}}\kappa_{\mathrm{fl}}\mathrm{Re}\left\{i\left(p_1^{lmn}+p_1^{l'm'n'}\right)\nabla\left(p_1^{lmn}+p_1^{l'm'n'}\right)^*\right\}\\ &= \tfrac{1}{2}\Gamma_{\mathrm{fl}}\kappa_{\mathrm{fl}}\left\{\mathrm{Re}\left[ip_1^{lmn}\nabla\left(p_1^{l'm'n'}\right)^*\right]-\mathrm{Re}\left[p_1^{l'm'n'}\nabla\left(ip_1^{lmn}\right)^*\right]\right\}.\end{aligned} \tag{16}$$

Inserting the resonance mode Eq. (12a) with P_1^{lmn} in polar form yields

$$\boldsymbol{f}_{l'm'n'}^{lmn} = \tfrac{1}{2}\Gamma_{\mathrm{fl}}\kappa_{\mathrm{fl}}\left|P_1^{lmn}\right|\left|P_1^{l'm'n'}\right|\mathcal{F}_{l'm'n'}^{lmn}(k_0)\,\boldsymbol{\mathcal{K}}_{l'm'n'}^{lmn}(\boldsymbol{r}), \tag{17a}$$

$$\mathcal{F}_{l'm'n'}^{lmn}(k_0) = \mathrm{Re}\left\{iF^{lmn}e^{i\phi_{\mathrm{act}}^{lmn}}\left(F^{l'm'n'}e^{i\phi_{\mathrm{act}}^{l'm'n'}}\right)^*\right\}, \tag{17b}$$

$$\boldsymbol{\mathcal{K}}_{l'm'n'}^{lmn}(\boldsymbol{r}) = R^{lmn}\nabla R^{l'm'n'} - R^{l'm'n'}\nabla R^{lmn}. \tag{17c}$$

Here, $\mathcal{F}_{l'm'n'}^{lmn}(k_0)$ gives the essential frequency dependency (as Γ_{fl} is nearly constant over the width of the double mode), while $\boldsymbol{\mathcal{K}}_{l'm'n'}^{lmn}(\boldsymbol{r})$ with the dimension of a wave vector gives the spatial dependency and direction of the double-mode body force. Furthermore, we obtain the double-mode energy flux density $\boldsymbol{S}_{lmn}^{l'm'n'}$ and acoustic angular momentum density $\boldsymbol{\mathcal{L}}_{l'm'n'}^{lmn}$ directly from Eq. (17a) by use of Eqs. (7d) and (8a):

$$\boldsymbol{S}_{l'm'n'}^{lmn} = \frac{1}{2}\frac{\left|P_1^{lmn}\right|\left|P_1^{l'm'n'}\right|}{\rho_{\mathrm{fl}}\omega}\mathcal{F}_{l'm'n'}^{lmn}(k_0)\boldsymbol{\mathcal{K}}_{l'm'n'}^{lmn}(\boldsymbol{r}), \tag{18a}$$

$$\boldsymbol{\mathcal{L}}_{l'm'n'}^{lmn} = \frac{1}{2}\frac{\left|P_1^{lmn}\right|\left|P_1^{l'm'n'}\right|}{\rho_{\mathrm{fl}}\omega^3}\mathcal{F}_{l'm'n'}^{lmn}(k_0)\nabla\times\boldsymbol{\mathcal{K}}_{l'm'n'}^{lmn}(\boldsymbol{r}). \tag{18b}$$

Note that $\mathcal{F}_{l'm'n'}^{lmn}(k_0)$ is normalized to be between -1 and 1, whereas $\boldsymbol{\mathcal{K}}_{l'm'n'}^{lmn}(\boldsymbol{r})$ and $\nabla\times\boldsymbol{\mathcal{K}}_{l'm'n'}^{lmn}(\boldsymbol{r}) = 2\nabla R^{lmn}\times\nabla R^{l'm'n'}$ has the maximum amplitudes k_0 and $2k_0^2$, respectively.

In Fig. 2 we show results for the nine lowest-frequency double modes $lm0 + ml0$ in a square cavity. We plot the body force $\boldsymbol{f}_{ml0}^{lm0} \propto \boldsymbol{\mathcal{K}}_{ml0}^{lm0}$ and the z component of the acoustic angular momentum $\boldsymbol{\mathcal{L}}_{ml0}^{lm0} \propto \nabla\times\boldsymbol{\mathcal{K}}_{ml0}^{lm0}$. In the Supplemental Material [41] we show 55 examples of double-mode resonances $lm0 + l'm'0$ with $l, m, l', m' = 0, 1, 2, 3, 4$ in rectangular

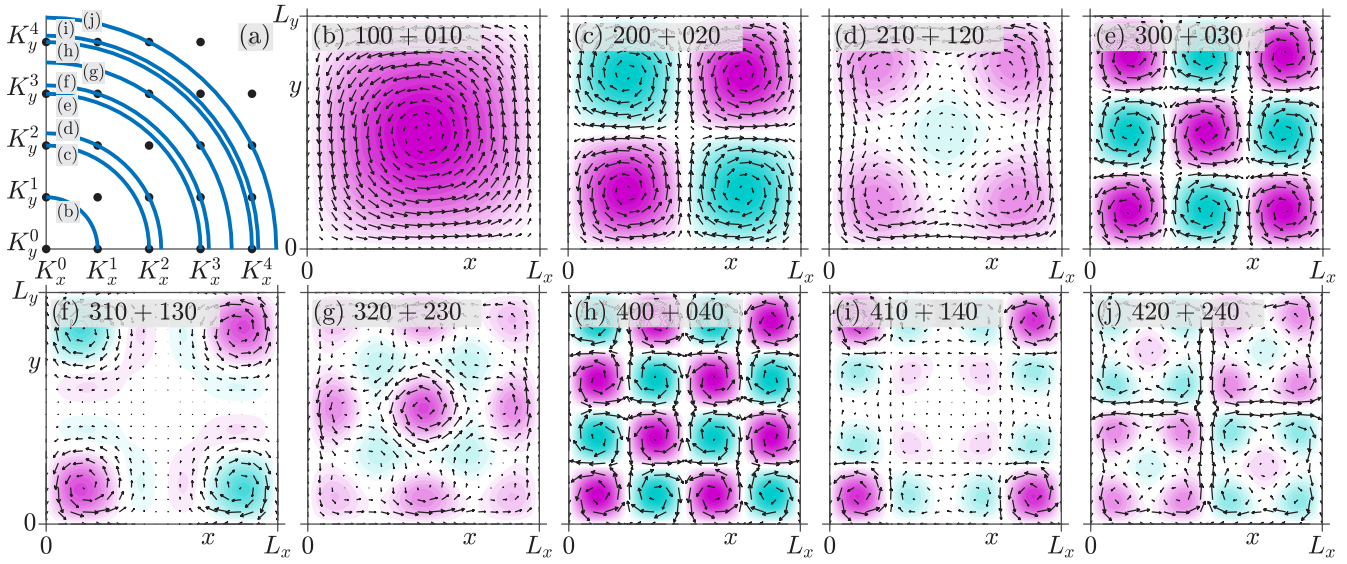

FIG. 2. Rotating acoustics in the xy plane ($K_z^n = 0$) of a square cavity with $L_x = L_y$. (a) $K_x - K_y$ space diagram showing the allowed values of K_x^l and K_y^m (black dots). Each quarter circle (b)–(j) corresponds to the angular frequency $c_{\mathrm{fl}}\sqrt{(K_x^l)^2 + (K_y^m)^2}$, where the double mode $lm0 + ml0$ is excited. (b)–(j) The corresponding acoustic rotation of the double mode $lm0 + ml0$, where the arrows represent the body force $\boldsymbol{f}_{ml0}^{lm0}$ and the colors show the z component of the spatial dependency $\boldsymbol{\nabla} \times \boldsymbol{\mathcal{K}}_{ml0}^{lm0}$ in Eq. (18b) of the acoustic angular momentum density from $-2k_0^2$ (light cyan) to $2k_0^2$ (dark magenta).

cavities with aspect ratios between 1 and 4, and we provide a MATLAB code to compute these modes.

IV. CONDITIONS FOR OBTAINING A STRONG ACOUSTIC BODY FORCE

The magnitude of the body force $\boldsymbol{f}_{l'm'n'}^{lmn}$, the acoustic energy flux density $\boldsymbol{S}_{l'm'n'}^{lmn}$, and the acoustic angular momentum density $\boldsymbol{\mathcal{L}}_{l'm'n'}^{lmn}$ are all proportional to the frequency-dependent factor $\mathcal{F}_{l'm'n'}^{lmn}(k_0)$ in Eq. (17b). To study this factor, we rewrite it to emphasize the total phase difference $\phi_{\mathrm{tot}}^{l'm'n'} - \phi_{\mathrm{tot}}^{lmn}$ between the single-mode phases given in Eq. (13):

$$\mathcal{F}_{l'm'n'}^{lmn}(k_0) = |F^{lmn}||F^{l'm'n'}| \sin\left(\phi_{\mathrm{tot}}^{l'm'n'} - \phi_{\mathrm{tot}}^{lmn}\right). \tag{19}$$

Consequently, two conditions must be fulfilled to yield a strong body force: (i) the overlap condition, i.e., the two single-mode resonances must have a large overlap in frequency space to ensure a large value of the amplitude $|F^{lmn}||F^{l'm'n'}|$, and (ii) the phase condition, i.e., the difference $\phi_{\mathrm{tot}}^{l'm'n'} - \phi_{\mathrm{tot}}^{lmn}$ in phases must be close to $\pm\frac{\pi}{2}$ to ensure a large value of the sine factor.

A. Overlap condition: Aspect ratios

The condition that both $|F^{lmn}|$ and $|F^{l'm'n'}|$ are large in Eq. (19) is satisfied if the modes overlap. This occurs if the resonance frequencies are nearly identical, $k_0^{lmn} \approx k_0^{l'm'n'}$ or, equivalently,

$$\left(\frac{l\pi}{L_x}\right)^2 + \left(\frac{m\pi}{L_y}\right)^2 + \left(\frac{n\pi}{L_z}\right)^2 \approx \left(\frac{l'\pi}{L_x}\right)^2 + \left(\frac{m'\pi}{L_y}\right)^2 + \left(\frac{n'\pi}{L_z}\right)^2, \tag{20}$$

where we have used that $\Gamma_{\mathrm{bl}}^{lmn} \ll 1$ in Eq. (10a) so $k_0^{lmn} \approx K_0^{lmn}$. In the general case, Eq. (20) gives a myriad of possible mode combinations. If we restrict ourselves to horizontal modes, where $n = n' = 0$, we can solve for the aspect ratio $A = \frac{L_x}{L_y}$ in Eq. (20):

$$A = \frac{L_x}{L_y} \approx \sqrt{\frac{l^2 - l'^2}{m'^2 - m^2}}. \tag{21}$$

Listing the integers l, m, l', m' for which A is real, we find that the square cavity with $A \approx 1$ is the richest case having the highest number of allowed double-mode excitations. In Fig. 2, we show the first nine horizontal double-mode excitations in a square cavity with $A = 1$ and $n = n' = 0$. In this case, the condition in Eq. (20) corresponds to two points $(\frac{l\pi}{L_x}, \frac{m\pi}{L_y})$ and $(\frac{l'\pi}{L_x}, \frac{m'\pi}{L_y})$ both lying on the same quarter circle of radius K_0, as illustrated by the black dots in Fig. 2(a).

B. Phase condition: Rotating versus nonrotating actuation

The straightforward way to obtain rotating acoustics is to actuate a given system with two transducers running with a phase difference of $\phi_{\mathrm{act}}^{l'm'n'} - \phi_{\mathrm{act}}^{lmn} = \pm\frac{\pi}{2}$, a technique that has been used in many experiments to generate acoustic radiation torques [26,31–35]. Remarkably, even in the standard case of microfluidic ultrasound experiments driven by a single piezoelectric transducer with a nonrotating actuation, $\phi_{\mathrm{act}}^{l'm'n'} - \phi_{\mathrm{act}}^{lmn} = 0$, a rotating acoustic field may nevertheless be generated because the total phase difference $\phi_{\mathrm{tot}}^{l'm'n'} - \phi_{\mathrm{tot}}^{lmn} = \phi_F^{l'm'n'} - \phi_F^{lmn}$ may be close to $\pm\frac{\pi}{2}$ due to the internal phases ϕ_F^{lmn} of the frequency-dependent factors $F^{lmn}(k_0)$ [see Eq. (12c) and Fig. 1].

V. NONROTATING ACTUATION OF ROTATING DOUBLE-MODE RESONANCES IN A NEARLY SQUARE CAVITY

We now show how a nonrotating actuation can lead to a rotating double-mode resonance in a nearly square cavity characterized by the average side length $L^\star = \frac{1}{2}(L_x + L_y)$ and the small symmetry breaking $d = L_x - L_y$:

$$L_x = L^\star + \tfrac{1}{2}d, \quad L_y = L^\star - \tfrac{1}{2}d, \quad \text{with } |d| \ll L^\star. \tag{22}$$

The magnitude of the resulting acoustic body force $\boldsymbol{f}_{\rm ac}$ depends strongly on the symmetry breaking d, and for a given double mode we determine how much the aspect ratio $A = L_x/L_y \approx 1 + d/L^\star$ should deviate from unity to maximize $\boldsymbol{f}_{\rm ac}$. Specifically, we consider the symmetric double-mode excitations $lm0 + ml0$ in the horizontal xy plane of the type shown in Fig. 2. For such double modes, the analysis simplifies significantly, not only because z drops out, but also because the damping coefficients Γ^{lm0} and Γ^{ml0} from Eqs. (10b) and (11) are almost identical. In short, we consider the following situation:

$$\text{Nearly square cavity:} \quad L_x \approx L^\star \approx L_y, \tag{23a}$$

$$\text{Horizontal } xy \text{ modes:} \quad n = n' = 0, \tag{23b}$$

$$\text{Symmetric double modes:} \quad l'm' = ml, \tag{23c}$$

$$\text{Nonrotating actuation:} \quad \phi_{\rm act}^{lm0} = \phi_{\rm act}^{ml0}, \tag{23d}$$

$$\text{Similar damping coefficients:} \quad \Gamma^{lm0} \approx \Gamma^{ml0}. \tag{23e}$$

To analyze the strength of the acoustic body force, we examine the factor $\mathcal{F}_{lm0}^{ml0}(k_0)$ in Eq. (17b) that describes the frequency dependency of the acoustic body force. For the double mode $lm0 + ml0$, we introduce the short two-subscript notation $\mathcal{F}_{lm}(k_0)$ for this quantity:

$$\begin{aligned}\mathcal{F}_{lm}(k_0) = \mathcal{F}_{ml0}^{lm0}(k_0) &= \mathrm{Re}\{i[F^{lm0}][F^{ml0}]^*\} \\ &= |F^{lm0}||F^{ml0}| \sin\left(\phi_F^{ml0} - \phi_F^{lm0}\right),\end{aligned} \tag{24}$$

where the functions $F^{lm0}(k_0)$ and $F^{ml0}(k_0)$ behave as shown in Fig. 1. Note that if the modes $lm0$ and $ml0$ have equal resonance frequencies, they have full mode overlap, and the product $|F^{lm0}||F^{ml0}|$ is maximized, while $\sin(\phi_F^{ml0} - \phi_F^{lm0})$ vanishes, and there is no body force. To maximize $\mathcal{F}_{lm}(k_0)$, the two modes must therefore be separated sufficiently to ensure that the phase difference $\phi_F^{ml0} - \phi_F^{lm0}$ deviates from zero, but not too much, as a decreased mode overlap reduces the modulus product $|F^{lm0}||F^{ml0}|$. Therefore, we cannot in this case perfectly fulfill both the overlap condition, Sec. IV A, and the phase condition, Sec. IV B, so the strongest body force is found at a certain mode separation $\Delta_{lm} = k_0^{lm0} - k_0^{ml0}$ between the resonance wave numbers, which gives only partial mode overlap and a phase difference that deviates from the ideal $\pm\frac{\pi}{2}$.

The mode separation Δ_{lm} is induced by the symmetry breaking d, and similar to Eq. (22), we introduce the center wave number $k_{lm}^\star = \frac{1}{2}(k_0^{lm0} + k_0^{ml0})$ corresponding to the center frequency between the two modes and write

$$k_0^{lm0} = k_{lm}^\star + \frac{1}{2}\Delta_{lm}, \quad k_0^{ml0} = k_{lm}^\star - \frac{1}{2}\Delta_{lm}, \tag{25a}$$

$$k_{lm}^\star \approx \left(1 - \frac{1}{2}\Gamma_{\rm bl}^{lm0}\right)\sqrt{l^2 + m^2}\,\frac{\pi}{L^\star}. \tag{25b}$$

TABLE I. Overview of the damping coefficients Γ, the full-width-at-half-maximum (FWHM) linewidths, and the mode separation Δ.

Parameter	Symbol	Reference
Bulk damping	$\Gamma_{\rm fl}$	Eq. (4)
Boundary-layer damping	$\Gamma_{\rm bl}^{lmn}$	Eq. (10b)
Total damping	Γ^{lmn}	Eq. (11)
FWHM of $\lvert F^{lmn}\rvert$	$\sqrt{3}k_0^{lmn}\Gamma^{lmn}$	Fig. 1
FWHM of $E_{\rm ac}^{lmn} \propto \lvert F^{lmn}\rvert^2$	$k_0^{lmn}\Gamma^{lmn}$	Eqs. (6),(12)
Optimal mode separation $\Delta_{lm}^{\rm opt}$	$\frac{1}{\sqrt{3}}\,k_{lm}^\star\Gamma_{lm}^\star$	Eq. (29b)

The relation between the mode separation Δ_{lm}, the symmetry breaking d, and the aspect ratio $A = L_x/L_y$ is found by inserting Eq. (22) into $k_0^{lm0} = \sqrt{(\frac{l\pi}{L_x})^2 + (\frac{m\pi}{L_y})^2} + \mathcal{O}(\Gamma^{lm0})$, expanding in the small ratio $\frac{d}{L^\star}$, and comparing with Eq. (25a),

$$\Delta_{lm} \approx \frac{m^2 - l^2}{\sqrt{m^2 + l^2}}\frac{\pi}{L^\star}\frac{d}{L^\star} \approx \frac{m^2 - l^2}{\sqrt{m^2 + l^2}}\frac{\pi}{L^\star}(A - 1). \tag{26}$$

Since the damping coefficients are nearly identical $\Gamma^{lm0} \approx \Gamma_{lm}^\star \approx \Gamma^{ml0}$, with $\Gamma_{lm}^\star = \frac{1}{2}(\Gamma^{lm0} + \Gamma^{ml0})$ being the average value, it is convenient to scale all wave-number quantities by their common linewidth $\Gamma_{lm}^\star k_{lm}^\star$ (see the overview listed in Table I):

$$\tilde{k}_0 = \frac{k_0}{k_{lm}^\star\Gamma_{lm}^\star}, \quad \tilde{k}_{lm}^\star = \frac{1}{\Gamma_{lm}^\star}, \quad \tilde{\Delta}_{lm} = \frac{\Delta_{lm}}{k_{lm}^\star\Gamma_{lm}^\star}. \tag{27}$$

In terms of these quantities, we write the frequency dependencies $F^{lm0}(k_0)$ and $F^{ml0}(k_0)$ from Eq. (12c) as

$$F^{lm0}(k_0) = \frac{1}{2(\tilde{k}_0 - \tilde{k}_{lm}^\star) - \tilde{\Delta}_{lm} + i}, \tag{28a}$$

$$F^{ml0}(k_0) = \frac{1}{2(\tilde{k}_0 - \tilde{k}_{lm}^\star) + \tilde{\Delta}_{lm} + i}. \tag{28b}$$

In Figs. 3(a) and 3(b) we show as in Fig. 1 the modulus and phase, respectively, of F^{lm0} and F^{ml0} for four different mode separations $\tilde{\Delta}_{lm} = 0.10, 0.58, 1.50, 3.00$. In Fig. 3(c) we show for the same values of $\tilde{\Delta}_{lm}$ the frequency dependency $\mathcal{F}_{lm}(k_0)$ from Eq. (24) of the acoustic body force. We note that there exists an optimal mode separation $\tilde{\Delta}_{lm}^{\rm opt}$ that yields the largest possible value $\mathcal{F}_{lm}^{\rm opt}$ of $\mathcal{F}_{lm}$ found at the optimal wave number $k_0^{\rm opt}$. In Eq. (B5) of Appendix B we show that

$$k_0^{\rm opt} = k_{lm}^\star, \tag{29a}$$

$$\tilde{\Delta}_{lm}^{\rm opt} = \pm\frac{1}{\sqrt{3}} = \pm 0.58, \tag{29b}$$

$$\mathcal{F}_{lm}^{\rm opt} = \pm\frac{3\sqrt{3}}{8} = \pm 0.65. \tag{29c}$$

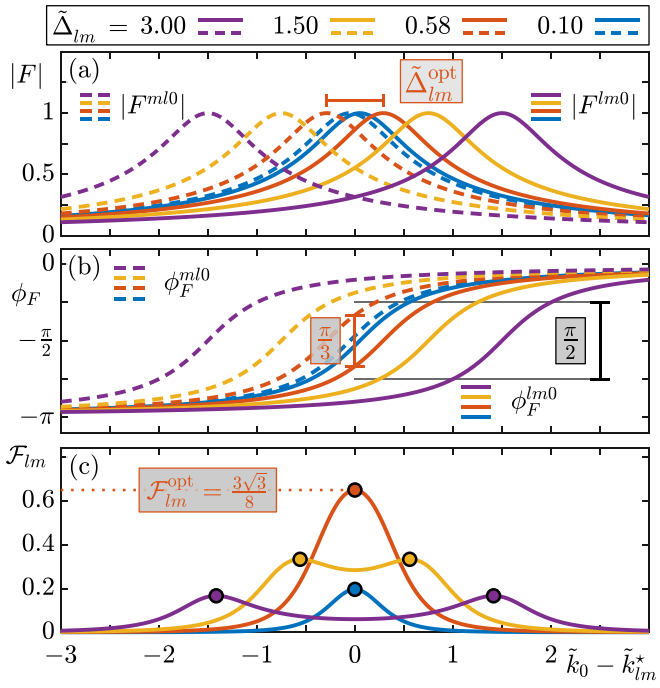

FIG. 3. Plots of $|F^{ml0}|$, $|F^{lm0}|$, ϕ_F^{ml0}, ϕ_F^{lm0}, and $\mathcal{F}_{lm}$ as a function of $\tilde{k}_0 - \tilde{k}^\star_{lm}$, each for the four values 3.00, 1.50, 0.58, and 0.10 of the mode separation $\tilde{\Delta}_{lm}$. (a) The modulus $|F|$ and (b) the phase ϕ_F of F^{lm0} (right, solid) and F^{ml0} (left, dashed) given in Eq. (28). At the optimal mode separation $\tilde{\Delta}^{\rm opt}_{lm} = \frac{1}{\sqrt{3}} \approx 0.58$ (orange), the phase difference at the center frequency is $\frac{\pi}{3}$. (c) The frequency-dependent factor $\mathcal{F}_{lm}(k_0)$, from Eq. (24), which describes the strength of the acoustic body force $\boldsymbol{f}_{\rm ac}$, when the modes of same color in (a) and (b) are combined.

This means that the optimal frequency is the center frequency between the modes, and the optimal mode separation is $\frac{1}{\sqrt{3}}$ of the full-width at half-maximum. Inserting the optimal conditions (29a) and (29b) into Eq. (28) reveals the phase difference between the modes at the optimal conditions, a value different from $\pm\frac{1}{2}\pi$,

$$\left(\phi_F^{ml0} - \phi_F^{lm0}\right)^{\rm opt} = \pm\tfrac{1}{3}\,\pi. \tag{29d}$$

By using Eq. (26), we translate the optimal mode separation $\tilde{\Delta}^{\rm opt}_{lm}$ into the optimal size of the symmetry breaking $d^{\rm opt}_{lm} = (L_x - L_y)^{\rm opt}_{lm}$ and the corresponding aspect ratio $A^{\rm opt}_{lm} = (\frac{L_x}{L_y})^{\rm opt}_{lm}$, where the acoustic body force $\boldsymbol{f}_{\rm ac}$ of the double mode $lm0 + ml0$ is maximized:

$$d^{\rm opt}_{lm} = \tilde{\Delta}^{\rm opt}_{lm}\frac{l^2+m^2}{m^2-l^2}\Gamma^\star_{lm}L^\star, \tag{29e}$$

$$A^{\rm opt}_{lm} = 1 + \frac{1}{L^\star}d^{\rm opt}_{lm}. \tag{29f}$$

For all the double modes shown in Fig. 2, we have $l > m$, so for a nonrotating actuation, the rotation direction of the body force will therefore be as shown in the case of $d < 0$ (corresponding to $L_x < L_y$ and $A < 1$), and opposite for $d > 0$. Note from Eq. (29e) that this asymmetry-induced rotating acoustics is extremely sensitive to d. In practice, it may be difficult to control this mechanism, as it requires a fabrication accuracy much smaller than $d/L^\star \sim \Gamma^\star_{lm}$, which in microfluidic devices typically is smaller than 1% [42].

TABLE II. Material parameters for water [45] and pyridine (C_5H_5N) [46] at 25 °C used in the numerical simulations.

Parameter	Symbol	Water	Pyridine	Unit
Mass density	$\rho_{\rm fl}$	997.05	982	kg m^{-3}
Compressibility	$\kappa_{\rm fl}$	448	507	TPa^{-1}
Speed of sound	$c_{\rm fl}$	1496.7	1417	m s^{-1}
Dynamic viscosity	$\eta_{\rm fl}$	0.890	0.879	mPa s
Bulk viscosity	$\eta^{\rm b}_{\rm fl}$	2.485	62.4	mPa s

VI. 3D SIMULATION OF ACOUSTIC STREAMING IN A NEARLY SQUARE CAVITY

In this section we validate by direct numerical simulation the theory for rotating acoustics induced by a nonrotating actuation in a weakly symmetry-broken geometry. We simulate the acoustic pressure p_1 and the acoustic streaming $\boldsymbol{v}_2$ in a shallow, nearly square cavity in three dimensions (3D). We choose a cavity similar to that investigated experimentally by Hagsäter *et al.* [39], and simulated in 3D using the hard-wall approximation by Lei *et al.* [43], and including the actuator and elastic walls by Skov *et al.* [44]. The cavity has the mean side length $L^\star = 2000\ \mu$m, $L_x = L^\star + \frac{1}{2}d$, $L_y = L^\star - \frac{1}{2}d$, and height $L_z = 200\ \mu$m. We use Eq. (29) to optimize the symmetry breaking d and actuation frequency $f = \frac{1}{2\pi}k_0 c_{\rm fl}$ to obtain the strongest possible rotating acoustic streaming. The coordinate system is the same as in Sec. III, with $0 \leqslant x \leqslant L_x$, $0 \leqslant y \leqslant L_y$, and $0 \leqslant z \leqslant L_z$. To mimic an actuation from a broad piezoelectric transducer, the boundary is taken to be stationary everywhere, except at the bottom boundary $z = 0$, where we apply the nonrotating Gaussian displacement in the normal direction z:

$$\boldsymbol{u}_1 = \begin{cases} u^0_{1z} G_1(x,y)\,\boldsymbol{e}_z & \text{for } z = 0, \\ \boldsymbol{0} & \text{otherwise,} \end{cases}$$

$$G_1(x,y) = \exp\left[-\frac{\left(x-\frac{L_x}{2}\right)^2}{\left(\frac{L_x}{2}\right)^2} - \frac{\left(y-\frac{L_y}{2}\right)^2}{\left(\frac{L_y}{2}\right)^2}\right]. \tag{30}$$

This actuation displacement has the maximum amplitude of u^0_{1z} in the cavity center and the minimum amplitude of $e^{-2}u^0_{1z} \approx 0.14\,u^0_{1z}$ in the corners of the cavity. In Secs. VI C 1–VI C 4 the fluid is water, and in Sec. VI C 6 it is pyridine. The material parameters for these fluids are listed in Table II.

In the following simulations, we excite the double-mode resonance $l00 + 0l0$ with $l = 2$, 4, and 6. Using our analytical expressions (17), we have in Fig. 2 shown the spatial dependency of the acoustic body force $\boldsymbol{f}_{\rm ac} = \boldsymbol{f}^{l00}_{0l0}$ for these particular double modes. As seen in Eq. (7), this body force is the source of the bulk-driven acoustic streaming, so we predict that the numerical simulation of the bulk-driven streaming will result in a 2×2 pattern as in Fig. 2(c) for $l = 2$, a 4×4 pattern as in Fig. 2(h) for $l = 4$, and similarly for $l = 6$ (not shown in Fig. 2).

A. Choosing the parameters

We derived in Sec. III analytical expressions for the acoustic resonance modes including the viscous boundary layers, and we derived in Sec. V the conditions on the geometry of a nearly square cavity for which the body force $\boldsymbol{f}_{\rm ac}$ and the acoustic rotation are maximized for a nonrotating actuation. Remarkably, these analytic results allow an analytical determination of the parameter values that lead to the strongest rotating acoustic streaming in the xy plane.

For the double mode $l00+0l0$, the small damping coefficients $\Gamma_{\rm fl}^{l00}\approx\Gamma_{\rm fl}^{0l0}$ in Eq. (4) and $\Gamma_{\rm bl}^{l00}\approx\Gamma_{\rm bl}^{0l0}$ in Eq. (10b) are computed by approximating the angular frequency by the constant value $\omega=c_{\rm fl}k_{l0}^\star\approx c_{\rm fl}\frac{l\pi}{L^\star}$ [see Eq. (25b)]:

$$\Gamma_{\rm fl}^{l00}\approx\left(\frac{4}{3}+\frac{\eta_{\rm fl}^{\rm b}}{\eta_{\rm fl}}\right)\frac{\eta_{\rm fl}}{\rho_{\rm fl}c_{\rm fl}}\frac{l\pi}{L^\star}\approx\Gamma_{\rm fl}^{0l0}, \tag{31a}$$

$$\Gamma_{\rm bl}^{l00}\approx\frac{\delta}{L^\star}+\frac{\delta}{L_z}\approx\Gamma_{\rm bl}^{0l0},\quad \delta\approx\sqrt{\frac{2\eta_{\rm fl}L^\star}{l\pi c_{\rm fl}\rho_{\rm fl}}}. \tag{31b}$$

Combining Eqs. (10a), (29a), and (25b), we obtain an expression for the boundary-layer shifted, optimal double-mode actuation frequency, which is the center frequency of the two single modes

$$f_{l0}^\star\approx\frac{l}{2}\left(1-\frac{1}{2}\Gamma_{\rm bl}^{l00}\right)\frac{c_{\rm fl}}{L^\star}. \tag{32}$$

The optimal symmetry breaking $d_{l0}^{\rm opt}$ and the corresponding aspect ratio $A_{l0}^{\rm opt}$ then follow from Eqs. (29e) and (29f):

$$d_{l0}^{\rm opt}\approx\frac{-1}{\sqrt{3}}\left(\Gamma_{\rm bl}^{l00}+\Gamma_{\rm fl}^{l00}\right)L^\star, \tag{33a}$$

$$A_{l0}^{\rm opt}\approx 1-\frac{1}{\sqrt{3}}\left(\Gamma_{\rm bl}^{l00}+\Gamma_{\rm fl}^{l00}\right). \tag{33b}$$

Finally, we set the pressure amplitudes $P_1^{l00}=P_1^{0l0}=1$ MPa in Eq. (12b), and compute the corresponding amplitude u_{1z}^0 of the actuation displacement in Eq. (30) as

$$u_{1z}^0=\frac{L_xL_yL_z\left(\Gamma_{\rm fl}^{l00}+\Gamma_{\rm bl}^{l00}\right)\kappa_{\rm fl}P_1^{l00}}{2\int_0^{L_x}\int_0^{L_y}G_1(x,y)\cos\left(\frac{l\pi}{L^\star}x\right)dx\,dy}. \tag{34}$$

For water and $l=2$, 4, and 6, the values of the expressions in Eq. (31)–(34) are listed in Table III. For pyridine, we adjust the actuation amplitude and actuation frequency to maintain the resonance amplitudes of $P_1^{l00}=P_1^{0l0}=1$ MPa. Note that for pyridine, we use the same optimal symmetry breaking $d_{l0}^{\rm opt}$ as used for water. Combining Eqs. (24), (28) and (29e) with the material parameters in Table II leads to the values $\mathcal{F}_{l0}=0.65$, 0.64, and 0.63 for $l=2$, 4, and 6, respectively, which are nearly the same as the optimal value $\mathcal{F}_{l0}^{\rm opt}=0.65$ given in Eq. (29c).

B. Implementation in COMSOL

As in our previous work [24,44,47], the simulation is performed in two steps using the *weak form PDE* module in the finite-element-method software COMSOL MULTIPHYSICS [48]. In the first step, we solve for the acoustic pressure p_1 by implementing Eq. (3) in weak form, and in the second step we solve Eq. (7) for the steady streaming $\boldsymbol{v}_2$ and pressure p_2.

TABLE III. Parameters used in the numerical simulations of the double modes $l00+0l0$. The geometry parameters are optimized for maximum acoustic rotation in water, and the resulting dependent parameters (damping factors and mode amplitudes) are listed for both water and pyridine.

Parameter	Eq.	Unit	$l=2$	$l=4$	$l=6$
Geometry (optimized for water)					
$d_{l0}^{\rm opt}$	Eq. (33a)	μm	−3.922	−2.785	−2.286
$A_{l0}^{\rm opt}$	Eq. (33b)	1	0.9980	0.9986	0.9989
$L^\star$		μm	2000	2000	2000
L_z		μm	200	200	200
Dependent parameters (water)					
u_{1z}^0	Eq. (34)	nm	1.450	7.474	14.027
$f_{l0}^\star$	Eq. (32)	MHz	0.747	1.494	2.243
$\Gamma_{\rm fl}^{l00}\approx\Gamma_{\rm fl}^{0l0}$	Eq. (31a)	10^{-3}	0.008	0.015	0.023
$\Gamma_{\rm bl}^{l00}\approx\Gamma_{\rm bl}^{0l0}$	Eq. (31b)	10^{-3}	3.389	2.396	1.957
Dependent parameters (pyridine)					
u_{1z}^0	Eq. (34)	nm	1.757	9.665	19.617
$f_{l0}^\star$	Eq. (32)	MHz	0.707	1.415	2.123
$\Gamma_{\rm fl}^{l00}\approx\Gamma_{\rm fl}^{0l0}$	Eq. (31a)	10^{-3}	0.144	0.287	0.431
$\Gamma_{\rm bl}^{l00}\approx\Gamma_{\rm bl}^{0l0}$	Eq. (31b)	10^{-3}	3.488	2.467	2.014

The zero level of p_2 is fixed by using the *global constraint* $\int_\Omega p_2\,dV=0$. Excerpts of the COMSOL code that we use are given in Ref. [44]. For numerical efficiency, we exploit the symmetry at the vertical planes $x=\frac{1}{2}L_x$ and $y=\frac{1}{2}L_y$, where we apply the symmetry conditions $\boldsymbol{n}\cdot\nabla p_1=0$, $\boldsymbol{n}\cdot\boldsymbol{v}_2=0$, and $\boldsymbol{n}\cdot\nabla\boldsymbol{v}_{2\parallel}=\boldsymbol{0}$. The computational domain is thus reduced to the quadrant $0\leqslant x\leqslant\frac{1}{2}L_x$ and $0\leqslant y\leqslant\frac{1}{2}L_y$. We use quartic-, cubic-, and quadratic-order Lagrangian shape functions for p_1, $\boldsymbol{v}_2$, and p_2, respectively, and with a tetrahedral finite-element mesh of mesh size $\frac{1}{6}L_z$, we obtain 1.3×10^6 degrees of freedom and a relative accuracy better than 1%. The simulations were performed on a workstation with a 3.5-GHz Intel Xeon CPU E5-1650 v2 dual-core processor, and with a memory of 128 GB RAM.

C. Simulation results

1. Acoustic pressure

In Fig. 4, we show the simulation results $p_1^{\rm num}$ of the acoustic pressure p_1 in water for $l=6$ in 3D and line plots for $l=2$, 4, and 6. These three modes are examples of rotating double modes actuated by the wide, single, nonrotating Gaussian actuation G_1 [Eqs. (30) and (34)] at the bottom boundary $z=0$. In the Supplemental Material [41] we show the rotating dynamics of the pressure contours similar to Fig. 4(a) for $l=2$, 4, and 6 as gif animations. In Fig. 4 we also show the analytical result $p_1^{\rm ana}=p_{0l0}^{l00}=p_1^{l00}+p_1^{0l0}$, which is obtained from Eqs. (12) and (15) with the optimal mode separation $k_0^{l00}-k_0^{0l0}=\frac{1}{\sqrt{3}}k_{l0}^\star\Gamma_{l0}^\star$ [Eq. (29b)] and mode amplitudes $P_1^{l00}=P_1^{0l0}=1$ MPa:

$$p_1^{\rm ana}=p_{0l0}^{l00}=1\text{ MPa}\times\left[\frac{\cos\left(\frac{l\pi x}{L^\star}\right)}{-\frac{1}{\sqrt{3}}+i}+\frac{\cos\left(\frac{l\pi y}{L^\star}\right)}{\frac{1}{\sqrt{3}}+i}\right]. \tag{35}$$

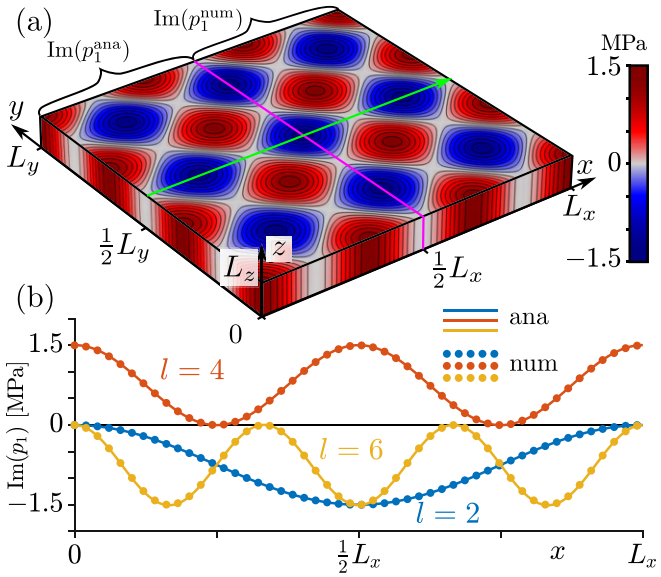

FIG. 4. The acoustic pressure p_1 for water in the nearly square cavity with parameters given in Tables II and III, where the double mode $l00 + 0l0$ is excited by the nonrotating actuation G_1 [Eqs. (30) and (34)]. (a) Pressure contour plot for $l = 6$ of the analytic solution $\mathrm{Im}(p_1^{\mathrm{ana}})$ [Eq. (35)] (for $x < \frac{1}{2}L_x$), and the numerical solution $\mathrm{Im}(p_1^{\mathrm{num}})$ (for $x > \frac{1}{2}L_x$). (b) Line plots of the pressure $\mathrm{Im}(p_1^{\mathrm{ana}})$ (solid) and $\mathrm{Im}(p_1^{\mathrm{num}})$ (dots) along the green line in (a) at $y = \frac{1}{2}L_y$ and $z = L_z$ for the modes $l = 2$ (blue), $l = 4$ (orange), and $l = 6$ (yellow). Animations of the rotating acoustic fields are shown in the Supplemental Material [41].

In Fig. 4(b), we compare $\mathrm{Im}\,(p_1^{\mathrm{num}})$ and $\mathrm{Im}\,(p_1^{\mathrm{ana}})$ and find a quantitative agreement better than 1%. The reason for choosing the imaginary part is to single out the resonant part of the field, which is phase shifted by the factor $\exp(i\frac{\pi}{2}) = i$ relative to the actuation displacement $\boldsymbol{u}_1$ at the boundary Eq. (30). All nonresonant contributions are in phase with $\boldsymbol{u}_1$. In the Supplemental Material [41] is shown an animated gif file[2] of the full cycle in the time domain of the line plots in Fig. 4(b) of p_1. These animations reveal that the deviation of the analytical solution from the numerical one is ∼1% for $l = 2$ at 0.75 MHz, ∼15% for $l = 4$ at 1.5 MHz, and ∼30% for $l = 6$ at 2.2 MHz. The deviation increases for increasing mode number because the wide vertical G_1 actuation couples strongly to the vertical 001 mode through the amplitude factor P_1^{001} of Eq. (12b), while the frequency-dependency factor $F^{001}(k_0)$ of Eq. (12c), which is very small away from resonance, increases significantly as the actuation frequency $f = c_{\mathrm{fl}}k_0$ approaches the vertical-mode resonance $f_0^{001} = 3.7$ MHz. We can reduce the coupling P_1^{001} to the vertical 001 mode by reducing the width of the G_1 actuation profile. This is demonstrated in the animated gif file[3] of the Supplemental Material [41], where the width of the G_1 actuation has been reduced by a factor of 6 from $\frac{1}{2}L^\star$ to $\frac{1}{12}L^\star$. This results in a decreased deviation, now less than ∼1%, of the analytical result from the numerical one for p_1 for all three modes $l = 2, 4, 6$.

[2]"p1_246_wide_G1.gif"
[3]"p1_246_narrow_G1.gif"

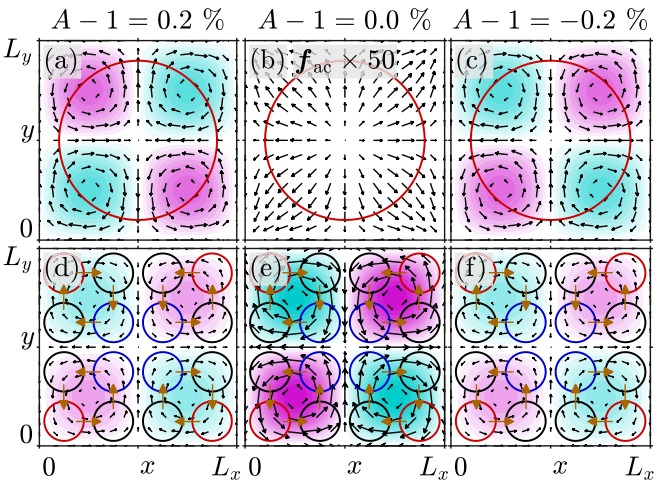

FIG. 5. Simulation of the rotating acoustics in the x-y plane for the double mode $200 + 020$ in water for three aspect ratios $A \approx 1.002$, 1, 0.998 each for the nonrotating (G_1) and rotating (G_{16}) actuation perpendicular to the plane. Color plots between $\pm 10^{-4}$ kg m^{-1}s^{-1} (light cyan to dark magenta) of the z component $\mathcal{L}_{\mathrm{ac},z}$ of the angular momentum density $\boldsymbol{\mathcal{L}}_{\mathrm{ac}}$, and vector plots of the acoustic body force $\boldsymbol{f}_{\mathrm{ac}}$ (max 2.00 N m^{-3}). In (a)–(c) we use the single nonrotating Gaussian actuation G_1 (large red circles) [Eqs. (30) and (34)]. In (d)–(f) we use the rotating actuation profile G_{16} of four quadruples of phase shifted Gaussian profiles given in Eq. (C1) of Appendix C [light red (up), black (0), dark blue (down), and black (0) circles, respectively] to generate an actuation rotating in the direction of the thick brown arrows. $A \approx 1.002$ and 0.998 are chosen to optimize the acoustic rotation for the nonrotating actuation [see Eq. (29)].

2. *Acoustic body force and angular momentum density*

In Fig. 5, we validate our analysis in Sec. V of rotating double modes induced by a nonrotating actuation. For the double mode $200 + 020$, we plot the body force $\boldsymbol{f}_{\mathrm{ac}} = \boldsymbol{f}_{020}^{200}$ from Eq. (17), which according to Eq. (7) is the source of the bulk-driven acoustic streaming, and the acoustic angular momentum density $\boldsymbol{\mathcal{L}}_{\mathrm{ac}} = \boldsymbol{\mathcal{L}}_{020}^{200}$ from Eq. (18b) in the center plane $z = \frac{1}{2}L_z$. We show results for three different cavity aspect ratios $A = L_x/L_y$ for both the nonrotating wide Gaussian actuation $G_1(x, y)$, given in Eq. (30), and for the externally controlled rotating actuation $G_{16}(x, y)$ consisting of four quadruples of narrow Gaussian actuations [see Eq. (C1) of Appendix C]. As expected, the nonrotating actuation G_1 used in Figs. 5(a)–5(c) induces no acoustic rotation for a perfect square cavity $A = 1$ [Fig. 5(b)], while it induces different rotation directions for A slightly larger and smaller than unity [see Figs. 5(a) and 5(c), respectively]. In contrast, the rotating actuation G_{16} used in Figs. 5(d)–5(f) for the same three aspect ratios, induces an acoustic rotation, which is maximized in the perfect square cavity $A = 1$ [see Fig. 5(e)]. We show in Eq. (C4) of Appendix C that this rotating actuation excites the modes 200 and 020 with a phase difference $\phi_{\mathrm{act}}^{020} - \phi_{\mathrm{act}}^{200} \approx 0.5\pi$ such that the factor $\mathcal{F}_{020}^{200}$ in Eq. (19) is positive, and consequently the rotation pattern in Figs. 5(d)–5(f) is in the same direction as shown in Fig. 2(c).

In Fig. 6 we investigate the strength and rotation direction of the body force $\boldsymbol{f}_{020}^{200}$ as a function of the mode separation

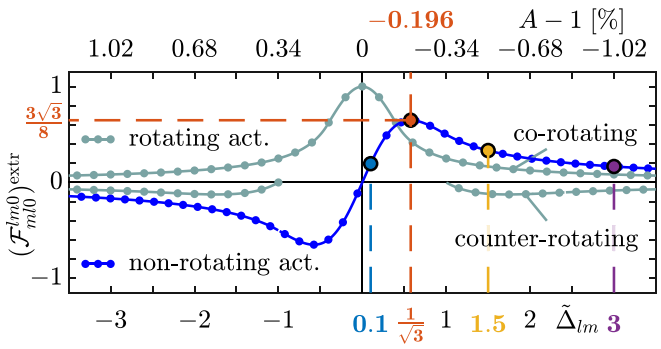

FIG. 6. The largest possible value (positive and negative) of $\mathcal{F}_{ml0}^{lm0} \propto \boldsymbol{f}_{\mathrm{ac}}$ versus varying mode separation $\tilde{\Delta}_{lm}$ (lower x axis) or aspect ratio A (upper x axis), shown for nonrotating actuations (blue) and rotating actuations (light cyan). The numerical values (dots) are found by evaluating $(\mathcal{F}_{020}^{200})_{\mathrm{num}}$ from Eq. (36) in the simulation of the double mode 200 + 020 shown in Figs. 5(a)–5(c) for the nonrotating and Figs. 5(d)–5(f) for the rotating actuation. The analytical curves (solid) are from the expressions derived in Eq. (B4a) (nonrotating act.), Eq. (B7a) (rotating act., corotating), and Eq. (B8a) (rotating act., counter-rotating) of Appendix B. The black-edged circles correspond to those of the same color in Fig. 3(c).

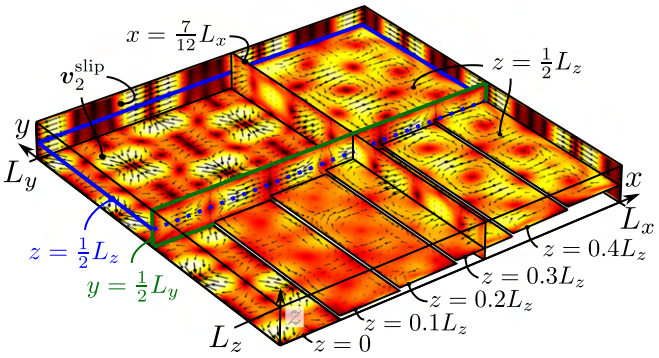

FIG. 7. Numerical simulation of the acoustic streaming velocity $\boldsymbol{v}_2$ (black arrows) and its magnitude from 0 (black) to 0.17 mm/s (white) induced by the nonrotating actuation G_1. The setup and the parameters are the same as in Fig. 4 with the parameters listed in Tables II and III. The horizontal plane at $z = \frac{1}{2}L_z$ (dark blue edge) and the vertical plane at $y = \frac{1}{2}L_y$ (light green edge) are displayed in Fig. 8.

$\tilde{\Delta}_{20}$ or, equivalently, the aspect ratio A. From Eq. (17a), this dependency is quantified through the factor $\mathcal{F}_{020}^{200}$ which we obtain numerically from the simulation of the double mode 200 + 020 in Fig. 5 by calculating the acoustic angular momentum $\boldsymbol{\mathcal{L}}_{\mathrm{ac}}$ and using Eq. (18b):

$$\left(\mathcal{F}_{020}^{200}\right)_{\mathrm{num}} \approx \frac{\mathcal{L}_{\mathrm{ac},z}\left(\frac{1}{4}L_x, \frac{1}{4}L_y\right)}{\left|P_1^{200}\right|\left|P_1^{020}\right|\left(\omega\rho_{\mathrm{fl}}c_0^2\right)^{-1}}. \tag{36}$$

Here, for pressure amplitudes $|P_1^{200}| = |P_1^{020}| = 1$ MPa, the denominator evaluates to 0.954×10^{-4} kg m^{-1} s^{-1}, which is indeed the maximum value found numerically in Fig. 5(e), such that $(\mathcal{F}_{020}^{200})_{\mathrm{num}}$ takes the maximum value of unity, as expected. In Fig. 6 we plot the largest possible value of $(\mathcal{F}_{020}^{200})_{\mathrm{num}}$ both for the nonrotating actuation used in Figs. 5(a)–5(c) and for the rotating actuation used in Figs. 5(d)–5(f). We also plot the analytical expressions for $(\mathcal{F}_{ml0}^{lm0})_{\mathrm{ana}}^{\mathrm{extr}}$ derived in Appendix B and find a quantitative agreement better than 1%. For the nonrotating actuation (the dark blue curve in Fig. 6), the acoustic rotation direction is determined by the aspect ratio A, and it reverses as A crosses over from $A < 1$ to $A > 1$ around the perfect square $A = 1$. For the rotating actuation (the light blue curves in Fig. 6), the rotation direction can be either corotating or counter-rotating (at different frequencies) with respect to the rotation direction of the actuation. However, for small mode separations $|\tilde{\Delta}_{lm}| < 1$, which for the double mode 200 + 020 corresponds to $|A - 1| < 0.34\%$, the rotation direction of the acoustic field can only be corotating. For further details, see Appendix B.

3. Acoustic streaming

In Fig. 7, we show the acoustic streaming velocity $\boldsymbol{v}_2$ in 3D resulting from the double mode 600 + 060 displayed in Fig. 4(a), which is excited by the nonrotating actuation G_1. As mentioned above, this situation is similar to that investigated experimentally by Hägsater *et al.* [39]. Remarkably, in the optimized geometry of Fig. 7, the horizontal 6 × 6 streaming-roll pattern at any height $0 \leqslant z \leqslant L_z$ is strongest in the center of the cavity, $z = \frac{1}{2}L_z$, thus indicating its bulk-driven origin. In the bottom plane $z = 0$ (shown in Fig. 7) and in the top plane $z = L_z$ (not shown in Fig. 7), the slip velocity $\boldsymbol{v}_2^{\mathrm{slip}}$ is dominated by the gradient term in the expression (7e) for the slip velocity, and has only a weak rotating component.

In Fig. 8, we compare the results for the acoustic streaming $\boldsymbol{v}_2$ [see Eq. (7)] for the double modes $l00 + 0l0$ with $l = 2, 4, 6$. The streaming is shown in the horizontal x-y center plane at height $z = \frac{1}{2}L_z$ (dark blue edge in Fig. 7) and in the vertical x-z center plane at $y = \frac{1}{2}L_y$ (light green edge in Fig. 7). In the first row [Figs. 8(a)–8(c)] we show the bulk-driven streaming alone ($\boldsymbol{f}_{\mathrm{ac}}$ on, $\boldsymbol{v}_2^{\mathrm{slip}}$ off); in the second row [Figs. 8(d)–8(f)] we show the boundary-driven streaming alone ($\boldsymbol{f}_{\mathrm{ac}}$ off, $\boldsymbol{v}_2^{\mathrm{slip}}$ on); in the third row [Figs. 8(g)–8(i)] we show the total streaming ($\boldsymbol{f}_{\mathrm{ac}}$ on, $\boldsymbol{v}_2^{\mathrm{slip}}$ on). Comparing the bottom-row and top-row panels in Fig. 8 strongly indicate that the respective 4 × 4 and 6 × 6 streaming-roll patterns in Figs. 8(h) and 8(i) are bulk driven. Furthermore, Figs. 8(a)–8(c) show that the bulk-driven acoustic streaming becomes stronger for higher mode number l and thus for higher frequency f. In contrast, the boundary-driven acoustic streaming [Figs. 8(d)–8(f)] stays almost constant in amplitude and shows no frequency dependency. Note that the bulk-driven streaming in Figs. 8(a)–8(c) has its maximum velocity v_2^{max} in the bulk of the fluid whereas the boundary-driven streaming in Figs. 8(d)–8(f) has its maximum velocity v_2^{max} at the boundaries.

4. Comparison with the analytical expression for the bulk-driven streaming

When the no-slip condition on the vertical side walls is ignored, we can derive an approximate analytical expression for the bulk-driven streaming $(\boldsymbol{v}_2^{\mathrm{blk}})_{l0}$ for the double modes $l00 + 0l0$. The details are given in Appendix D, where we find $(\boldsymbol{v}_2^{\mathrm{blk}})_{l0}$ to be proportional to the acoustic energy flux density

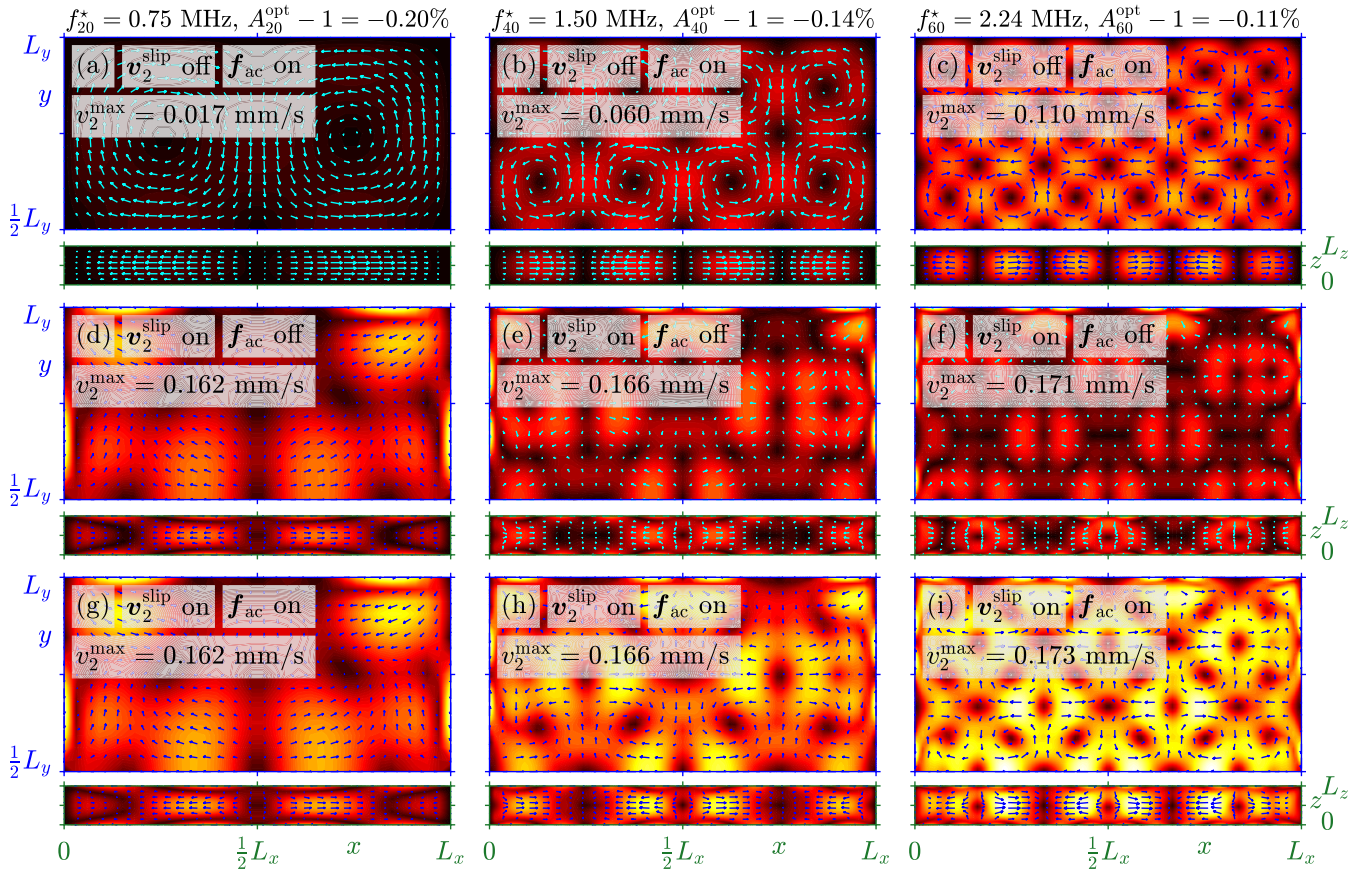

FIG. 8. Simulation of the acoustic streaming velocity $\boldsymbol{v}_2$ in water from 0 (black) to 0.17 mm/s (white) in the horizontal (x-y) center plane at $z = \frac{1}{2}L_z$ (dark blue edge as in Fig. 7) and the vertical (x-z) center plane at $y = \frac{1}{2}L_y$ (light green edge as in Fig. 7). The length of the longest arrow represents $v_2^{\rm max}$ listed in each plot. The used parameters are listed in Tables II and III. In each column the double mode $l00 + 0l0$ is excited for $l = 2$, 4, and 6, respectively. The first row (a)–(c) shows the bulk-driven streaming, the second row (d)–(f) shows the boundary-driven streaming, and the third row (g)–(i) shows the total streaming. 3D results corresponding to (i) are shown in Fig. 7.

$\boldsymbol{S}_{l0} = \boldsymbol{S}_{0l0}^{l00}$ of Eq. (18a):

$$\left(\boldsymbol{v}_2^{\rm blk}\right)_{l0} = \frac{1}{2}\left(\frac{4}{3} + \frac{\eta_{\rm fl}^{\rm b}}{\eta_{\rm fl}}\right)\left[1 - \frac{\cosh\left(\frac{2z-L_z}{\sqrt{2}}k_{l0}^\star\right)}{\cosh\left(\frac{1}{\sqrt{2}}k_{l0}^\star L_z\right)}\right]\kappa_{\rm fl}\boldsymbol{S}_{l0}. \quad (37)$$

Inserting here $k_{l0}^\star = \frac{l\pi}{L^\star}$ and expression (18a) for $\boldsymbol{S}_{l0}$ with $\mathcal{F}_{l0} = \frac{3\sqrt{3}}{8}$ from Eq. (29c), we obtain the maximum value of the bulk-driven streaming velocity in the center plane $z = \frac{1}{2}L_z$:

$$\left(v_2^{\rm blk}\right)_{l0}^{\rm max} = \frac{3\sqrt{3}\left[1 - \operatorname{sech}\left(\frac{l\pi L_z}{\sqrt{2}L^\star}\right)\right]\left(\frac{4}{3} + \frac{\eta_{\rm fl}^{\rm b}}{\eta_{\rm fl}}\right)\left|P_1^{l00}\right|\left|P_1^{0l0}\right|}{32\rho_{\rm fl}^2 c_{\rm fl}^3}. \quad (38)$$

For the three cases shown in Figs. 8(a)–8(c), where we have used $P_1^{l00} = P_1^{0l0} = 1$ MPa and $l = 2, 4, 6$, respectively, we calculate from Eq. (38) the maximum values 0.018, 0.060, and 0.102 mm/s, which deviate less than 7% from the corresponding results 0.017, 0.060, and 0.110 mm/s from the numerical simulation, listed in Figs. 8(a)–8(c). For $l = 2$, the analytical prediction of 0.018 mm/s overestimates by 5% the numerical value 0.017 mm/s because it neglects the significant viscous damping from the vertical side walls in this case. For $l = 6$, the analytical prediction of 0.102 mm/s underestimates by 7% the numerical value 0.110 mm/s because the latter includes the coupling to the vertical 001 mode through the wide $\frac{1}{2}L^\star$-width vertical G_1 actuation as discussed in Sec. VI C 1. When changing to the narrow $\frac{1}{12}L^\star$-width vertical G_1 actuation, also discussed in Sec. VI C 1, the coupling to the vertical 001 mode diminishes so much that the numerical streaming amplitudes become 0.017, 0.060, and 0.103 mm/s for $l = 2, 4, 6$, respectively, where the latter now deviates less than 1% from the analytical prediction 0.102 mm/s. These numerical results for the acoustic streaming are shown in a pdf file[4] in the Supplemental Material [41].

5. *Bulk-driven versus boundary-driven streaming rolls*

We address the question on whether the horizontal streaming rolls in the xy plane are due to the bulk-driven streaming or the boundary-driven streaming. We restrict the discussion to horizontal double modes $l00 + 0l0$, for which we have found the analytical expressions for the bulk-driven streaming $(\boldsymbol{v}_2^{\rm blk})_{l0}$ [Eq. (37)] and the slip velocity $\boldsymbol{v}_2^{\rm slip}$ [Eq. (7e)] at the top ($z = L_z$) and bottom ($z = 0$) boundaries.

[4] "`fig_08_narrow_G1.pdf`"

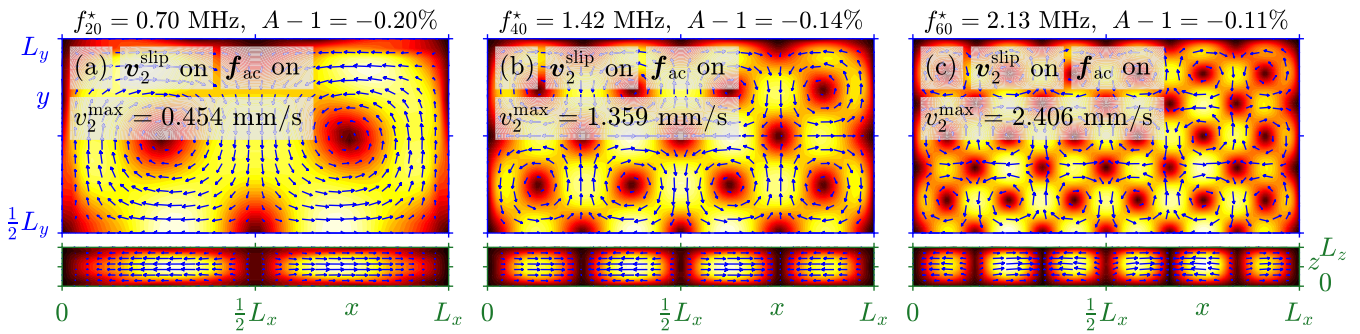

FIG. 9. Simulation of the acoustic streaming $\boldsymbol{v}_2$ from 0 mm/s (black) to $v_2^{\max}$ (white) for the exact same geometry as in Figs. 8(g)–8(i), but with the water replaced by pyridine, having the material parameters listed in Table II and actuation amplitude u^0_{1z} and actuation frequency $f^\star_{l0}$ given in Table III. The maximum values in (a)–(c) are 2.8, 8.2, and 13.9 times the corresponding values in Figs. 8(g)–8(i).

According to Eq. (7e), the boundary-driven streaming velocity at the double-mode resonance $l00 + 0l0$ is driven by a slip velocity, which contains the term $\frac{1}{2}\kappa_{\text{fl}}\boldsymbol{S}_{\text{ac}}$ that rotates in the direction of the acoustic energy flux density $\boldsymbol{S}_{\text{ac}}$, just as the bulk-driven streaming [see Eq. (37)]. The other terms in the slip velocity have similar magnitude, but they are gradient terms which cannot drive a rotating streaming in the horizontal xy plane. Therefore, as seen in Figs. 8(d)–8(f), the boundary-driven streaming does not lead to horizontal flow rolls as clearly as the bulk-driven streaming does [see Figs. 8(a)–8(c)]. There may, however, exist horizontal planes at a few specific heights z, where the horizontal flow-roll pattern appears more clearly as suggested by Lei *et al.* [43] and analyzed further by Skov *et al.* [44].

By using Eqs. (7e) and (37), we compute the ratio of the horizontally rotating bulk-driven streaming $|[\boldsymbol{v}_2^{\text{blk}}(z = \frac{L_z}{2})]_{l0}|$ in the center of the cavity to the horizontally rotating boundary-driven streaming $|\frac{1}{2}\kappa_{\text{fl}}\boldsymbol{S}_{\text{ac}}(z = 0)|$ at the bottom boundary,

$$\frac{\left|\left[\boldsymbol{v}_2^{\text{blk}}\left(z = \frac{L_z}{2}\right)\right]_{l0}\right|}{\left|\frac{1}{2}\kappa_{\text{fl}}\boldsymbol{S}_{l0}(z = 0)\right|} = \left(\frac{4}{3} + \frac{\eta^{\text{b}}_{\text{fl}}}{\eta_{\text{fl}}}\right)\left[1 - \operatorname{sech}\left(\frac{l\pi L_z}{\sqrt{2}L^\star}\right)\right]. \quad (39)$$

This velocity ratio takes values from 0 (boundary-driven streaming dominates) for a flat cavity $lL_z \ll L^\star$ to $\frac{4}{3} + \frac{\eta^{\text{b}}_{\text{fl}}}{\eta_{\text{fl}}}$ (bulk-driven streaming dominates) for a high cavity $lL_z \gg L^\star$. For water, the velocity ratio (39) lies between 0 and 4.13, and in the setup of Figs. 4–8 with $L_z = 0.1L^\star$ and water as the fluid, we obtain the values of the velocity ratio to be 0.38, 1.22, and 2.09 for $l = 2$, 4, and 6, respectively. This result indicates that the 6×6 streaming roll pattern with $l = 6$ observed by Hagsäter *et al.* [39] is predominantly bulk-driven, as also seen by comparing Figs. 8(c) and 8(i). In contrast, for the lower mode $l = 2$, the horizontal streaming rolls are predominantly boundary driven, which is seen by comparing Figs. 8(d) and 8(g).

The crossover from boundary- to bulk-driven horizontal streaming rolls may be characterized by the height-to-width ratio $B = lL_z/L^\star$: we compute the critical value B^{crit}, where the velocity ratio (39) is unity, and thus,

$$l\frac{L_z}{L^\star} < B^{\text{crit}}, \quad \text{boundary-driven streaming dominates},$$
$$l\frac{L_z}{L^\star} > B^{\text{crit}}, \quad \text{bulk-driven streaming dominates}. \quad (40)$$

For water, Eq. (39) leads to the ratio $B^{\text{crit}}_{\text{water}} = 0.35$, and since $L_z = 0.1L^\star$ in the setup of Figs. 4–8, we find that the horizontal streaming rolls in the double modes $l00 + 0l0$ with $l \leqslant 3$ are predominantly boundary driven, while for $l \geqslant 4$ they are bulk driven.

6. *Enhancement of the bulk-driven streaming velocity by increasing the bulk viscosity*

For a given resonance mode with a given acoustic pressure amplitude in a given geometry, we obtain from Eqs. (38) and (7e) the following scaling laws for the bulk- and boundary-driven streaming, respectively:

$$v_2^{\text{blk}} \propto \frac{1}{\rho_{\text{fl}}^2 c_{\text{fl}}^3}\left(\frac{4}{3} + \frac{\eta^{\text{b}}_{\text{fl}}}{\eta_{\text{fl}}}\right), \quad (41a)$$
$$v_2^{\text{slip}} \propto \frac{1}{\rho_{\text{fl}}^2 c_{\text{fl}}^3}. \quad (41b)$$

To study the consequences of these scaling laws, we have chosen to compare water with the heterocyclic organic compound pyridine having the chemical formula C_5H_5N. Table II reveals that pyridine has the same material parameters (within 5%) as water, but a bulk viscosity $\eta^{\text{b}}_{\text{fl}}$ that is 25.1 times larger than that of water. Using these parameter values in Eq. (41), we find a large enhancement of the bulk-driven streaming, while the boundary-driven streaming is nearly unchanged:

$$v^{\text{blk}}_{2,\text{pyridine}} = 21.3\, v^{\text{blk}}_{2,\text{water}}, \quad (42a)$$
$$v^{\text{slip}}_{2,\text{pyridine}} = 1.2\, v^{\text{slip}}_{2,\text{water}}. \quad (42b)$$

We test this prediction in Fig. 9, where we show simulations of the total acoustic streaming in pyridine in the same geometry as in Figs. 8(g)–8(i) but with adjusted actuation amplitude u^0_{1z} and frequency f given in Table III to maintain the same pressure amplitudes $P_1^{l00} = P_1^{0l0} = 1$ MPa. As expected, we find that the total acoustic streaming for the three double modes is enhanced compared to that in water shown in Figs. 8(g)–8(i), and the enhancement factors are 2.8, 8.2, and 13.9, respectively. The increasing factors reflect the increasing weight of bulk-driven relative to boundary-driven streaming as the mode index l increases. The enhancement factors for the bulk-driven streaming alone (not shown in Fig. 9) are 21.4, 21.1, and 21.2, as predicted by Eq. (42a), while they are 1.2,

1.2, and 1.3 for boundary-driven streaming alone (also not shown in Fig. 9) in good agreement with Eq. (42b).

For all three cases $l = 2$, 4, and 6, the horizontally rotating bulk-driven streaming in the center $z = \frac{1}{2}L_z$ is larger than the horizontally rotating boundary-driven streaming at the top-bottom boundaries $z = 0$ and $z = L_z$. This is also predicted by Eq. (40) since $l\frac{L_z}{L^\star} = 0.2, 0.4, 0.6 > B^{\text{crit}}_{\text{pyridine}} = 0.08$ for all three modes in pyridine.

VII. DISCUSSION

In the following, we raise a few discussion points related to the results of the above analysis, which are based on the single- and double-mode resonances occurring in a closed rectangular-box-shaped cavity with narrow viscous boundary layers. We note that the idealized, hard-wall, numerical model for the acoustic streaming is strikingly sensitive to small differences of only 0.1% between the cavity side lengths L_x and L_y. Our results for the resonance frequency in Eq. (10) and the optimal aspect ratio in Eq. (29f) are therefore crucial in the investigation of the largest possible bulk-driven acoustic streaming. This optimization was not taken into account in the experimental study by Hagsäter *et al.* [39], and the corresponding numerical simulation by Skov *et al.* [44] of the shallow, nearly square cavity of aspect ratio of $A = 0.990$. As this aspect ratio differs from the optimal value $A = 0.999$ for the hard-wall device in Fig. 8(i), it may be possible to increase the bulk-driven acoustic streaming significantly by fine tuning the geometry.

A priori, one may argue that it is difficult to obtain these optimal conditions with a relative precision of the order of 0.1% in experiments. However, comparing our Fig. 7 with the experimental results in Hagsäter *et al.* [39], we find good qualitative agreement even though none of the optimal conditions were considered when designing the nearly square fluid cavity. Another example is provided by the straight microchannel with a square cross section and nonrotating actuation that was studied experimentally by Antfolk *et al.* [11]. There, a single large vertical streaming roll similar to Fig. 2(b) was observed experimentally and analyzed numerically in terms of a double-mode excitation.

There may be several reasons for why the bulk-driven acoustic streaming can be observed experimentally in spite of the low 0.1%-tolerance level of the aspect ratio suggested by our simplified, hard-wall, microcavity analysis in Fig. 6. First, there are other damping mechanisms in a real experiment [42], aside from the bulk and boundary-layer damping considered here, which may broaden the resonance peaks significantly and thereby increase the change for overlapping resonances. Second, the double-mode body force $\boldsymbol{f}^{lmn}_{l'm'n'}$ in Eq. (17a), which is the source of the bulk-driven acoustic streaming, depends on the product $|P_1^{lmn}||P_1^{l'm'n'}|$ of the mode amplitudes, and therefore one can obtain a rotating body force even if the pressure is dominated by one of the modes, say lmn, as long as the other mode $l'm'n'$ is just weakly represented. Third, in typical experiments, the driving frequency is scanned over a broad span of frequencies, say 100 kHz around 2 MHz, which increases the possibility for exciting double-mode resonances. Fourth, unintentional asymmetries and imperfections in the experimental setup may cause modes to overlap locally in some regions at some frequencies and in other regions at other frequencies, rather than the idealized homogeneous pattern at a single frequency shown in Fig. 7. This point was also mentioned by Hagsäter *et al.*: "*If the frequency is shifted slightly in the vicinity of 2.17 MHz, the same vortex pattern will still be visible, but the strength distribution between the vortices will be altered.*" Moreover, in the 3D simulation by Skov *et al.* [44], including the surrounding solid and the piezoelectric transducer, this inhomogeneous distribution of the streaming was indeed reproduced in their Fig. 2(b2). Revisiting the experiment by Antfolk *et al.* [11] of a long straight capillary of square cross section, this effect may also be observed because it is likely that the aspect ratio is slightly less than unity in some regions of the capillary and slightly above unity in other regions, thereby causing the rotation direction to alternate along the channel.

We have in this work mainly considered horizontal acoustics with $n = 0$ half-waves in the vertical z direction. A similar analysis can be done for perpendicular acoustics (with respect to the top and bottom boundaries). In Secs. VI C 1 and VI C 4, we have already briefly discussed the role of the vertical single mode 001 for the pressure p_1 and the streaming $\boldsymbol{v}_2$. It is of course also possible to consider vertical rotating double modes involving, say, a single half-wave in the vertical direction $lm1 + l'm'1$. For relatively shallow cavities, a vertical excitation implies a relatively high frequency and a correspondingly increased body force $\boldsymbol{f}_{\text{ac}}$. Furthermore, for perpendicular acoustics where $\partial_\perp v_{1\perp} \approx \boldsymbol{\nabla}\cdot\boldsymbol{v}_1 = i\omega\kappa_{\text{fl}}p_1$, the slip velocity $\boldsymbol{v}_2^{\text{slip}}$ on the top and bottom boundaries is dominated by the first and last terms in Eq. (7e), $\boldsymbol{v}_2^{\text{slip}} \approx \frac{1}{2}\kappa_{\text{fl}}\boldsymbol{S}_{\text{ac}} + \frac{3}{4\omega}\text{Re}[i\partial_\perp v_{1\perp}\boldsymbol{v}^*_{1\parallel}] \approx -\kappa_{\text{fl}}\boldsymbol{S}_{\text{ac}}$. Remarkably, this slip velocity is in the opposite direction of the body force $\boldsymbol{f}_{\text{ac}} \propto \boldsymbol{S}_{\text{ac}}$, so we expect that the bulk- and boundary-driven streaming will be in opposite directions, and thus the cavity could be designed such that these streaming flows tend to cancel. A study of this effect is left for future work.

The bulk-driven acoustic streaming is due to the body force $\boldsymbol{f}_{\text{ac}}$, which we have given in Eq. (7d) for homogeneous fluids. As shown by Karlsen and Bruus [49], this body force contains additional terms if the fluid is inhomogeneous. Furthermore, the analysis by Muller and Bruus [45] showed how thermoviscous effects strongly influence the boundary-driven streaming. The incorporation of inhomogeneities and thermodynamics in future work is therefore expected to reveal a strong effect also on the bulk-driven streaming.

VIII. CONCLUSION

We have derived analytical expressions for the single-mode pressure resonances $p_1^{lmn} = P_1^{lmn}F^{lmn}R^{lmn}$ and the corresponding boundary-layer damping coefficients Γ_{bl}^{lmn} for a closed rectangular-box-shaped cavity with narrow viscous boundary layers (see Sec. III A and Appendix A). Based on these expressions, we have shown that the body force $\boldsymbol{f}_{\text{ac}}$ can drive a strong bulk-driven acoustic streaming, if two overlapping single modes are excited simultaneously at the same frequency, thereby forming a double-mode resonance $lmn + l'm'n'$ (see Secs. III B and IV). In contrast to the conventional wisdom that the bulk-driven streaming can be ignored

on the scale of a few acoustic wavelengths, these double modes constitute an important example where the bulk-driven streaming is significant.

We have shown in Eq. (8) that the appearance of bulk-driven streaming in closed microcavities is directly related to the amount of rotation (acoustic angular momentum density) of the underlying acoustic fields. Whereas there is no rotation in a single mode, we have demonstrated in Secs. IV B and V that the double modes can be rotating not only due to an externally controlled rotating actuation, but, remarkably, also due to a nonrotating actuation coupled with a weak asymmetry in the geometry of the cavity. Furthermore, in Sec. V we have derived analytical expressions for the optimal aspect ratios that maximize the bulk-driven streaming in a nearly square cavity with a nonrotating actuation. We found that the bulk-driven acoustic streaming is sensitive to small deviations between the cavity side lengths of only 0.1%.

We have validated the theory by direct numerical simulation in Sec. VI of the double modes $200+020$, $400+040$, and $600+060$ in a nearly square cavity with side lengths $L_x \approx 2000\ \mu$m and $L_y \approx 2000\ \mu$m and height $L_z = 200\ \mu$m, similar to the device investigated experimentally by Hagsäter *et al.* [39]. Using the analytically known optimal conditions (29), for which the bulk-driven acoustic streaming is maximized, we have avoided the otherwise required time-consuming parametric sweeping in geometry and frequency to locate these optimal conditions. The numerical results shown in Figs. 4–6 agree with the analytical expressions with a relative accuracy better than 1%.

In Fig. 7, the 3D simulation of the acoustic streaming of the double mode $600+060$ is seen to reproduce the horizontally rotating 6×6 streaming-roll pattern observed by Hagsäter *et al.* In Fig. 8 we showed that this streaming pattern at the higher frequency 2.24 MHz is dominated by the bulk-driven streaming, whereas the streaming of the double mode $200+020$ at the lower frequency 0.75 MHz is dominated by the boundary-driven streaming. This frequency-dependent crossover occurs because the body force $\boldsymbol{f}_{\rm ac}$ increases as frequency to the power two, whereas the slip velocity $\boldsymbol{v}_2^{\rm slip}$ depends only weakly on frequency [see Eq. (7)]. An analytical expression for computing the crossover for the double mode $l00+0l0$ is given in Eq. (39).

Finally, in agreement with Eckart [29], we have shown in Eq. (37) that the bulk-driven acoustic streaming increases with the ratio $\frac{\eta_{\rm fl}^{\rm b}}{\eta_{\rm fl}}$ between the bulk and the dynamic viscosity. This dependency on $\eta_{\rm fl}^{\rm b}$ was studied numerically in Sec. VI C 6 by exchanging the water in the microcavity with pyridine. As shown in Fig. 9, we found that the bulk-driven streaming for pyridine was enhanced by a factor $\simeq$21 relative to water. This prediction obviously calls for experimental validation.

In this paper we have pointed out the significance of the bulk-driven acoustic streaming in resonating acoustic cavities even when the geometry length scale is comparable to a few half-wavelengths. The fundamental requirement for obtaining this effect is the existence of two overlapping resonance modes excited simultaneously at the same frequency. This requirement is easily fulfilled in integrable geometries in 3D, such as rectangular, cylindrical, and spherical cavities, or in 2D, such as rectangular and circular cross sections of long, straight capillary channels, all of which are frequently encountered in experiments reported in the literature. The insight provided by our analysis is therefore relevant and important for acoustofluidics in general, both for fundamental studies and for technological applications.

APPENDIX A: ACOUSTIC PRESSURE IN A RECTANGULAR BOX WITH BOUNDARY LAYERS

In this Appendix, we derive the solution for the acoustic pressure p_1 with boundary layers in a rectangular-box-shaped cavity Ω for which $0\leqslant x\leqslant L_x$, $0\leqslant y\leqslant L_y$, and $0\leqslant z\leqslant L_z$. The governing equation and boundary conditions for p_1 are given in Eq. (3). We consider first an actuation $U_{1\perp}(x,y)$ which is only nonzero at the bottom boundary $z=0$. The solution for a general actuation on all six boundaries is then finally constructed by superposition. Using separation of variables to solve the Helmholtz equation (3a) gives p_1 in the following form:

$$\begin{aligned} p_1 &= X(x)Y(y)Z(z), \quad k_{\rm c}^2 = k_x^2+k_y^2+k_z^2,\\ X(x) &= C_x\cos(k_x x)+S_x\sin(k_x x),\\ Y(y) &= C_y\cos(k_y y)+S_y\sin(k_y y),\\ Z(z) &= C_z\cos(k_z z)+S_z\sin(k_z z). \end{aligned} \tag{A1}$$

Inserting this form into boundary condition (3b) gives

$$[\partial_\perp+\alpha_\perp]p_1 = \frac{k_0^2 U_{1\perp}}{\kappa_{\rm fl}}, \tag{A2a}$$

$$\alpha_\perp = \alpha_\perp(k_\perp) = \frac{1+i}{2}\delta\left(k_{\rm c}^2-k_\perp^2\right), \quad \perp = x,y,z, \tag{A2b}$$

where $\perp$ is the *inward* direction perpendicular to the boundary, and the quantity $\alpha_\perp$ is the boundary-layer correction to the *inward*-normal derivative of p_1. Note that $\partial_\perp$ has a sign change at two opposite boundaries, say $x=0$ and L_x, for which $\partial_\perp=\partial_x$ and $-\partial_x$, respectively, whereas $\alpha_\perp(k_\perp)$ depends on $k_\perp^2=k_x^2$, without a sign change at opposite boundaries. We assume in the following that the length scale introduced by $\alpha_\perp$ is much longer than the cavity length scale $L_\perp$:

$$|\alpha_\perp|L_\perp \ll 1, \quad \perp = x,y,z. \tag{A3}$$

According to Eq. (A2), the boundary conditions at the stationary boundaries at $x=0$ and L_x are

$$\underline{x=0}: \qquad C_x\alpha_x + S_x k_x = 0, \tag{A4a}$$

$$\begin{aligned} \underline{x=L_x}: \quad & C_x[k_x\sin(k_x L_x)+\alpha_x\cos(k_x L_x)]\\ & + S_x[-k_x\cos(k_x L_x)+\alpha_x\sin(k_x L_x)] = 0, \end{aligned} \tag{A4b}$$

where $\alpha_\perp=\alpha_x$ in both equations, whereas $\partial_\perp=\partial_x$ in Eq. (A4a), while $\partial_\perp=-\partial_x$ in Eq. (A4b). Nontrivial solutions with C_x and S_x different from zero must satisfy the usual criterion for the equation determinant $\mathcal{D}_x(k_x)$:

$$\mathcal{D}_x(k_x) = 0, \text{ with} \tag{A5a}$$

$$\mathcal{D}_x(k_x) = \left(k_x^2-\alpha_x^2\right)\sin(k_x L_x)+2k_x\alpha_x\cos(k_x L_x). \tag{A5b}$$

We write the solutions $k_x = k_x^l$ to Eq. (A5a) as perturbations away from the inviscid solutions K_x^l,

$$k_x^l = K_x^l + \epsilon_x^l, \quad K_x^l = \frac{l\pi}{L_x}, \quad l = 0, 1, 2, \ldots, \tag{A6}$$

where $\epsilon_x^l L_x \ll 1$. By inserting this into Eq. (A5b), expanding in ϵ_x^l, and writing $\alpha_x^l = \alpha_x(k_x^l)$, we find

$$\mathcal{D}_x(k_x^l) = (-1)^l\left\{\left[\left(K_x^l + \epsilon_x^l\right)^2 - \left(\alpha_x^l\right)^2\right]\epsilon_x^l L_x + 2\left(K_x^l + \epsilon_x^l\right)\alpha_x^l\right\}. \tag{A7}$$

From assumption (A3), $(\alpha_x^l)^2\epsilon_x^l L_x = [\alpha_x^l L_x]\epsilon_x^l\alpha_x^l$ is much smaller than $2\epsilon_x^l\alpha_x^l$, so it can be ignored. We then factorize out $K_x^l + \epsilon_x^l = k_x^l$ and obtain

$$\begin{aligned}\mathcal{D}_x(k_x^l) &\approx (-1)^l k_x^l\left\{\left(K_x^l + \epsilon_x^l\right)\epsilon_x^l L_x + 2\alpha_x^l\right\} \\ &= (-1)^l k_x^l\left\{k_x^l\left(k_x^l - K_x^l\right)L_x + 2\alpha_x^l\right\}.\end{aligned} \tag{A8}$$

For $l = 0$, we have $K_x^0 = 0$ and $k_x^0(k_x^0 - K_x^0) = (k_x^0)^2$, while for $l > 0$ we have $k_x^l(k_x^l - K_x^l) \approx \frac{1}{2}(k_x^l + K_x^l)(k_x^l - K_x^l)$ to first order in ϵ_x^l. In either case, by introducing L_x^l as

$$L_x^l = \tfrac{1}{2}(1 + \delta_{0l})L_x, \tag{A9}$$

the resulting expression for $\mathcal{D}_x(k_x^l)$ for all l is written as

$$\mathcal{D}_x\left(k_x^l\right) \approx (-1)^l k_x^l L_x^l\left[\left(k_x^l\right)^2 - \left(K_x^l\right)^2 + \frac{2\alpha_x^l}{L_x^l}\right]. \tag{A10}$$

The wave numbers k_x^l thus fulfill the zero-determinant criterion (A5a) $\mathcal{D}_x(k_x^l) = 0$ if

$$\left(k_x^l\right)^2 = \left(K_x^l\right)^2 - \frac{2\alpha_x^l}{L_x^l}, \tag{A11}$$

and similarly for $(k_y^m)^2$ for all l and m. From Eqs. (A1) and (A4a) with $k_x = k_x^l$, we obtain the corresponding eigenfunctions $X^l(x)$,

$$X^l(x) = \cos\left(k_x^l x\right) - \frac{\alpha_x^l}{k_x^l}\sin\left(k_x^l x\right), \tag{A12}$$

where the prefactor C_x^l is absorbed into $Z(z)$ in Eq. (A1). We examine the ratio $\frac{\alpha_x^l}{k_x^l}$ for all l using Eq. (A11):

$$\left(\frac{\alpha_x^0}{k_x^0}\right)^2 = -\frac{1}{2}L_x\alpha_x^0 \ll 1, \quad l = 0, \tag{A13a}$$

$$\frac{\alpha_x^l}{k_x^l} = \frac{1}{l\pi}L_x\alpha_x^l \ll 1, \quad l > 0. \tag{A13b}$$

By assumption (A3), we note that even for $l = 0$ this ratio is small, but not as small as for $l > 0$.

By inserting k_x^l from Eq. (A11) into Eq. (A12) and Taylor expanding in α_x^l/k_x^l, we recover the usual inviscid hard-wall eigenfunctions $\cos(K_x^l x)$ plus a small correction of the order $\alpha_x^l L_x$, due to the boundary layers

$$X^l(x) \approx \cos\left(K_x^l x\right) + \alpha_x^l L_x\begin{cases}\frac{x}{L_x}\left(\frac{x}{L_x} - 1\right), & l = 0, \\ \frac{\sin(K_x^l x)}{K_x^l L_x}\left(\frac{2x}{L_x} - 1\right), & l > 0.\end{cases} \tag{A14}$$

Note that $(\partial_x + \alpha_x^l)X^l|_{x=0} = (\partial_{-x} + \alpha_x^l)X^l|_{x=L_x} = 0$ as required by the boundary condition (A2). Similar expressions are valid for the y eigenfunctions $Y^m(y)$.

In general, the pressure is an infinite sum of the eigenfunctions

$$p_1 = \sum_{l,m=0}^{\infty} X^l Y^m Z^{lm}(z), \tag{A15a}$$

$$Z^{lm}(z) = C_z^{lm}\cos\left(k_z^{lm}z\right) + S_z^{lm}\sin\left(k_z^{lm}z\right), \tag{A15b}$$

$$\left(k_z^{lm}\right)^2 = k_c^2 - \left(k_x^l\right)^2 - \left(k_y^m\right)^2, \tag{A15c}$$

where k_z^{lm} depends on the angular frequency ω of the actuation through k_c. At $z = L_z$, the sets of coefficients C_z^{lm} and S_z^{lm} satisfy a condition similar to Eq. (A4b), which leads to

$$S_z^{lm} = \frac{k_z^{lm}\sin\left(k_z^{lm}L_z\right) + \alpha_z^{lm}\cos\left(k_z^{lm}L_z\right)}{k_z^{lm}\cos\left(k_z^{lm}L_z\right) - \alpha_z^{lm}\sin\left(k_z^{lm}L_z\right)}C_z^{lm}, \tag{A16}$$

where $\alpha_z^{lm} = \alpha_z(k_z^{lm})$. Further, at $z = 0$ we have a condition similar to Eq. (A4a) with $k_0^2\kappa_{\mathrm{fl}}^{-1}U_{1z}(x, y)$ on the right-hand side. Combined with Eqs. (A15) and (A16), the boundary condition at $z = 0$ becomes

$$\sum_{l,m=0}^{\infty}\frac{X^l(x)Y^m(y)\mathcal{D}_z\left(k_z^{lm}\right)C_z^{lm}}{k_z^{lm}\cos\left(k_z^{lm}L_z\right) - \alpha_z^{lm}\sin\left(k_z^{lm}L_z\right)} = \frac{k_0^2 U_{1z}(x, y)}{\kappa_{\mathrm{fl}}}, \tag{A17}$$

where $\mathcal{D}_z$ is defined similar to Eq. (A5b). To find the coefficients C_z^{lm}, we write the wall actuation function $U_{1z}(x, y)$ as a generalized Fourier series in the functions $X^l(x)$ and $Y^m(y)$ that form a complete basis set on the interval $0 \leqslant x \leqslant L_x$ and $0 \leqslant y \leqslant L_y$ to order $\alpha_x^l L_x$ and $\alpha_y^m L_y$, respectively:

$$U_{1z}(x, y) = \sum_{l,m=0}^{\infty}\hat{U}_{1z}^{lm}X^l(x)Y^m(y), \tag{A18a}$$

$$\hat{U}_{1z}^{lm} = \frac{\int_0^{L_y}\int_0^{L_x}U_{1z}(x, y)X^l(x)Y^m(y)\,dA}{\int_0^{L_y}\int_0^{L_x}[X^l(x)Y^m(y)]^2\,dA}. \tag{A18b}$$

Inserting the expansion (A18a) into Eq. (A17), we obtain the amplitudes C_z^{lm}:

$$C_z^{lm} \approx \frac{k_z^{lm}\cos\left(k_z^{lm}L_z\right) - \alpha_z^{lm}\sin\left(k_z^{lm}L_z\right)}{\mathcal{D}_z\left(k_z^{lm}\right)}\frac{k_0^2\hat{U}_{1z}^{lm}}{\kappa_{\mathrm{fl}}}. \tag{A19}$$

Finally, using Eq. (A16) for S_z^{lm} and Eq. (A19) for C_z^{lm} in Eq. (A15) for p_1, yields the expression for the pressure

$$p_1 = \sum_{lm=0}^{\infty}\frac{k_0^2 k_z^{lm}\hat{U}_{1z}^{lm}}{\kappa_{\mathrm{fl}}\mathcal{D}_z\left(k_z^{lm}\right)}X^l(x)Y^m(y)Z^{lm}(z), \tag{A20a}$$

$$Z^{lm}(z) = \cos\left[k_z^{lm}(L_z - z)\right] - \frac{\alpha_z^{lm}}{k_z^{lm}}\sin\left[k_z^{lm}(L_z - z)\right], \tag{A20b}$$

$$\left[k_z^{lm}(k_0)\right]^2 = (1 + i\Gamma_{\mathrm{fl}})k_0^2 - \left(k_x^l\right)^2 - \left(k_y^m\right)^2. \tag{A20c}$$

The infinite sum in Eq. (A20a) is general and applies to all frequencies and actuations at the bottom boundary. For a given actuation U_{1z}, this solution is largest for frequencies $\omega = c_{\rm fl}k_0$ where $\mathcal{D}_z(k_z^{lm})$ is smallest, which gives the hard-wall resonances lmn studied below. In real systems, the surrounding solid will have its own resonance properties and, therefore, the actuation U_{1z} will depend strongly on the frequency. In this case, the largest value of the prefactor $\frac{k_0^2 k_z^{lm}\hat{U}_{1z}^{lm}}{\kappa_{\rm fl}\mathcal{D}_z(k_z^{lm})}$ is not necessarily found where $\mathcal{D}_z(k_z^{lm})$ is smallest.

1. Single-mode resonances in a rectangular box

Resonance occurs when $k_0 = \frac{1}{c_{\rm fl}}\omega$ equals one of the values k_0^{lmn} that minimize $\mathcal{D}_z(k_z^{lm})$ in Eq. (A20a). We expect these values of k_0^{lmn} to be near the inviscid values K_0^{lmn}, and write, similar to Eq. (A6),

$$k_0^{lmn} = K_0^{lmn} + \epsilon_0^{lmn}, \tag{A21a}$$

$$K_0^{lmn} = \sqrt{\left(K_x^l\right)^2 + \left(K_y^m\right)^2 + \left(K_z^n\right)^2}, \tag{A21b}$$

$$K_x^l = \frac{l\pi}{L_x}, \quad K_y^m = \frac{m\pi}{L_y}, \quad K_z^n = \frac{n\pi}{L_z}, \tag{A21c}$$

where ϵ_0^{lmn} should be chosen to minimize $\mathcal{D}_z(k_z^{lm})$. The modes l and m in the x and y directions together with the resonance condition $k_0 = k_0^{lmn}$ fix the wave number $k_z^{lmn} = k_z^{lm}(k_0^{lmn})$ in Eq. (A20c) pertaining to the z direction:

$$\left(k_z^{lmn}\right)^2 = (1 + i\Gamma_{\rm fl})\left(k_0^{lmn}\right)^2 - \left(k_x^l\right)^2 - \left(k_y^m\right)^2. \tag{A22}$$

Combining this expression with Eq. (A11) for $(k_x^l)^2$ and $(k_y^m)^2$, we find

$$\begin{aligned}(k_z^{lmn})^2 &= \left(K_0^{lmn} + \epsilon_0^{lmn}\right)^2\left(1 + i\Gamma_{\rm fl}^{lmn}\right) \\ &\quad - \left[\left(K_x^l\right)^2 - \frac{2\alpha_x^l}{L_x^l}\right] - \left[\left(K_y^m\right)^2 - \frac{2\alpha_y^m}{L_y^m}\right] \\ &\approx \left(K_z^n\right)^2 + 2K_0^{lmn}\epsilon_0^{lmn} + i\Gamma_{\rm fl}^{lmn}\left(k_0^{lmn}\right)^2 + \frac{2\alpha_x^l}{L_x^l} + \frac{2\alpha_y^m}{L_y^m}.\end{aligned} \tag{A23}$$

To evaluate $\mathcal{D}_z(k_z^{lmn})$ in Eq. (A20a), we note that k_z^{lmn} is close to K_z^n, so we can use Eq. (A10) with $(k_x^l)^2 - (K_x^l)^2 \to (k_z^{lmn})^2 - (K_z^n)^2$, which is found from Eq. (A23):

$$\begin{aligned}\mathcal{D}_z\left(k_z^{lmn}\right) \approx (-1)^n L_z^n k_z^{lmn}\Bigg[&2K_0^{lmn}\epsilon_0^{lmn} + i\Gamma_{\rm fl}^{lmn}\left(k_0^{lmn}\right)^2 \\ &+ \frac{2\alpha_x^l}{L_x^l} + \frac{2\alpha_y^m}{L_y^m} + \frac{2\alpha_z^n}{L_z^n}\Bigg].\end{aligned} \tag{A24}$$

The (real) value of ϵ_0^{lmn}, which minimizes this expression and leads to the resonance wave number k_0^{lmn}, is then

$$\begin{aligned}\epsilon_0^{lmn} &= -{\rm Re}\left[\frac{\alpha_x^l}{K_0^{lmn}L_x^l} + \frac{\alpha_y^m}{K_0^{lmn}L_y^m} + \frac{\alpha_z^n}{K_0^{lmn}L_z^n}\right] \\ &= -\frac{1}{2}K_0^{lmn}\Gamma_{\rm bl}^{lmn},\end{aligned} \tag{A25a}$$

$$\begin{aligned}\Gamma_{\rm bl}^{lmn} &= \frac{1}{\left(K_0^{lmn}\right)^2}{\rm Re}\left[\frac{2\alpha_x^l}{L_x^l} + \frac{2\alpha_y^m}{L_y^m} + \frac{2\alpha_z^n}{L_z^n}\right] \\ &= \left(\frac{K_x^l}{K_0^{lmn}}\right)^2\left(\frac{\delta}{L_y^m} + \frac{\delta}{L_z^n}\right) + \left(\frac{K_y^m}{K_0^{lmn}}\right)^2\left(\frac{\delta}{L_z^n} + \frac{\delta}{L_x^l}\right) \\ &\quad + \left(\frac{K_z^n}{K_0^{lmn}}\right)^2\left(\frac{\delta}{L_x^l} + \frac{\delta}{L_y^m}\right),\end{aligned} \tag{A25b}$$

where we have inserted the expressions for α_x^l, α_y^m, and α_z^n defined by Eq. (A2b), and introduced the boundary-layer damping coefficients $\Gamma_{\rm bl}^{lmn}$.

We are now in a position to determine the third and last wave number k_z^{lmn}, the one in the actuation direction. Using the value of ϵ_0^{lmn} from Eq. (A25a) in expression (A23) for k_z^{lmn}, we find

$$\begin{aligned}\left(k_z^{lmn}\right)^2 &= \left(K_z^n\right)^2 + i\Gamma_{\rm fl}^{lmn}\left(k_0^{lmn}\right)^2 \\ &\quad + i\,{\rm Re}\left[\frac{2\alpha_x^l}{L_x^l} + \frac{2\alpha_y^m}{L_y^m}\right] - {\rm Re}\left[\frac{2\alpha_z^n}{L_z^n}\right] \\ &= \left(K_z^n\right)^2 + i\Gamma_{\rm fl}^{lmn}\left(k_0^{lmn}\right)^2 + i\left(K_0^{lmn}\right)^2\Gamma_{\rm bl}^{lmn} - \frac{2\alpha_z^n}{L_z^n} \\ &\approx \left(K_z^n\right)^2 - \frac{2\alpha_z^n}{L_z^n} + i\left(k_0^{lmn}\right)^2\Gamma^{lmn} \\ &= \left(k_z^n\right)^2 + i\left(k_0^{lmn}\right)^2\Gamma^{lmn},\end{aligned} \tag{A26}$$

with k_z^n defined similar to k_x^l in Eq. (A11) and the total damping coefficient given by

$$\Gamma^{lmn} = \Gamma_{\rm bl}^{lmn} + \Gamma_{\rm fl}^{lmn}. \tag{A27}$$

Note that in comparison with k_x^l and k_y^m, the wave number k_z^{lmn} has an additional dependency on Γ^{lmn}. The corresponding z-dependent functions $Z^{lmn}(z)$ are computed to lowest order in the small parameters by inserting Eq. (A26) into Eq. (A20b):

$$Z^{lmn}(z) \approx (-1)^n\left[Z^n(z) + i\left(k_0^{lmn}L_z\right)^2\Gamma^{lmn}Z_{\rm act}^n(z)\right], \tag{A28a}$$

$$Z_{\rm act}^n(z) = \begin{cases} -\frac{1}{2}\left(1 - \frac{z}{L_z}\right)^2, & n = 0, \\ \frac{1}{2}\frac{\sin\left(K_z^n z\right)}{K_z^n L_z}\left(1 - \frac{z}{L_z}\right), & n > 0. \end{cases} \tag{A28b}$$

Here, $Z^{lmn}(z)$ is close to the eigenfunction $Z^n(z)$ for stationary boundaries, analogous to $X^l(x)$ and $Y^m(y)$ [see Eq. (A12)], but it contains an extra term, which satisfies the boundary condition at the moving actuated boundary $z = 0$.

Finally, we evaluate $\mathcal{D}_z(k_z^{lmn})$ in Eq. (A24) at resonance $k_0 = k_0^{lmn}$ where ϵ_0^{lmn} takes the value given in Eq. (A25a),

$$\mathcal{D}_z\left(k_z^{lmn}\right) \approx (-1)^n L_z^n k_z^{lmn} i\Gamma^{lmn}\left(k_0^{lmn}\right)^2, \tag{A29}$$

and by inserting Eqs. (A29) and (A28) into Eq. (A20a), we find an expression for each resonance mode p_1^{lmn}:

$$\begin{aligned}p_1^{lmn} &= \frac{\left(k_0^{lmn}\right)^2 k_z^{lmn}\hat{U}_{1z}^{lm}}{\kappa_{\rm fl}\mathcal{D}_z\left(k_z^{lmn}\right)}X^l(x)Y^m(y)Z^{lmn}(z) \\ &= \frac{\left(k_0^{lmn}\right)^2\hat{U}_{1z}^{lm}}{\kappa_{\rm fl}L_z^n}X^l(x)Y^m(y)\left[\frac{Z^n(z)}{i\left(k_0^{lmn}\right)^2\Gamma^{lmn}} + L_z^2 Z_{\rm act}^n(z)\right].\end{aligned} \tag{A30}$$

Note that for any l, m, and n, the product term $X^l(x)Y^m(y)Z^n(z)$ only satisfies the boundary condition (A2a) for a *stationary* boundary $U_{1\perp}=0$. The actual boundary condition is satisfied by the infinite sum (A20a) over terms $X^l(x)Y^m(y)Z^n_{\rm act}(z)$ because $\partial_z Z^n_{\rm act}=\frac{L_z^n}{(L_z)^2}$ at $z=0$ and $\partial_z Z^n_{\rm act}=0$ at $z=L_z$.

As Eq. (A30) is only valid exactly at resonance $k_0=k_0^{lmn}$, it must be corrected to deal with frequencies $k_0\approx k_0^{lmn}$. This is done by adding $k_0-k_0^{lmn}$ to the right-hand side of Eq. (A21). By Eq. (A24), this procedure is seen to be equivalent to the substitution

$$i\big(k_0^{lmn}\big)^2\Gamma^{lmn}\to 2k_0^{lmn}\big(k_0-k_0^{lmn}\big)+i\big(k_0^{lmn}\big)^2\Gamma^{lmn} \tag{A31}$$

in Eq. (A30).

2. Approximate solutions near resonance for actuation at all boundaries

At resonance, the expression (A30) satisfies all boundary conditions to first order in $\alpha_x^l L_x$, $\alpha_y^m L_y$, and $\alpha_z^n L_z$. Ignoring these first-order corrections as well as the small $Z^n_{\rm act}$ term in Eq. (A30), the eigenfunctions are approximately equal to the usual hard-wall eigenfunctions R^{lmn}:

$$R^{lmn}(x,y,z)=\cos\big(K_x^l x\big)\cos\big(K_y^m y\big)\cos\big(K_z^n z\big). \tag{A32}$$

To generalize our results from an actuation acting on only the bottom boundary $z=0$ to all six boundaries, we note first that $L_z^n\approx\int_0^{L_z}[Z^n(z))]^2\,dz$, whereby Eq. (A18b) can be rewritten as

$$\begin{aligned}\frac{\hat U_{1z}^{lm}}{L_z^n}&=\frac{\int_0^{L_y}\int_0^{L_x}U_{1z}(x,y)X^l(x)Y^m(y)\,dA}{L_z^n\int_0^{L_y}\int_0^{L_x}[X^l(x)Y^m(y)]^2\,dA}\\&\approx\frac{\int_0^{L_y}\int_0^{L_x}U_{1z}(x,y)R^{lmn}(x,y,0)\,dA}{\int_0^{L_z}\int_0^{L_y}\int_0^{L_x}[R^{lmn}(x,y,z)]^2\,dV}.\end{aligned} \tag{A33}$$

Using this expression together with the substitution (A31) valid for $k_0\approx k_0^{lmn}$, we obtain the following expression for the resonance modes lmn in a rectangular box Ω with viscous boundary layers and an *inward* normal displacement $U_{1\perp}(\boldsymbol{r})$ specified on all six boundaries $\partial\Omega$ [Eq. (3c)]:

$$p_1^{lmn}=P_1^{lmn}F^{lmn}(k_0)R^{lmn}(\boldsymbol{r}), \tag{A34a}$$

$$P_1^{lmn}=\frac{\rho_{\rm fl}c_{\rm fl}^2}{\Gamma^{lmn}}\frac{\int_{\partial\Omega}U_{1\perp}R^{lmn}\,dA}{\int_\Omega(R^{lmn})^2\,dV}, \tag{A34b}$$

$$F^{lmn}(k_0)=\frac{\frac12 k_0^{lmn}\Gamma^{lmn}}{\big(k_0-k_0^{lmn}\big)+i\frac12 k_0^{lmn}\Gamma^{lmn}}. \tag{A34c}$$

The quality factor Q^{lmn} for resonance mode lmn is obtained from the linewidth of the acoustic energy density $E_{\rm ac}$ in Eq. (6), and since $E_{\rm ac}\propto|p_1^{lmn}|^2\propto|F^{lmn}|^2$, we find

$$Q^{lmn}\approx\frac{1}{\Gamma^{lmn}}, \tag{A35}$$

where Γ^{lmn} is given in Eq. (A27).

APPENDIX B: MAXIMUM ACOUSTIC ROTATION

In the following, we evaluate the frequency-dependent factor $\mathcal{F}_{ml0}^{lm0}$ in Eq. (17b) for rotating and nonrotating actuations of the nearly square cavity considered in Sec. V. For convenience, we first introduce the double-mode quantities $\tilde\xi_{lm}$ and $\phi_{lm}^{\rm act}$,

$$\tilde\xi_{lm}=\tilde k_0-\tilde k_{lm}^\star,\quad \phi_{lm}^{\rm act}=\phi_{\rm act}^{ml0}-\phi_{\rm act}^{lm0}, \tag{B1}$$

where $\tilde k_0$ and $\tilde k_{lm}^\star$ are defined in Eq. (27), and $\phi_{lm}^{\rm act}$ is the difference in the phases by which the modes $lm0$ and $ml0$ are actuated [see Eq. (12b)]. By using these quantities and the expressions for F^{lm0} and F^{ml0} in Eq. (28), we calculate the frequency-dependency $\mathcal{F}_{ml0}^{lm0}$ from Eq. (17b):

$$\begin{aligned}\mathcal{F}_{ml0}^{lm0}&=\mathrm{Re}\big\{ie^{i\phi_{lm}^{\rm act}}F^{lm0}[F^{ml0}]^*\big\}\\&=\frac{\cos\big(\phi_{lm}^{\rm act}\big)2\tilde\Delta_{lm}+\sin\big(\phi_{lm}^{\rm act}\big)[1+(2\tilde\xi_{lm})^2-\tilde\Delta_{lm}^2]}{[(2\tilde\xi_{lm}-\tilde\Delta_{lm})^2+1][(2\tilde\xi_{lm}+\tilde\Delta_{lm})^2+1]}.\end{aligned} \tag{B2}$$

This equation expresses the magnitude of the acoustic rotation as a function of the actuation phase difference $\phi_{lm}^{\rm act}$, the actuation frequency $\tilde\xi_{lm}$, and the mode separation $\tilde\Delta_{lm}$, which by Eq. (26) is related to the aspect ratio A. In the following, we study the nonrotating actuation with $\phi_{lm}^{\rm act}=0$ and the rotating actuation with $\phi_{lm}^{\rm act}=\pm\frac12\pi$, and we determine the optimal mode separation $\tilde\Delta_{lm}^{\rm opt}$ and frequency $\tilde\xi_{lm}^{\rm opt}$, for which $\mathcal{F}_{ml0}^{lm0}$ takes its largest positive or negative value $(\mathcal{F}_{ml0}^{lm0})^{\rm extr}$.

1. Extremum values of $\mathcal{F}_{ml0}^{lm0}$ for a nonrotating actuation $\phi_{lm}^{\rm act}=0$

For a nonrotating actuation, we have $\phi_{lm}^{\rm act}=0$, and Eq. (B2) becomes

$$\mathcal{F}_{ml0}^{lm0}=\frac{2\tilde\Delta_{lm}}{[(2\tilde\xi_{lm}-\tilde\Delta_{lm})^2+1][(2\tilde\xi_{lm}+\tilde\Delta_{lm})^2+1]}. \tag{B3}$$

The extremum values of this expressions are

$$\big(\mathcal{F}_{ml0}^{lm0}\big)^{\rm extr}=\begin{cases}\frac{2\tilde\Delta_{lm}}{(\tilde\Delta_{lm}^2+1)^2}, & |\tilde\Delta_{lm}|<1,\\ \frac{1}{2\tilde\Delta_{lm}}, & |\tilde\Delta_{lm}|>1,\end{cases} \tag{B4a}$$

which are obtained at the frequencies $\tilde\xi_{lm}^{\rm extr}$ given by

$$\tilde\xi_{lm}^{\rm extr}=\begin{cases}0, & |\tilde\Delta_{lm}|<1,\\ \pm\frac12\sqrt{\tilde\Delta_{lm}^2-1}, & |\tilde\Delta_{lm}|>1.\end{cases} \tag{B4b}$$

In Fig. 6 ("nonrotating act."), we plot the value $(\mathcal{F}_{ml0}^{lm0})^{\rm extr}$ from this expression as a function of $\tilde\Delta_{lm}$. The optimal value $(\mathcal{F}_{ml0}^{lm0})^{\rm opt}$ of $(\mathcal{F}_{ml0}^{lm0})^{\rm extr}$ is found at the optimal mode separation $\tilde\Delta_{lm}^{\rm opt}$, and optimal rescaled frequency $\tilde\xi_{lm}^{\rm opt}$:

$$\tilde\xi_{lm}^{\rm opt}=0,\quad \tilde\Delta_{lm}^{\rm opt}=\pm\frac{1}{\sqrt3},\quad \big(\mathcal{F}_{ml0}^{lm0}\big)^{\rm opt}=\pm\frac{3\sqrt3}{8}. \tag{B5}$$

2. Extremum values of $\mathcal{F}_{ml0}^{lm0}$ for a rotating actuation $\phi_{lm}^{\rm act}=\pm\frac12\pi$

For an externally controlled rotating actuation, we have $\phi_{lm}^{\rm act}=\pm\frac12\pi$ and Eq. (B2) becomes

$$\mathcal{F}_{ml0}^{lm0}=\frac{\big[1+(2\tilde\xi_{lm})^2-\tilde\Delta_{lm}^2\big]\mathrm{sgn}_\phi^{lm}}{[(2\tilde\xi_{lm}-\tilde\Delta_{lm})^2+1][(2\tilde\xi_{lm}+\tilde\Delta_{lm})^2+1]}, \tag{B6a}$$

$$\mathrm{sgn}_\phi^{lm}=\mathrm{sign}\big(\phi_{lm}^{\rm act}\big). \tag{B6b}$$

This expression is more complicated than Eq. (B3) since it only has one extremum for a sufficiently small mode separation $\tilde{\Delta}_{lm}$, namely, where the angular momentum and the actuation are corotating, $\mathrm{sign}(\mathcal{F}^{lm0}_{ml0}) = \mathrm{sgn}^{lm}_{\phi}$. For larger values of $\tilde{\Delta}_{lm}$, the frequency can be tuned to two different extremum values, namely, both the corotating and counter-rotating cases, $\mathrm{sign}(\mathcal{F}^{lm0}_{ml0}) = \pm\mathrm{sgn}^{lm}_{\phi}$. We therefore identify two branches of extremum values. The corotating branch $(\mathcal{F}^{lm0}_{ml0})^{\mathrm{extr}}_{\mathrm{co}}$ with subscript "co" and the counter-rotating branch $(\mathcal{F}^{lm0}_{ml0})^{\mathrm{extr}}_{\mathrm{cntr}}$ with subscript "cntr."

For the corotating branch, $(\mathcal{F}^{lm0}_{ml0})^{\mathrm{extr}}_{\mathrm{co}}$ is

$$\left(\mathcal{F}^{lm0}_{ml0}\right)^{\mathrm{extr}}_{\mathrm{co}} = \mathrm{sgn}^{lm}_{\phi}\begin{cases}\frac{1-\tilde{\Delta}^2_{lm}}{(\tilde{\Delta}^2_{lm}+1)^2}, & |\tilde{\Delta}_{lm}| \leqslant \sqrt{2}-1,\\ \frac{1}{4|\tilde{\Delta}_{lm}|}, & |\tilde{\Delta}_{lm}| \geqslant \sqrt{2}-1,\end{cases} \tag{B7a}$$

found at the frequencies $\tilde{\xi}_{lm} = \tilde{\xi}^{\mathrm{extr}}_{lm,\mathrm{co}}$:

$$\tilde{\xi}^{\mathrm{extr}}_{lm,\mathrm{co}} = \begin{cases}0, & |\tilde{\Delta}_{lm}| \leqslant \sqrt{2}-1,\\ \pm\frac{1}{2}\sqrt{\tilde{\Delta}^2_{lm}+2\tilde{\Delta}_{lm}-1}, & |\tilde{\Delta}_{lm}| \geqslant \sqrt{2}-1.\end{cases} \tag{B7b}$$

For the counter-rotating branch, $(\mathcal{F}^{lm0}_{ml0})^{\mathrm{extr}}_{\mathrm{cntr}}$ is

$$\left(\mathcal{F}^{lm0}_{ml0}\right)^{\mathrm{extr}}_{\mathrm{cntr}} = -\mathrm{sgn}^{lm}_{\phi}\begin{cases}\frac{\tilde{\Delta}^2_{lm}-1}{(\tilde{\Delta}^2_{lm}+1)^2}, & 1 \leqslant |\tilde{\Delta}_{lm}| \leqslant \sqrt{2}+1,\\ \frac{1}{4|\tilde{\Delta}_{lm}|}, & |\tilde{\Delta}_{lm}| \geqslant \sqrt{2}+1,\end{cases} \tag{B8a}$$

found at the frequencies $\tilde{\xi}_{lm} = \tilde{\xi}^{\mathrm{extr}}_{lm,\mathrm{cntr}}$:

$$\tilde{\xi}^{\mathrm{extr}}_{lm,\mathrm{cntr}} = \begin{cases}0, & 1 \leqslant |\tilde{\Delta}_{lm}| \leqslant \sqrt{2}+1,\\ \pm\frac{1}{2}\sqrt{\tilde{\Delta}^2_{lm}-2\tilde{\Delta}_{lm}-1}, & |\tilde{\Delta}_{lm}| \geqslant \sqrt{2}+1.\end{cases} \tag{B8b}$$

In Fig. 6 (rotating act.), we plot for $\phi^{\mathrm{act}}_{lm} = +\frac{1}{2}\pi$ both the corotating and counter-rotating branches $(\mathcal{F}^{lm0}_{ml0})^{\mathrm{extr}}_{\mathrm{co}}$ and $(\mathcal{F}^{lm0}_{ml0})^{\mathrm{extr}}_{\mathrm{cntr}}$.

From Eqs. (B7a) and (B8a), we find that the largest value $(\mathcal{F}^{lm0}_{ml0})^{\mathrm{opt}}$ of $(\mathcal{F}^{lm0}_{ml0})$ is the corotating double mode found at the optimal mode separation $\tilde{\Delta}^{\mathrm{opt}}_{lm}$, and the rescaled frequency $\tilde{\xi}^{\mathrm{opt}}_{lm}$:

$$\tilde{\xi}^{\mathrm{opt}}_{lm} = 0, \quad \tilde{\Delta}^{\mathrm{opt}}_{lm} = 0, \quad (\mathcal{F}^{lm0}_{ml0})^{\mathrm{opt}} = \mathrm{sgn}^{lm}_{\phi}. \tag{B9}$$

We see that in contrast to the nonrotating actuation (B5), the rotating actuation optimizes the acoustic rotation for zero-mode separation $\tilde{\Delta}^{\mathrm{opt}}_{lm} = 0$.

APPENDIX C: ROTATING ACTUATION G_{16} OF THE DOUBLE MODE 200 + 020

In the simulation shown in Figs. 5(d)–5(f) of Sec. VI C 2 we excite the double mode 200 + 020 by using the rotating actuation

$$u_{1z} = u^0_{1z}G_{16}(x,y), \quad 0 < x < L_x,\ 0 < y < L_y. \tag{C1a}$$

Here, $G_{16}(x,y)$ is constructed as the sum of 16 narrow Gaussians $G^{\odot}_1$ as follows. The primary narrow Gaussian $G^{\odot}_1(x,y)$ is centered around $(\frac{1}{8}L_x, \frac{1}{8}L_y)$ in the lower left corner of the domain:

$$G^{\odot}_1(x,y) = \exp\left[-\frac{\left(x-\frac{L_x}{8}\right)^2}{\left(\frac{L_x}{16}\right)^2} - \frac{\left(y-\frac{L_y}{8}\right)^2}{\left(\frac{L_y}{16}\right)^2}\right]. \tag{C1b}$$

Four versions of $G^{\odot}_1$, centered at $(\frac{2\pm1}{8}L_x, \frac{2\pm1}{8}L_y)$ and multiplied by specific phase factors in order to create a positive rotation direction in the x-y plane, are added to form a quadruple G_4 centered around $(\frac{1}{4}L_x, \frac{1}{4}L_y)$:

$$\begin{aligned}G_4(x,y) = {} & e^{-i\frac{0\pi}{2}}G^{\odot}_1(x,y) + e^{-i\frac{1\pi}{2}}G^{\odot}_1\left(x, y-\tfrac{1}{4}L_y\right)\\ & + e^{-i\frac{2\pi}{2}}G^{\odot}_1\left(x-\tfrac{1}{4}L_x, y-\tfrac{1}{4}L_y\right)\\ & + e^{-i\frac{3\pi}{2}}G^{\odot}_1\left(x-\tfrac{1}{4}L_x, y\right).\end{aligned} \tag{C1c}$$

Finally, by mirroring the quadruple $G_4(x,y)$ across the center lines $x = \frac{1}{2}L_x$ and $y = \frac{1}{2}L_y$, G_{16} is formed by adding the four resulting quadruples

$$\begin{aligned}G_{16}(x,y) = {} & G_4(x,y) + G_4(L_x-x,y)\\ & + G_4(L_x-x,L_y-y) + G_4(x,L_y-y).\end{aligned} \tag{C1d}$$

To obtain the complex pressure amplitudes P^{200}_1 and P^{020}_1 resulting from G_{16}, we first evaluate the integral in the denominator of Eq. (34), where G_1 is substituted by G_{16}:

$$\int_0^{L_x}\int_0^{L_y} G_{16}(x,y)R^{200}\,\frac{dx}{L_x}\,\frac{dy}{L_y} = 0.0942\times e^{i0.250\pi}, \tag{C2a}$$

$$\int_0^{L_x}\int_0^{L_y} G_{16}(x,y)R^{020}\,\frac{dx}{L_x}\,\frac{dy}{L_y} = 0.0942\times e^{-i0.250\pi}. \tag{C2b}$$

We then use Eq. (34) to compute the desired amplitudes

$$P^{200}_1 = \frac{2u^0_{1z}}{L_z\left(\Gamma^{200}_{\mathrm{fl}}+\Gamma^{200}_{\mathrm{bl}}\right)\kappa_{\mathrm{fl}}}0.0942\times e^{i0.250\pi}, \tag{C3a}$$

$$P^{020}_1 = \frac{2u^0_{1z}}{L_z\left(\Gamma^{200}_{\mathrm{fl}}+\Gamma^{200}_{\mathrm{bl}}\right)\kappa_{\mathrm{fl}}}0.0942\times e^{-i0.250\pi}. \tag{C3b}$$

We see that the actuation in Eq. (C1a) excites the two modes 200 and 020 with a phase difference of

$$\phi^{020}_{\mathrm{act}} - \phi^{200}_{\mathrm{act}} = 0.500\pi. \tag{C4}$$

Finally, we use Eq. (C3) to choose the amplitude u^0_{1z} of the actuation such that $|P^{200}_1| = |P^{020}_1| = 1$ MPa,

$$u^0_{1z} = \frac{L_z\left(\Gamma^{200}_{\mathrm{fl}}+\Gamma^{200}_{\mathrm{bl}}\right)\kappa_{\mathrm{fl}}\left|P^{200}_1\right|}{2\times 0.0942} = 1.614\ \mathrm{nm}, \tag{C5}$$

where we used the parameters for water given in Table II.

APPENDIX D: APPROXIMATE SOLUTION FOR THE BULK-DRIVEN STREAMING FROM DOUBLE MODES $l00 + 0l0$

In this Appendix, we calculate an approximate expression for the bulk-driven acoustic streaming velocity $(\boldsymbol{v}^{\mathrm{blk}}_2)^{l00}_{0l0} = (\boldsymbol{v}^{\mathrm{blk}}_2)_{l0}$ driven by the acoustic body force $\boldsymbol{f}_{\mathrm{ac}} = \boldsymbol{f}^{l00}_{0l0} = \boldsymbol{f}_{l0}$ resulting from the combination of the two perpendicular, horizontal modes $l00$ and $0l0$ in a square cavity. As in Eq. (24), the double subscript $l0$ refers to the double mode $l00 + 0l0$. The

bulk-driven streaming velocity $(\boldsymbol{v}_2^{\mathrm{blk}})_{l0}$ satisfies an equation similar to Eq. (7) except for having no-slip at the boundaries:

$$0 = \boldsymbol{\nabla}\cdot\left(\boldsymbol{v}_2^{\mathrm{blk}}\right)_{l0}, \quad \boldsymbol{r}\in\Omega, \tag{D1a}$$

$$\boldsymbol{\nabla}\left(p_2^{\mathrm{blk}}\right)_{l0} = \eta_{\mathrm{fl}}\nabla^2\left(\boldsymbol{v}_2^{\mathrm{blk}}\right)_{l0} + \frac{\Gamma_{\mathrm{fl}}\omega}{c_{\mathrm{fl}}^2}\boldsymbol{S}_{l0}, \quad \boldsymbol{r}\in\Omega, \tag{D1b}$$

$$\left(\boldsymbol{v}_2^{\mathrm{blk}}\right)_{l0} = \boldsymbol{0}, \quad \boldsymbol{r}\in\partial\Omega. \tag{D1c}$$

Here, $\boldsymbol{S}_{l0}$ is defined in Eq. (18a) combined with Eq. (24) for $\mathcal{F}_{l0}(k_0)$, Eq. (17c) for $\boldsymbol{\mathcal{K}}_{l0}(\boldsymbol{r})$, and Eq. (9a) for $R_{l0}(\boldsymbol{r})$:

$$\boldsymbol{S}_{l0}(\boldsymbol{r}) = \frac{1}{2}\frac{\left|P_1^{l00}\right|\left|P_1^{0l0}\right|}{\rho_{\mathrm{fl}}\omega}\mathcal{F}_{l0}(k_0)\boldsymbol{\mathcal{K}}_{l0}(\boldsymbol{r}), \tag{D2a}$$

$$\mathcal{F}_{l0}(k_0) = \mathrm{Re}\{i[F^{l00}(k_0)][F^{0l0}(k_0)]^*\}, \tag{D2b}$$

$$\boldsymbol{\mathcal{K}}_{l0}(\boldsymbol{r}) = k_{l0}^\star[\sin(k_{l0}^\star x)\cos(k_{l0}^\star y)\boldsymbol{e}_x - \cos(k_{l0}^\star x)\sin(k_{l0}^\star y)\boldsymbol{e}_y]. \tag{D2c}$$

The impact on the bulk-driven streaming from the no-slip condition at the side walls will decrease exponentially with the length scale w away from the side walls, where w is the minimum shear length scale, i.e., either the vertical length scale L_z or the horizontal length scale $(k_{l0}^\star)^{-1}$,

$$w = \min\{L_z, (k_{l0}^\star)^{-1}\}. \tag{D3}$$

For the narrow channel considered in Sec. VI where $L_z/L^\star = 0.1$, we have $w/L^\star = 0.1$ for $l = 2$, $w/L^\star = \frac{1}{4\pi} = 0.08$ for $l = 4$, and $w/L^\star = \frac{1}{6\pi} = 0.05$ for $l = 6$, and therefore the vertical side walls can be ignored in the majority of the cavity for these three double modes.

To compute the acoustic streaming velocity, we ignore the side walls and assume that $(\boldsymbol{v}_2^{\mathrm{blk}})_{l0}$ is proportional to the xy-dependent acoustic energy flux density $\boldsymbol{S}_{l0}(x, y)$ and some z-dependent function $\zeta(z)$ to be found:

$$\left(\boldsymbol{v}_2^{\mathrm{blk}}\right)_{l0} = \kappa_{\mathrm{fl}}\zeta(z)\boldsymbol{S}_{l0}(x, y). \tag{D4}$$

By using $\boldsymbol{S}_{l0}$ from Eq. (D2a), we find the three identities

$$\boldsymbol{\nabla}\cdot\boldsymbol{S}_{l0} = 0, \tag{D5a}$$

$$\nabla^2\boldsymbol{S}_{l0} = -2(k_{l0}^\star)^2\boldsymbol{S}_{l0}, \tag{D5b}$$

$$\boldsymbol{\nabla}\times\boldsymbol{S}_{l0} = \frac{\left|P_1^{l00}\right|\left|P_1^{0l0}\right|\mathcal{F}_{l0}}{\rho_{\mathrm{fl}}\omega}(k_{l0}^\star)^2\sin(k_{l0}^\star x)\sin(k_{l0}^\star y)\boldsymbol{e}_z. \tag{D5c}$$

Consequently, by Eq. (D5a), the ansatz (D4) satisfies the continuity equation (D1a). Moreover, inserting Eq. (D4) into Eq. (D1b) using $\Gamma_{\mathrm{fl}} = (\frac{4}{3} + \frac{\eta_{\mathrm{fl}}^{\mathrm{b}}}{\eta_{\mathrm{fl}}})\eta_{\mathrm{fl}}\kappa_{\mathrm{fl}}\omega$ from Eqs. (4) and (D5b) we find

$$\boldsymbol{\nabla}\left(p_2^{\mathrm{blk}}\right)_{l0} = \eta_{\mathrm{fl}}\kappa_{\mathrm{fl}}\left[\frac{\zeta''(z)}{(\sqrt{2}k_{l0}^\star)^2} - \zeta(z) + \frac{1}{2}\left(\frac{4}{3} + \frac{\eta_{\mathrm{fl}}^{\mathrm{b}}}{\eta_{\mathrm{fl}}}\right)\right]\boldsymbol{S}_{l0}. \tag{D6}$$

Since $\boldsymbol{S}_{l0}(x, y)$ has no z component, $(p_2^{\mathrm{blk}})_{l0}$ on the left-hand side is independent of z. Therefore, the square bracket on the right-hand side must be a constant. This constant must be zero since otherwise taking the curl of Eq. (D6) would lead to $\boldsymbol{0} = \boldsymbol{\nabla}\times\boldsymbol{S}_{l0}$ in conflict with Eq. (D5c). The condition of a vanishing square bracket in Eq. (D6) and the no-slip boundary conditions $\zeta(0) = \zeta(L_z) = 0$ lead to the following expression for $\zeta(z)$:

$$\zeta(z) = \frac{1}{2}\left(\frac{4}{3} + \frac{\eta_{\mathrm{fl}}^{\mathrm{b}}}{\eta_{\mathrm{fl}}}\right)\left[1 - \frac{\cosh\left(\sqrt{2}k_{l0}^\star\left(z - \frac{L_z}{2}\right)\right)}{\cosh\left(\sqrt{2}k_{l0}^\star\frac{L_z}{2}\right)}\right]. \tag{D7}$$

The solution for $(\boldsymbol{v}_2^{\mathrm{blk}})_{l0}$ is then obtained by inserting Eqs. (D2) and (D7) in Eq. (D4).

[1] F. Petersson, L. Åberg, A. M. Swärd-Nilsson, and T. Laurell, Free flow acoustophoresis: Microfluidic-based mode of particle and cell separation, Anal. Chem. **79**, 5117 (2007).

[2] O. Manneberg, B. Vanherberghen, J. Svennebring, H. M. Hertz, B. Önfelt, and M. Wiklund, A three-dimensional ultrasonic cage for characterization of individual cells, Appl. Phys. Lett. **93**, 063901 (2008).

[3] X. Ding, Z. Peng, S.-C. S. Lin, M. Geri, S. Li, P. Li, Y. Chen, M. Dao, S. Suresh, and T. J. Huang, Cell separation using tilted-angle standing surface acoustic waves, Proc. Natl. Acad. Sci. USA **111**, 12992 (2014).

[4] B. Hammarström, T. Laurell, and J. Nilsson, Seed particle enabled acoustic trapping of bacteria and nanoparticles in continuous flow systems, Lab Chip **12**, 4296 (2012).

[5] M. Evander, O. Gidlof, B. Olde, D. Erlinge, and T. Laurell, Non-contact acoustic capture of microparticles from small plasma volumes, Lab Chip **15**, 2588 (2015).

[6] D. J. Collins, C. Devendran, Z. Ma, J. W. Ng, A. Neild, and Y. Ai, Acoustic tweezers via sub-time-of-flight regime surface acoustic waves, Sci. Adv. **2**, e1600089 (2016).

[7] H. G. Lim, Y. Li, M.-Y. Lin, C. Yoon, C. Lee, H. Jung, R. H. Chow, and K. K. Shung, Calibration of trapping force on cell-size objects from ultrahigh-frequency single-beam acoustic tweezer, IEEE T. Ultrason. Ferr. **63**, 1988 (2016).

[8] D. Baresch, J.-L. Thomas, and R. Marchiano, Observation of a Single-Beam Gradient Force Acoustical Trap for Elastic Particles: Acoustical Tweezers, Phys. Rev. Lett. **116**, 024301 (2016).

[9] P. Augustsson, C. Magnusson, M. Nordin, H. Lilja, and T. Laurell, Microfluidic, label-free enrichment of prostate cancer cells in blood based on acoustophoresis, Anal. Chem. **84**, 7954 (2012).

[10] M. Antfolk, C. Magnusson, P. Augustsson, H. Lilja, and T. Laurell, Acoustofluidic, label-free separation and simultaneous concentration of rare tumor cells from white blood cells, Anal. Chem. **87**, 9322 (2015).

[11] M. Antfolk, P. B. Muller, P. Augustsson, H. Bruus, and T. Laurell, Focusing of sub-micrometer particles and bacteria enabled by two-dimensional acoustophoresis, Lab Chip **14**, 2791 (2014).

[12] S. Li, F. Ma, H. Bachman, C. E. Cameron, X. Zeng, and T. J. Huang, Acoustofluidic bacteria separation, J. Micromech. Microeng. **27**, 015031 (2017).

[13] P. Augustsson, J. T. Karlsen, H.-W. Su, H. Bruus, and J. Voldman, Iso-acoustic focusing of cells for size-insensitive

acousto-mechanical phenotyping, Nat. Commun. **7**, 11556 (2016).
[14] L. V. King, On the acoustic radiation pressure on spheres, Proc. R. Soc. London, Ser. A **147**, 212 (1934).
[15] K. Yosioka and Y. Kawasima, Acoustic radiation pressure on a compressible sphere, Acustica **5**, 167 (1955).
[16] A. A. Doinikov, Acoustic radiation force on a spherical particle in a viscous heat-conducting fluid.1. general formula, J. Acoust. Soc. Am. **101**, 713 (1997).
[17] M. Settnes and H. Bruus, Forces acting on a small particle in an acoustical field in a viscous fluid, Phys. Rev. E **85**, 016327 (2012).
[18] J. T. Karlsen and H. Bruus, Forces acting on a small particle in an acoustical field in a thermoviscous fluid, Phys. Rev. E **92**, 043010 (2015).
[19] L. Rayleigh, On the circulation of air observed in Kundt's tubes, and on some allied acoustical problems, Philos. Trans. R. Soc. London **175**, 1 (1884).
[20] H. Schlichting, Berechnung ebener periodischer grenzeschichtströmungen, Phys. Z. **33**, 327 (1932).
[21] P. Westervelt, The theory of steady rotational flow generated by a sound field, J. Acoust. Soc. Am. **25**, 60 (1953).
[22] W. L. Nyborg, Acoustic streaming near a boundary, J. Acoust. Soc. Am. **30**, 329 (1958).
[23] P. B. Muller, M. Rossi, A. G. Marin, R. Barnkob, P. Augustsson, T. Laurell, C. J. Kähler, and H. Bruus, Ultrasound-induced acoustophoretic motion of microparticles in three dimensions, Phys. Rev. E **88**, 023006 (2013).
[24] P. B. Muller, R. Barnkob, M. J. H. Jensen, and H. Bruus, A numerical study of microparticle acoustophoresis driven by acoustic radiation forces and streaming-induced drag forces, Lab Chip **12**, 4617 (2012).
[25] R. Barnkob, P. Augustsson, T. Laurell, and H. Bruus, Acoustic radiation- and streaming-induced microparticle velocities determined by microparticle image velocimetry in an ultrasound symmetry plane, Phys. Rev. E **86**, 056307 (2012).
[26] C. Lee and T. Wang, Near-boundary streaming around a small sphere due to 2 orthogonal standing waves, J. Acoust. Soc. Am. **85**, 1081 (1989).
[27] J. Vanneste and O. Bühler, Streaming by leaky surface acoustic waves, Proc. R. Soc. A **467**, 1779 (2011).
[28] J. S. Bach and H. Bruus, Theory of pressure acoustics with viscous boundary layers and streaming in curved elastic cavities, J. Acoust. Soc. Am. **144**, 766 (2018).
[29] C. Eckart, Vortices and streams caused by sound waves, Phys. Rev. **73**, 68 (1948).
[30] A. Riaud, M. Baudoin, O. Bou Matar, J.-L. Thomas, and P. Brunet, On the influence of viscosity and caustics on acoustic streaming in sessile droplets: An experimental and a numerical study with a cost-effective method, J. Fluid Mech. **821**, 384 (2017).
[31] F. Busse and T. Wang, Torque generated by orthogonal acoustic-waves theory, J. Acoust. Soc. Am. **69**, 1634 (1981).
[32] S. B. Q. Tran, P. Marmottant, and P. Thibault, Fast acoustic tweezers for the two-dimensional manipulation of individual particles in microfluidic channels, Appl. Phys. Lett. **101**, 114103 (2012).
[33] J. Dual, P. Hahn, I. Leibacher, D. Möller, T. Schwarz, and J. Wang, Acoustofluidics 19: Ultrasonic microrobotics in cavities: Devices and numerical simulation, Lab Chip **12**, 4010 (2012).
[34] C. R. P. Courtney, B. W. Drinkwater, C. E. M. Demore, S. Cochran, A. Grinenko, and P. D. Wilcox, Dexterous manipulation of microparticles using bessel-function acoustic pressure fields, Appl. Phys. Lett. **102**, 123508 (2013).
[35] Z. Mao, P. Li, M. Wu, H. Bachman, N. Mesyngier, X. Guo, S. Liu, F. Costanzo, and T. J. Huang, Enriching nanoparticles via acoustofluidics, ACS Nano **11**, 603 (2017).
[36] D. Baresch, J.-L. Thomas, and R. Marchiano, Orbital Angular Momentum Transfer to Stably Trapped Elastic Particles in Acoustical Vortex Beams, Phys. Rev. Lett. **121**, 074301 (2018).
[37] P. L. Marston, Axial radiation force of a bessel beam on a sphere and direction reversal of the force, J. Acoust. Soc. Am. **120**, 3518 (2006).
[38] A. Marzo, S. A. Seah, B. W. Drinkwater, D. R. Sahoo, B. Long, and S. Subramanian, Holographic acoustic elements for manipulation of levitated objects, Nat. Commun. **6**, 8661 (2015).
[39] S. M. Hagsäter, T. G. Jensen, H. Bruus, and J. P. Kutter, Acoustic resonances in microfluidic chips: Full-image micro-PIV experiments and numerical simulations, Lab Chip **7**, 1336 (2007).
[40] J. T. Karlsen, W. Qiu, P. Augustsson, and H. Bruus, Acoustic Streaming and its Suppression in Inhomogeneous Fluids, Phys. Rev. Lett. **120**, 054501 (2018).
[41] See Supplemental Material at http://link.aps.org/supplemental/10.1103/PhysRevE.100.023104 for extensions of the results of the following three figures: (1) Fig. 2 turned into one pdf file with 55 subfigures of the acoustic body force $\boldsymbol{f}_{\rm ac}$ of the double modes $lm0 + l'm'0$ with $l, m, l', m' = 0, 1, 2, 3, 4$ (the MATLAB source code is also provided); (2) Fig. 4 turned into five animated gif files of the pressure p_1 in 3D and as line plots of the double modes $200 + 020$, $400 + 040$, and $600 + 060$ both for the wide $\frac{1}{2}L^\star$-width and the narrow $\frac{1}{12}L^\star$-width G_1 actuation; and (3) Fig. 8 recalculated using the narrow $\frac{1}{12}L^\star$-width G_1 actuation.
[42] P. Hahn and J. Dual, A numerically efficient damping model for acoustic resonances in microfluidic cavities, Phys. Fluids **27**, 062005 (2015).
[43] J. Lei, M. Hill, and P. Glynne-Jones, Numerical simulation of 3D boundary-driven acoustic streaming in microfluidic devices, Lab Chip **14**, 532 (2014).
[44] N. R. Skov, J. S. Bach, B. G. Winckelmann, and H. Bruus, 3D modeling of acoustofluidics in a liquid-filled cavity including streaming, viscous boundary layers, surrounding solids, and a piezoelectric transducer, AIMS Math. **4**, 99 (2019).
[45] P. B. Muller and H. Bruus, Numerical study of thermoviscous effects in ultrasound-induced acoustic streaming in microchannels, Phys. Rev. E **90**, 043016 (2014).
[46] A. S. Dukhin and P. J. Goetz, Bulk viscosity and compressibility measurement using acoustic spectroscopy, J. Chem. Phys. **130**, 124519 (2009).
[47] M. W. H. Ley and H. Bruus, Continuum modeling of hydrodynamic particle-particle interactions in microfluidic high-concentration suspensions, Lab Chip **16**, 1178 (2016).
[48] COMSOL MULTIPHYSICS 5.4, http://www.comsol.com.
[49] J. T. Karlsen, P. Augustsson, and H. Bruus, Acoustic Force Density Acting on Inhomogeneous Fluids in Acoustic Fields, Phys. Rev. Lett. **117**, 114504 (2016).

Supplemental material for paper "Bulk-driven acoustic streaming at resonance in closed microcavities"

See description in Ref. [41] of the bibliography of the paper.

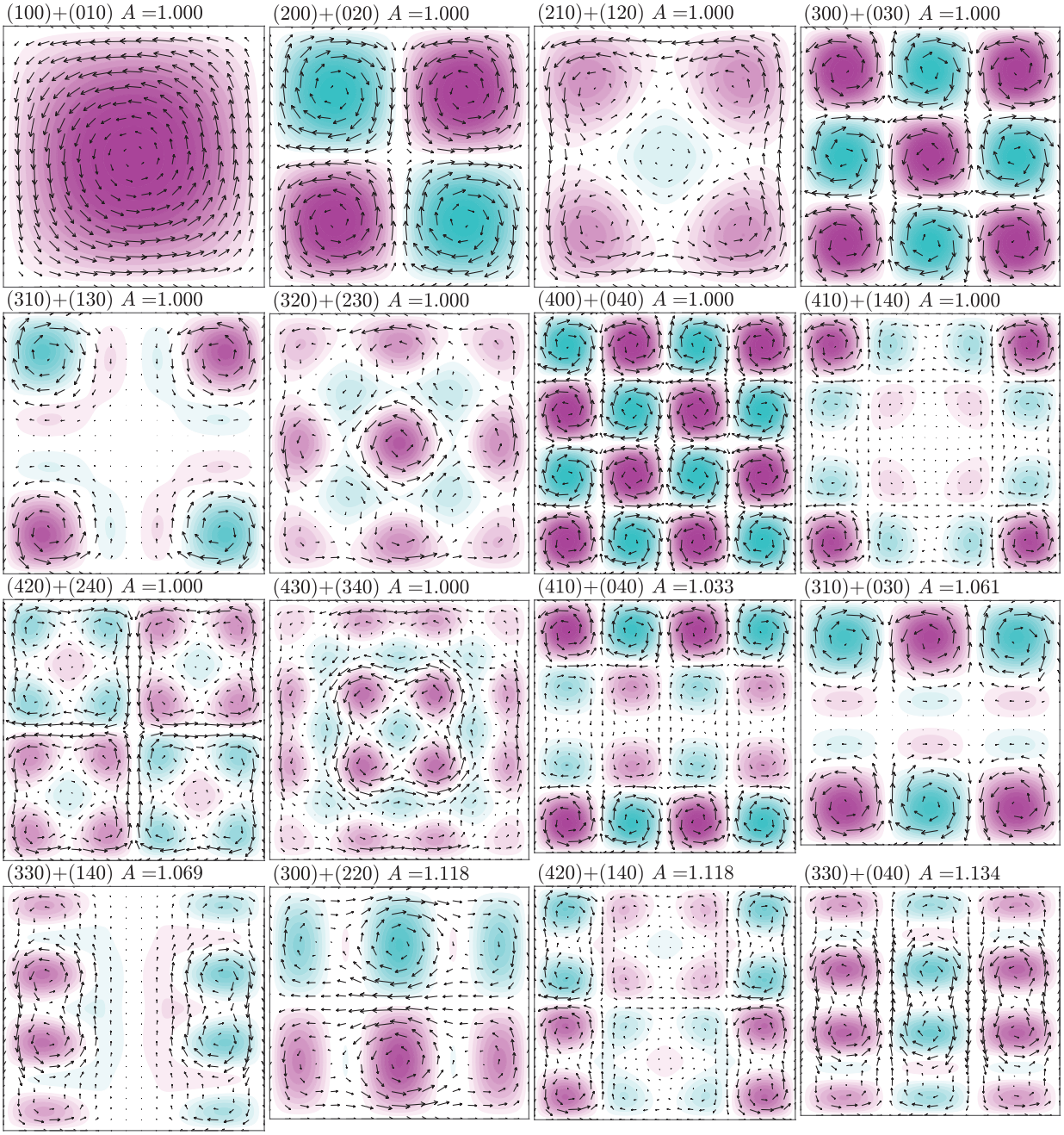

Fig. 1/3 (1-16/55). Maximum mode number : 4

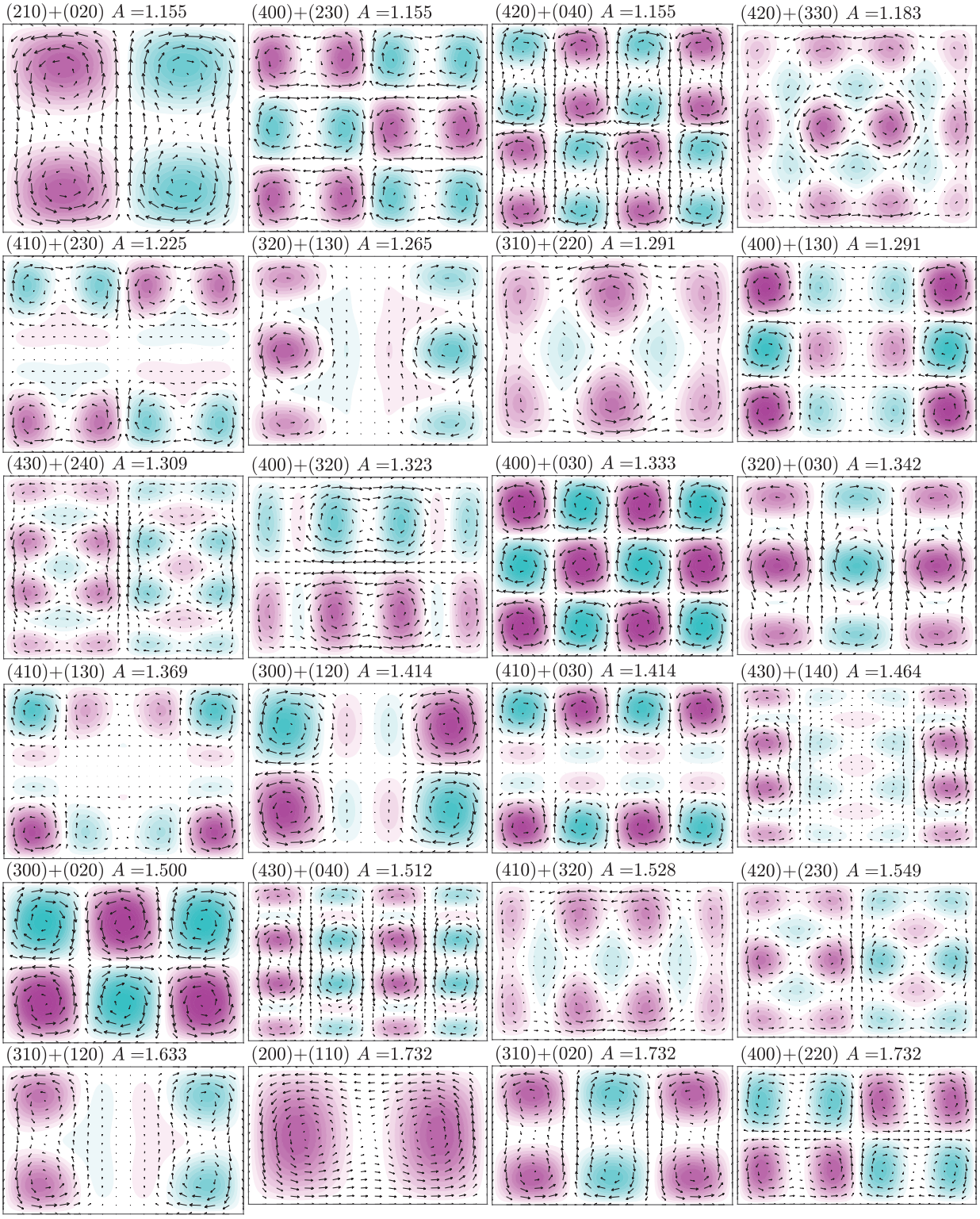

Fig. 2/3 (17-40/55). Maximum mode number : 4

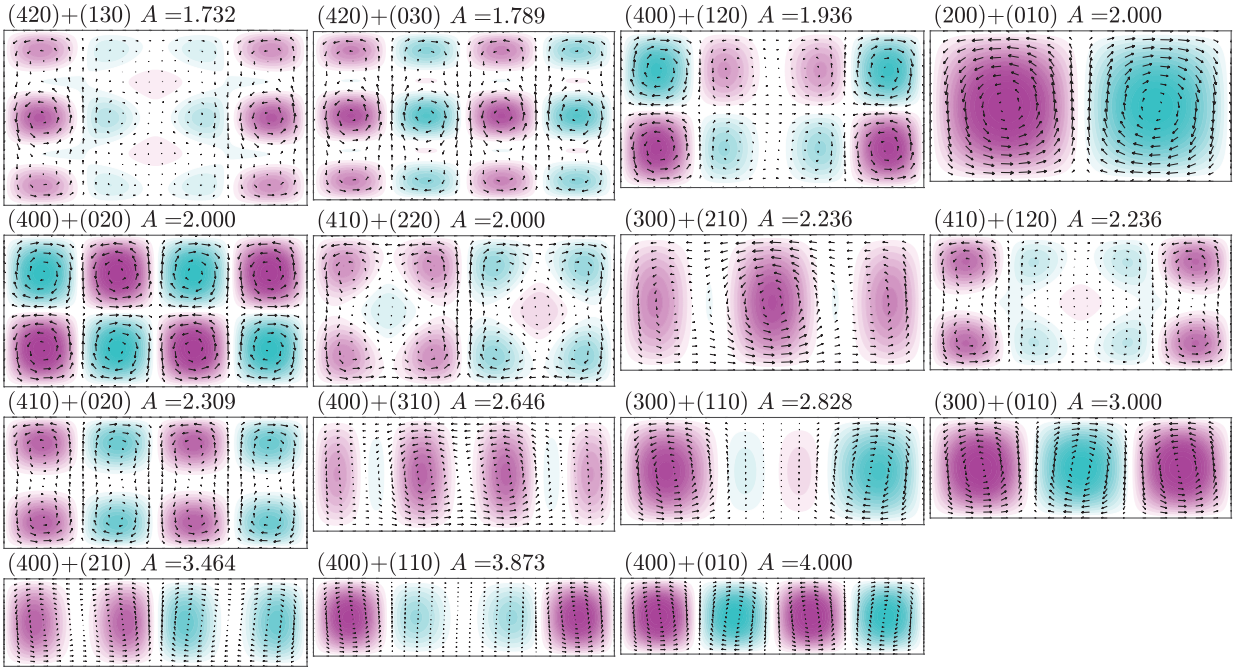

Fig. 3/3 (41-55/55). Maximum mode number : 4

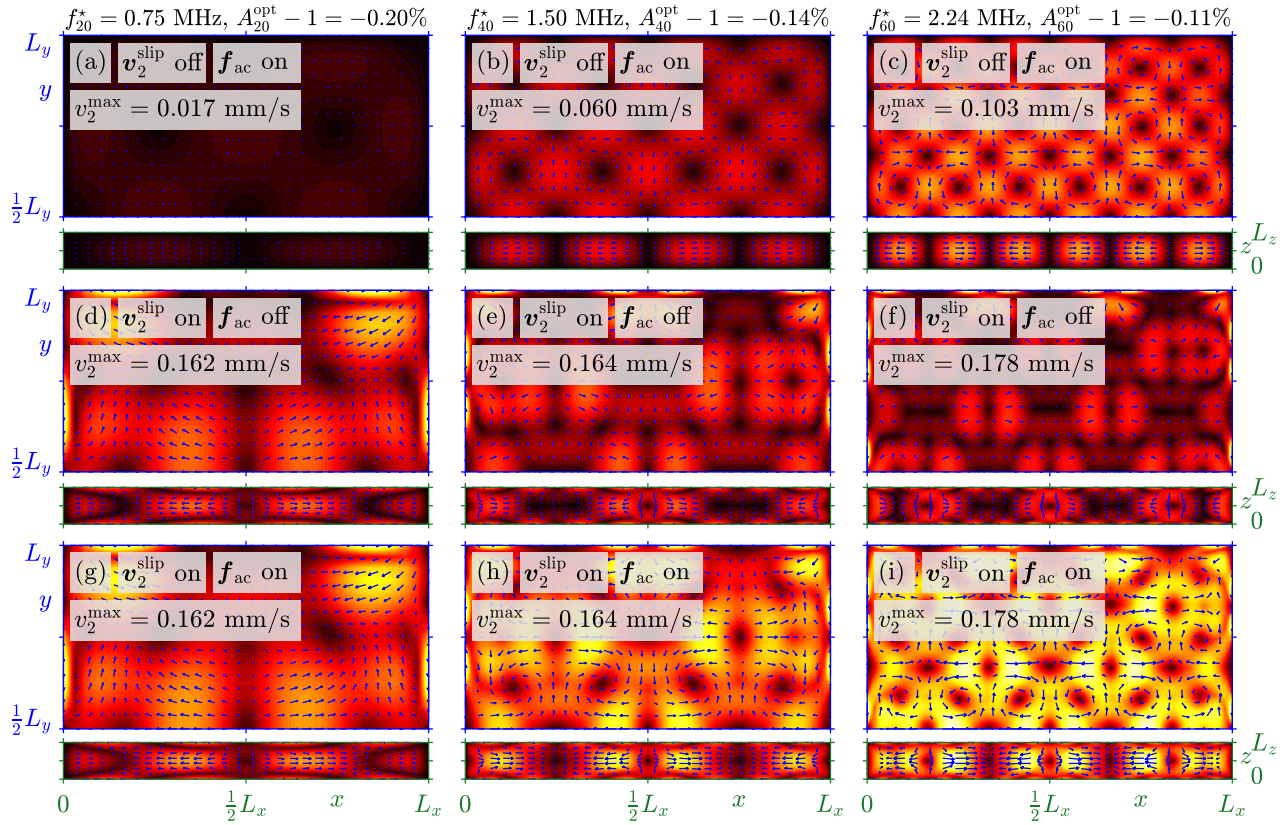
$f_{20}^{\star} = 0.75$ MHz, $A_{20}^{\mathrm{opt}} - 1 = -0.20\%$
$f_{40}^{\star} = 1.50$ MHz, $A_{40}^{\mathrm{opt}} - 1 = -0.14\%$
$f_{60}^{\star} = 2.24$ MHz, $A_{60}^{\mathrm{opt}} - 1 = -0.11\%$
(a) $\boldsymbol{v}_2^{\mathrm{slip}}$ off $\boldsymbol{f}_{\mathrm{ac}}$ on
$v_2^{\mathrm{max}} = 0.017$ mm/s
(b) $\boldsymbol{v}_2^{\mathrm{slip}}$ off $\boldsymbol{f}_{\mathrm{ac}}$ on
$v_2^{\mathrm{max}} = 0.060$ mm/s
(c) $\boldsymbol{v}_2^{\mathrm{slip}}$ off $\boldsymbol{f}_{\mathrm{ac}}$ on
$v_2^{\mathrm{max}} = 0.103$ mm/s
(d) $\boldsymbol{v}_2^{\mathrm{slip}}$ on $\boldsymbol{f}_{\mathrm{ac}}$ off
$v_2^{\mathrm{max}} = 0.162$ mm/s
(e) $\boldsymbol{v}_2^{\mathrm{slip}}$ on $\boldsymbol{f}_{\mathrm{ac}}$ off
$v_2^{\mathrm{max}} = 0.164$ mm/s
(f) $\boldsymbol{v}_2^{\mathrm{slip}}$ on $\boldsymbol{f}_{\mathrm{ac}}$ off
$v_2^{\mathrm{max}} = 0.178$ mm/s
(g) $\boldsymbol{v}_2^{\mathrm{slip}}$ on $\boldsymbol{f}_{\mathrm{ac}}$ on
$v_2^{\mathrm{max}} = 0.162$ mm/s
(h) $\boldsymbol{v}_2^{\mathrm{slip}}$ on $\boldsymbol{f}_{\mathrm{ac}}$ on
$v_2^{\mathrm{max}} = 0.164$ mm/s
(i) $\boldsymbol{v}_2^{\mathrm{slip}}$ on $\boldsymbol{f}_{\mathrm{ac}}$ on
$v_2^{\mathrm{max}} = 0.178$ mm/s
L_y
y
$\frac{1}{2}L_y$
z
L_z
0
0
$\frac{1}{2}L_x$
x
L_x

7.4 Paper IV: Phys. Rev. E 101, 023107 1-12 (2020)

Theory of acoustic trapping of microparticles in capillary tubes

DOI: 10.1103/PhysRevE.101.023107

Authors: J. S. Bach and H. Bruus.
Journal: Phys. Rev. E **101**, 023107 (2020)

Theory of acoustic trapping of microparticles in capillary tubes

Jacob S. Bach* and Henrik Bruus†

Department of Physics, Technical University of Denmark, and DTU Physics Building 309, DK-2800 Kongens Lyngby, Denmark

(Received 29 November 2019; accepted 5 February 2020; published 20 February 2020)

We present a semianalytical theory for the acoustic fields and particle-trapping forces in a viscous fluid inside a capillary tube with arbitrary cross section and ultrasound actuation at the walls. We find that the acoustic fields vary axially on a length scale proportional to the square root of the quality factor of the two-dimensional (2D) cross-section resonance mode. This axial variation is determined analytically based on the numerical solution to the eigenvalue problem in the 2D cross section. The analysis is developed in two steps: First, we generalize a recently published expression for the 2D standing-wave resonance modes in a rectangular cross section to arbitrary shapes, including the viscous boundary layer. Second, based on these 2D modes, we derive analytical expressions in three dimensions for the acoustic pressure, the acoustic radiation and trapping force, as well as the acoustic energy flux density. We validate the theory by comparison to three-dimensional numerical simulations.

DOI: 10.1103/PhysRevE.101.023107

I. INTRODUCTION

Acoustophoresis is the acoustically induced migration of particles. During the past few decades the scientific field of microscale acoustofluidics has emerged, where this phenomenon is exploited for controlled handling of microparticles. Microscale acoustophoresis is gentle, label-free, and contact-less, and therefore it is useful for bioanalytics in lab-on-a-chip technologies. Examples include particle separation [1–4], concentration of red blood cells [5], iso-acoustic focusing of cells [6], acoustic tweezing [7–9], and cell patterning [10,11]. One particularly prominent acoustofluidic application is acoustic trapping of suspended microparticles against an external flow in cheap, disposable glass capillary tubes [12–17], which has been used for fast biological assays [18,19] and for trapping of sub-micrometer particles by use of larger trapped seed particles [20,21]. In these systems, a piezoelectric transducer is attached to the capillary tube and driven at MHz frequencies to generate a standing-wave resonance mode localized inside the capillary tube above the transducer.

The physics behind acoustophoresis is primarily described by two time-averaged forces acting on the suspended particles. First, due to differences in density and compressibility between the particles and the carrier fluid, the particles experience the acoustic radiation force, which scales with the particle volume [22–27] and tends to focus particles. Second, due to time-averaged momentum fluxes induced by the acoustic fields, a steady acoustic streaming flow is generated, and suspended particles therefore experience a drag force, which scales with the particle radius and tends to mix particles [28–30].

Both the acoustic radiation force and the acoustic streaming are important in the acoustic trap. Aside from the one-dimensional (1D) or two-dimensional (2D) focusing in the cross section due to the transverse acoustic radiation force, the axial variations in the acoustic fields also give rise to an axial acoustic radiation force, or trapping force. Furthermore, acoustic streaming in the plane parallel to the transducer surface is often observed above the edges of the transducer, strongly affecting the trapping characteristics [15,20]. The acoustic trapping in capillaries is therefore a three-dimensional (3D) problem, see Fig. 1, which complicates both the experimental characterization and the theoretical analysis needed for further development. Further complications arise from the many different 2D cross-sectional shapes that have been employed in the experimental studies of acoustofluidics in capillary channels: rectangular and trapezoidal shapes in etched silicon devices [31], flat channels with quarter-circle-shaped or tapered side walls in wet-etched glass devices [32], circular shapes in glass tubes [17], rectangular shapes of different aspect ratios in glass tubes such as 1:1 [16], 1:10 [14], and 1:20 [14,33], and flat glass tubes with a bulging lid [14]. In addition, given the technique of pulling structured multimaterial fibers recently applied in microfluidics [34], practically any cross-sectional shape of capillary tubes for acoustofluidics can now be fabricated. This multitude of shapes needs to be addressed theoretically.

In this work, we present a method to semianalytically calculate the 3D acoustic pressure in a capillary tube of arbitrary cross section actuated in an axially confined region of length L_{act} at the walls, see Fig. 1. Based on the either analytical or numerical solution to the 2D eigenvalue problem in the cross section, we derive analytical expressions in three dimensions for the acoustic pressure, the acoustic radiation force, the acoustic energy flux density, and the ratio between the axial and transverse acoustic trapping force. In particular, we show that for a 2D resonance mode α, the axial component of the radiation force is proportional to $\sqrt{\tilde{\Gamma}^{\alpha}}$, where $\tilde{\Gamma}^{\alpha}$ is the damping coefficient of the resonance mode α. In the special case of a 1D standing pressure wave in the cross

*jasoba@fysik.dtu.dk
†bruus@fysik.dtu.dk

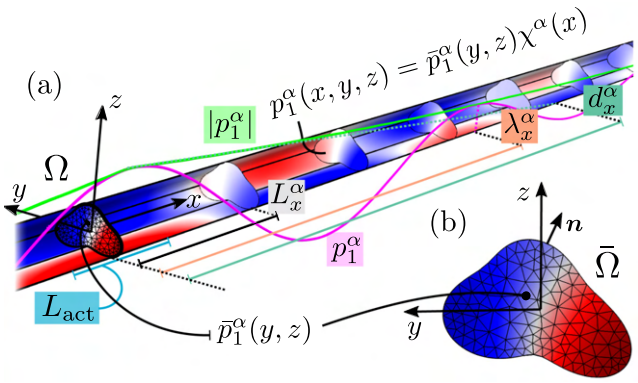

FIG. 1. A computed pressure resonance mode (dark red and light blue for high and low pressure) in a capillary tube of arbitrary cross section. (a) The complex-valued pressure mode $p_1^\alpha(x,y,z)$ in the 3D tube Ω is the product of the 2D pressure mode $\bar{p}_1^\alpha(y,z)$ in the cross section $\bar{\Omega}$ and the axial dependency $\chi^\alpha(x)$. It is excited by an actuation confined to a region of length $L_{\rm act}$. The dark magenta and light green curves represent the real part of p_1^α and the magnitude $|p_1^\alpha|$, respectively. The relevant length scales in the x direction are shown: the wave length λ_x^α, the decay length d_x^α, and the characteristic length scale L_x^α; see Eqs. (20) and (21). (b) The pressure $\bar{p}_1^\alpha(y,z)$ in the 2D cross section $\bar{\Omega}$ with the surface normal vector $\boldsymbol{n}$ and the mesh used in the numerical simulations.

section, our results agree with Woodside *et al.* [35], who obtained an analytical expression for the axial radiation force being proportional to the axial gradient of the acoustic energy density $E_{\rm ac}$. However, whereas they left $E_{\rm ac}$ undetermined, we calculate it analytically.

We validate our analytical results by direct 3D numerical simulations. Recent contributions in the 3D numerical modeling of capillary tubes include Gralinski *et al.* [17] who modeled a circular capillary tube with fluid and glass, Lei *et al.* [15], who modeled the fluid domain of a capillary tube and found four in-plane streaming rolls, and Ley and Bruus [36], who took into account absorption of outgoing waves in both the glass and the fluid. Also the piezoelectric transducer may be included in a full-device simulation as done by Skov *et al.* [37]. In the numerical validation of this paper, we model the fluid domain with a prescribed movement of the fluid-solid interface and implement a perfectly matched layer (PML) to absorb outgoing waves.

The paper is organized as follows: We present the governing equations in Sec. II, and in Sec. III we describe the numerical implementation used for validation of the presented theory. In Sec. IV, we generalize our previous analytical results for the acoustic pressure in rectangular cross sections [38] to arbitrary cross sections. Using the residue theorem, we derive the axial dependency of the 3D acoustic pressure. We proceed in Sec. V by calculating the axial dependency of the pressure in the case of a box-shaped actuation, and in Sec. V C we validate the analytical results by 3D numerical simulations. In Sec. VI, we present analytical expressions for time-averaged acoustic quantities such as the axial radiation force and the axial energy flux density. Finally, we discuss our results in Sec. VII and conclude in Sec. VIII.

II. GOVERNING EQUATIONS

The physical displacement $\boldsymbol{u}_{\rm phys}^0(\boldsymbol{r},t)$ of the fluid-solid interface oscillates harmonically with the angular frequency $\omega = 2\pi f$ and induces the physical pressure field $p_{\rm phys}(\boldsymbol{r},t)$ in the fluid. These fields are represented as the real part of the complex-valued linear perturbations $\boldsymbol{u}_1^0$ and p_1,

$$\boldsymbol{u}_{\rm phys}^0(\boldsymbol{r},t) = \mathrm{Re}\big[\boldsymbol{u}_1^0(\boldsymbol{r})e^{-i\omega t}\big], \tag{1a}$$

$$p_{\rm phys}(\boldsymbol{r},t) = \mathrm{Re}[p_1(\boldsymbol{r})e^{-i\omega t}]. \tag{1b}$$

In a fluid of dynamic viscosity $\eta_{\rm fl}$, bulk viscosity $\eta_{\rm fl}^{\rm b}$, isentropic compressibility $\kappa_{\rm fl}$, and mass density $\rho_{\rm fl}$, the acoustic fields are characterized by the compressional wave number $k_{\rm c}$ with real part $k_0 = \frac{\omega}{c_{\rm fl}}$, the bulk damping coefficient $\Gamma_{\rm fl}$, the shear wave number $k_{\rm s}$, and the viscous boundary-layer width $\delta_{\rm s}$ [27,30,37],

$$k_{\rm c} = \left(1 + i\frac{1}{2}\Gamma_{\rm fl}\right)k_0, \quad \Gamma_{\rm fl} = \left(\frac{4}{3} + \frac{\eta_{\rm fl}^{\rm b}}{\eta_{\rm fl}}\right)\eta_{\rm fl}\kappa_{\rm fl}\omega, \tag{2a}$$

$$k_{\rm s} = \frac{1+i}{\delta_{\rm s}}, \qquad \delta_{\rm s} = \sqrt{\frac{2\eta_{\rm fl}}{\rho_{\rm fl}\omega}}, \tag{2b}$$

where $i = \sqrt{-1}$ is the imaginary unit. In this work, we assume that the viscous boundary layer is much thinner than the acoustic wave length, as is the case in most acoustofluidic applications,

$$k_0\delta_{\rm s} \ll 1, \quad \Gamma_{\rm fl} = \frac{1}{2}\left(\frac{4}{3} + \frac{\eta_{\rm fl}^{\rm b}}{\eta_{\rm fl}}\right)(k_0\delta_{\rm s})^2 \ll 1. \tag{3}$$

The acoustic pressure p_1 satisfies the Helmholtz equation with the compressional wave number $k_{\rm c}$ and with the boundary-layer boundary condition recently derived in Ref. [30], valid for walls having a curvature radius much larger than the viscous boundary layer width $\delta_{\rm s}$,

$$\nabla^2 p_1 + k_{\rm c}^2 p_1 = 0, \quad \boldsymbol{r} \in \Omega, \tag{4a}$$

$$\mathcal{D}_\perp p_1 = k_0^2 U_{1\perp}(\boldsymbol{r}), \quad \boldsymbol{r} \in \partial\Omega, \tag{4b}$$

$$\mathcal{D}_\perp = \partial_\perp + \frac{i}{k_{\rm s}}\left(k_{\rm c}^2 + \partial_\perp^2\right), \quad \boldsymbol{r} \in \partial\Omega, \tag{4c}$$

$$U_{1\perp}(\boldsymbol{r}) = \frac{\rho_{\rm fl}c_{\rm fl}^2}{1 - i\Gamma_{\rm fl}}\left(-\boldsymbol{n} - \frac{i}{k_{\rm s}}\nabla\right)\cdot\boldsymbol{u}_1^0, \quad \boldsymbol{r} \in \partial\Omega. \tag{4d}$$

Here, the subscript $\perp$ represents the *inward* direction $(-\boldsymbol{n})$ opposite to the outward-pointing normal vector $\boldsymbol{n}$, and $U_{1\perp}(\boldsymbol{r})$ is the effective actuation function defined in terms of the physical interface displacement $\boldsymbol{u}_1^0$ of the fluid-solid interface $\partial\Omega$. Finally, we write the following standard time-averaged acoustic quantities, all defined in terms of the pressure p_1: The acoustic potential energy density $E_{\rm pot}$, the acoustic kinetic energy density $E_{\rm kin}$, the acoustic mechanical energy density $E_{\rm ac}$, the acoustic radiation potential $U_{\rm rad}$ for a suspended spherical particle of radius a, the acoustic radiation force $\boldsymbol{F}_{\rm rad}$, and the acoustic energy flux density $\boldsymbol{S}_{\rm ac}$,

$$E_{\rm pot} = \frac{1}{4}\kappa_{\rm fl}|p_1|^2, \quad E_{\rm kin} = \frac{1}{4}\kappa_{\rm fl}k_0^{-2}|\nabla p_1|^2, \tag{5a}$$

$$E_{\rm ac} = E_{\rm pot} + E_{\rm kin}, \quad \boldsymbol{S}_{\rm ac} = \frac{1}{2\rho_{\rm fl}\omega}\mathrm{Im}(p_1^*\nabla p_1), \tag{5b}$$

$$\boldsymbol{F}_{\rm rad} = -\nabla U_{\rm rad}, \quad U_{\rm rad} = \frac{4}{3}\pi a^3\left[f_0 E_{\rm pot} - \frac{3}{2}f_1 E_{\rm kin}\right]. \tag{5c}$$

TABLE I. Parameters used in the numerical simulations of water as the fluid medium at 25°C [42]; see also Sec. V C.

Parameter	Symbol	Value	Unit
Mass density	ρ_{fl}	997.05	kg m^{-3}
Compressibility	κ_{fl}	448	TPa^{-1}
Speed of sound	c_{fl}	1496.7	m s^{-1}
Dynamic viscosity	η_{fl}	0.890	mPa s
Bulk viscosity	$\eta^{\mathrm{b}}_{\mathrm{fl}}$	2.485	mPa s
Actuation displacement	d_0	0.1	nm
Cross-section length	L_{cr}	300	μm
Axial domain length	L_x^{num}	5.46	cm
PML length	L_{PML}	500	μmm
PML strength	K_{PML}	1000	–

Here, f_0 and f_1 are the monopole and dipole scattering coefficients that are real-valued because we consider particles with radius a much larger than both the viscous and the thermal boundary-layer thickness [22,25–27]. Furthermore, in Eq. (5b) "Im" and "$*$" denotes imaginary part and complex conjugation, respectively.

III. NUMERICAL VALIDATION METHOD

Our key theoretical results for the pressure p_1, to be presented in Secs. IV and V, are validated by the following direct-numerical-simulation method. We use the weak form PDE module in COMSOL MULTIPHYSICS [39] as described in Refs. [30,37,40], see also an example COMSOL script in the supplemental material of Ref. [41].

This validation is carried out in both a 3D and a 2D version solving the harmonically-driven problem (4) using the COMSOL "`Stationary study.`" Moreover, as explained in Sec. IV, a main result of this work is that we can express the 3D pressure in terms of 2D pressure eigenmodes and eigenvalues, which we compute numerically using the COMSOL "`Eigenvalue study.`" In the numerical simulations we use Lagrangian shape functions of quartic order, and the parameters listed in Table I.

For the numeric validation, we choose a capillary with the generic cross section shown in Fig. 1. This cross section has a linear size of around $2L_{\mathrm{cr}}$, and its boundary $\partial\bar{\Omega}$ is given by the arbitrarily chosen, smooth, wavy parametric curve in the yz cross section, $[y(s), z(s)]$ with $s \in [0; 2\pi]$, defined by $y(s) = L_{\mathrm{cr}} h_{\mathrm{cr}}(s)\cos(s)$, $z(s) = 0.9 L_{\mathrm{cr}} h_{\mathrm{cr}}(s)\sin(s + 0.2)$, and the radius function $h_{\mathrm{cr}}(s) = 1 + 0.15\sin(2s + 1.5) - 0.2\sin(3s)$.

The mesh is chosen to resolve the pressure on the relevant length scales. It is created as a 2D triangular mesh in the cross section with mesh size $\frac{1}{3}L_{\mathrm{cr}}$ in the bulk and $\frac{1}{6}L_{\mathrm{cr}}$ at the boundary; see Fig. 1(b). The 3D mesh is generated by sweeping the 2D mesh along the axial direction with a separation distance of $\frac{1}{6}L_x^{\alpha}$, where L_x^{α} is the characteristic axial length scale of the pressure introduced in Sec. IV C and shown in Fig. 1(a). The mesh is validated by standard mesh convergence tests [36].

For the 3D modeling of the long capillary tube, we use symmetry considerations to halve the computational domain [36], and a perfectly matched layer (PML) placed at the tube end to suppress acoustic reflections there; see Sec. II C of Ref. [36].

This numerical implementation of the model leads to 2×10^3 degrees of freedom (DOF) for the 2D simulations and 4×10^5 DOF for the 3D simulations. The simulations were performed on a workstation with a 3.5 GHz Intel Xeon CPU E5-1650 v2 dual-core processor and with a memory of 128 GB RAM.

Finally, we use the L^2-norm to numerically compute the relative deviation $\mathcal{E}(p, p^{\mathrm{ref}})$ of a pressure field p from a reference pressure field p^{ref} in the 3D domain Ω as

$$\mathcal{E}(p, p^{\mathrm{ref}}) = \sqrt{\frac{\int_\Omega |p - p^{\mathrm{ref}}|^2\, dV}{\int_\Omega |p^{\mathrm{ref}}|^2\, dV}}. \tag{6}$$

The analogous relative deviation in the 2D domain $\bar{\Omega}$ is called $\bar{\mathcal{E}}(\bar{p}, \bar{p}^{\mathrm{ref}})$, where an overbar denote a 2D quantity.

IV. THE ACOUSTIC PRESSURE IN A LONG STRAIGHT CAPILLARY TUBE OF ARBITRARY CROSS SECTION

In the following, we calculate the acoustic pressure $p_1(x, y, z)$ satisfying Eq. (4) to lowest order in the small parameters $k_0\delta_{\mathrm{s}}$, Eq. (3), in a long, straight capillary tube of arbitrary cross section that is invariant in the axial x direction as shown in Fig. 1(a). Our strategy has two key steps: First, based on our previous analysis of the 2D cross-sectional resonance modes $\bar{p}_1^{mn}(x, y)$ in a rectangular cross section having integer m and n half-waves in the y and z direction, and including the viscous boundary layer [38], we write an expression for the 2D cross-sectional resonance modes $\bar{p}_1^{\alpha}(x, y)$ in an arbitrary cross section. Second, by using these 2D modes together with the residue theorem, we evaluate the 3D acoustic pressure $p_1(x, y, z)$ satisfying Eq. (4) for any frequency $f = \frac{1}{2\pi}\omega$ and actuation function $U_{1\perp}$ as a sum over all resonance modes α. This approach is valuable because it provides a physical understanding of the acoustic trapping in the axial direction and analytical scaling laws for various length scales and trapping forces in terms of the properties of the 2D cross-sectional resonance modes for any given shape.

A. The 2D pressure resonance modes in an arbitrary cross section

In Ref. [38], we studied the special case of a rectangular cross section of side lengths L_y and L_z. We derived to lowest order in the small parameter $k_0\delta_{\mathrm{s}}$, the resonance modes $\bar{p}_1^{mn}$ with m half-waves in the y direction and n half-waves in the z direction, valid for wave numbers k_0 close to the resonance wave number $\bar{k}_0^{mn}$. Here, and in the following, we use the overbar to denote a quantity defined in the cross section $\bar{\Omega}$. With this notation, the expression for $\bar{p}_1^{mn}$ given in Eq. (12) of Ref. [38] becomes

$$\bar{p}_1^{mn}(k_0; y, z) = \bar{P}_1^{mn}\bar{\mathcal{G}}^{mn}(k_0)\bar{R}^{mn}(y, z), \quad \text{for } k_0 \approx \bar{k}_0^{mn}, \tag{7a}$$

$$\bar{R}^{mn}(y, z) = \cos\left(\frac{m\pi y}{L_y}\right)\cos\left(\frac{n\pi z}{L_z}\right), \tag{7b}$$

$$\bar{P}_1^{mn} = \frac{\oint_{\partial\bar{\Omega}} \bar{U}_{1\perp}\bar{R}^{mn}\, dl}{\int_{\bar{\Omega}} (\bar{R}^{mn})^2\, dA}, \tag{7c}$$

$$\bar{\mathcal{G}}^{mn}(k_0) = \frac{\frac{1}{2}\bar{k}_0^{mn}}{k_0 - \bar{k}_0^{mn} + \frac{1}{2}i\bar{k}_0^{mn}\bar{\Gamma}^{mn}}. \tag{7d}$$

The quantities used here have the following meaning: $\bar{R}^{mn}(y,z)$ in Eq. (7b) is the spatial dependency of a given 2D cross-sectional resonance mode. $\bar{P}_1^{mn}$ in Eq. (7c) is a coupling coefficient related to the overlap between $\bar{R}^{mn}(y,z)$ and the actuation function $\bar{U}_{1\perp}(y,z)$ defined in Eq. (4d) on the boundary $\partial\bar{\Omega}$ of the cross section $\bar{\Omega}$. $\bar{\mathcal{G}}^{mn}(k_0)$ in Eq. (7d) is the line-shape function of the mode defined in terms of three parameters: the wave number $k_0 = \frac{\omega}{c_{\mathrm{fl}}}$, the resonance wave number $\bar{k}_0^{mn}$, and the minute damping coefficient $\bar{\Gamma}^{mn} = \bar{\Gamma}_{\mathrm{bl}}^{mn} + \Gamma_{\mathrm{fl}} \ll 1$, where the latter is defined in Eq. (10) of Ref. [38] as the sum of the boundary-layer damping coefficient $\bar{\Gamma}_{\mathrm{bl}}^{mn}$ and the bulk damping coefficient Γ_{fl} of Eq. (2a).

1. Generalization to an arbitrarily shaped 2D cross section

To generalize from the rectangular cross section to an arbitrarily shaped cross section, it is helpful to write $\bar{\mathcal{G}}^{mn}$ as a function not of k_0 but of the complex-valued wave number k_{c} from Eq. (2a) for $k_{\mathrm{c}} \approx \bar{k}_{\mathrm{c}}^{mn}$, where $\bar{k}_{\mathrm{c}}^{mn}$ is the complex-valued resonance wave number. This variable shift is obtained by inserting $\bar{\Gamma}^{mn} = \bar{\Gamma}_{\mathrm{bl}}^{mn} + \Gamma_{\mathrm{fl}}$ in Eq. (7d),

$$\bar{\mathcal{G}}^{mn}(k_{\mathrm{c}}) \approx \frac{\left(\bar{k}_{\mathrm{c}}^{mn}\right)^2}{k_{\mathrm{c}}^2 - \left(\bar{k}_{\mathrm{c}}^{mn}\right)^2}, \quad \bar{k}_{\mathrm{c}}^{mn} = \left(1 - i\frac{\bar{\Gamma}_{\mathrm{bl}}^{mn}}{2}\right)\bar{k}_0^{mn}. \tag{8}$$

In Eqs. (7) and (8), we substitute the mode index mn by α, and thereby introduce our main assumption, which is validated numerically below, namely, an expression for the pressure resonance mode $\bar{p}_1^{\alpha}$ in an arbitrary cross section valid close to resonance $k_{\mathrm{c}} \approx \bar{k}_{\mathrm{c}}^{\alpha}$ and to lowest order in the small parameter $k_0\delta_{\mathrm{s}}$,

$$\bar{p}_1^{\alpha}(k_{\mathrm{c}}; y, z) = \bar{P}_1^{\alpha}\bar{\mathcal{G}}^{\alpha}(k_{\mathrm{c}})\bar{R}^{\alpha}(y,z), \quad \text{for } k_{\mathrm{c}} \approx \bar{k}_{\mathrm{c}}^{\alpha}, \tag{9a}$$

$$\bar{P}_1^{\alpha} = \frac{\oint_{\partial\bar{\Omega}} \bar{U}_{1\perp}\bar{R}^{\alpha}\, dl}{\int_{\bar{\Omega}} (\bar{R}^{\alpha})^2\, dA}, \tag{9b}$$

$$\bar{\mathcal{G}}^{\alpha}(k_{\mathrm{c}}) = \frac{\left(\bar{k}_{\mathrm{c}}^{\alpha}\right)^2}{k_{\mathrm{c}}^2 - \left(\bar{k}_{\mathrm{c}}^{\alpha}\right)^2}, \quad \bar{k}_{\mathrm{c}}^{\alpha} = \left(1 - i\frac{\bar{\Gamma}_{\mathrm{bl}}^{\alpha}}{2}\right)\bar{k}_0^{\alpha}. \tag{9c}$$

Here, the eigenvalue $\bar{k}_{\mathrm{c}}^{\alpha}$ and eigenfunction $\bar{R}^{\alpha}$ are defined through the 2D eigenvalue problem, corresponding to Eq. (4), in the cross section $\bar{\Omega}$ without actuation,

$$\nabla^2\bar{R}^{\alpha} + \left(\bar{k}_{\mathrm{c}}^{\alpha}\right)^2\bar{R}^{\alpha} = 0, \quad \boldsymbol{r} \in \bar{\Omega}, \tag{10a}$$

$$\mathcal{D}_{\perp}\bar{R}^{\alpha} = 0, \quad \boldsymbol{r} \in \partial\bar{\Omega}. \tag{10b}$$

The resonance frequency $\bar{f}^{\alpha}$ of the 2D mode α is found from the real part $\bar{k}_0^{\alpha} = \mathrm{Re}(\bar{k}_{\mathrm{c}}^{\alpha})$ of the eigenvalue $\bar{k}_{\mathrm{c}}^{\alpha}$,

$$\bar{f}^{\alpha} = \frac{1}{2\pi}\bar{\omega}^{\alpha} = \frac{1}{2\pi}c_{\mathrm{fl}}\bar{k}_0^{\alpha}. \tag{11}$$

The damping coefficient $\bar{\Gamma}^{\alpha}$ of mode α is written as the sum of the bulk damping coefficient Γ_{fl} of Eq. (2a) and the boundary-layer damping coefficient $\bar{\Gamma}_{\mathrm{bl}}^{\alpha}$ of Eq. (9c),

$$\bar{\Gamma}^{\alpha} = \bar{\Gamma}_{\mathrm{bl}}^{\alpha} + \Gamma_{\mathrm{fl}}, \quad \bar{\Gamma}_{\mathrm{bl}}^{\alpha} = -\frac{2\mathrm{Im}\left(\bar{k}_{\mathrm{c}}^{\alpha}\right)}{\mathrm{Re}\left(\bar{k}_{\mathrm{c}}^{\alpha}\right)}. \tag{12}$$

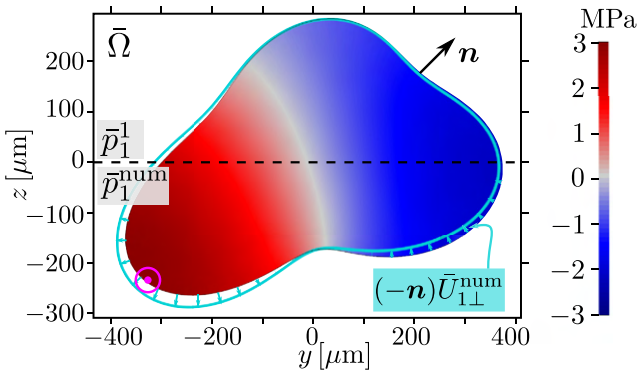

FIG. 2. Comparison in the cross section $\bar{\Omega}$ (defined in the text of Sec. III and shown in Fig. 1) between the 2D pressure mode $\bar{p}_1^1$ from Eqs. (9) and (10) with $\alpha = 1$ plotted for $z > 0$, and the 2D numerical pressure $\bar{p}_1^{\mathrm{num}}$ from Eq. (4) plotted for $z < 0$, both actuated by the actuation function $\bar{U}_{1\perp}^{\mathrm{num}}$ [light cyan curve and arrows, see Eq. (13)] at the fundamental resonance frequency $\bar{f}^1 = 1.1341$ MHz. The relative deviation defined in Eq. (6) between $\bar{p}_1^1$ and $\bar{p}_1^{\mathrm{num}}$ is $\bar{\mathcal{E}}(\bar{p}_1^1, \bar{p}_1^{\mathrm{num}}) = 0.14\,\%$. The encircled magenta point marks the position of the line used in the 3D line plots of Sec. V C.

2. Numerical validation in the 2D cross section

In Fig. 2, we validate numerically the generalized resonance-mode structure Eq. (9) by using the cross section $\bar{\Omega}$ and the numerical procedure described in Sec. III. We choose the actuation function $\bar{U}_{1\perp}^{\mathrm{num}}$ along the boundary $\partial\bar{\Omega}$ of $\bar{\Omega}$ to be

$$\bar{U}_{1\perp}^{\mathrm{num}}(y,z) = \rho_{\mathrm{fl}}c_{\mathrm{fl}}^2 d_0 \sin\left(\frac{\pi}{L_{\mathrm{cr}}}y\right)e^{-\frac{z}{L_{\mathrm{cr}}}}. \tag{13}$$

We determine numerically the lowest eigenmode $\alpha = 1$ in terms of the eigenfunction $\bar{R}^1(y,z)$, Eq. (10), and eigenfrequency $\bar{f}^1$, Eq. (11), listed in Table II together with other relevant mode parameters for $\alpha = 1$. Inserting this eigenmode together with $\bar{U}_{1\perp}^{\mathrm{num}}(y,z)$ and $k_{\mathrm{c}} = \frac{2\pi}{c_0}(1 + i\frac{1}{2}\Gamma_{\mathrm{fl}})\,\bar{f}^1$ into Eq. (9), we compute the pressure resonance mode $\bar{p}_1^1(k_{\mathrm{c}}; y, z)$ at the resonance frequency. In Fig. 2 we compare this theoretical result $\bar{p}_1^1$ with the direct numerical simulation $\bar{p}_1^{\mathrm{num}}$ obtained from the 2D version of Eq. (4) at the resonance frequency $\bar{f}^1$. Qualitatively, we see a smooth transition passing from $\bar{p}_1^1$ above the dashed line ($z > 0$) to $\bar{p}_1^{\mathrm{num}}$ below the dashed line ($z < 0$). Quantitatively, the relative difference (6) between the semianalytical $\bar{p}_1^1$ and the numerical $\bar{p}_1^{\mathrm{num}}$ is found to be $\bar{\mathcal{E}}(\bar{p}_1^1, \bar{p}_1^{\mathrm{num}}) = 0.14\,\%$, which is satisfactory in this approximation to lowest order in the small boundary-layer-width parameter $k_0\delta_{\mathrm{s}} = 0.24\,\%$.

TABLE II. Values for the fundamental mode $\alpha = 1$ of the 2D eigenvalue problem obtained by numerical simulation.

Parameter	Symbol	Eq.	Value	Unit
Eigenvalue	$\bar{k}_{\mathrm{c}}^1$	Eq. (10)	$4761.01 - 3.49i$	m^{-1}
Eigenfrequency	$\bar{f}^1$	Eq. (11)	1.1341	MHz
Damping coefficient	$\bar{\Gamma}^1$	Eq. (12)	0.00148	–
x length scale	L_x^1	Eq. (20)	5.46	mm

B. The 3D pressure

Based on Eq. (9) for the 2D cross-sectional pressure modes $\bar{p}_1^\alpha$, we now derive the pressure $p_1(x, y, z)$ satisfying Eq. (4) in the 3D capillary tube. For any given x-dependent function $\phi(x)$, we denote its Fourier transform by $\hat{\phi}(k_x)$, see Appendix A. The 3D pressure is calculated from the inverse Fourier transform,

$$p_1(x, y, z) = \int_{-\infty}^{\infty} \hat{p}_1(k_x; y, z)\, e^{ik_x x}\, \frac{dk_x}{2\pi}. \tag{14a}$$

Since the integrand $\hat{p}_1(k_x; y, z)\, e^{ik_x x}$ is a function of the complex-valued wave number k_x, we evaluate the integral using the residue theorem for an appropriate closed contour γ in the complex k_x plane and find

$$p_1(x, y, z) = \sum_{k_x^\alpha \text{ inside } \gamma} i\, \mathrm{Res}\big(\hat{p}_1(k_x; y, z) e^{ik_x x}, k_x^\alpha\big), \tag{14b}$$

summing over the residues $\mathrm{Res}(\hat{p}_1(k_x; y, z)e^{ik_x x}, k_x^\alpha)$ of all poles k_x^α inside the closed contour γ. To obtain these residues, we only need an expression for $\hat{p}_1(k_x; y, z)e^{ik_x x}$ valid close to k_x^α. The Fourier transform $\hat{p}_1(k_x; y, z)$ satisfies the Fourier-transformed Helmholtz problem Eq. (4),

$$\nabla^2 \hat{p}_1(k_x; y, z) + \big(k_c^2 - k_x^2\big)\hat{p}_1(k_x; y, z) = 0, \quad \boldsymbol{r} \in \bar{\Omega}, \tag{15a}$$

$$\mathcal{D}_\perp \hat{p}_1(k_x; y, z) = k_0^2 \hat{U}_{1\perp}(k_x; y, z), \quad \boldsymbol{r} \in \partial\bar{\Omega}, \tag{15b}$$

where $\partial\bar{\Omega}$ is the boundary of $\bar{\Omega}$. We note that Eq. (15) for $\hat{p}_1(k_x; y, z)$ is similar to Eq. (4) for an x-independent pressure $p_1 = \bar{p}_1(y, z)$ with the substitutions $k_c^2 \to k_c^2 - k_x^2$ and $\bar{U}_{1\perp}(y, z) \to \hat{U}_{1\perp}(k_x; y, z)$, see Appendix B for details. Using these substitutions in Eq. (9), we obtain the result for $\hat{p}_1(k_x; y, z)e^{ik_x x}$ valid for $k_c^2 - k_x^2 \approx (\bar{k}_c^\alpha)^2$ and to lowest order in the small parameter $k_0\delta_s$,

$$\hat{p}_1(k_x; y, z)e^{ik_x x} \approx \frac{-\big(\bar{k}_c^\alpha\big)^2 \bar{R}^\alpha e^{ik_x x}}{(k_x)^2 - \big(k_x^\alpha\big)^2} \frac{\int_{\partial\bar{\Omega}} \hat{U}_{1\perp}(k_x; y, z)\bar{R}^\alpha\, dl}{\int_{\bar{\Omega}} (\bar{R}^\alpha)^2\, dA}, \tag{16a}$$

$$k_x^\alpha = \sqrt{k_c^2 - \big(\bar{k}_c^\alpha\big)^2}. \tag{16b}$$

From Eq. (16a) we see that $\hat{p}_1(y, z, k_x)e^{ik_x x}$ has simple poles in the complex k_x plane at $k_x = \pm k_x^\alpha$, and therefore the residues $\mathrm{Res}(\hat{p}_1(k_x; y, z)e^{ik_x x}, k_x^\alpha)$ used in the sum Eq. (14b) can be found analytically; see Appendix C. The resulting expression for $p_1(x, y, z)$, valid for *all* frequencies and to lowest order in $k_0\delta_s$, is

$$p_1(x, y, z) = \sum_\alpha p_1^\alpha(x, y, z), \tag{17a}$$

$$p_1^\alpha(x, y, z) = P_1^\alpha(x)\bar{\mathcal{G}}^\alpha(k_c)\bar{R}^\alpha(y, z), \tag{17b}$$

$$P_1^\alpha(x) = \left[\frac{\int_{\partial\bar{\Omega}} U_{1\perp}\bar{R}^\alpha\, dl}{\int_{\bar{\Omega}} (\bar{R}^\alpha)^2\, dA} * g^\alpha\right](x), \tag{17c}$$

$$g^\alpha(x) = \frac{-ik_x^\alpha}{2} e^{ik_x^\alpha |x|}. \tag{17d}$$

Here, the asterisk "$*$" denotes the usual functional convolution in the x coordinate; see Eq. (A3). $g^\alpha(x)$ is the Green's function in the axial direction of mode α corresponding to a delta-function actuation at $x = 0$, given by $U_{1\perp}(x, y, z) = \bar{U}_{1\perp}(y, z)L_{\mathrm{act}}\delta(x)$, as this actuation yields

$$P_1^\alpha(x) = \bar{P}_1^\alpha L_{\mathrm{act}} g^\alpha(x), \tag{18}$$

where L_{act} is an actuation strength of dimension length, and $\bar{P}_1^\alpha$ is the 2D coupling coefficient defined in Eq. (7c).

C. The axial length scales of each mode

The axial dependency of the pressure $p_1(x, y, z)$ is given in Eqs. (17c) and (17d) by the actuation function $U_{1\perp}$ and the Green's function g^α. The latter leads to three axial length scales that characterize each mode α. Here the strength of our approach become apparent, as it allows us to extract analytical expressions for these length scales. First, by using $k_c^2 = (1 + i\Gamma_{\mathrm{fl}})k_0^2$, Eq. (2a), and $(\bar{k}_c^\alpha)^2 = (1 - i\bar{\Gamma}_{\mathrm{bl}}^\alpha)(\bar{k}_0^\alpha)^2$, Eq. (9c), as well as the assumption $\bar{\Gamma}^\alpha \ll 1$, we write the x wave number k_x^α in Eq. (16b) of mode α as

$$k_x^\alpha = \bar{k}_c^\alpha \frac{1}{\sqrt{\bar{\mathcal{G}}^\alpha}} \approx \bar{k}_0^\alpha \sqrt{\bar{\Gamma}^\alpha}\sqrt{\Delta^\alpha + i}, \quad \Delta^\alpha = \frac{k_0^2 - \big(\bar{k}_0^\alpha\big)^2}{\big(\bar{k}_0^\alpha\big)^2 \bar{\Gamma}^\alpha}. \tag{19}$$

Here, Δ^α is the difference between the square of the wave number $k_0 = \frac{\omega}{c_{\mathrm{fl}}}$ and the resonance wave number $\bar{k}_0^\alpha$, Eq. (11), of the mode α scaled by $(\bar{k}_0^\alpha)^2\bar{\Gamma}^\alpha$. From Eq. (19), we identify the characteristic length scale L_x^α of variation of the mode α in the x direction as

$$L_x^\alpha = \frac{1}{\bar{k}_0^\alpha \sqrt{\bar{\Gamma}^\alpha}}. \tag{20}$$

Then, by using Eqs. (19) and (20), we write the decay length d_x^α and wave length λ_x^α of the function $g^\alpha(x)$ in Eq. (17d) as

$$d_x^\alpha = \frac{1}{\mathrm{Im}\big(k_x^\alpha\big)} = L_x^\alpha \frac{1}{\mathrm{Im}(\sqrt{\Delta^\alpha + i})}, \tag{21a}$$

$$\lambda_x^\alpha = 2\pi \frac{1}{\mathrm{Re}\big(k_x^\alpha\big)} = L_x^\alpha \frac{2\pi}{\mathrm{Re}(\sqrt{\Delta^\alpha + i})}. \tag{21b}$$

In the following, a tilde is used to denote rescaling by L_x^α in the axial direction,

$$\tilde{x} = \frac{x}{L_x^\alpha}, \quad \tilde{d}_x^\alpha = \frac{d_x^\alpha}{L_x^\alpha}, \quad \tilde{\lambda}_x^\alpha = \frac{\lambda_x^\alpha}{L_x^\alpha}, \tag{22a}$$

$$\tilde{k}_x^\alpha = L_x^\alpha k_x^\alpha, \quad \tilde{g}^\alpha = L_x^\alpha g^\alpha. \tag{22b}$$

In Fig. 3(a), we plot the rescaled Green's function $\tilde{g}^\alpha(x)$ for three different frequencies: above resonance ($k_0 = \bar{k}_0^\alpha + \bar{k}_0^\alpha\bar{\Gamma}^\alpha$, $\Delta^\alpha = 2$), where it is propagating, at resonance ($k_0 = \bar{k}_0^\alpha$, $\Delta^\alpha = 0$), and below resonance ($k_0 = \bar{k}_0^\alpha - \bar{k}_0^\alpha\bar{\Gamma}^\alpha$, $\Delta^\alpha = -2$), where it is evanescent. In Fig. 3(b), we plot the decay length d_x^α and the wave length λ_x^α of Eq. (21) as a function of the actuation frequency for frequencies close to resonance $k_0 \approx \bar{k}_0^\alpha$. For frequencies just below resonance, d_x^α is small and λ_x^α is large, and vice versa for frequencies just above the resonance frequency. The three values of Δ^α used in Fig. 3(a) are marked by dashed vertical lines of the same color in Fig. 3(b).

As an example of the characteristic length scale of the axial pressure variation L_x^α, we consider a standing vertical half wave in a rectangular cross section of height L_z with the

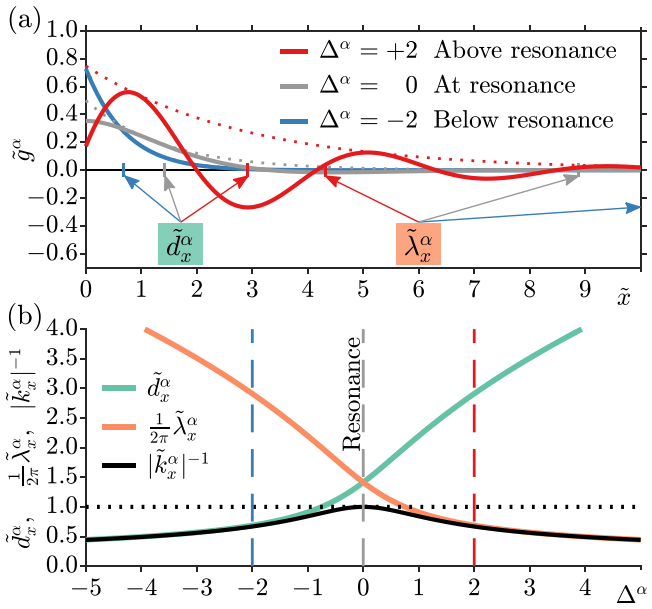

FIG. 3. Plots of the rescaled quantities of Eq. (22). (a) The complex-valued Green's function $\tilde{g}^\alpha(x)$ of Eq. (17d) plotted as the real part (solid) and modulus (dotted) for three values of Δ^α of Eq. (19): Below (-2), at (0), and above (2) the α resonance. (b) The decay length $\tilde{d}_x^\alpha$ and wave length $\tilde{\lambda}_x^\alpha$, Eq. (21), as well as $|\tilde{k}_x^\alpha|^{-1}$, Eq. (19), plotted versus Δ^α. The three vertical dashed lines mark the values used in (a).

wave number $\bar{k}_0^\alpha \approx \frac{\pi}{L_z}$, for which Eq. (20) leads to the estimate $L_x^\alpha \approx \frac{1}{\pi\sqrt{\bar{\Gamma}^\alpha}} L_z$. For realistic values of the damping coefficient, $0.001 < \bar{\Gamma}^\alpha < 0.01$ [43], we obtain $10L_z > L_x^\alpha > 3L_z$.

V. THE AXIAL DEPENDENCY OF THE PRESSURE FOR A SEPARABLE ACTUATION

Above, we derived analytical expressions for the characteristic length scales of the Green's function $g^\alpha(x)$ entering in Eq. (17c) for the pressure amplitude $P_1^\alpha(x)$. Now, we show analytically that the full 3D pressure at resonance separates into a product of the 2D resonance mode and a trivial axial dependency. We first calculate the axial variation of the pressure mode p_1^α for a given separable model-actuation $U_{1\perp}$ having the dimensionless axial dependency $\psi_{\text{act}}(x)$,

$$U_{1\perp}(x,y,z) = \bar{U}_{1\perp}(y,z)\,\psi_{\text{act}}(x). \tag{23}$$

In this case, the 3D mode $p_1^\alpha(x,y,z)$ in Eq. (17b) becomes a product of the 2D mode $\bar{p}_1^\alpha(y,z)$ and the dimensionless axial dependency $\chi^\alpha(x)$ of the pressure,

$$p_1^\alpha(x,y,z) = \bar{p}_1^\alpha(y,z)\chi^\alpha(x), \tag{24a}$$

$$\chi^\alpha(x) = [\psi_{\text{act}} * g^\alpha](x), \tag{24b}$$

which by Eq. (17a) leads to the pressure $p_1(x,y,z)$,

$$p_1(x,y,z) = \sum_\alpha \bar{p}_1^\alpha(y,z)\chi^\alpha(x), \quad \text{for any frequency } f. \tag{25}$$

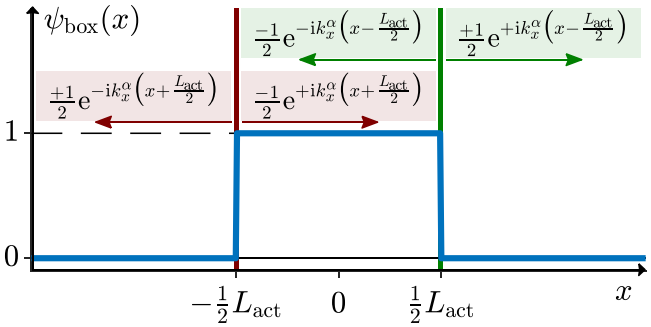

FIG. 4. The box-shaped axial dependency $\psi_{\text{act}}^{\text{box}}(x)$ (dark blue line) of the model actuation of width L_{act}, as well as the resulting traveling-wave components excited by the left step at $x = -\frac{1}{2}L_{\text{act}}$ (dark red arrows) and by the right step at $x = \frac{1}{2}L_{\text{act}}$ (light green arrows).

When actuating the system near one of the 2D resonances, say $\alpha = \alpha'$, we obtain the simplified expression

$$p_1(x,y,z) \approx \bar{p}_1^{\alpha'}(y,z)\chi^{\alpha'}(x), \quad \text{for } f \approx \bar{f}^{\alpha'}. \tag{26}$$

A. A box actuation with sharp steps

In capillary-tube devices used for acoustic trapping, a piezoelectric transducer is usually placed below the capillary tube in a confined region [14–16,20,21,44]. To mimic such an actuation, we consider the box-shaped axial dependency $\psi_{\text{act}}^{\text{box}}(x)$ of the actuation, which is unity in the actuation region of length L_{act} and sharply steps down to zero outside this region, as sketched in Fig. 4,

$$\psi_{\text{act}}^{\text{box}}(x) = \begin{cases} 1, & |x| < \frac{1}{2}L_{\text{act}}, \\ 0, & |x| > \frac{1}{2}L_{\text{act}}. \end{cases} \tag{27a}$$

Using this actuation in the convolution Eq. (24b) yields the axial dependency $\chi_{\text{box}}^\alpha(x)$ of the pressure,

$$\chi_{\text{box}}^\alpha(x) = \begin{cases} 1 - e^{ik_x^\alpha \frac{L_{\text{act}}}{2}} \cos\left(k_x^\alpha x\right), & |x| < \frac{1}{2}L_{\text{act}}, \\ -i\sin\left(k_x^\alpha \frac{L_{\text{act}}}{2}\right) e^{ik_x^\alpha |x|}, & |x| > \frac{1}{2}L_{\text{act}}. \end{cases} \tag{27b}$$

By writing the sine and cosine factors in terms of traveling waves, it is found that two waves travel away from each step at $x = \pm\frac{1}{2}L_{\text{act}}$ as sketched in Fig. 4.

In the limit $L_{\text{act}} \ll L_x^\alpha$, where the actuation is confined to a region much narrower than the axial pressure length scale L_x^α of Eq. (20), the axial dependency of the pressure is well approximated by a simplified expression $\chi_\delta^\alpha(x)$ as

$$\chi_{\text{box}}^\alpha(x) \approx \chi_\delta^\alpha(x) = L_{\text{act}} g^\alpha(x), \quad \text{for } L_{\text{act}} \ll L_x^\alpha, \tag{28}$$

where $g^\alpha(x)$ is defined in Eq. (17d) and plotted in Fig. 3(a) for different frequencies.

B. A box actuation with smooth steps

In the following numerical validation, we consider the more realistic box-actuation function $U_{1\perp}^{\text{num}}(x,y,z) = \bar{U}_{1\perp}^{\text{num}}(y,z)\psi_{\text{act}}^{\text{num}}(x)$, which separates as Eq. (23) with an axial dependency $\psi_{\text{act}}^{\text{num}}(x)$, similar to the box shape $\psi_{\text{act}}^{\text{box}}(x)$ in

Eq. (27a), but which has smooth transistions of width $d_{\rm act}$ at the steps $x = \pm\frac{1}{2}L_{\rm act}$,

$$U_{1\perp}^{\rm num}(x,y,z) = \bar{U}_{1\perp}^{\rm num}(y,z)\psi_{\rm act}^{\rm num}(x), \quad \text{at } \partial\Omega, \tag{29a}$$

$$\psi_{\rm act}^{\rm num}(x) = \frac{1}{1+e^{\frac{4(x-\frac{1}{2}L_{\rm act})}{d_{\rm act}}}} - \frac{1}{1+e^{\frac{4(x+\frac{1}{2}L_{\rm act})}{d_{\rm act}}}}. \tag{29b}$$

Here, $\bar{U}_{1\perp}^{\rm num}$ is defined in Eq. (13) and shown in Fig. 2.

C. Numerical validation of the 3D mode method

Using COMSOL Multiphysics as described in Sec. III, we validate the semianalytical Eq. (26) for $p_1(x,y,z)$ by the direct numerical solution $p_1^{\rm num}$ of Eq. (4) in the capillary tube Ω sketched in Fig. 1, both actuated at the resonance frequency $f = \bar{f}^1$ of the fundamental mode $\alpha = 1$ of the 2D cross section $\bar{\Omega}$. We assume that the tube is mirror-symmetric around the y-z plane through $x = 0$, and take the length of the computational domain to be $L_x^{\rm num} = 10L_x^1 = 5.46\,\text{cm}$, see Table II. At $x = 0$ we impose the symmetry boundary condition $\partial_x p_1^{\rm num} = 0$, and at $x = L_x^{\rm num}$ we place the perfectly matched layer (PML) mentioned in Sec. III to remove pressure wave reflections from the tube end. The wavy boundary $\partial\bar{\Omega}$ of the cross section $\bar{\Omega}$ is defined in Sec. III.

Using the 2D pressure mode (9) $\bar{p}_1^1(y,z)$ obtained from the eigenvalue problem (10), we construct the 3D pressure mode (24), as $p_1^1(x,y,z) = \bar{p}_1^1(y,z)\chi^1(x)$. In the following, we use the analytically known axial dependencies $\chi_{\rm box}^1(x)$, Eq. (27b), and χ_δ^1, Eq. (18), of the pressure to estimate the pressure obtained numerically from the actuation profile $\psi_{\rm act}^{\rm num}(x)$ in Eq. (29b).

To quantify the numerical validation, we compute at the resonance $f = \bar{f}^1$ the relative deviation $\mathcal{E}(p_1^1, p_1^{\rm num})$ defined in Eq. (6) between the semianalytical 3D pressure mode p_1^1 with the box actuation $\psi_{\rm act}^{\rm box}(x)$ of Eq. (27a) and the direct numerical 3D pressure $p_1^{\rm num}$ with the smoothen-box actuation $\psi_{\rm act}^{\rm num}(x)$ of Eq. (29b),

$$p_1^1 = \bar{p}_1^1(y,z)\chi_{\rm box}^1(x), \quad \text{with } \psi_{\rm act}^{\rm box}(x) \text{ at } \bar{f}^1, \tag{30a}$$

$$p_1^{\rm num} = p_1(x,y,z), \quad \text{with } \psi_{\rm act}^{\rm num}(x) \text{ at } \bar{f}^1. \tag{30b}$$

In Fig. 5, we study the axial dependency of the pressure for varying actuation step width $d_{\rm act}$ and fixed actuation length of $L_{\rm act} = 2L_x^1$, rescaled as in Eq. (22) by the characteristic length scale L_x^1,

$$\tilde{d}_{\rm act} = \frac{d_{\rm act}}{L_x^1}, \quad \tilde{L}_{\rm act} = \frac{L_{\rm act}}{L_x^1}. \tag{31}$$

In Fig. 5(b) is shown that for small $d_{\rm act}$ the semianalytical expression (30a) is a good approximation for all $\tilde{x}$. For large $d_{\rm act}$ it deviates significantly from the numerical solution (30b) inside the actuation region for $|\tilde{x}| < 1$, whereas it remains a good approximation outside for $|\tilde{x}| < 1$. This is quantified in the inset of Fig. 5(b), showing that the deviation $\mathcal{E}_{\rm box}$ (solid line) is around 1 % for a sufficiently narrow actuation step width $\tilde{d}_{\rm act} \lesssim 0.4$.

In Fig. 6 we vary the actuation length $L_{\rm act}$ and keep the actuation step width fixed at $\tilde{d}_{\rm act} = 0.1$. For all actuation lengths $\tilde{L}_{\rm act}$, the semianalytical expression (30a) $\bar{p}_1^1\chi_{\rm box}^1$ (dashed magenta lines) approximates well the full numerical solution $p_1^{\rm num}$ (30b) (solid green lines), whereas $\bar{p}_1^1(y,z)\chi_\delta^1(x)$ (black dotted lines), see Eq. (18), as expected is only a good approximation in the narrow-actuation limit $\tilde{L}_{\rm act} \ll 1$. In the inset of Fig. 6(b) the relative deviations of these approximations from $p_1^{\rm num}$ are quantified by $\mathcal{E}_{\rm box}$ (solid line) and $\mathcal{E}_\delta$ (dotted line).

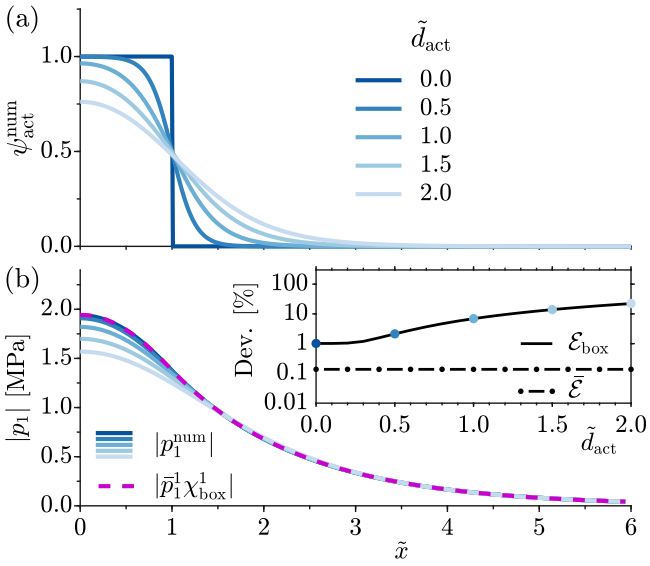

FIG. 5. The acoustic pressure for varying actuation step width $\tilde{d}_{\rm act}$ and fixed actuation length $\tilde{L}_{\rm act} = 2$. (a) The actuation profile $\psi_{\rm act}^{\rm num}(x)$ used in the full numerical simulation for $\tilde{d}_{\rm act} = 0.0$ (dark blue) to $\tilde{d}_{\rm act} = 2.0$ (light blue). (b) Line plots of the magnitude of the acoustic pressure along the axis parallel to the x-axis shown in Fig. 2, with $|p_1^1| = |\bar{p}_1^1\chi_{\rm box}^1|$ (magenta dashed line) from Eq. (30a), and $|p_1^{\rm num}|$ (blue lines) from Eq. (30b) obtained from the 3D simulation by using the actuation of same color shown in (a). The inset shows the relative deviation (6) $\mathcal{E}_{\rm box}$ (solid line) of the pressure mode $\bar{p}_1^1(y,z)\chi_{\rm box}^1(x)$ from the numerical pressure $p_1^{\rm num}$, as well as the deviation for the 2D calculation given in Sec. IV A, $\bar{\mathcal{E}} = 0.14\,\%$ (dot-dashed line).

VI. TIME-AVERAGED ACOUSTIC QUANTITIES CLOSE TO RESONANCE

In typical experiments on acoustofluidic devices, the MHz oscillation of the acoustic pressure p_1 is not observed directly. We therefore study the time-averaged acoustic quantities given in Eq. (5).

A. Time-averaged quantities for a single mode

We study a single-mode pressure resonance of the form $p_1 \approx p_1^\alpha = \bar{p}_1^\alpha(y,z)\chi^\alpha(x)$, see Eq. (26). Inserting this form in Eq. (5) together with the rescaled axial coordinate $\tilde{x} = x/L_x^\alpha$ and the corresponding derivative $\partial_{\tilde{x}} = L_x^\alpha\,\partial_x$, both scaled with the characteristic axial length scale L_x^α from Eq. (20), we obtain the time-averaged quantities,

$$E_{\rm pot}^\alpha = \bar{E}_{\rm pot}^\alpha|\chi^\alpha|^2, \tag{32a}$$

$$E_{\rm kin}^\alpha = \bar{E}_{\rm kin}^\alpha|\chi^\alpha|^2 + \frac{\bar{E}_{\rm pot}^\alpha}{(k_0L_x^\alpha)^2}|\partial_{\tilde{x}}\chi^\alpha|^2 \approx \bar{E}_{\rm kin}^\alpha|\chi^\alpha|^2, \tag{32b}$$

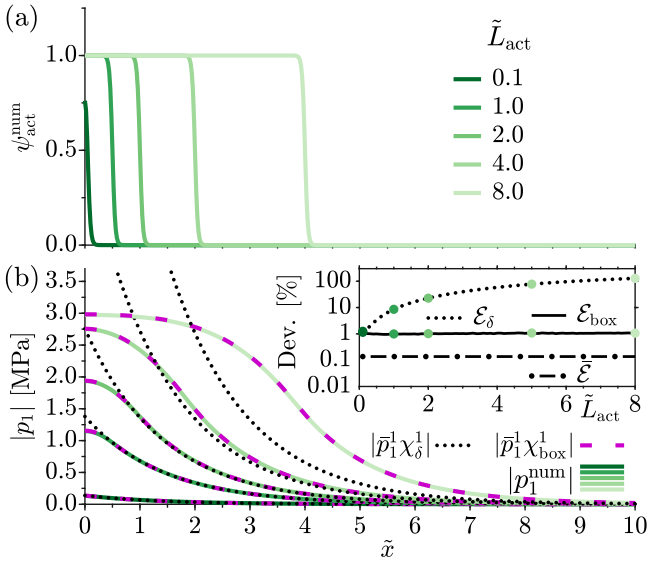

FIG. 6. The acoustic pressure for varying actuation length $\tilde{L}_{\rm act}$ and fixed actuation step width $\tilde{d}_{\rm act} = 0.1$. (a) The actuation profile $\psi^{\rm num}_{\rm act}(x)$ used in the full numerical simulations for $\tilde{L}_{\rm act} = 0.1$ (dark green) to $\tilde{L}_{\rm act} = 8.0$ (light green). (b) Line plots of the magnitude of the acoustic pressure along the axis parallel to the x axis shown in Fig. 2. The green graphs show the pressure $p_1^{\rm num}$ obtained from the 3D simulation by using the actuation of same color shown in (a). The dashed magenta lines show $p_1^1 = \bar{p}_1^1\chi_{\rm box}^1$ from Eq. (30b), and the dotted black lines show the pressure $\bar{p}_1^1\chi_\delta^1$ valid in limit $\tilde{L}_{\rm act} \ll 1$, see Eq. (18). The inset shows the deviation $\mathcal{E}$ from to the reference pressure $p_1^{\rm num}$ Eq. (6), for $\bar{p}_1^1\chi_{\rm box}^1$ ($\mathcal{E}_{\rm box}$, solid), for $\bar{p}_1^1\chi_\delta^1$ ($\mathcal{E}_\delta$, dotted), as well as the deviation for the 2D calculation given in Sec. IV A, $\bar{\mathcal{E}} = 0.14\,\%$ (dot-dashed line).

$$E^\alpha_{\rm ac} \approx \bar{E}^\alpha_{\rm ac}|\chi^\alpha|^2, \tag{32c}$$

$$U^\alpha_{\rm rad} \approx \bar{U}^\alpha_{\rm rad}|\chi^\alpha|^2, \tag{32d}$$

$$\boldsymbol{F}^\alpha_{\rm rad} \approx \bar{\boldsymbol{F}}^\alpha_{\rm rad}|\chi^\alpha|^2 - \sqrt{\bar{\Gamma}^\alpha}\bar{k}^\alpha_0\bar{U}^\alpha_{\rm rad}\partial_{\tilde{x}}|\chi^\alpha|^2\boldsymbol{e}_x, \tag{32e}$$

$$\boldsymbol{S}^\alpha_{\rm ac} = \bar{\boldsymbol{S}}^\alpha_{\rm ac}|\chi^\alpha|^2 + \sqrt{\bar{\Gamma}^\alpha}c_{\rm fl}\bar{E}^\alpha_{\rm pot}{\rm Im}[2(\chi^\alpha)^*\partial_{\tilde{x}}\chi^\alpha]\boldsymbol{e}_x. \tag{32f}$$

Here, the overbar denote a cross-section quantity obtained by using the cross-section resonance pressure $\bar{p}^\alpha_1(y,z)$ in Eq. (5). In Eqs. (32b)–(32e) we used that $(k_0L^\alpha_x)^{-2} \approx \bar{\Gamma}^\alpha$, see Eq. (20), which is here assumed to be much smaller than unity. We note that the time-averaged quantities listed in Eq. (32) have three different axial dependencies: $|\chi^\alpha|^2$ which is the axial dependency of $E^\alpha_{\rm kin}$, $E^\alpha_{\rm pot}$, $E^\alpha_{\rm ac}$, $U^\alpha_{\rm rad}$, $(\boldsymbol{F}^\alpha_{\rm rad})_{yz}$, and $(\boldsymbol{S}^\alpha_{\rm ac})_{yz}$. $\partial_{\tilde{x}}|\chi^\alpha|^2$ which is the axial dependency of the axial radiation force $F^\alpha_{{\rm rad},x}$. And finally ${\rm Im}[2(\chi^\alpha)^*\partial_{\tilde{x}}\chi^\alpha]$ which is the axial dependency of the axial energy flux density $S^\alpha_{{\rm ac},x}$.

B. Time-averaged quantities for the box actuation

In Fig. 7, we use the box actuation with $\chi^\alpha = \chi^\alpha_{\rm box}$, see Eq. (27b), to make contour plots in the $\tilde{L}_{\rm act}$-$\tilde{x}$ plane of the axial dependency of the time-averaged quantities listed in Eq. (32). For each quantity, we choose the rescaled frequency $\Delta^\alpha \approx \frac{f_0 - f^\alpha_0}{\frac{1}{2}f_0\bar{\Gamma}^\alpha}$, see Eq. (19), to obtain the largest possible value

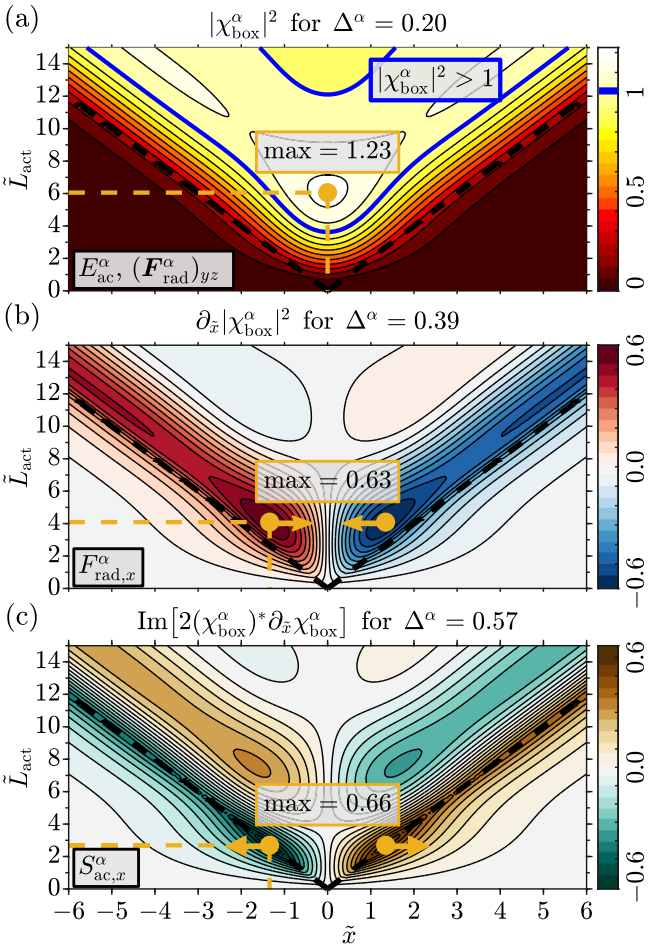

FIG. 7. The axial dependency of the time-averaged acoustic quantities of Eq. (32) obtained by using $\chi^\alpha_{\rm box}$ from Eq. (27b) as the axial dependency of the pressure. In each plot, the rescaled frequency $\Delta^\alpha \approx \frac{f_0 - f^\alpha_0}{\frac{1}{2}f_0\Gamma^\alpha}$, Eq. (19), is chosen to maximize the corresponding physical quantity, and the maximum value is marked by yellow points. The black dashed lines show the actuation edge $\tilde{x} = \pm\frac{1}{2}\tilde{L}_{\rm act}$. (a) The axial dependency $|\chi^\alpha_{\rm box}|^2$ of the acoustic energy density $E^\alpha_{\rm ac}$, and the cross-sectional radiation force $(\boldsymbol{F}_{\rm rad})_{yz}$, where the contours are separated by 0.1 and the thick blue lines mark the area where the axial dependency of $|\chi^\alpha_{\rm box}|^2$ exceeds unity. (b) The axial dependency $\partial_{\tilde{x}}|\chi^\alpha_{\rm box}|^2$ of the axial radiation force $F^\alpha_{{\rm rad},x}$. (c) The axial dependency ${\rm Im}[2(\chi^\alpha_{\rm box})^*\partial_{\tilde{x}}\chi^\alpha_{\rm box}]$ of the axial energy flux density $S^\alpha_{{\rm ac},x}$.

of that quantity, *i.e.* to optimize $|\bar{\mathcal{G}}^\alpha|^2|\chi^\alpha_{\rm box}|^2$, $|\bar{\mathcal{G}}^\alpha|^2\partial_{\tilde{x}}|\chi^\alpha_{\rm box}|^2$, and $|\bar{\mathcal{G}}^\alpha|^2{\rm Im}[2(\chi^\alpha_{\rm box})^*\partial_{\tilde{x}}\chi^\alpha_{\rm box}]$, respectively.

In Fig. 7(a) is shown a contour plot of the axial dependency $|\chi^\alpha_{\rm box}(x)|^2$ of the acoustic energy density $E^\alpha_{\rm ac}$, Eq. (32c), and cross-sectional radiation force $(\boldsymbol{F}^\alpha_{\rm rad})_{y,z}$, Eq. (32e). The blue contour delimit the region where the 3D acoustic energy density $E^\alpha_{\rm ac}$ is larger than the 2D acoustic energy density $\bar{E}^\alpha_{\rm ac}$. The orange dot marks the maximum obtainable acoustic energy density which is $\max\{E^\alpha_{\rm ac}\} = 1.23\bar{E}^\alpha_{\rm ac}$, found at the optimal actuation length $\tilde{L}_{\rm act} \approx 6.1$.

In Fig. 7(b) is shown a contour plot of the axial dependency $\partial_{\tilde{x}}|\chi^\alpha_{\rm box}(x)|^2$ of the axial acoustic radiation force $F^\alpha_{{\rm rad},x}$, see Eq. (32e). The orange dots mark the maximum obtainable axial trapping force which is found to be $\max\{F^\alpha_{{\rm rad},x}\} =$

$\mp 0.63\sqrt{\bar{\Gamma}^\alpha}\bar{k}_0^\alpha \bar{U}_{\rm rad}^\alpha$, for the optimal actuation length $\tilde{L}_{\rm act} \approx 4.1$. For this optimal value, the force is largest at the axial position $\tilde{x} = \pm 1.3$, which is around 17% inside the actuation region.

Finally, in Fig. 7(c) is shown a contour plot of the axial dependency $\mathrm{Im}[2(\chi_{\rm box}^\alpha)^* \partial_{\tilde{x}} \chi_{\rm box}^\alpha]$ of the axial acoustic energy flux density $S_{{\rm ac},x}^\alpha$; see Eq. (32f). Clearly, the energy is always transported away from the actuation region at the edges of the actuation domain $\tilde{x} \approx \pm \frac{1}{2}\tilde{L}_{\rm act}$. The orange dots mark the largest obtainable axial energy flux density which is $\max\{S_{{\rm ac},x}^\alpha\} = \pm 0.66\sqrt{\bar{\Gamma}^\alpha} c_{\rm fl} \bar{E}_{\rm pot}^\alpha$.

C. Example: A standing half-wave resonance in a rectangular cross section

A standard device for acoustic trapping is the capillary tube with the rectangular cross section $0 < y < L_y$ and $0 < z < L_z$, where a standing-half-wave resonance in the vertical z direction is excited [14–16,20,21,44]. Using Eq. (7) with $\bar{k}_0^{01} = \frac{\pi}{L_z}$ for the 2D pressure mode $\bar{p}_1^{01} = \bar{P}_1^{01}\bar{\mathcal{G}}^{01}\cos(\bar{k}_0^{01} z)$, we evaluate the cross-sectional radiation force $F_{{\rm rad},z}^{01}(x,z)$ from Eq. (32e) as

$$\frac{F_{{\rm rad},z}^{01}(x,z)}{4\pi a^3 \bar{k}_0^{01}\langle \bar{E}_{\rm ac}^{01}\rangle} \approx \Phi \sin\left(2\bar{k}_0^{01} z\right)|\chi^{01}(x)|^2, \tag{33a}$$

where $\Phi = \frac{1}{3}f_0 + \frac{1}{2}f_1$ is the usual acoustic contrast factor [23,26,27], and $\langle \bar{E}_{\rm ac}^{01}\rangle = \frac{1}{4}\kappa_{\rm fl}|\bar{P}^{01}\bar{\mathcal{G}}^{01}|^2$ is the spatial average of the acoustic energy density Eq. (32c) in the cross section $\bar{\Omega}$. Similarly, we use Eqs. (7) and (32e) to evaluate the axial radiation force,

$$\frac{F_{{\rm rad},x}^{01}(x,z)}{4\pi a^3 \bar{k}_0^{01}\langle \bar{E}_{\rm ac}^{01}\rangle} \approx \left[\frac{1}{2}f_1 - \Phi\cos^2\left(\bar{k}_0^{01} z\right)\right]\sqrt{\bar{\Gamma}^{01}}\partial_{\tilde{x}}|\chi^{01}|^2. \tag{33b}$$

From Eqs. (33a) and (33b), we calculate the ratio between the maximum axial radiation force and the maximum cross section radiation force for the single standing-wave resonance by using $\max\{\partial_{\tilde{x}}|\chi^{01}(x)|^2\} \sim 2\max\{|\chi^{01}(x)|^2\}$,

$$\frac{\max\left\{F_{{\rm rad},x}^{01}\right\}}{\max\left\{F_{{\rm rad},z}^{01}\right\}} \approx \frac{f_1}{\Phi}\sqrt{\bar{\Gamma}^{01}} = \frac{2}{1+\frac{2f_0}{3f_1}}\sqrt{\bar{\Gamma}^{01}},$$
$$\approx 0.21\sqrt{\bar{\Gamma}^{01}}, \quad \text{for polystyrene particles.} \tag{33c}$$

In the last step we use the scattering coefficients $f_0 = 0.443$ and $f_1 = 0.034$ for large polystyrene particles [26]. As examples, Ley and Bruus [36] studied numerically the pyrex-glass capillary tubes named "C1" (used by Hammerström *et al.* [20] with inner dimensions $L_y = 2\,\mathrm{mm}$ and $L_z = 0.2\,\mathrm{mm}$) and "C5" (proposed by the authors with inner dimensions $L_y = 0.5\,\mathrm{mm}$ and $L_z = 0.2\,\mathrm{mm}$). In both cases, they found the quality factor for the standing half-wave resonance in the z direction to be $Q = 53$, corresponding to the damping coefficient $\bar{\Gamma}^{01} = \frac{1}{53}$. Using this value in (33c) gives the ratio $\frac{1}{35}$, where Ley and Bruus found the ratio to be $\frac{0.44\,\mathrm{pN}}{22\,\mathrm{pN}} = \frac{1}{50}$ for C1 (see their Fig. 6) and $\frac{0.13\,\mathrm{pN}}{7\,\mathrm{pN}} = \frac{1}{54}$ for C5 (see their Fig. 9). Hence, even though Eq. (33c) is obtained from a hard-wall analysis, it predicts values close to the full simulation where the surrounding glass capillary is included.

Furthermore, for the capillary tube C1 with the experimentally found resonance frequency $f = \frac{1}{2\pi}k_0 c_{\rm fl} = 3.970\,\mathrm{MHz}$ and transducer length $L_{\rm act} = 1160\,\mu\mathrm{mm}$ [20], we calculate $\tilde{L}_{\rm act} = L_{\rm act}k_0\sqrt{\bar{\Gamma}^{01}} = 2.6$. From Figs. 7(a) and 7(b) follows the prediction that the acoustic energy density $E_{\rm ac}^\alpha$ and trapping force $F_{{\rm rad},x}^\alpha$ may be approximately doubled by doubling $L_{\rm act}$.

VII. DISCUSSION

The theory presented in Sec. IV relies on the main assumption that the 2D resonance modes in an arbitrary cross section can be written as in Eq. (9) for wave numbers k_0 very close to the cross-section eigenvalues $\bar{k}_0^\alpha$. Whereas this generalization is not proven mathematically, it is physically reasonable, and we have validated it numerically in Fig. 2 with a relative deviation of 0.14%. We note that the eigenfunctions $\bar{R}^\alpha(y,z)$ in the cross section do not exactly form a complete set, because the eigenvalues of the eigenvalue problem Eq. (10) has a small imaginary part. However, in the limit $k_0\delta_{\rm s} \ll 1$ the viscous boundary layer introduces a minute imaginary part to the eigenvalues, and thus Eq. (9) is a good approximation. It may be possible to come up with a special cross section where our theory fails, but it does apply to all capillary tube cross sections used in the experiments that are reported in the literature.

We have presented detailed results for the special simplifying, but experimentally relevant, condition that the actuation frequency is near a resonance characterized by a single mode that does not overlap with other modes, such that the 3D pressure p_1 is described by only a single term of the sum Eq. (17). We emphasize, however, that this is not a necessary condition, as the general theory allows both for nonresonant actuation and for multiple overlapping modes. In fact, we have done equally successful validations for frequencies away from resonance, where more modes are taken into account.

We have considered the actuation to have a box-shaped axial dependency given by Eq. (27a) to mimic a piezoelectric transducer confined in the axial direction to a length $L_{\rm act}$. In a realistic glass-capillary system, the motion of the wall will be more complicated as found from the numerical simulations by Ley and Bruus [36] and the simulations and experiments by Reichert *et al.* [45]. Nevertheless, when calculating the ratio between the axial and cross-sectional radiation force in the end of Sec. VI C and using the damping coefficient $\bar{\Gamma}^1 = \frac{1}{53}$ found from the numerical simulation by Ley and Bruus, we almost reproduce their values, namely, $\frac{F_{{\rm rad},x}}{F_{{\rm rad},z}} \approx \frac{1}{50}$. This agreement indicates that the predictions from our theory of the axial variations of the pressure remain valid for more complicated wall actuation, and that the important effect from the capillary walls is well described by a change in the damping coefficient $\bar{\Gamma}^\alpha$ for the mode. The probable cause for this increased damping factor of the fluid resonance is not dissipation in the capillary tube but instead an axial transport of energy in the solid away from the fluid, as pointed out by Ley and Bruus [36]. This can be seen from Eq. (32f), which states that the axial transport $(\boldsymbol{S}_{\rm ac})_x$ of energy is proportional to the speed of sound $c_{\rm fl}$, and because the speed of sound in the capillary tube is usually larger than in the fluid, energy

is efficiently transported away from the trapping region. For example, the longitudinal sound speed in pyrex glass is 3.7 times larger than in water [46].

VIII. CONCLUSION AND OUTLOOK

We have presented a semianalytical method to calculate the acoustic pressure in a long, straight capillary tube of arbitrary cross section with a localized ultrasound actuation at the walls. Moreover, we have analytically derived the axial dependencies Eq. (32) of the time-averaged response and used it to derive an expression for the key aspect in the acoustic trap, namely, the axial acoustic radiation force Eq. (33) acting on suspended particles. The viscous boundary layer is taken into account through an effective boundary condition Eq. (4b), which is valid when the width δ_s of the viscous boundary layer is much smaller than both the acoustic wavelength ($k_0\delta_s \ll 1$) and the radius of curvature of the cross section. This condition is usually satisfied in typical experiments.

In Eq. (9), the acoustic 2D cross-section resonance mode $\bar{p}_1^\alpha(y,z)$ in an arbitrary cross section was obtained by a generalization of the well-studied case Eq. (7) of a rectangular cross section. The 2D mode $\bar{p}_1^\alpha(y,z)$ can be found analytically for integrable shapes, such as rectangles, circles and ellipses, and otherwise numerically as shown in Fig. 1. The theory results in the correct amplitude and phase of $\bar{p}_1^\alpha(y,z)$ by combining the eigenvalue $\bar{k}_c^\alpha$ and the dimensionless eigenfunction $\bar{R}^\alpha$ of Eq. (10) with the actuation function $\bar{U}_{1\perp}$ of Eq. (4d) and the inclusion of the viscous boundary layer through the boundary operator $\mathcal{D}_\perp$ in Eq. (4c).

From the 2D pressure modes $\bar{p}_1^\alpha(y,z)$ in the cross section, known for frequencies near resonance, we derived in Eq. (17b) the 3D pressure modes $p_1^\alpha(x,y,z)$. The sum over α of these modes, see Eq. (17a), constitutes the full 3D pressure $p_1(x,y,z)$ including the axial dependency and valid for all frequencies. In Eq. (20) we extracted for 3D resonance mode p_1^α the characteristic axial length scale $L_x^\alpha = (\bar{k}_0^\alpha\sqrt{\bar{\Gamma}^\alpha})^{-1}$, where $\bar{k}_0^\alpha$ is the 2D resonance wave number and $\bar{\Gamma}^\alpha$ is the 2D damping coefficient. Because the axial radiation force $(\boldsymbol{F}_{\mathrm{rad}}^\alpha)_x$ and the axial energy flux density $(\boldsymbol{S}_{\mathrm{ac}}^\alpha)_x$ of resonance mode α, depend on the axial gradient of the pressure, we find in Eqs. (32e) and (32f) that these are both proportional to $\sqrt{\bar{\Gamma}^\alpha}$. These analytical results constitute the main theoretical insight obtained by our mode analysis. Furthermore, from a purely numerical-modeling point of view, the theoretical method implies a drastic reduction in the computer-memory requirements and in computation times, because the full 3D system can be obtained from a 2D simulation of the cross-section eigenproblem combined with the analytical expressions for the axial dependencies. This reduction will facilitate any numerical parametric study of the 3D acoustic trap.

To further study the physics of the acoustic trap, we chose a box-shaped actuation which mimics a piezoelectric transducer attached to the capillary walls in a confined region of length L_{act}, and which allows for analytic solutions. In Fig. 7 is shown the resulting axial dependencies of the acoustic energy density E_{ac}^α, the cross-sectional acoustic radiation force $(\boldsymbol{F}_{\mathrm{rad}})_{yz}$, the axial acoustic radiation force $F_{\mathrm{rad},x}^\alpha$, and the axial energy flux density $S_{\mathrm{rad},x}^\alpha$. Remarkably, we found an optimal actuation length $L_{\mathrm{act}} \approx 2\text{-}5L_x^\alpha$ that maximizes these quantities. Furthermore, whereas the maximum acoustic energy density E_{ac}^α is found in the center of the channel, maximum axial radiation force $F_{\mathrm{rad},x}^\alpha$ is located around 17% inside the actuation region, and the maximum axial energy flux density $S_{\mathrm{rad},x}^\alpha$ is located at the edge of the actuation region.

We validated numerically our theory in Figs. 5 and 6 for the 3D system shown in Fig. 1 near the resonance $\alpha = 1$, by using the box-shaped actuation given in Eq. (27a). We found a relative agreement around 1 % between theory and simulation, even when the box-shaped actuation had smooth steps. This agreement is satisfactory as the theory was developed in the limit of a small boundary-layer width ($k_0\delta_s \ll 1$), and $k_0\delta_s = 0.0024$ in the numerical model.

The presented theory motivates further studies of capillary tubes. One obvious extension of this work is to compute the acoustic streaming, in particular the horizontal in-plane streaming rolls observed by Hammarström, Laurell, and Nilsson [20] and by Lei, Glynne-Jones, and Hill [15]. The streaming can be computed numerically by combining the presented theory with the recently published methods of calculating the time-averaged streaming velocity [30,37]. Another future study, would be to include the elastic walls in the mode analysis. For example, by combining the wall velocity $U_{1\perp}$ obtained from a full 3D numerical simulation with the solution of the 2D eigenvalue problem Eq. (10), the coupling strength P_1^α for each pressure mode p_1^α can be calculated from Eq. (17). In this way the relative importance of each pressure mode in the acoustic trap can be characterized. A last example of further work is to investigate the loss of acoustic energy in the fluid into the solid as briefly discussed in the last paragraph of Sec. VII.

We have provided theoretical predictions of the axial variation of the acoustic fields in capillary tubes and pointed out that there is an optimal actuation length leading to a maximum acoustic radiation force, both in the axial and cross-sectional directions. Our analysis provides a theoretical understanding of the complicated 3D characteristics of acoustofluidics in capillary tubes, and in long, straight channels in general. Our resulting expressions can be used to aid in the design of acoustic trapping devices, and we hope that our work will inspire further systematic experimental characterization and optimization of acoustic traps.

APPENDIX A: THE FOURIER TRANSFORM AND THE CONVOLUTION RELATIONS

We define the Fourier transform $\mathcal{F}_x$ and the inverse Fourier transform $\mathcal{F}_k^{-1}$ as

$$\hat{\phi}(k) = \mathcal{F}_x[\phi(x)](k) = \int_{-\infty}^{\infty} \phi(x)e^{-ikx}\,dx, \tag{A1a}$$

$$\phi(x) = \mathcal{F}_k^{-1}[\hat{\phi}(k)](x) = \int_{-\infty}^{\infty} \hat{\phi}(k)e^{+ikx}\,\frac{dk}{2\pi}. \tag{A1b}$$

For this convention, the convolution relations are

$$\mathcal{F}[\phi_1 * \phi_2] = \mathcal{F}[\phi_1]\mathcal{F}[\phi_2], \tag{A2a}$$

$$\mathcal{F}[\phi_1\phi_2] = \mathcal{F}[\phi_1] * \mathcal{F}[\phi_2], \tag{A2b}$$

where the in-line asterisk denote the convolution,

$$[f * g](x) = \int_{-\infty}^{\infty} f(x')g(x - x')\,dx'. \tag{A3}$$

APPENDIX B: DETAILS ABOUT THE USE OF THE BOUNDARY OPERATOR $\mathcal{D}_\perp$ IN Eq. (15)

The boundary operator $\mathcal{D}_\perp$ defined in Eq. (4c) takes into account the viscous boundary layer. To be able to compare Eq. (15) for $\hat{p}_1$ to Eq. (4) for $\bar{p}_1$, we need to express $\mathcal{D}_\perp$ in terms of $k_c^2 - k_x^2$. This is achieved by subtracting and adding k_x^2 as $\mathcal{D}_\perp = \partial_\perp + \frac{i}{k_s}[(k_c^2 - k_x^2) + k_x^2 + \partial_\perp^2]$. Close to the poles we have $k_x \approx k_x^\alpha$, and thus Eq. (16b) gives $k_c^2 - k_x^2 \approx (\bar{k}_c^\alpha)^2$, whereby $\mathcal{D}_\perp \approx \partial_\perp + \frac{i}{k_s}[(\bar{k}_c^\alpha)^2 + (k_x^\alpha)^2 + \partial_\perp^2]$. If we assume $(\bar{k}_c^\alpha)^2 \gg (k_x^\alpha)^2$, then we may ignore $(k_x^\alpha)^2$. Later, this assumption is proven correct by noticing that Eq. (19) yields $(k_x^\alpha)^2 \sim \bar{\Gamma}^\alpha(\bar{k}_c^\alpha)^2$ with $\bar{\Gamma}^\alpha \ll 1$. Consequently, Eq. (16) for the Fourier transform $\hat{p}_1$ at k_x-values close to the complex poles k_x^α is valid to $\mathcal{O}(\bar{\Gamma}^\alpha)$.

APPENDIX C: DETAILS IN APPLYING THE RESIDUE THEOREM

To obtain the residues $\mathrm{Res}(\hat{p}_1(k_x; y, z)e^{ik_x x}, k_x^\alpha)$ used in Eq. (14b), we first rewrite Eq. (16a) by inserting $\hat{U}_{1\perp}(k_x; y, z) = \int_{-\infty}^{\infty} U_{1\perp}(x', y, z)e^{-ik_x x'}\,dx'$,

$$\hat{p}_1(k_x; y, z)\, e^{ik_x x} \approx \frac{-\left(\bar{k}_c^\alpha\right)^2 \bar{R}^\alpha}{(k_x)^2 - \left(k_x^\alpha\right)^2} \frac{\int_{\partial\bar{\Omega}} \int_{-\infty}^{\infty} U_{1\perp}(x', y, z)e^{ik_x(x-x')}\,dx'\bar{R}^\alpha\,dl}{\int_{\bar{\Omega}} (\bar{R}^\alpha)^2\,dA}. \tag{C1}$$

This expression is valid for k_x close to the simple poles given by $\pm k_x^\alpha = \pm\sqrt{k_c^2 - (\bar{k}_c^\alpha)^2}$; see Eq. (16b). Based on Eq. (C1), the integral in Eq. (14a) is calculated using the residue theorem over a closed contour γ in the complex k_x-plane chosen as follows: (1) For $x - x' > 0$, the integrand Eq. (C1) vanishes for $k_x \to i\infty$, and we choose the closed contour γ to be the counterclockwise contour consisting of the real $\mathrm{Re}(k_x)$ axis connected to a semicircle of radius $|k_x| \to \infty$ in the *upper* complex k_x plane. This contour encloses the residues at $k_x = +k_x^\alpha = +\sqrt{k_c^2 - (\bar{k}_c^\alpha)^2}$ having positive imaginary part. (2) For $x - x' < 0$, the integrand Eq. (C1) vanishes for $k_x \to -i\infty$, and we choose the closed contour γ to be the clock-wise contour consisting of the real $\mathrm{Re}(k_x)$-axis connected to a semicircle of radius $|k_x| \to \infty$ in the *lower* complex k_x-plane. This contour encloses the residues at $k_x = -k_x^\alpha = -\sqrt{k_c^2 - (\bar{k}_c^\alpha)^2}$ having negative imaginary part. In either case (1) or (2), the residues inside the closed contour γ are

$$\begin{aligned}
&\mathrm{Res}\left(\hat{p}_1(k_x; y, z)e^{ik_x x}, k_x^\alpha\right) \\
&= \frac{-\left(\bar{k}_c^\alpha\right)^2 \bar{R}^\alpha}{2k_x^\alpha} \frac{\int_{\partial\bar{\Omega}} \int_{-\infty}^{\infty} U_{1\perp}(x', y, z)e^{ik_x^\alpha|x-x'|}\,dx'\bar{R}^\alpha\,dl}{\int_{\bar{\Omega}} (\bar{R}^\alpha)^2\,dA} \\
&= -i\bar{\mathcal{G}}^\alpha(k_c)\bar{R}^\alpha \frac{\int_{\partial\bar{\Omega}} \int_{-\infty}^{\infty} U_{1\perp}(x', y, z)g(x - x')\,dx'\bar{R}^\alpha\,dl}{\int_{\bar{\Omega}} (\bar{R}^\alpha)^2\,dA},
\end{aligned} \tag{C2}$$

where we inserted $\bar{\mathcal{G}}^\alpha(k_c)$ from Eq. (9c) and introduced the normalized function $g^\alpha(x)$ given by Eq. (17d). Finally, using the residues Eq. (C2) in the sum Eq. (14b), we obtain Eq. (17) for the acoustic pressure p_1.

[1] T. Laurell, F. Petersson, and A. Nilsson, Chip integrated strategies for acoustic separation and manipulation of cells and particles, Chem. Soc. Rev. **36**, 492 (2007).

[2] M. K. Tan, R. Tjeung, H. Ervin, L. Y. Yeo, and J. Friend, Double aperture focusing transducer for controlling microparticle motions in trapezoidal microchannels with surface acoustic waves, Appl. Phys. Lett. **95**, 134101 (2009).

[3] A. Lenshof and T. Laurell, Continuous separation of cells and particles in microfluidic systems, Chem. Soc. Rev. **39**, 1203 (2010).

[4] X. Ding, Z. Peng, S.-C. S. Lin, M. Geri, S. Li, P. Li, Y. Chen, M. Dao, S. Suresh, and T. J. Huang, Cell separation using tilted-angle standing surface acoustic waves, Proc. Natl. Acad. Sci. USA **111**, 12992 (2014).

[5] A. Lenshof, A. Ahmad-Tajudin, K. Jaras, A.-M. Sward-Nilsson, L. Aberg, G. Marko-Varga, J. Malm, H. Lilja, and T. Laurell, Acoustic whole blood plasmapheresis chip for prostate specific antigen microarray diagnostics, Anal. Chem. **81**, 6030 (2009).

[6] P. Augustsson, J. T. Karlsen, H.-W. Su, H. Bruus, and J. Voldman, Iso-acoustic focusing of cells for size-insensitive acousto-mechanical phenotyping, Nat. Commun. **7**, 11556 (2016).

[7] J. Shi, D. Ahmed, X. Mao, S.-C. S. Lin, A. Lawit, and T. J. Huang, Acoustic tweezers: Patterning cells and microparticles using standing surface acoustic waves (SSAW), Lab Chip **9**, 2890 (2009).

[8] A. Riaud, M. Baudoin, O. Bou Matar, L. Becerra, and J.-L. Thomas, Selective Manipulation of Microscopic Particles with Precursor Swirling Rayleigh Waves, Phys. Rev. Appl. **7**, 024007 (2017).

[9] Z. Gong and M. Baudoin, Particle Assembly with Synchronized Acoustic Tweezers, Phys. Rev. Appl. **12**, 024045 (2019).

[10] D. J. Collins, B. Morahan, J. Garcia-Bustos, C. Doerig, M. Plebanski, and A. Neild, Two-dimensional single-cell patterning with one cell per well driven by surface acoustic waves, Nat. Commun. **6**, 8686 (2015).

[11] D. J. Collins, R. O'Rorke, C. Devendran, Z. Ma, J. Han, A. Neild, and Y. Ai, Self-Aligned Acoustofluidic Particle Focusing and Patterning in Microfluidic Channels from Channel-Based Acoustic Waveguides, Phys. Rev. Lett. **120**, 074502 (2018).

[12] T. Lilliehorn, U. Simu, M. Nilsson, M. Almqvist, T. Stepinski, T. Laurell, J. Nilsson, and S. Johansson, Trapping of microparticles in the near field of an ultrasonic transducer, Ultrasonics **43**, 293 (2005).

[13] M. Evander, L. Johansson, T. Lilliehorn, J. Piskur, M. Lindvall, S. Johansson, M. Almqvist, T. Laurell, and J. Nilsson, Noninvasive acoustic cell trapping in a microfluidic perfusion system for online bioassays, Anal. Chem. **79**, 2984 (2007).

[14] B. Hammarström, M. Evander, H. Barbeau, M. Bruzelius, J. Larsson, T. Laurell, and J. Nillsson, Non-contact acoustic cell trapping in disposable glass capillaries, Lab Chip **10**, 2251 (2010).

[15] J. Lei, P. Glynne-Jones, and M. Hill, Acoustic streaming in the transducer plane in ultrasonic particle manipulation devices, Lab Chip **13**, 2133 (2013).

[16] P. Mishra, M. Hill, and P. Glynne-Jones, Deformation of red blood cells using acoustic radiation forces, Biomicrofluidics **8**, 034109 (2014).

[17] I. Gralinski, S. Raymond, T. Alan, and A. Neild, Continuous flow ultrasonic particle trapping in a glass capillary, J. Appl. Phys. **115**, 054505 (2014).

[18] M. Grundy, W. Bolek, W. Coakley, and E. Benes, Rapid agglutination testing in an ultrasonic standing wave, J. Immunol. Methods **165**, 47 (1993).

[19] M. Tenje, H. Xia, M. Evander, B. Hammarström, A. Tojo, S. Belák, T. Laurell, and N. LeBlanc, Acoustic trapping as a generic noncontact incubation site for multiplex bead-based assays, Anal. Chim. Acta **853**, 682 (2014).

[20] B. Hammarström, T. Laurell, and J. Nilsson, Seed particle enabled acoustic trapping of bacteria and nanoparticles in continuous flow systems, Lab Chip **12**, 4296 (2012).

[21] M. Evander, O. Gidlof, B. Olde, D. Erlinge, and T. Laurell, Non-contact acoustic capture of microparticles from small plasma volumes, Lab Chip **15**, 2588 (2015).

[22] L. V. King, On the acoustic radiation pressure on spheres, Proc. R. Soc. London, Ser. A **147**, 212 (1934).

[23] K. Yosioka and Y. Kawasima, Acoustic radiation pressure on a compressible sphere, Acustica **5**, 167 (1955).

[24] L. P. Gorkov, On the forces acting on a small particle in an acoustical field in an ideal fluid, Sov. Phys. Dokl. **6**, 773 (1962) [On the forces acting on a small particle in an acoustical field in an ideal fluid, Doklady Akademii Nauk SSSR **140**, 88 (1961)].

[25] A. A. Doinikov, Acoustic radiation force on a spherical particle in a viscous heat-conducting fluid.1. general formula, J. Acoust. Soc. Am. **101**, 713 (1997).

[26] M. Settnes and H. Bruus, Forces acting on a small particle in an acoustical field in a viscous fluid, Phys. Rev. E **85**, 016327 (2012).

[27] J. T. Karlsen and H. Bruus, Forces acting on a small particle in an acoustical field in a thermoviscous fluid, Phys. Rev. E **92**, 043010 (2015).

[28] Lord Rayleigh, On the circulation of air observed in Kundt's tubes, and on some allied acoustical problems, Philos. Trans. R. Soc. London **175**, 1 (1884).

[29] C. Eckart, Vortices and streams caused by sound waves, Phys. Rev. **73**, 68 (1948).

[30] J. S. Bach and H. Bruus, Theory of pressure acoustics with viscous boundary layers and streaming in curved elastic cavities, J. Acoust. Soc. Am. **144**, 766 (2018).

[31] S. M. Hagsäter, A. Lenshof, P. Skafte-Pedersen, J. P. Kutter, T. Laurell, and H. Bruus, Acoustic resonances in straight micro channels: Beyond the 1D-approximation, Lab Chip **8**, 1178 (2008).

[32] M. Evander, A. Lenshof, T. Laurell, and J. Nilsson, Acoustophoresis in wet-etched glass chips, Anal. Chem. **80**, 5178 (2008).

[33] D. Carugo, T. Octon, W. Messaoudi, A. L. Fisher, M. Carboni, N. R. Harris, M. Hill, and P. Glynne-Jones, A thin-reflector microfluidic resonator for continuous-flow concentration of microorganisms: A new approach to water quality analysis using acoustofluidics, Lab Chip **14**, 3830 (2014).

[34] R. Yuan, J. Lee, H.-W. Su, E. Levy, T. Khudiyev, J. Voldman, and Y. Fink, Microfluidics in structured multimaterial fibers, PNAS **115**, E10830 (2018).

[35] P. J. Woodside SM, Bowen BD, Measurement of ultrasonic forces for particle-liquid separations, AIChE J. **43**, 1727 (1997).

[36] M. W. H. Ley and H. Bruus, Three-Dimensional Numerical Modeling of Acoustic Trapping in Glass Capillaries, Phys. Rev. Appl. **8**, 024020 (2017).

[37] N. R. Skov, J. S. Bach, B. G. Winckelmann, and H. Bruus, 3D modeling of acoustofluidics in a liquid-filled cavity including streaming, viscous boundary layers, surrounding solids, and a piezoelectric transducer, AIMS Mathematics **4**, 99 (2019).

[38] J. S. Bach and H. Bruus, Bulk-driven acoustic streaming at resonance in closed microcavities, Phys. Rev. E **100**, 023104 (2019).

[39] COMSOL Multiphysics 5.4, http://www.comsol.com.

[40] P. B. Muller, R. Barnkob, M. J. H. Jensen, and H. Bruus, A numerical study of microparticle acoustophoresis driven by acoustic radiation forces and streaming-induced drag forces, Lab Chip **12**, 4617 (2012).

[41] P. B. Muller and H. Bruus, Theoretical study of time-dependent, ultrasound-induced acoustic streaming in microchannels, Phys. Rev. E **92**, 063018 (2015).

[42] P. B. Muller and H. Bruus, Numerical study of thermoviscous effects in ultrasound-induced acoustic streaming in microchannels, Phys. Rev. E **90**, 043016 (2014).

[43] P. Hahn and J. Dual, A numerically efficient damping model for acoustic resonances in microfluidic cavities, Phys. Fluids **27**, 062005 (2015).

[44] D. Carugo, D. N. Ankrett, P. Glynne-Jones, L. Capretto, R. J. Boltryk, X. Zhang, P. A. Townsend, and M. Hill, Contrast agent-free sonoporation: The use of an ultrasonic standing wave microfluidic system for the delivery of pharmaceutical agents, Biomicrofluidics **5**, 044108 (2011).

[45] P. Reichert, D. Deshmukh, L. Lebovitz, and J. Dual, Thin film piezoelectrics for bulk acoustic wave (BAW) acoustophoresis, Lab Chip **18**, 3655 (2018).

[46] *Glass Silicon Constraint Substrates*, CORNING, New York, USA, http://www.valleydesign.com/Datasheets/Corning%20Pyrex%207740.pdf.

7.5 Paper V: Phys. Rev. Lett., submitted (2020)

Suppression of acoustic streaming in shape-optimized microchannels

Authors: J. S. Bach and H. Bruus.
Journal: Submitted to Phys. Rev. Lett. (Feb. 2020).
ArXiv preprint: arxiv.org/abs/2002.11058

Suppression of acoustic streaming in shape-optimized channels

Jacob S. Bach* and Henrik Bruus†
Department of Physics, Technical University of Denmark,
DTU Physics Building 309, DK-2800 Kongens Lyngby, Denmark
(Dated: 25 February 2020)

Acoustic streaming is an ubiquitous phenomenon resulting from time-averaged nonlinear dynamics in oscillating fluids. In this theoretical study, we show that acoustic streaming can be suppressed by two orders of magnitude in major regions of a fluid by optimizing the shape of its confining walls. Remarkably, the acoustic pressure is not suppressed in this shape-optimized cavity, and neither is the acoustic radiation force on suspended particles. This basic insight may lead to applications, such as acoustophoretic handling of nm-sized particles, which is otherwise impaired by acoustic streaming.

When a fluid executes oscillatory motion due to an imposed acoustic field or a vibrating boundary, the inherent fluid-dynamical nonlinearities spawn a steady flow adding to the oscillatory motion. This phenomenon, called acoustic streaming, has a rich, 200 year old history. Early observations by Ørsted (1809) and Savart (1827) of the difference in the motion of coarse and fine grained powders over vibrating Chladni plates, were in 1831 conclusively attributed to acoustic streaming in the air by Faraday in his seminal experiments on Chladni plates placed in a partial vacuum [1]. In 1876, Dvořák observed acoustic streaming caused by standing sound waves in a Kundt's tube [2]. A theoretical explanation of this boundary-induced streaming in various geometries was provided in 1884 by Lord Rayleigh in terms of an oscillatory boundary layer flow, which by time-averaging induces a steady slip velocity near the boundary that drives the steady streaming [3]. A further experimental and theoretical analysis of streaming invoking Prandtl boundary layers was presented by Schlichting in 1932 [4], who identified counter-rotating vortices inside the thin viscous boundary layer near the wall co-existing with the rotating vortices outside the boundary layer. Rayleigh's slip-velocity formalism was later generalized to curved surfaces moving in the normal direction [5, 6], to flat surfaces moving in arbitrary directions [7], and to curved surfaces with arbitrary velocity [8]. Eckart found in 1948 that acoustic streaming also can be induced by attenuation of sound in the bulk [9]. This effect is mainly considered important for systems much larger than the acoustic wavelength [10, 11], but as was pointed out recently, it can also be significant on the length scale of a single wave length for rotating acoustic fields [12].

Acoustic streaming is a truly ubiquitous phenomenon that has been observed not only in Newtonian fluids, but also in superfluid helium [13] and non-Newtonian viscoelastic liquids [14]. It has found many applications within a wide range of topics such as thermoacoustic engines [15], enhancement of electrodedeposition [16], mixing in microfluidics [17], biofouling removal [18], and lysing of vesicles [19]. Given its widespread appearance, a fundamental question naturally arises: is it possible to suppress acoustic streaming? Recently, Karlsen *et al.* showed experimentally and theoretically that for inhomogeneous fluids inside a microchannel, the acoustic streaming can be suppressed in the bulk of the fluid as long as a density gradient is present there [20], an effect caused by the acoustic body force [21].

But what about homogeneous fluids? In this work, using the same experimentally-validated numerical modeling as in Refs. [20, 21], we demonstrate that for homogeneous fluids confined in cavities or channels, the acoustic streaming can be suppressed by more than two orders of magnitude in large parts of the bulk by optimizing the shape of the confinement. This discovery not only provides physical insight into a time-honored fundamental phenomenon in fluid dynamics, but it is also of considerable practical interest in the field of microscale acoustofluidics, where ultrasound fields routinely are used to handle suspended microparticles. Such a particle of radius a is affected by two forces: the acoustic radiation force that scales with a^3 and tends to focus particles at the acoustic nodal planes; and the streaming-induced drag force that scales with a and by virtue of the streaming vortices tends to defocus particles. Consequently, there exists a lower limit of a that allows for controlled handling by the focusing radiation force, and it has been shown to be $a_{\min} \approx 1$ µm for dilute aqueous particle solutions [22, 23]. A suppression of the acoustic streaming would enable a desirable controlled handling of nanoparticles, such as bacteria, viruses and exosomes.

Modeling the acoustofluidic fields.—To optimize the shape, efficient and fast computation of the acoustofluidic fields is required. For that, we use the method described in Refs. [8, 24], where the thin viscous boundary layer is taken into account analytically and therefore needs not to be resolved numerically. We consider a domain Ω with hard boundary walls, see Fig. 1, containing a homogeneous and quiescent fluid of dynamic viscosity η_{fl}, bulk viscosity $\eta_{\mathrm{fl}}^{\mathrm{b}}$, density ρ_{fl}, and sound speed c_{fl} at pressure p_{fl}. An acoustic field is created by letting the boundary oscillate harmonically with the angular frequency ω around its equilibrium position $\partial\Omega$ with a prescribed displacement $\boldsymbol{u}^{\mathrm{bdr}}(\boldsymbol{r},t)$ expressed as the real part of the

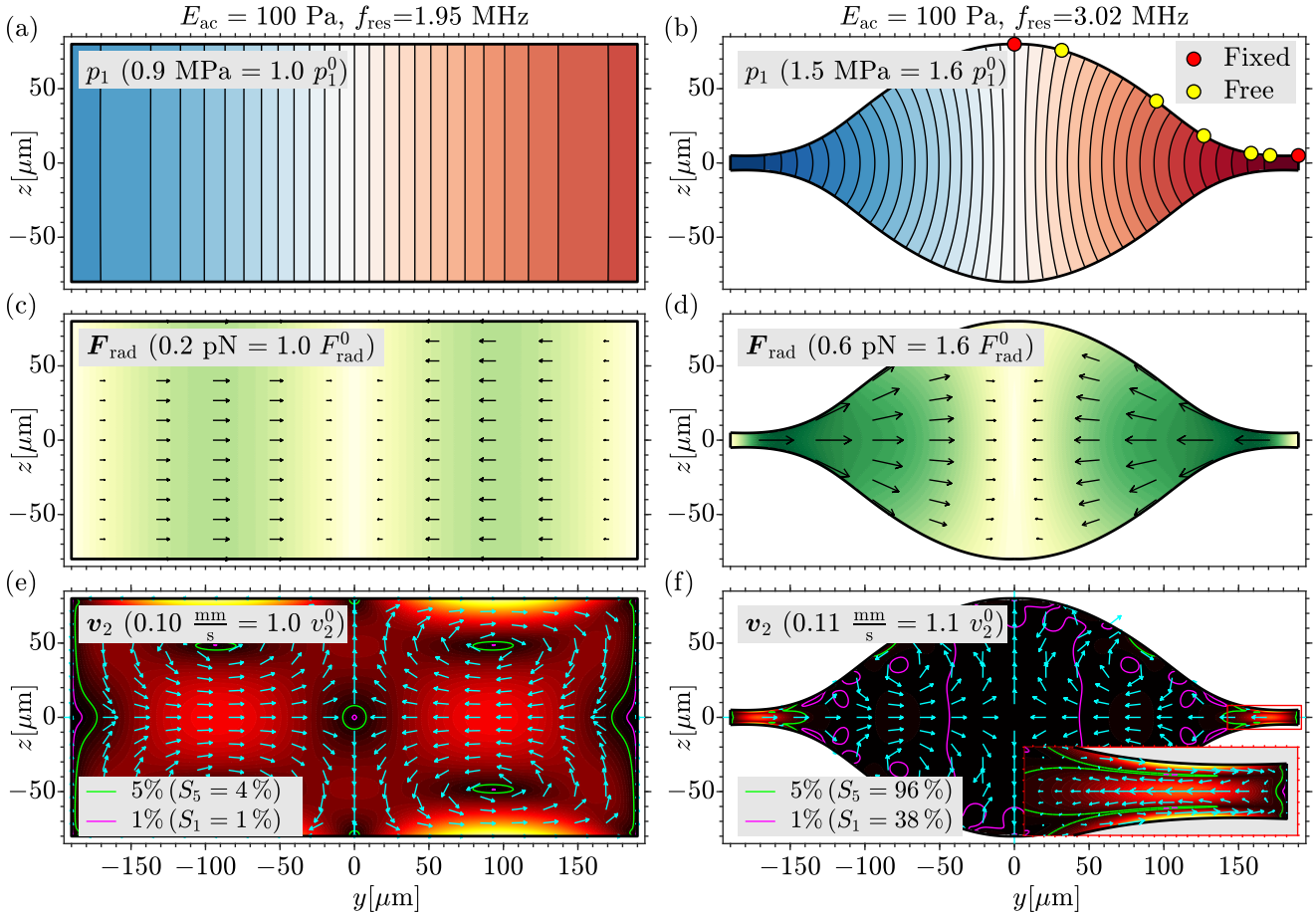

FIG. 1. Simulation results for MHz-acoustics at E_{ac} = 100 Pa in straight microchannels with a rectangular and a shape-optimized cross section. (a)-(b) The acoustic pressure p_1 from −1.5 MPa (light blue) to +1.5 MPa (dark red). The shape in (b) is defined by a spline interpolation between the colored points, where the z-coordinate of the yellow points are free in the optimization, and the red points are fixed. (c)-(d) The radiation force $\boldsymbol{F}_{rad}$ (black arrows) on 1-µm-diameter polystyrene particles from 0 (white) to 0.6 pN (dark green). (e)-(f) The acoustic streaming $\boldsymbol{v}_2$ (cyan unit arrows) from 0 (black) to 0.11 $\frac{mm}{s}$ (light yellow). The two contours mark 1 % (magenta) and 5 % (green) of the characteristic streaming speed v_2^0 from Eq. (8).

complex amplitude $\boldsymbol{u}_1^{bdr}(\boldsymbol{r})$,

$$\boldsymbol{u}^{bdr}(\boldsymbol{r},t) = \mathrm{Re}\big[\boldsymbol{u}_1^{bdr}(\boldsymbol{r})\,\mathrm{e}^{-\mathrm{i}\omega t}\big], \tag{1}$$

where $\mathrm{i} = \sqrt{-1}$. The resulting pressure p is written as a perturbation series,

$$p(\boldsymbol{r},t) = p_{fl} + \mathrm{Re}\big[p_1(\boldsymbol{r})\mathrm{e}^{-\mathrm{i}\omega t}\big] + p_2(\boldsymbol{r}), \tag{2}$$

and likewise for the density ρ and the fluid velocity $\boldsymbol{v}$. All first-order fields (subscript "1") oscillate harmonically with the angular frequency ω, whereas all second-order fields (subscript "2") are steady, being averaged in time over a full oscillation period $\frac{2\pi}{\omega}$.

The first-order acoustic pressure p_1 satisfies the Helmholtz equation in the bulk Ω and a boundary-layer boundary condition at $\partial\Omega$ expressed in terms of the inward normal derivative $\partial_\perp = -\boldsymbol{n}\cdot\boldsymbol{\nabla}$ and the outward-pointing normal vector $\boldsymbol{n}$ [8],

$$\nabla^2 p_1 + k_c^2 p_1 = 0, \quad \text{inside } \Omega, \tag{3a}$$

$$\Big[\partial_\perp + \frac{\mathrm{i}}{k_s}(k_c^2 + \partial_\perp^2)\Big]p_1 = \frac{-\rho_{fl}\omega^2}{1-\mathrm{i}\Gamma_{fl}}\Big(\boldsymbol{n} + \frac{\mathrm{i}}{k_s}\boldsymbol{\nabla}\Big)\cdot\boldsymbol{u}_1^{bdr}, \quad \text{at the boundary } \partial\Omega. \tag{3b}$$

Here, $k_c = \big(1 + \frac{1}{2}\mathrm{i}\Gamma_{fl}\big)k_0$ is the complex-valued compressional wave number having the real part $k_0 = \frac{\omega}{c_{fl}}$, $\Gamma_{fl} = \frac{1}{2}\big(\frac{4}{3} + \frac{\eta_{fl}^b}{\eta_{fl}}\big)(k_0\delta)^2$ is the minute acoustic damping coefficient with $\Gamma_{fl} \ll 1$, and $k_s = \frac{1+\mathrm{i}}{\delta}$ is the shear wave number related to the viscous boundary layer of thin width $\delta = \sqrt{\frac{2\eta_{fl}}{\omega\rho_{fl}}}$ with $k_0\delta \ll 1$. From p_1, we obtain the acoustic velocity $\boldsymbol{v}_1$ and density ρ_1 outside the thin viscous boundary layer [8],

$$\boldsymbol{v}_1 = \frac{-\mathrm{i}(1-\mathrm{i}\Gamma_{fl})}{\omega\rho_{fl}}\boldsymbol{\nabla}p_1, \qquad \rho_1 = \kappa_{fl}p_1, \tag{4}$$

with the isentropic compressibility $\kappa_{\rm fl} = \frac{1}{\rho_{\rm fl} c_{\rm fl}^2}$. The space-and-time-averaged acoustic energy density $E_{\rm ac}$ in Ω of volume $\mathcal{V}_\Omega$ is,

$$E_{\rm ac} = \int_\Omega \left[\frac{1}{4}\kappa_{\rm fl}\left|p_1\right|^2 + \frac{1}{4}\rho_{\rm fl}\left|\boldsymbol{v}_1\right|^2\right]\frac{\mathrm{d}V}{\mathcal{V}_\Omega}. \tag{5}$$

The second-order steady boundary-driven streaming velocity $\boldsymbol{v}_2$ outside the viscous boundary layer is a Stokes flow with the slip velocity $\boldsymbol{v}_2^{\rm slip}$ at the boundary [8],

$$\boldsymbol{0} = -\boldsymbol{\nabla} p_2 + \eta_{\rm fl}\nabla^2\boldsymbol{v}_2, \tag{6a}$$

$$\text{with}\quad 0 = \boldsymbol{\nabla}\cdot\boldsymbol{v}_2 \text{ in } \Omega, \quad \text{and} \quad \boldsymbol{v}_2 = \boldsymbol{v}_2^{\rm slip} \text{ at } \partial\Omega. \tag{6b}$$

For the slip velocity $\boldsymbol{v}_2^{\rm slip}$, we use expression (55) of Ref. [8] for an oscillating, curved surface with a curvature radius much larger than the viscous boundary-layer width δ.

The time-averaged forces acting on a suspended particle of radius a and velocity $\boldsymbol{v}_{\rm pa}$ are the Stokes drag force $\boldsymbol{F}_{\rm drag}$ and the acoustic radiation force $\boldsymbol{F}_{\rm rad}$ [25],

$$\boldsymbol{F}_{\rm drag} = 6\pi\eta_{\rm fl} a(\boldsymbol{v}_2 - \boldsymbol{v}_{\rm pa}), \tag{7a}$$

$$\boldsymbol{F}_{\rm rad} = -\boldsymbol{\nabla}\left[\frac{4\pi a^3}{3}\left(\frac{f_0}{4}\kappa_{\rm fl}|p_1|^2 - \frac{3f_1}{8}\rho_{\rm fl}|v_1|^2\right)\right], \tag{7b}$$

where f_0 and f_1 are the monopole and dipole scattering coefficients for the particle. All parameter values are given in the Supplemental Material [26].

Shape optimization for suppression of acoustic streaming.—We consider straight microchannels placed along the x axis with different y-z cross sections, see Fig. 1. To quantify the comparison between these channels, we revert to the classical results for a standing half-wave resonance $p_1 = p_a\sin(k_0 y)$ in a rectangular cross section, for which $E_{\rm ac} = \frac{1}{4}\kappa_{\rm fl}p_a^2$, the slip velocity $\boldsymbol{v}_2^{\rm slip} = \frac{3E_{\rm ac}}{2\rho_{\rm fl}c_{\rm fl}}\sin(2k_0 y)\boldsymbol{e}_y$ [3], and the acoustic radiation force $\boldsymbol{F}_{\rm rad} = -4\pi a^3 k_0 \Phi E_{\rm ac}\sin(2k_0 y)\boldsymbol{e}_y$, with the acoustic contrast factor $\Phi = \frac{1}{3}f_0 + \frac{1}{2}f_1$ [27]. We then introduce the following characteristic scaling quantities based on the acoustic energy density $E_{\rm ac}$ (5): the acoustic pressure p_1^0, the streaming speed v_2^0, and the radiation force $F_{\rm rad}^0$,

$$p_1^0 = \sqrt{\frac{4E_{\rm ac}}{\kappa_{\rm fl}}}, \quad v_2^0 = \frac{3E_{\rm ac}}{2\rho_{\rm fl}c_{\rm fl}}, \quad F_{\rm rad}^0 = 4\pi a^3 k_0 \Phi E_{\rm ac}. \tag{8}$$

To optimize the shape for suppression of the acoustic streaming, we define a cost function $\mathcal{C}$ that penalizes large streaming,

$$\mathcal{C} = \frac{1}{v_2^0}\int_\Omega \left|\boldsymbol{v}_2\right|\frac{\mathrm{d}V}{\mathcal{V}_\Omega}. \tag{9}$$

The suppression of the acoustic streaming is quantified by the suppression parameter S_q, the volumetric fraction in which the streaming speed $|\boldsymbol{v}_2|$ is smaller than the percentage q of v_2^0,

$$S_q = \int_\Omega \Theta\Big(\frac{q}{100}v_2^0 - \left|\boldsymbol{v}_2\right|\Big)\frac{\mathrm{d}V}{\mathcal{V}_\Omega}. \tag{10}$$

Here, $\Theta(x)$ is Heaviside's step function being 0 for $x < 0$ and 1 for $x > 0$.

For a given cross-section shape, we evaluate the cost function $\mathcal{C}$ by the following numerical two-step simulation in COMSOL Multiphysics [28], see *e.g.* Refs. [8, 22, 24]: (1) We compute p_1 from Eq. (3) in the idealized case of a prescribed displacement d_0 of the wall in the y direction, $\boldsymbol{u}_1^{\rm bdr} = d_0\boldsymbol{e}_y$. (2) We solve Eq. (6) for $\boldsymbol{v}_2$ with $\boldsymbol{v}_2^{\rm slip}$ calculated from p_1.

The cross-section shape is constrained to have width $W_0 = 380$ µm and height $H_0 = 160$ µm, and to be symmetric in y and z, see Fig. 1(b). The upper right edge is represented by a cubic spline interpolation through 7 points (y_i, z_i), $i = 0, 1, \ldots, 6$, where the y positions y_i are fixed at $[0, \frac{1}{6}, \frac{3}{6}, \frac{4}{6}, \frac{5}{6}, \frac{9}{10}, 1]\frac{W_0}{2}$. Furthermore, the z positions of the end points are fixed at $z_0 = \frac{1}{2}H_0$ and $z_6 = \frac{1}{2}h_0$, where $h_0 = 10$ µm is the height of the channel at the neck $y_6 = \frac{1}{2}W_0$. The optimization algorithm minimizes the cost function $\mathcal{C}$ (9) by varying the five free heights z_1-z_5 with the constraint $\frac{1}{2}h_0 \le z_i \le \frac{1}{2}H_0$. This optimization is implemented in Matlab [29] using the routine `fminsearchbnd` [30] that calls COMSOL. It typically requires ∼200 iterations, each taking 5 seconds on a workstation with a 3.5-GHz Intel Xeon CPU E5-1650 v2 dual-core processor and with a memory of 128 GB RAM.

In Fig. 1, simulation results are shown for the well-studied rectangular cross section [22] and compared to the results for the optimized spline cross section. For the optimized shape, the acoustic streaming is dramatically suppressed, whereas the radiation force is still present in the entire channel. Quantitatively, we obtain from Eq. (10) the streaming-suppression parameters $S_5 = 96$ % and $S_1 = 63$ % for the optimized shape, and $S_5 = 4$ % and $S_1 = 0.6$ % for the rectangle.

In Fig. 2(a), we show the family of optimized shapes obtained as above, but varying the maximum height as $H = [0.1, 0.2, \ldots, 1.5]\,H_0$. In Fig. 2(b), we plot p_1 along the upper boundary and note that it is approximately linear along a large part of the arc length for all the optimized shapes. This may be explained by inspecting the simplified expression for the slip velocity $\boldsymbol{v}_2^{\rm slip}$ adapted from Eq. (61) in Ref. [8] to the 2D standing-wave resonance considered here,

$$\boldsymbol{v}_{2\parallel}^{\rm slip} \approx -\frac{3}{8\omega}\boldsymbol{\nabla}_\parallel\left|\boldsymbol{v}_{1\parallel}\right|^2, \qquad v_{2\perp}^{\rm slip} \approx 0. \tag{11}$$

Clearly, because $\boldsymbol{v}_{1\parallel} \propto \boldsymbol{\nabla}_\parallel p_1$, the tangential slip velocity $\boldsymbol{v}_{2\parallel}^{\rm slip}$ is small when p_1 is linear along the boundary. Remarkably, as seen in Fig. 2(b), this linearity is maintained along nearly 90 % of the optimized boundaries,

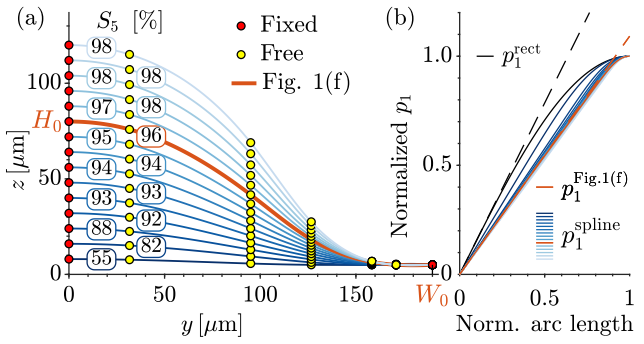

FIG. 2. (a) The optimized shapes, each defined by 2 fixed (red) and 5 free (yellow) points, obtained as in Fig. 1 but for different maximum height constraints ranging from $0.1H_0$ (dark blue) to $1.5H_0$ (light blue). The curves are labeled by the suppression parameter S_5, see Eq. (10). The thick orange shape is the one shown in Fig. 1(f). (b) The acoustic pressure p_1 versus arc length along the boundaries shown in (a) using the same color scheme. The black curve shows the pressure obtained in the rectangular cross section, where $p_1^{\rm rect} \propto \sin(\frac{\pi y}{W})$, and the dashed lines are selected tangents.

but eventually, due to the no-slip boundary condition, the pressure gradient must tend to zero at the end-point $(\frac{1}{2}W_0, \frac{1}{2}h_0)$. The last 10 % of the boundary therefore generates streaming, so by forming narrow necks there, the streaming becomes localized in a small region.

In Fig. 3(a), we study the importance of the narrow necks of the shape in Fig. 1(f) by cutting them off, leaving 90 % of the width, $-\frac{9}{20} < \frac{y}{W_0} < \frac{9}{20}$. In this case, the streaming is still suppressed: with $S_5 = 63$ % and $S_1 = 3$ %, it is worse compared to Fig. 1(f) with the necks, where $S_5 = 96$ % and $S_1 = 38$ %, but much better than for the rectangle of Fig. 1(e), where $S_5 = 4$ % and $S_1 = 1$ %. As it might prove difficult in practice to fabricate the exact optimized shape, we study in Fig. 3(b) a generic shape with a narrow neck and a wide bulk given by a cosine, $z(y) = \pm\frac{h}{2} \pm \left(\frac{H_0}{2} - \frac{h}{2}\right)\left[\frac{1}{2} + \frac{1}{2}\cos(\frac{2\pi y}{W_0})\right]$. Here, the neck height h is the only free parameter. Using the cost function $\mathcal{C}$ again, the optimal value is found to be $h = 3.14$ µm with a fair streaming suppression of $S_5 =$

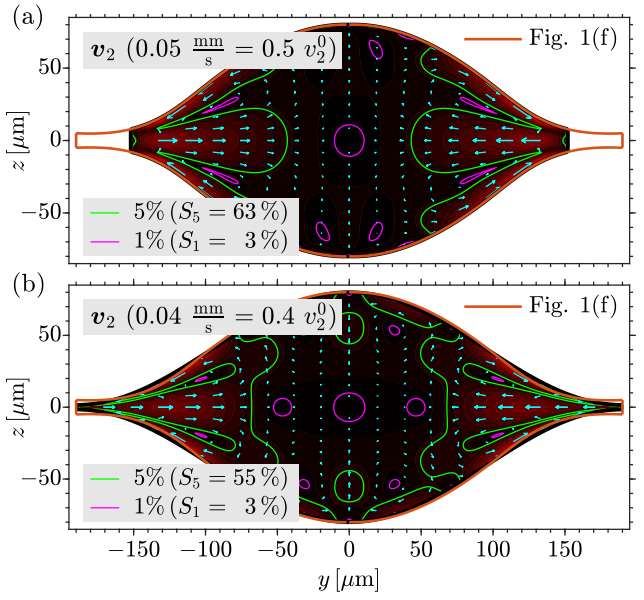

FIG. 3. The acoustic streaming velocity $\boldsymbol{v}_2$ (cyan arrows), its magnitude v_2 from 0 (black) to 0.05 $\frac{\rm mm}{\rm s}$ (light yellow), and the 5-% (light green) and 1-% (dark magenta) contour lines of v_2 as in Fig. 1(f), but for two different hard-wall shapes. (a) The optimized shape Fig. 1(f) (orange dashed curve) with its necks cut off, and (b) an optimized cosine shape.

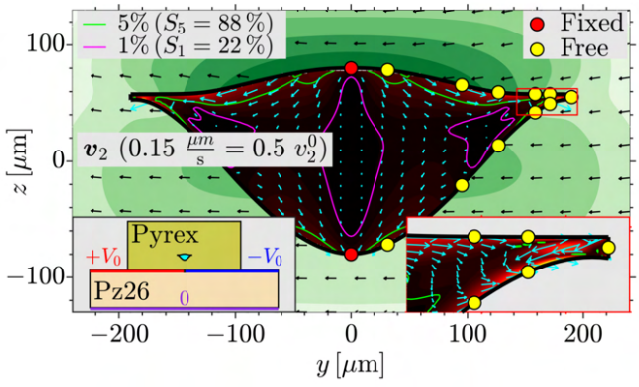

FIG. 4. The streaming field (black-to-red contour plot) in the fluid channel and the displacement field (light-to-dark-green contour plot) in the surrounding glass in a full-device simulation including a Pz26 transducer with split top and grounded bottom electrode (bottom-left inset). The neck is shown in the lower-right inset. The optimized fluid channel shape is obtained by varying the z-coordinates of the 11 yellow points (the 2 red being fixed), see Supplemental Material for more details [26].

cross section, the minimum radius $a_{\min}$ of particles that can be focused is estimated by equating $F^0_{\rm rad}$ and the drag force $6\pi\eta_{\rm fl}av_2^0$ [22, 23] from Eq. (8), leading to $a^{\rm rect}_{\min} = \sqrt{\frac{9\eta_{\rm fl}}{4\rho_{\rm fl}\omega\Phi}} = 0.9$ µm for polystyrene particles with $\Phi = 0.16$ in water at $f = 1.95$ MHz. In the optimized shape, the streaming is suppressed by 95 % at $f = 3.02$ MHz leading to a substantial six-fold reduction of $a_{\min}$ to $a^{\rm opt}_{\min} \approx 0.15$ µm.

Conclusion.—By exploiting effective boundary conditions [8], we have implemented an optimization algorithm that computes the shape of an acoustic cavity, which at resonance has the remarkable property that the acoustic streaming is dramatically suppressed relative to the conventional rectangular cavity. Notably, the acoustic pressure amplitude and the acoustic radiation force acting on suspended particles are not suppressed, and therefore, the optimized cavity shape is particularly ideal for applications within controlled handling of nm-sized particles in acoustophoresis.

We have demonstrated how shape optimization can be used to gain insight in fundamental acoustofluidics, in particular how to suppress the ubiquitous acoustic streaming by ensuring a linear acoustic pressure profile along the wall; and how such an insight can be used for practical applications. By applying other optimization methods, say topology optimization [32], or other cost functions, such as one based on acoustophoretic force fields, our method may be extended to other fundamental studies within nonlinear acoustics.

* jasoba@fysik.dtu.dk
† bruus@fysik.dtu.dk

[1] M. Faraday, On a peculiar class of acoustical figures; and on certain forms assumed by groups of particles upon vibrating elastic surfaces, Philos. Trans. R. Soc. London **121**, 299 (1831), http://www.jstor.org/stable/107936.
[2] V. Dvořák, Ueber die akustische Anziehung und Abstossung, Ann. Phys. Chem. **157**, 42 (1876).
[3] Lord Rayleigh, On the circulation of air observed in Kundt's tubes, and on some allied acoustical problems, Philos. Trans. R. Soc. London **175**, 1 (1884).
[4] H. Schlichting, Berechnung ebener periodischer Grenzeschichtströmungen, Phys. Z. **33**, 327 (1932).
[5] W. L. Nyborg, Acoustic streaming near a boundary, J. Acoust. Soc. Am. **30**, 329 (1958).
[6] T. Wang, E. Trinh, A. Croonquist, and D. Elleman, Shapes of rotating free drops: Spacelab experimental results, Phys. Rev. Lett. **56**, 452 (1986).
[7] J. Vanneste and O. Bühler, Streaming by leaky surface acoustic waves, Proc. R. Soc. A **467**, 1779 (2011).
[8] J. S. Bach and H. Bruus, Theory of pressure acoustics with viscous boundary layers and streaming in curved elastic cavities, J. Acoust. Soc. Am. **144**, 766 (2018).
[9] C. Eckart, Vortices and streams caused by sound waves, Phys. Rev. **73**, 68 (1948).
[10] P. Westervelt, The theory of steady rotational flow generated by a sound field, J. Acoust. Soc. Am. **25**, 60 (1953).
[11] A. Riaud, M. Baudoin, O. Bou Matar, L. Becerra, and J.-L. Thomas, Selective manipulation of microscopic particles with precursor swirling Rayleigh waves, Phys. Rev. Applied **7**, 024007 (2017).
[12] J. S. Bach and H. Bruus, Bulk-driven acoustic streaming at resonance in closed microcavities, Phys. Rev. E **100**, 023104 (2019).
[13] J. Rooney, C. Smith, and R. Carey, Acoustic streaming in superfluid-helium, J. Acoust. Soc. Am. **72**, 245 (1982).
[14] G. Vishwanathan and G. Juarez, Steady streaming flows in viscoelastic liquids, J. Non-Newton. Fluid **271**, UNSP 104143 (2019).
[15] I. A. Ramadan, H. Bailliet, and J.-C. Valiere, Experimental investigation of the influence of natural convection and end-effects on Rayleigh streaming in a thermoacoustic engine, J. Acoust. Sos. Am. **143**, 361 (2018).
[16] J. G. Kaufmann, M. P. Y. Desmulliez, Y. Tian, D. Price, M. Hughes, N. Strusevich, C. Bailey, C. Liu, and D. Hutt, Megasonic agitation for enhanced electrodeposition of copper, Microsyst. Technol. **15**, 1245 (2009).
[17] K. Sritharan, C. Strobl, M. Schneider, A. Wixforth, and Z. Guttenberg, Acoustic mixing at low Reynold's numbers, Appl Phys Lett **88**, 054102 (2006).
[18] S. K. R. S. Sankaranarayanan, S. Cular, V. R. Bhethanabotla, and B. Joseph, Flow induced by acoustic streaming on surface-acoustic-wave devices and its application in biofouling removal: A computational study and comparisons to experiment, Phys. Rev. E **77**, 066308 (2008).
[19] P. Marmottant and S. Hilgenfeldt, Controlled vesicle deformation and lysis by single oscillating bubbles, Nature **423**, 153 (2003).
[20] J. T. Karlsen, W. Qiu, P. Augustsson, and H. Bruus, Acoustic streaming and its suppression in inhomogeneous fluids, Phys. Rev. Lett. **120**, 054501 (2018).
[21] J. T. Karlsen, P. Augustsson, and H. Bruus, Acoustic force density acting on inhomogeneous fluids in acoustic fields, Phys. Rev. Lett. **117**, 114504 (2016).
[22] P. B. Muller, R. Barnkob, M. J. H. Jensen, and H. Bruus, A numerical study of microparticle acoustophoresis driven by acoustic radiation forces and streaming-induced drag forces, Lab Chip **12**, 4617 (2012).
[23] R. Barnkob, P. Augustsson, T. Laurell, and H. Bruus, Acoustic radiation- and streaming-induced microparticle velocities determined by microparticle image velocimetry in an ultrasound symmetry plane, Phys. Rev. E **86**, 056307 (2012).
[24] N. R. Skov, J. S. Bach, B. G. Winckelmann, and H. Bruus, 3D modeling of acoustofluidics in a liquid-filled cavity including streaming, viscous boundary layers, surrounding solids, and a piezoelectric transducer, AIMS Mathematics **4**, 99 (2019).
[25] M. Settnes and H. Bruus, Forces acting on a small particle in an acoustical field in a viscous fluid, Phys. Rev. E **85**, 016327 (2012).
[26] See Supplemental Material at [URL] for a list of material parameters and a description of the shape optimization for a fluid domain embedded in an elastic solid.
[27] K. Yosioka and Y. Kawasima, Acoustic radiation pressure on a compressible sphere, Acustica **5**, 167 (1955).
[28] COMSOL Multiphysics 5.4, http://www.comsol.com (2018).
[29] Matlab 2019b, http://www.mathworks.com (2019).

[30] John D'Errico, Matlab file exchange (2012), https://www.mathworks.com/matlabcentral/fileexchange/8277-fminsearchbnd-fminsearchcon, accessed 17 January 2020.

[31] R. P. Moiseyenko and H. Bruus, Whole-system ultrasound resonances as the basis for acoustophoresis in all-polymer microfluidic devices, Phys. Rev. Applied **11**, 014014 (2019).

[32] L. Olesen, F. Okkels, and H. Bruus, A high-level programming-language implementation of topology optimization applied to steady-state Navier-stokes flow, Int. J. Numer. Meth. Eng. **65**, 975 (2006).

Supplemental material for paper "Suppression of acoustic streaming in shape-optimized channels"

See description in Ref. [26] of the bibliography of the paper.

Supplemental material for paper: Suppression of acoustic streaming in shape-optimized channels

Jacob S. Bach* and Henrik Bruus†
Department of Physics, Technical University of Denmark,
DTU Physics Building 309, DK-2800 Kongens Lyngby, Denmark
(Dated: 18 January 2020)

This supplemental material provides details about the numerical simulations, five tables listing all the parameters related to the simulations, and details about the shape-optimization in COMSOL via MATLAB including a MATLAB pseudo code.

Hard-wall simulation

In Table I, we list some evaluated physical quantities for each of the hard-wall shapes shown in Figs. (1) and (3). This list includes the space-and-time-averaged input power per area P_{in} delivered by the surroundings at $\partial\Omega$ of area $\mathcal{A}_\Omega$ is,

$$P_{\text{in}} = \int_{\partial\Omega} \frac{1}{2}\text{Re}\left[p_1^*(-\text{i}\omega \boldsymbol{u}_1^{\text{bdr}} \cdot \boldsymbol{n})\right] \frac{\text{d}A}{\mathcal{A}_\Omega}. \tag{A.1a}$$

In all the hard-wall simulations with the prescribed wall displacement given in Eq. (1), we choose the frequency to be at the resonance $\omega = \omega_{\text{res}}$ where E_{ac} peaks. At resonance, the input power P_{in} is related to the quality factor Q of the resonance as,

$$P_{\text{in}} = \frac{\mathcal{V}_\Omega}{\mathcal{A}_\Omega}\frac{\omega_{\text{res}} E_{\text{ac}}}{Q}, \qquad \text{at resonance } \omega = \omega_{\text{res}}, \tag{A.1b}$$

where the asterisk denote complex conjugation. We choose the actuation displacement d_0 such that the average acoustic energy density E_{ac} is 100 Pa in all the simulations.

TABLE I. Quantities of the numerical simulation of the four hard-wall cross sections. $\mathcal{C}$ (the cost function) is the normalized averaged streaming speed given in Eq. (9), and S_q is the fraction of the volume where the streaming speed is suppressed to q % of v_2^0 given in Eq. (8).

Quantity ↓ Figure →	Rectangle 1(e)	Spline 1(f)	Spline cut 3(a)	Cosine 3(b)	Unit
Area	0.061	0.031	0.030	0.031	mm^2
Cicumference	1.080	0.858	0.717	0.841	mm
f_{res}, Eq. (3)	1.95	3.20	3.39	3.21	MHz
E_{ac}, Eq. (5)	100	100	100	100	Pa
P_{in}, Eq. (A.1a)	157	245	237	226	$\frac{\text{W}}{\text{m}^2}$
Q, Eq. (A.1b)	440	298	390	332	-
d_0, Eq. (11)	0.92	0.77	0.57	0.98	Å
$\mathcal{C}$, Eq. (9)	0.26	0.021	0.059	0.062	-
S_5, Eq. (10)	3.8	95.8	62.7	55.3	%
S_1, Eq. (10)	0.6	38.0	3.2	2.7	%

Full-device simulation

The numerical full-device simulation presented in Fig. 4 of the main paper, is based directly on the method presented by Skov *et al.* [1]. The material parameters for water, Pyrex glass, the suspended polystyrene particles, and the piezoelectric element are listed in Tables II-IV.

TABLE II. Material parameters for water at 25 °C [2].

Parameter	Symbol	Value	Unit
Mass density	ρ_{fl}	997.05	kg m^{-3}
Sound speed	c_{fl}	1496.7	m s^{-1}
Dyn. viscosity	η_{fl}	0.890	mPa s
Bulk viscosity	$\eta_{\text{fl}}^{\text{b}}$	2.485	mPa s
Damping coefficient	Γ_{fl}	0.00002	–
Compressibility	κ_{fl}	452	TPa^{-1}

TABLE III. Material parameters for isotropic Pyrex borosilicate glass at 25 °C for [3]. Note that the isotropy implies that $c_{12} = c_{11} - 2c_{44}$.

Parameter	Symbol	Value	Unit
Mass density	ρ_{sl}	2230	kg m^{-3}
Elastic modulus 11	c_{11}	69.72	GPa
Elastic modulus 44	c_{44}	26.15	GPa
Elastic modulus 12	c_{12}	17.43	GPa
Damping coefficient	Γ_{sl}	0.0004	–

TABLE IV. Material parameters for polystyrene particles of diameter $2a = 2$ µm in water at frequency $f = 2$ MHz. The imaginary part of the dipole coefficient f_1 is negligible for standing waves [4], and the contrast factor is defined as $\Phi = \frac{1}{3}\text{Re}(f_0) + \frac{1}{2}\text{Re}(f_2)$.

Parameter	Symbol	Value	Unit
Mass density [5]	ρ_{ps}	1050	kg m^{-3}
Compressibility [6]	κ_{ps}	249	TPa^{-1}
Monopole coefficient[4]	$\text{Re}(f_0)$	0.45	–
Dipole coefficient[4]	$\text{Re}(f_1)$	0.02	–
Contrast factor[4]	Φ	0.16	–

TABLE V. Material parameters of Ferroperm Ceramic Pz26 from Meggitt A/S [7]. Isotropy in the x-y plane implies $c_{66} = \frac{1}{2}(c_{11} - c_{12})$. The damping coefficient is $\Gamma_s = 0.02$ [8]. $\varepsilon_0 = 8.854 \times 10^{-12}$ is the vacuum permittivity.

Parameter	Symbol	Value	Unit
Mass density	ρ_{pz}	7700	kg/m^3
Elastic modulus 11	c_{11}	168	GPa
Elastic modulus 12	c_{12}	110	GPa
Elastic modulus 13	c_{13}	99.9	GPa
Elastic modulus 33	c_{33}	123	GPa
Elastic modulus 44	c_{44}	30.1	GPa
Elastic modulus 66	c_{66}	29.0	GPa
Permittivity 11	ε_{11}	828	ε_0
Permittivity 33	ε_{33}	700	ε_0
Coupling coefficient 31	e_{31}	-2.8	C/m^2
Coupling coefficient 33	e_{33}	14.7	C/m^2
Coupling coefficient 15	e_{15}	9.86	C/m^2
Damping coefficient	Γ_{pz}	0.02	–

In Fig. 5(a) and (b) below, we show results for full-device simulations for the rectangular and optimized cross section shapes of in Figs. 1(e)-(f) obtained for the simplified hard-wall models, but here embedded in glass without further changes in shape. For the full-device model, the resulting streaming speed in the rectangular cross section is still around the predicted scale v_2^0 in large parts of channel. When embedded in the full-device model, the hard-wall optimized shape in Fig. 5(b) still shows suppression of streaming with a streaming speed less than 5 % of v_2^0 in 59 % of the channel. However, the streaming suppression is stronger in Fig. 5(c), where the surrounding solid motion is included in the optimization algorithm, giving a streaming speed less than 5 % of v_2^0 in 88 % of the channel, and less than 1 % of v_2^0 in 22 % of the channel.

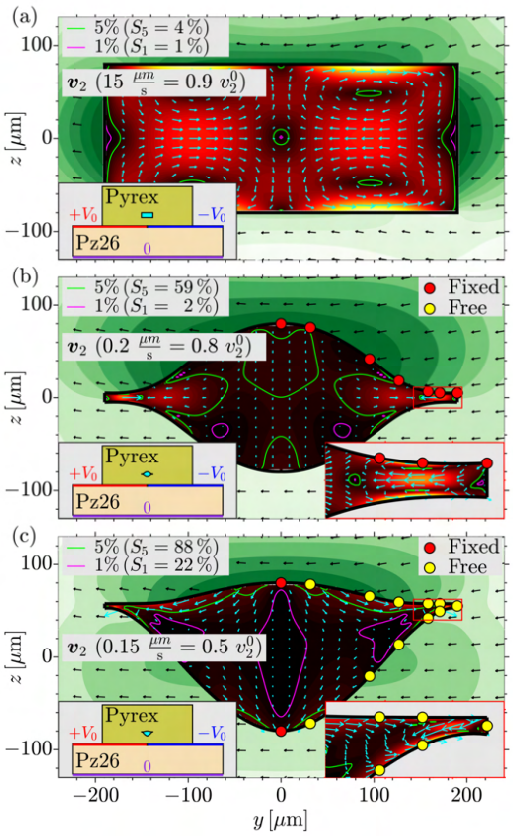

FIG. 5. The streaming velocity $\boldsymbol{v}_2$ for three channel shapes embedded in Pyrex glass with a piezoelectric transducer attached at the bottom as shown in the lower-left insets. A zoom of the streaming in the neck is shown the lower-right insets. The color in the fluid represent the streaming speed v_2 from 0 $\frac{\mu m}{s}$ (black) to the maximum value $v_2^{\max}$ (yellow) given in parenthesis in the figure, and the color in the solid represents the solid displacement u from 0 nm to the maximum value $u^{\max}$. (a) The fixed-shape rectangle with $v_2^{\max} = 15\ \frac{\mu m}{s}$ and $u^{\max} = 3.6$ nm. (b) The fixed-shape hard-wall optimized shape with $v_2^{\max} = 0.3\ \frac{\mu m}{s}$ and $u^{\max} = 1.8$ nm. (c) The full-device-optimized shape with $v_2^{\max} = 0.15\ \frac{\mu m}{s}$ and $u^{\max} = 1.8$ nm.

Full-device shape optimization

In the full-device model, the presence of the piezoelectric transducer breaks the up-down symmetry of the system. Therefore, in the shape optimization including the surrounding solid as shown in Fig. 4 of the main paper, we represent the shape in a slightly different way than for the up-down-symmetric hard-wall case shown in Fig 1(b) of the main paper. Using our insight from the symmetric hard-wall shape, we constrain the height of the shape in the full-device model to be monotonically decreasing as a function of y from H_0 at $y = 0$ to h_0 at $y = \frac{1}{2}W_0$, thus preventing any wavy shapes to be suggested by the algorithm. As a further degree of freedom, we allow the z-position z_{neck} of the neck to be free within specified bounds between $H_{\min} < z_{\text{neck}} < H_{\max}$, such that

$$z_{\text{neck}} = H_{\min} + s_{\text{neck}}(H_{\max} - H_{\min}), \quad 0 < s_{\text{neck}} < 1. \tag{A.2}$$

where s_{neck} is a free parameter. In the simulation, we chose $H_{\min} = -\frac{1}{2}H_0$ and $H_{\max} = \frac{3}{2}H_0$. We use one cubic spline interpolation through 7 points (y_i, z_i^{top}), $i = 0, 1, 2, \ldots, 6$ to represent the top, and another cubic spline interpolation through 7 points (y_i, z_i^{bot}), $i = 0, 1, 2, \ldots, 6$ to represent the bottom. The y positions y_i are fixed at $[0, \frac{1}{6}, \frac{3}{6}, \frac{4}{6}, \frac{5}{6}, \frac{9}{10}, 1]\frac{W_0}{2}$ as before. The point $(y_0, z_0^{\text{top}}) = (0, \frac{1}{2}H_0)$ is fixed for the top and the point

$(y_0, z_0^{\mathrm{bot}}) = (0, -\frac{1}{2}H_0)$ is fixed for the bottom.

The z-position z_i^{top} of the top spline interpolation are chosen to be between its neighbouring points $z_{i-1}^{\mathrm{top}} < z_i^{\mathrm{top}} < z_{i+1}^{\mathrm{top}}$ by introducing the parameter s_i^{top}, such that the z-positions at the top become

$$\begin{aligned} z_0^{\mathrm{top}} &= \frac{1}{2}H_0, \\ z_i^{\mathrm{top}} &= z_{i-1}^{\mathrm{top}} + s_i^{\mathrm{top}}(z_{i+1}^{\mathrm{top}} - z_{i-1}^{\mathrm{top}}), \quad \mathrm{i}=1,2,\ldots,5, \\ z_6^{\mathrm{top}} &= z_{\mathrm{neck}} + \frac{h_0}{2}, \end{aligned} \tag{A.3}$$

where $0 < s_i^{\mathrm{top}} < 1$ are free parameters and h_0 is a fixed height of the neck which is chosen to be 10 µm. A similar scheme is used for the bottom heights z_i^{bot} except for the change $z_6^{\mathrm{bot}} = z_{\mathrm{neck}} - \frac{h_0}{2}$. This procedure gives in total 5+5+1=11 free parameters: s_i^{top}, s_i^{bot} and s_{neck}.

Matlab algoritm for shape optimization

The optimization algorithm is run in MATLAB [9] by passing the COMSOL model to the optimization routine `fminsearchbnd` [10] as described in the pseudo code (A.4) below. The algorithm builds a new geometry for each optimization step based on the N values z_i stored in the array `z`, where N is the number of free parameters. The tolerances `tolX` on the z_i convergence and `tolFun` on the cost function are set to 10^{-3}.

```
% Load COMSOL model and set initial value, lower bound, and upper bound
model   = mphload('COMSOL_FileName.mph');
z_init  = ...  % set initial value (vector of length N)
z_lower = ...  % set upper bound (vector of length N)
z_upper = ...  % set lower bound (vector of length N)
% Run optimization by passing the above to fminsearchbnd
options = optimset('tolX',1e-3,'tolFun',1e-3) % set the tolerance level for fminsearchbnd
z_opt   = fminsearchbnd(@(z) get_CostFun(model,z),z_init,z_lower,z_upper,options)
% Define the function get_CostFun that evaluates the cost function of Eq. (9) in the paper
function CostFun = get_CostFun(model, z)
    (1) Set the geometry of the COMSOL model "model" via MATLAB based on the input heights "z"
    (2) Run the COMSOL simulation via MATLAB (find resonance frequency if needed).
    (3) Calculate the cost function C defined in Eq. (9) of the main paper.
CostFun  = ...  % calculated value of the cost function
end
```

(A.4)

* jasoba@fysik.dtu.dk
† bruus@fysik.dtu.dk

[1] N. R. Skov, J. S. Bach, B. G. Winckelmann, and H. Bruus, 3D modeling of acoustofluidics in a liquid-filled cavity including streaming, viscous boundary layers, surrounding solids, and a piezoelectric transducer, AIMS Mathematics **4**, 99 (2019).

[2] P. B. Muller and H. Bruus, Numerical study of thermoviscous effects in ultrasound-induced acoustic streaming in microchannels, Phys. Rev. E **90**, 043016 (2014).

[3] *Glass Silicon Constraint Substrates*, CORNING, Houghton Park C-8, Corning, NY 14831, USA, http://www.valleydesign.com/Datasheets/Corning%20Pyrex%207740.pdf, accessed 11 November 2016.

[4] M. Settnes and H. Bruus, Forces acting on a small particle in an acoustical field in a viscous fluid, Phys. Rev. E **85**, 016327 (2012).

[5] *CRC Handbook of Chemistry and Physics*, 95th ed. (CRC Press, Boca Raton, FL, 2014).

[6] P. B. Muller, R. Barnkob, M. J. H. Jensen, and H. Bruus, A numerical study of microparticle acoustophoresis driven by acoustic radiation forces and streaming-induced drag forces, Lab Chip **12**, 4617 (2012).

[7] *Ferroperm Matdat 2017*, Meggit A/S, Porthusvej 4, DK-3490 Kvistgaard, Denmark, uRL https://www.meggittferroperm.com/materials/, accessed 17 January 2020.

[8] P. Hahn and J. Dual, A numerically efficient damping model for acoustic resonances in microfluidic cavities, Physics of Fluids **27**, 062005 (2015).

[9] Matlab 2019b, http://www.mathworks.com (2019).

[10] John D'Errico, Matlab file exchange (2012), https://www.mathworks.com/matlabcentral/fileexchange/8277-fminsearchbnd-fminsearchcon, accessed 17 January 2020.

7.6 Paper VI: Proc. Mtgs. Acoust. 34, 022005 (2018)

Different origins of acoustic streaming at resonance

DOI: 10.1121/2.0000927

Authors: J. S. Bach and H. Bruus.
Journal: Proc. Mtgs. Acoust. **34**, 022005 (2018)

Proceedings of Meetings on Acoustics

Volume 34 http://acousticalsociety.org/

21st International Symposium on Nonlinear Acoustics

21st ISNA Santa Fe, New Mexico, USA July 9-13, 2018, 50th Anniversary

Computational Acoustics: Paper S25-2

Different origins of acoustic streaming at resonance

Jacob Bach and Henrik Bruus
Department of Physics, Technical University of Denmark, Kongens Lyngby, Capital Region, 2800, DENMARK; jasoba@fysik.dtu.dk; bruus@fysik.dtu.dk

Acoustic streaming is a nonlinear phenomenon that plays an essential role in microscale acoustofluidic devices for handling of sub-micrometer particles. However, the streaming patterns observed in experiments can be of complicated and non-intuitive character, and therefore, experiments, and device optimization are often carried out in a trial-and-error manner. To overcome this obstacle, we classify acoustic streaming based on our recently developed theory of acoustic streaming. Using this theory we have shown that acoustic streaming is driven partly by Reynolds stresses in the bulk and partly by a slip-velocity condition at the walls due to Reynolds stresses in the acoustic boundary layers. Hence, in our classification, we distinguish between boundary-layer-driven and bulk-driven streaming. For boundary-layer-driven streaming at resonance, we classify the two physically relevant limits of parallel and perpendicular acoustics as well as the intermediate range. For bulk-driven streaming we find that the acoustic intensity vector plays a central role, and that this quantity can give rise to a strong bulk-driven streaming, if the acoustic fields have large angular momentum. In this context, we analyze mechanisms that can lead to rotating resonant modes in acoustic microchannels.

Published by the Acoustical Society of America

 https://doi.org/10.1121/2.0000927

1. INTRODUCTION - ACOUSTIC STREAMING IN MICROCHANNELS

One of the main goals in the field of microfluidics is to scale down laboratory instruments and study microscopic biological samples precisely and efficiently. In this context, acoustofluidics offers a method to handle microparticles in a gentle and contact-free way by the use of acoustophoresis *i.e.* the migration of particles due to sound. Applications include *e.g.* size-independent sorting of cells,[1] acoustic tweezing,[2] and acoustic trapping.[3] The first central nonlinear phenomena in acoustophoresis is the acoustic radiation force which scales with the particle volume and tends to focus particles based on their acoustic contrast. The other is the rotating acoustic streaming, which tends to mix suspended particles due to the Stokes drag that scales with the particle radius. Due to these scalings, acoustic streaming is insignificant for large particles but important for small particles, where the critical particle size is around 1 μm.[4] A deep understanding of acoustic streaming is therefore important in order to control sub-micron particles using acoustophoresis.

In this work, we analyse theoretically acoustic streaming at fluid resonance, where the acoustic fluid velocity is enhanced a quality factor $Q \gg 1$ compared to velocity of the confining wall. In particular, we investigate the ill-characterized *in-plane streaming* which rotate in a plane parallel to the surrounding solid surface. Examples from the literature of such horizontal in-plane streaming patterns are the 6-by-6 flow roll-pattern observed in a 2 mm × 2 mm × 0.2 mm cavity in a silicon-glass chip shown in Fig. 4(b) of Ref. [5], and the 2-by-2 flow-roll pattern observed in a cm-long glass capillary tube with a 2 mm × 0.2 mm inner cross section in Fig. 3 of Ref. [6].

We find that this kind of streaming can be generated in closed cavities if the acoustic motion is rotating and that this rotation can be obtained spontaneously in channel geometries with small deviation from symmetry. Acoustic streaming is partly driven by a slip-boundary condition which compensates for the Reynolds stress in the narrow acoustic boundary layer of width $\delta \sim 0.5$ μm and partly by a bulk force density which arises due to viscous dissipation in the bulk. We show in relevant limits, that both of these non-linear driving mechanisms are closely related to the acoustic intensity vector.

2. THEORY OF ACOUSTIC FIELDS AND STREAMING NEAR ELASTIC SURFACES

The acoustic fields in microchannels arrise due to vibrations of the surrounding solid which is actuated externally, usually by a piezoelectric transducer. We express the instantaneous position $\boldsymbol{s}$ of the confining wall as a small harmonic displacement $\boldsymbol{s}_1(\boldsymbol{s}_0)\,\mathrm{e}^{-\mathrm{i}\omega t}$ around the equilibrium position $\boldsymbol{s}_1$,

$$\boldsymbol{s}(\boldsymbol{s}_0,t) = \boldsymbol{s}_0 + \boldsymbol{s}_1(\boldsymbol{s}_0)\,\mathrm{e}^{-\mathrm{i}\omega t}, \qquad \text{instantaneous surface position } \boldsymbol{s}. \tag{1}$$

Correspondingly, we expand the fluid pressure p and velocity $\boldsymbol{v}$ in perturbation series and relate the pressure perturbation and density perturbation through the isentropic compressibility κ_0,

$$p = p_0 + p_1(\boldsymbol{r})\mathrm{e}^{-\mathrm{i}\omega t} + p_2(\boldsymbol{r}), \qquad \boldsymbol{v} = \boldsymbol{0} + \boldsymbol{v}_1(\boldsymbol{r})\mathrm{e}^{-\mathrm{i}\omega t} + \boldsymbol{v}_2(\boldsymbol{r}), \qquad \kappa_0 = \frac{1}{\rho_0}\Big(\frac{\partial\rho}{\partial p}\Big)_S = \frac{1}{\rho_0 c_0^2}, \tag{2}$$

with equilibrium density ρ_0 and sound speed c_0. Here, superscripts indicate order of smallness in the acoustic Mach number $\mathrm{Ma} = \frac{|\boldsymbol{v}_1|}{c_0} \sim |p_1|\kappa_0$ with superscript "0" being the equilibrium value, "1" being the amplitude of the first-order linear acoustic motion and "2" referring to a second-order time-averaged quantity generated by products of first-order fields. In particular, $\boldsymbol{v}_2$ is the acoustic streaming which, away from the acoustic boundary layer of width $\delta \sim 0.5$ μm, is governed by an incompressible Stokes equation with a driving force density $\boldsymbol{f}^{\mathrm{str}}$ proportional to the time-averaged acoustic intensity vector $\langle \boldsymbol{S}_{\mathrm{ac}} \rangle = \langle p_1 \boldsymbol{v}_1 \rangle$,[7]

$$\boldsymbol{\nabla}\cdot\boldsymbol{v}_2 = 0, \qquad \boldsymbol{0} = -\boldsymbol{\nabla}\tilde{p}_2 + \eta_0\nabla^2\boldsymbol{v}_2 + \boldsymbol{f}^{\mathrm{str}}, \qquad \boldsymbol{f}^{\mathrm{str}} = \Big(\frac{4}{3}\eta_0 + \eta_0^{\mathrm{b}}\Big)\kappa_0 k_0^2 \langle \boldsymbol{S}_{\mathrm{ac}} \rangle. \tag{3}$$

where η_0 is dynamic viscosity and η_0^{b} is the bulk viscosity. To fulfil no slip at the instantaneous surface position $\boldsymbol{s}(\boldsymbol{s}_0,t)$, the streaming outside the boundary-layer must take a finite slip velocity at the wall to compensate for the inner streaming inside the boundary layer,

$$\boldsymbol{v}_2 = \boldsymbol{v}_2^{\mathrm{slip}}, \qquad \text{streaming-slip velocity at the wall equilibrium position } \boldsymbol{s}_0. \tag{4}$$

In general $\boldsymbol{v}_2^{\mathrm{slip}}$ involves complicated curvilinear derivatives of both the acoustic velocity $\boldsymbol{v}_1$ and the surface velocity $\boldsymbol{V}_1^0 = \partial_t \boldsymbol{s}$ but in the special case of fluid resonance, where the fluid velocity is enhanced a quality factor $Q \gg 1$ compared to the wall velocity, we have shown[7] that this slip-boundary condition simplifies in the two relevant limits of parallel and perpendicular acoustics,

$$\boldsymbol{v}_{2\parallel}^{\mathrm{slip}} \approx \frac{\kappa_0}{2}\big\langle \boldsymbol{S}_{\mathrm{ac}\parallel}\big\rangle - \frac{1}{2\omega\rho_0}\boldsymbol{\nabla}_\parallel\big(E_{\mathrm{kin}} - 2E_{\mathrm{pot}}\big) \quad \text{for parallel acoustics,} \qquad |\nabla_\perp^2 p_1| \ll |\nabla_\parallel^2 p_1|, \tag{5a}$$

$$\boldsymbol{v}_{2\parallel}^{\mathrm{slip}} \approx -\kappa_0\big\langle \boldsymbol{S}_{\mathrm{ac}\parallel}\big\rangle, \qquad \text{for perpendicular acoustics,} \qquad |\nabla_\perp^2 p_1| \gg |\nabla_\parallel^2 p_1|, \tag{5b}$$

with $v_{2\perp}^{\mathrm{slip}} \approx 0$ in both cases. Here $E_{\mathrm{kin}} = \frac{1}{4}\rho_0|\boldsymbol{v}_1|^2$ is the kinetic energy and $E_{\mathrm{pot}} = \frac{1}{4}\kappa_0|p_1|^2$ is the potential energy of the first order acoustic motion.

A. IN-PLANE STREAMING AND ROTATING ACOUSTICS

From Eq. (3) and Eq. (5) we see that acoustic streaming is driven partly by the bulk force density $\boldsymbol{f}^{\mathrm{str}}$ and partly by a slip condition $\boldsymbol{v}_2^{\mathrm{slip}}$. Only terms with non-zero curl can drive in-plane streaming so only $\big\langle \boldsymbol{S}_{\mathrm{ac}}\big\rangle$ is relevant if it has non-zero curl, which we find to be proportional to the acoustic angular momentum $\boldsymbol{\mathcal{L}}$,[7]

$$\boldsymbol{\nabla}\times\big\langle \boldsymbol{S}_{\mathrm{ac}}\big\rangle = \omega^2\big\langle \boldsymbol{r}_1^d\times(\rho_0\boldsymbol{v}_1^d)\big\rangle = \omega^2\boldsymbol{\mathcal{L}}, \qquad \boldsymbol{r}_1^d = \frac{\mathrm{i}}{\omega}\boldsymbol{v}_1^d. \tag{6}$$

Therefore, in-plane streaming at resonance is associated with rotating acoustics. As illustrated in Fig. 1, this rotation can be obtained if two resonances are oscillating perpendicularly with phase difference of around $\frac{\pi}{2}$. The geometry is similar to Fig. 4(b) in Ref. [5] with actuation from the bottom and a small symmetry deviation where introduced by the aspect ratio $\Delta = \frac{W_x}{W_y}$ which is slightly larger than unity.

B. IN-PLANE BULK-DRIVEN AND BOUNDARY-DRIVEN STREAMING

Bulk-driven streaming is governed by Eq. (3) and assuming $\nabla_\perp^2 \sim L_\perp^{-2}$, we can estimate the ratio of bulk-driven to boundary-driven in-plane streaming velocity from the curl of Eqs. (3) and (5),

$$\frac{|(\nabla\times\boldsymbol{v}_2^{\text{bulk-driven}})_\perp|}{|(\nabla\times\boldsymbol{v}_2^{\text{boundary-driven}})_\perp|} \propto (k_0 L_\perp)^2. \tag{7}$$

In conclusion, bulk-driven in-plane streaming will dominate for sufficiently high frequency $f = \frac{1}{2\pi}c_0k_0$ or sufficiently large height ($\sim L_\perp$), whereas boundary-driven streaming will dominate else for low frequencies and narrow channels. This point is shown in Fig. 2 where we show that $\boldsymbol{f}^{\mathrm{str}}$ increases for higher frequencies whereas $\boldsymbol{v}_2^{\mathrm{slip}}$ stays almost constant. Fig. 2(c) reproduces the experimental results of 6x6 rolls shown in Fig. 5(b) of Ref. [5] and shows that the observed streaming is bulk-driven by $\boldsymbol{f}^{\mathrm{str}}$ rather than boundary-driven by $\boldsymbol{v}_2^{\mathrm{slip}}$. Further, from Fig. 2(a) we expect that 2×2 rolls will not be clearly observable in this setup.

The investigations in Figs. 1 and 2 are examples of *parallel acoustics*. Increasing the frequency to obtain a half standing wave in the z-direction will change the situation to *perpendicular acoustics* where we should instead use the boundary condition (5b), which is always counteracting the bulk force.

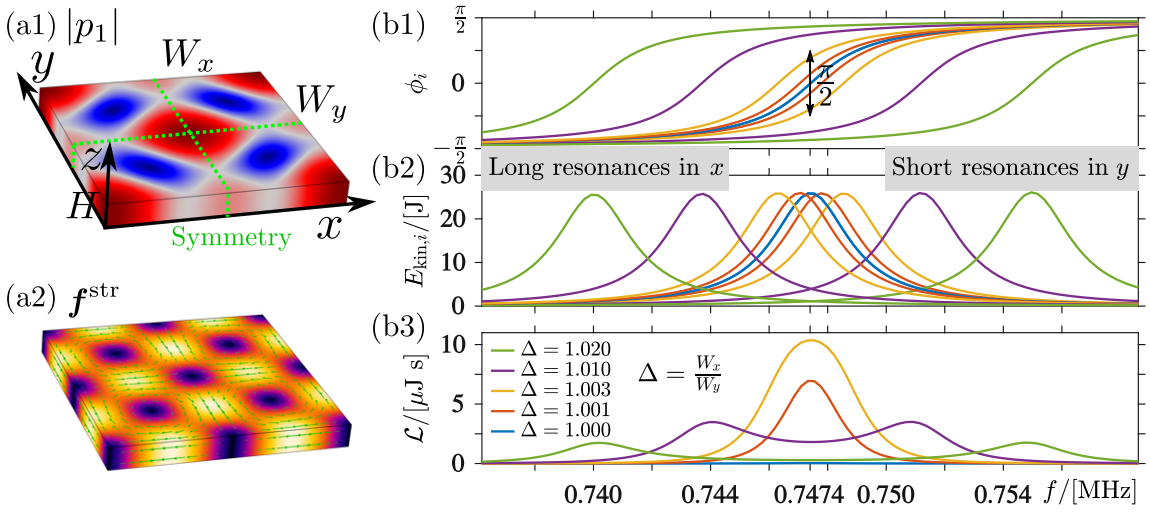

Figure 1: Simulation of rotating acoustics at resonance in a closed cavity of widths $W_x = 2000\ \mu\mathrm{m}(1 + \frac{1}{2}\Delta)$, $W_y = 2000\ \mu\mathrm{m}(1 - \frac{1}{2}\Delta)$ ***and height*** $H = 200\ \mu\mathrm{m}$ ***for small aspect ratio*** $\Delta \approx \frac{W_x}{W_y}$. ***(a1) Absolute pressure*** $|p_1|$ ***and the green symmetry lines used in Fig. 2. (a2) The generated rotating streaming force*** $\boldsymbol{f}^{\mathrm{str}}$. ***(b1) Temporal phase*** ϕ_i ***and (b1) the kinetic energy*** $E_{\mathrm{kin},i}$ ***for the long (left curves) and short resonances (right curves) for different aspect ratios. (a3) shows the resulting acoustic angular momentum*** $\mathcal{L}$.

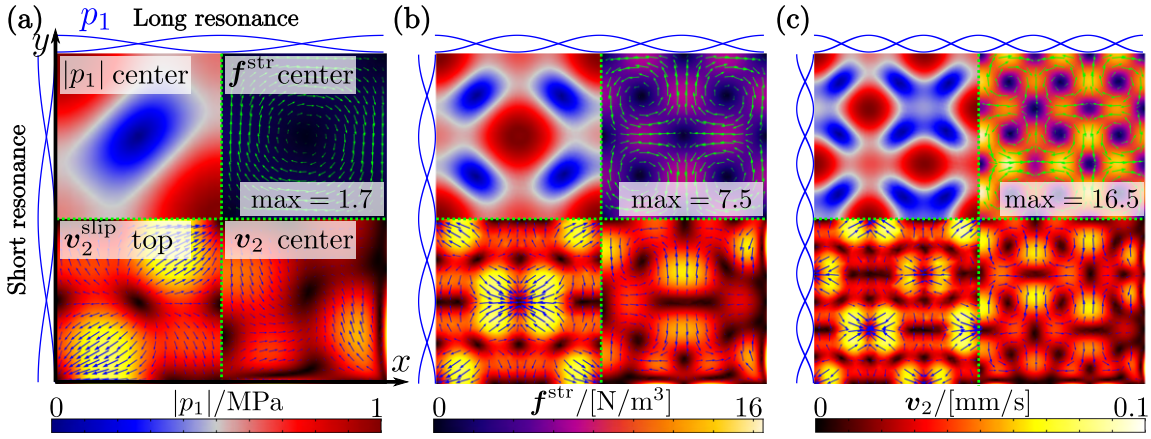

Figure 2: $|p1|$, $\boldsymbol{f}^{\mathrm{str}}$, $\boldsymbol{v}_2^{\mathrm{slip}}$ ***and*** $\boldsymbol{v}_2$ ***in the*** xy***-plane of the setup and green symmetry lines shown in Fig. 1 (a1) for three different frequencies giving 1 (a), 2 (b) and 3 (c) wavelengths in each direction respectively. Note that boundary-driven streaming generated by*** $\boldsymbol{v}_2^{\mathrm{slip}}$ ***dominates for low frequencies (a) whereas bulk-driven streaming generated by*** $\boldsymbol{f}^{\mathrm{str}}$ ***dominates for high frequencies (c).***

3. CONCLUSION AND OUTLOOK

We have presented driving mechanisms for in-plane acoustic streaming in a closed cavity and shown that this kind of streaming is associated with rotating acoustics. The two fundamental driving mechanisms are the slip velocity $\boldsymbol{v}_2^{\mathrm{slip}}$ and the bulk force density $\boldsymbol{f}^{\mathrm{str}}$, and these are both related to the acoustic intensity vector $\langle \boldsymbol{S}_{\mathrm{ac}} \rangle$. Rotating acoustics at resonance is obtained at small deviations from symmetry where two pressure modes resonate at the same frequency with a relative phase shift. We introduced the limits of parallel and perpendicular acoustics and showed that in these limits $\langle \boldsymbol{S}_{\mathrm{ac}} \rangle$ is the only physical quantity that can lead to in-plane streaming. In a setup with parallel acoustics similar to experiments[5] we found that the in-plane streaming was bulk-driven and predicted that it would not be clearly observable for lower frequencies, since the bulk force density $\boldsymbol{f}_{\mathrm{ac}}$ increases with the the frequency squared.

We are currently working on a similar characterization of acoustic streaming in long open capillaries. Here, small reflections and damping in the open direction may become important and not straight forward to model. We believe however, that the presented principle of rotating acoustics leading to in-plane streaming carries over in many different experimental setups.

REFERENCES

[1] P. Augustsson, C. Magnusson, M. Nordin, H. Lilja, and T. Laurell, “Microfluidic, label-free enrichment of prostate cancer cells in blood based on acoustophoresis”, Anal. Chem. **84**(18), 7954-7962 (2012)

[2] B. W. Drinkwater,“Dynamic-field devices for the ultrasonic manipulation of microparticles”, Lab Chip **16**, 2360-2375 (2016)

[3] B. Hammerström, M. Evander, J. Wahlström, and J. Nilsson, “Frequency tracking in acoustic trapping for improved performance stability and system surveillance,” Lab Chip **14**, 1005-1013 (2014)

[4] P. B. Muller, R. Barnkop, M. J. H. Jensen, and H. Bruus, “A numerical study of microparticle acoustophoresis driven by acoustoc radiation forces and streaming-induced drag forces,” Lab Chip **12**, 4617-4627 (2012)

[5] S. M. Hagster, T.G. Jensen, H. Bruus and J.P. Kutter, “Acoustic resonances in piezo-actuated microfluidic chips: full-image micro-PIV experiments and numerical simulations”, Lab Chip **7**, 1336-1344 (2007)

[6] B. Hammarström, T. Laurell, and J. Nilsson, “Seed particle enabled acoustic trapping of bacteria and nanoparticles in continuous flow systems”, Lab Chip **12**, 4296-4304 (2012)

[7] J. S. Bach and H. Bruus, “Theory of pressure acoustics with viscous boundary layers and streaming in curved elastic cavities”, JASA **44**(2), 766-784 (2018)

Chapter 8

Conclusion and outlook

In this thesis, the physics of acoustic fields and streaming in microsystems has been studied theoretically and numerically with the overall scope of contributing to the development of acoustofluidic devices. As stated in Chapter 1, the research carried out in the thesis has three major parts: (1) The viscous boundary layer and effective boundary conditions, (2) theoretical understanding of experimental observations, and (3) suppression of acoustic streaming. A summary of the results of each individual paper is provided in Chapter 6. This chapter presents a broader conclusion based on the three major parts, as well as a theoretical and experimental outlook.

8.1 Broard conclusion of the thesis

(1) **The viscous boundary layer and effective boundary conditions**
In the context of pressure acoustics, the concept of *effective modelling* has been introduced in this thesis. In this approach, the narrow viscous boundary layer is not resolved numerically, but taken into account analytically through an effective boundary condition. In addition, the well-known slip-velocity theory for the acoustic streaming has been extended to apply in the general case of a curved oscillating wall. These effective models has been formulated generically which allows for implementation in almost any geometry with a length scale much larger than the narrow viscous boundary-layer width. It is the hope that this calculation method will be used for numerically efficient simulations of acoustofluidic devices in the future and thus accelerate the further development. The effective models developed in this part (1) of the thesis has been used throughout the research in part (2) and part (3).

(2) **Theoretical understanding of experimental observations**
One advantage of the effective model for acoustic streaming is that "boundary-driven streaming", and "bulk-driven streaming" may be calculated and understood separately as was done in Paper III [3]. This separation simplifies the analysis of the often complicated acoustic streaming. In contrast to common knowledge, it was found in this thesis, that bulk-driven acoustic streaming can easily be stronger than

the boundary-driven streaming in typical acoustofluidic devices of length scale comparable to the acoustic wave length. Chapter 4 provides a length-scale condition for ignoring the bulk-driven streaming which is rarely satisfied in acoustofluidic devices. It was found that bulk-driven streaming is excited by rotating acoustic resonances, which can be excited in geometries, where two perpendicular resonances has close-lying resonance frequencies. Remarkably, this rotation is very sensitive to small geometry variations, and therefore it may be difficult to control in practice. This thesis has taken steps towards a better understanding and control of bulk-driven streaming at resonance.

The effective model not only eases numerical simulations but also analytical calculations. In this thesis, the acoustic pressure has been calculated in both closed and open cavities, where the boundary layers are included. This has lead to analytical expressions for resonance frequencies, damping coefficients, and axial length scales, which may be used in future studies of such devices, *e.g.* in the study of acoustic streaming.

(3) **Suppression of acoustic streaming**
Finally, the effective models has been used for efficient shape optimization. The discovery of Paper V [5] that acoustic streaming in a cavity can be suppressed by optimizing the shape of the cavity offers a simple solution to one of the most important problems in the field of acoustofluidics; namely that the acoustic streaming ruins the focusing of small particles. As such, this result is one of the most important contributions of the thesis and represents a step towards a future where acoustic streaming can be tailored for a specific purpose.

8.2 Theoretical outlook

The effective model has been tested in several cases by comparison to direct boundary-layer resolved simulations. However, it is encouraged that this testing continues in the future for different settings. This is especially true for the slip velocity on the acoustic streaming derived in Eq. (55) of Paper I [1], which is less straight forward than the boundary condition on the acoustic pressure in Eq. (25) of Paper I [1]. Although the confidence about the derivation is relatively high, further testing is always useful, and any inconsistencies may potentially lead to new insights.

An obvious extension of the boundary-layer theory is to account for the acoustic temperature fluctuations and the resulting thermoviscous effects similar to that done by Rednikov and Sadhal [75] for a motionless wall. Another obvious extension is to allow for inhomogeneous fluids as done outside the viscous boundary layer by Karlsen and Bruus [103]. This should be possible for inhomogeneities varying on a length scale much longer than the boundary-layer width δ.

The shape-optimization procedure presented in this theses for suppression of acoustic streaming could be used with many other goals. One example is an optimization based on both the streaming and the acoustic radiation force. A theoretically appealing exercise regarding the shape-optimization is to derive an analytical expression for the cavity shape,

where the acoustic streaming is minimized. Paper V [5]suggests that such a cavity should have a pressure resonance where the pressure varies linearly along its edge. In theory, it should be possible to suppress the acoustic streaming completely, by using a perfect shape.

The theoretical analysis in Paper IV [4] of long straight capillaries succeeded in calculating the acoustic pressure and the acoustic radiation force, but the acoustic streaming was not calculated. An obvious continuation of that study is therefore to use the provided solutions to analyse the acoustic streaming analytically. Potentially, the peculiar transducer-plane streaming observed in acoustic traps [42, 43] could be further understood.

8.3 Experimental outlook

The results of this thesis motivate several experimental studies of which the most promising are listed below.

Firstly, the surprising prediction that acoustic streaming at resonance can be suppressed by optimizing the shape of the resonator, is a result that calls for experimental realization. The simulation method used in this thesis has previously been tested against both experimental and analytical results [93] so the prediction is relatively confident. As a first approach, an experimental validation could be done in channels made of materials having a high acoustic impedance in order to replicate the ideal hard-wall-optimized shape. The next step could be to use polymer fibers, which can be drawn with almost any complex cross-section shape [160]. In contrast to the case of "hard" channels, the latter situation may require a method to actuate the channel in a well-defined manner. If the acoustic streaming is indeed two orders of magnitude smaller than in the rectangular cross section, the suggested optimized shape could potentially be the preferred geometry for handling of nanoparticles in the field of acoustofluidics.

Secondly, the theoretical study of capillary tubes in Paper IV [4], motivates an experimental study of the influence of the actuator length used for acoustic trapping in such devices. Potentially, the axial acoustic trapping performance could be enhanced by an order of magnitude by choosing the right actuation length.

Thirdly, the presented study of bulk-driven streaming induced by rotating resonances may have practical perspectives. As shown in Fig. 2 and in the supplemental material of Paper III [3], bulk-driven streaming can take many different shapes depending on the excited acoustic resonance in a closed cavity. By using a sufficiently controlled actuation method of a fluid cavity such as Capacitive Micromachined Ultrasonic Transducers (CMUTs) [176], one could excite sequences of different streaming patterns and ideally be able to manipulate the fluid in a microcavity in a controlled manner. Acoustofluidics offers a unique opportunity to apply mechanical body forces on a fluid, and potentially, the excitation of bulk-driven streaming could be a way to exploit that.

Appendix A

Time-averaged conservation of mass for a closed system

The Lagrangian no-slip boundary condition (2.6c) on the fluid velocity reads $\boldsymbol{v}_1 = \boldsymbol{V}_1^0$ in the first-order perturbation, and $\boldsymbol{v}_2 + \langle \tilde{\boldsymbol{s}}_1 \cdot \boldsymbol{\nabla} \tilde{\boldsymbol{v}}_1 \rangle = \boldsymbol{0}$ in the time-averaged second-order perturbation. For this boundary condition to be self consistent with the second-order continuity equation (2.22a), the total mass flux out of the fluid domain Ω must vanish. To show this, the mass flux is evaluated in the general case of an inhomogeneous fluid by using $\boldsymbol{v}_2 = -\frac{1}{2\omega}\mathrm{Re}\big[(\mathrm{i}\boldsymbol{v}_1 \cdot \boldsymbol{\nabla})\boldsymbol{v}_1^*\big]$ at the boundary and $\rho_1 = -\frac{1}{\omega}\boldsymbol{\nabla}\cdot[\rho_0 \mathrm{i}\boldsymbol{v}_1]$,

$$\oint_{\partial\Omega} \big[\rho_0 \boldsymbol{v}_2 + \langle \tilde{\rho}_1 \tilde{\boldsymbol{v}}_1 \rangle\big] \cdot \boldsymbol{n}\, \mathrm{d}A = -\frac{\rho_0}{2\omega} \oint_{\partial\Omega} \mathrm{Re}\Big[(\mathrm{i}\boldsymbol{v}_1 \cdot \boldsymbol{\nabla})\boldsymbol{v}_1^* + \boldsymbol{v}_1^* \boldsymbol{\nabla}\cdot[\mathrm{i}\boldsymbol{v}_1]\Big] \cdot \boldsymbol{n}\, \mathrm{d}A, \tag{A.1}$$

$$= \frac{\rho_0}{4\omega} \oint_{\partial\Omega} \mathrm{Re}\Big[\boldsymbol{\nabla} \times (\mathrm{i}\boldsymbol{v}_1 \times \boldsymbol{v}_1^*)\Big] \cdot \boldsymbol{n}\, \mathrm{d}A, \tag{A.2}$$

$$= \frac{1}{4\omega} \oint_{\partial\partial\Omega} \mathrm{Re}\Big[\boldsymbol{s}_1 \times \rho_0 \boldsymbol{v}_1^*\Big] \cdot \mathrm{d}\boldsymbol{\ell}. \tag{A.3}$$

In the second step, it was used that $(\mathrm{i}A)A^* = \frac{1}{2}\big[(\mathrm{i}A)A^* - A(\mathrm{i}A)^*\big]$ and in order to apply the vector-calculus identity $\boldsymbol{\nabla} \times (\boldsymbol{A} \times \boldsymbol{B}) = -\big[(\boldsymbol{A}\cdot\boldsymbol{\nabla})\boldsymbol{B} + \boldsymbol{B}(\boldsymbol{\nabla}\cdot\boldsymbol{A}) - \boldsymbol{A}(\boldsymbol{\nabla}\cdot\boldsymbol{B}) - (\boldsymbol{B}\cdot\boldsymbol{\nabla})\boldsymbol{A}\big]$ with $\boldsymbol{A} = \mathrm{i}\boldsymbol{v}_1$ and $\boldsymbol{B} = \boldsymbol{v}_1^*$. Furthermore, in the last step $\boldsymbol{s}_1 = \frac{1}{\omega}\mathrm{i}\boldsymbol{v}_1$ was inserted and Stokes theorem was used to convert the surface integral over the surface $\partial\Omega$ of the fluid domain to a line integral over the enclosing line $\partial\partial\Omega$ of the surface $\partial\Omega$. For a closed fluid domain Ω, there is no enclosing line and the total time-averaged mass flux out of the system vanishes. QED.

Appendix B

Energy, power, and dissipation in acoustic fields with boundary layers

The acoustic fields in a fluid conserve mass and momentum as stated in the conservation laws (2.1). The mechanical energy of the acoustic fields is however not conserved but lost to heat through viscous dissipation, both inside and outside of the viscous boundary layers. This appendix gives an overview of these details, first in general and second, in the case of pressure acoustics with boundary layers.

B.1 The energy balance in fluids

It is useful to write the stress tensor $\tilde{\boldsymbol{\sigma}}$ in terms of the pressure $\tilde{p}$ and the viscous part $\tilde{\boldsymbol{\tau}}$,

$$\tilde{\boldsymbol{\sigma}} = -\tilde{p}\mathbf{I} + \tilde{\boldsymbol{\tau}}, \qquad \tilde{\boldsymbol{\tau}} = 2\eta_0\tilde{\boldsymbol{\varepsilon}} + \eta_0^{\mathrm{b}}(\boldsymbol{\nabla}\cdot\tilde{\boldsymbol{v}})\mathbf{I}, \quad \tilde{\boldsymbol{\varepsilon}} = \frac{1}{2}\Big[\boldsymbol{\nabla}\tilde{\boldsymbol{v}} + (\boldsymbol{\nabla}\tilde{\boldsymbol{v}})^{\mathrm{T}}\Big] - \frac{1}{3}(\boldsymbol{\nabla}\cdot\tilde{\boldsymbol{v}})\mathbf{I}, \tag{B.1}$$

where $\tilde{\boldsymbol{\varepsilon}}$ is the traceless shear-rate tensor, $\frac{1}{2}\big[\boldsymbol{\nabla}\tilde{\boldsymbol{v}} + (\boldsymbol{\nabla}\tilde{\boldsymbol{v}})^{\mathrm{T}}\big]$ is the strain-rate tensor, and $\frac{1}{3}(\boldsymbol{\nabla}\cdot\tilde{\boldsymbol{v}})\mathbf{I}$ is the expansion-rate tensor [80]. An expression for the rate of change of kinetic energy implied by the mass- and momentum conservation equations (2.1), is found by taking the dot product between $\tilde{\boldsymbol{v}}$ and the momentum equation (2.1b) and using Eq. (2.1a),

$$\partial_t\Big(\frac{1}{2}\tilde{\rho}\tilde{v}^2\Big) = \boldsymbol{\nabla}\cdot\Big[-\tilde{p}\tilde{\boldsymbol{v}} + \tilde{\boldsymbol{v}}\cdot\tilde{\boldsymbol{\tau}} - \Big(\frac{1}{2}\tilde{\rho}\tilde{v}^2\Big)\tilde{\boldsymbol{v}}\Big] + \tilde{p}\boldsymbol{\nabla}\cdot\tilde{\boldsymbol{v}} - \tilde{\boldsymbol{\tau}} : (\boldsymbol{\nabla}\tilde{\boldsymbol{v}})^{\mathrm{T}}, \tag{B.2a}$$

$$\tilde{\boldsymbol{\tau}} : (\boldsymbol{\nabla}\tilde{\boldsymbol{v}})^{\mathrm{T}} = 2\eta_0\tilde{\boldsymbol{\varepsilon}} : \tilde{\boldsymbol{\varepsilon}}^{\mathrm{T}} + \eta_0^{\mathrm{b}}(\boldsymbol{\nabla}\cdot\tilde{\boldsymbol{v}})^2. \tag{B.2b}$$

Here, the left-hand side is the local rate of change of the kinetic energy density $\frac{1}{2}\tilde{\rho}\tilde{v}^2$, and the divergence-term on the right-hand side represents the energy transport due to the pressure, internal friction, and the kinetic energy density flux $\big(\frac{1}{2}\tilde{\rho}\tilde{v}^2\big)\tilde{\boldsymbol{v}}$, respectively. The last two terms in Eq. (B.2a) represent the conversion of kinetic energy into internal energy, where the very last term $\tilde{\boldsymbol{\tau}} : (\boldsymbol{\nabla}\tilde{\boldsymbol{v}})^{\mathrm{T}}$ is the viscous dissipation power density defined in Eq. (B.2b) and seen to be always positive, as required.

B.2 The acoustic energy balance of homogeneous fluids

Inserting the perturbation expansion of Eq. (2.4a) into Eq. (B.2) and using $\boldsymbol{\nabla}\cdot\tilde{\boldsymbol{v}}_1 = -\kappa_0\partial_t\tilde{p}_1$ from Eq. (2.7a), the second-order time-averaged equation for the acoustic energy balance is obtained

$$\Big\langle \partial_t\Big(\frac{1}{2}\rho_0\tilde{v}_1^2 + \frac{1}{2}\kappa_0\tilde{p}_1^2\Big)\Big\rangle = \boldsymbol{\nabla}\cdot\Big[-\langle\tilde{p}_1\tilde{\boldsymbol{v}}_1\rangle + \langle\tilde{\boldsymbol{v}}_1\cdot\tilde{\boldsymbol{\tau}}_1\rangle\Big] - P_{\text{diss}}, \tag{B.3a}$$

$$P_{\text{diss}} = \langle\tilde{\boldsymbol{\tau}}_1 : (\boldsymbol{\nabla}\tilde{\boldsymbol{v}}_1)^{\text{T}}\rangle = 2\eta_0\langle\tilde{\boldsymbol{\varepsilon}}_1 : \tilde{\boldsymbol{\varepsilon}}_1^{\text{T}}\rangle + \eta_0^{\text{b}}\langle(\boldsymbol{\nabla}\cdot\tilde{\boldsymbol{v}}_1)^2\rangle, \tag{B.3b}$$

where the local time-averaged viscous dissipation density $\mathcal{P}_{\text{visc}}^{\text{diss}}$ is introduced. Since left-hand side of Eq. (B.3a) vanishes for time-harmonic fields, the local energy balance may be written as $\boldsymbol{\nabla}\cdot\langle\tilde{\boldsymbol{v}}_1\cdot\tilde{\boldsymbol{\sigma}}_1\rangle = P_{\text{diss}}$ and the global energy balance is obtained by taking the integral over the entire domain Ω,

$$\mathcal{A}\bar{P}_{\text{wall}} = \mathcal{V}\bar{P}_{\text{diss}}, \tag{B.4}$$

$$\bar{P}_{\text{wall}} = \frac{1}{\mathcal{A}}\int_{\partial\Omega} P_{\text{wall}}\,\mathrm{d}A, \qquad P_{\text{wall}} = \langle\tilde{\boldsymbol{V}}_1^0\cdot\tilde{\boldsymbol{\sigma}}_1\rangle\cdot\boldsymbol{n}, \tag{B.5}$$

$$\bar{P}_{\text{diss}} = \frac{1}{\mathcal{V}}\int_{\Omega} P_{\text{diss}}\,\mathrm{d}V, \qquad P_{\text{diss}} = \langle\tilde{\boldsymbol{\tau}}_1 : (\boldsymbol{\nabla}\tilde{\boldsymbol{v}}_1)^{\text{T}}\rangle, \tag{B.6}$$

where the overbar denote a volume- or surface-averaged quantity. From the energy equation (B.3a), it is noted that viscosity leads to both a local dissipation density $\mathcal{P}_{\text{diss}}$ and the energy-transport term $\boldsymbol{\nabla}\cdot\langle\tilde{\boldsymbol{v}}_1\cdot\tilde{\boldsymbol{\tau}}_1\rangle$, which together constitute the local power loss density P_{loss} due to viscosity,

$$P_{\text{loss}} = P_{\text{diss}} - \boldsymbol{\nabla}\cdot\langle\tilde{\boldsymbol{v}}_1\cdot\tilde{\boldsymbol{\tau}}_1\rangle = -\langle\tilde{\boldsymbol{v}}_1\cdot(\boldsymbol{\nabla}\cdot\tilde{\boldsymbol{\tau}}_1)\rangle. \tag{B.7}$$

Far from the walls, the boundary layer is insignificant and $\boldsymbol{v}_1 = \boldsymbol{v}_1^d$ may be used in Eq. (B.7) together with $\boldsymbol{\nabla}\cdot\boldsymbol{\tau}_1^d = \mathrm{i}\Gamma\boldsymbol{\nabla}p_1 \approx -\Gamma_0\omega\rho_0\boldsymbol{v}_1^d$ from Eqs. (2.7b) and (2.11b). With that, the viscous power loss density $\mathcal{P}_{\text{visc}}^{\text{loss},d}$ outside the boundary layer is,

$$P_{\text{loss}}^d = \frac{1}{2}\Gamma_0\omega\rho_0\big|\boldsymbol{v}_1^d\big|^2, \tag{B.8}$$

where Γ_0 is the bulk damping factor defined in Eq. (2.8). This result is also obtained in Section IV of Paper I [1]. Eq. (B.3a) may therefore be stated outside the boundary layers as,

$$0 = -\boldsymbol{\nabla}\cdot\langle\tilde{p}_1\tilde{\boldsymbol{v}}_1^d\rangle - P_{\text{loss}}^d. \tag{B.9}$$

A major question is now how the energy dissipation in the boundary layer is represented in the effective model, where the boundary layer is taken into account through the boundary condition (3.6) on the pressure p_1. Here, it is important to note that the acoustic velocity perpendicular to the wall is given by Eq. (3.5) to be $v_{1\perp}^{d0} = V_{1\perp}^0 - v_{1\perp}^{\delta 0}$ and therefore, there are two contributions to the energy flux $\langle\tilde{p}_1\tilde{\boldsymbol{v}}_1^d\rangle$ at the boundary: one from the wall, which is input power and one from the boundary-layer velocity $v_{1\perp}^{\delta 0}$, which represents the loss of

energy in the boundary-layer. Calculating the global energy flux out of the system using Eq. (3.4) gives,

$$\begin{aligned}\oint_{\partial\Omega}\langle\tilde{p}_1\tilde{\boldsymbol{v}}_1^d\rangle\cdot\boldsymbol{n}\,\mathrm{d}A &= -\frac{1}{2}\oint_{\partial\Omega}\mathrm{Re}\big(p_1^* v_{1\zeta}^d\big)\,\mathrm{d}A, \\ &\approx -\frac{1}{2}\oint_{\partial\Omega}\mathrm{Re}\Big\{p_1^*\Big[V_{1\zeta}-\frac{\mathrm{i}}{k_\mathrm{s}}\boldsymbol{\nabla}_\parallel\cdot\Big(\boldsymbol{V}_{1\parallel}^0-\boldsymbol{v}_{1\parallel}^{d0}\Big)\Big]\Big\}\,\mathrm{d}A, \\ &= -\frac{1}{2}\oint_{\partial\Omega}\mathrm{Re}\Big\{p_1^*\Big[V_{1\zeta}-\frac{\mathrm{i}}{k_\mathrm{s}}\boldsymbol{\nabla}_\parallel\cdot\boldsymbol{V}_{1\parallel}^0\Big]-\frac{\mathrm{i}}{k_\mathrm{s}}\boldsymbol{\nabla}_\parallel p_1^*\cdot\boldsymbol{v}_{1\parallel}^{d0}\Big\}\,\mathrm{d}A, \\ &\approx -\frac{1}{2}\oint_{\partial\Omega}\mathrm{Re}\Big\{p_1^*\Big[V_{1\zeta}-\frac{\mathrm{i}}{k_\mathrm{s}}\boldsymbol{\nabla}_\parallel\cdot\boldsymbol{V}_{1\parallel}^0\Big]-\frac{\delta}{2}\omega\rho_0\big|\boldsymbol{v}_{1\parallel}^{d0}\big|^2\Big\}\,\mathrm{d}A,\end{aligned} \tag{B.10}$$

Here, integration by parts is used in the third line as well as Gauss's theorem for a *closed* integral causing $\oint\boldsymbol{\nabla}_\parallel\cdot\boldsymbol{B}_\parallel\,\mathrm{d}A$ to vanishes for any vector $\boldsymbol{B}$. Furthermore, in the fourth, line it is used that $\boldsymbol{\nabla}_\parallel p_1^*\approx\mathrm{i}\omega\rho_0\boldsymbol{v}_{1\parallel}^{d0}$ from Eq. (2.11b). Hence, the global expression for the energy balance of the long-range fields, is found by integrating Eq. (B.9) and using Eq. (B.10),

$$\oint_{\partial\Omega}\frac{1}{2}\mathrm{Re}\Big[p_1^*\Big(V_{1\zeta}-\frac{\mathrm{i}}{k_\mathrm{s}}\boldsymbol{\nabla}_\parallel\cdot\boldsymbol{V}_{1\parallel}^0\Big)\Big]\,\mathrm{d}A=\int_\Omega\frac{1}{2}\Gamma_0\rho_0\omega\big|\boldsymbol{v}_1^d\big|^2\,\mathrm{d}V+\oint_{\partial\Omega}\frac{1}{4}\delta\rho_0\omega\big|\boldsymbol{v}_{1\parallel}^{d0}\big|^2\,\mathrm{d}A. \tag{B.11}$$

where all wall-velocity terms are gathered on the left-hand side to represent the power input and all the fluid-velocity-terms are gathered on the right-hand side to represent power loss due to viscous effects in the bulk and in the boundary layer, respectively. In classical pressure acoustics where the boundary layer is neglected [80], only the first term on each side is present. Here it is seen that the boundary layer introduces an additional input-power term on the left-hand side and an additional loss term on the right-hand side.

Bibliography

[1] J. S. Bach and H. Bruus, *Theory of pressure acoustics with viscous boundary layers and streaming in curved elastic cavities*. J. Acoust. Soc. Am. **144**, 766–784 (2018).

[2] N. R. Skov, J. S. Bach, B. G. Winckelmann, and H. Bruus, *3D modeling of acoustofluidics in a liquid-filled cavity including streaming, viscous boundary layers, surrounding solids, and a piezoelectric transducer*. AIMS Mathematics **4**, 99–111 (2019).

[3] J. S. Bach and H. Bruus, *Bulk-driven acoustic streaming at resonance in closed microcavities*. Phys. Rev. E **100**, 023104 (2019).

[4] J. S. Bach and H. Bruus, *Theory of acoustic trapping of microparticles in capillary tubes*. Phys. Rev. E **101**, 023107 (2020).

[5] J. S. Bach and H. Bruus, *Suppression of acoustic streaming in shape-optimized channels*. Submitted to Phys Rev. Lett. (Feb 2020). ArXiv preprint: 2002.11058 [physics.flu-dyn].

[6] J. S. Bach and H. Bruus, *Different origins of acoustic streaming at resonance*. Proc. Mtgs. Acoust. **34**, 022005 (2018).

[7] G. M. Whitesides, *The origins and the future of microfluidics*. Nature **442**(7101), 368–373 (2006).

[8] Y. Song, Y. . Huang, X. Liu, X. Zhang, M. Ferrari, and L. Qin, *Point-of-care technologies for molecular diagnostics using a drop of blood*. Trends in biotechnology **32**(3), 132–139 (2014).

[9] D. Wu and J. Voldman, *An integrated and automated electronic system for point-of-care protein testing*. Proceedings of the Annual International Conference of the Ieee Engineering in Medicine and Biology Society, Embs **2019**, 8857362, 1571–1574 (2019).

[10] J. D. Caplin, N. G. Granados, M. R. James, R. Montazami, and N. Hashemi, *Microfluidic organ-on-a-chip technology for advancement of drug development and toxicology*. Advanced Healthcare Materials **4**(10), 1426–1450 (2015).

[11] Y. Wang, W. Y. Lin, K. Liu, R. J. Lin, M. Selke, H. C. Kolb, N. Zhang, X. Z. Zhao, M. E. Phelps, C. K. Shen, K. F. Faull, and H. R. Tseng, *An integrated microfluidic*

device for large-scale in situ click chemistry screening. Lab on a Chip **9**(16), 2281–2285 (2009).

[12] H. Bruus, *Theoretical Microfluidics* (Oxford University Press, Oxford) (2008).

[13] D. R. Gossett, W. M. Weaver, A. J. MacH, S. C. Hur, H. T. K. Tse, W. Lee, H. Amini, and D. Di Carlo, *Label-free cell separation and sorting in microfluidic systems*. Analytical and Bioanalytical Chemistry **397**(8), 3249–3267 (2010).

[14] H. Amini, W. Lee, and D. Di Carlo, *Inertial microfluidic physics*. Lab Chip **14**, 2739–2761 (2014).

[15] X. B. Zhang, Z. Q. Wu, K. Wang, J. Zhu, J. J. Xu, X. H. Xia, and H. Y. Chen, *Gravitational sedimentation induced blood delamination for continuous plasma separation on a microfluidics chip*. Analytical Chemistry **84**(8), 3780–3786 (2012).

[16] R. Dylla-Spears, J. E. Townsend, L. Jen-Jacobson, L. L. Sohn, and S. J. Muller, *Single-molecule sequence detection via microfluidic planar extensional flow at a stagnation point*. Lab on a Chip **10**(12), 1543–1549 (2010).

[17] S. J. Kim, Y. C. Wang, J. H. Lee, H. Jang, and J. Han, *Concentration polarization and nonlinear electrokinetic flow near a nanofluidic channel*. Physical Review Letters **99**(4), 044501 (2007).

[18] F. Alnaimat, S. Dagher, B. Mathew, A. Hilal-Alnqbi, and S. Khashan, *Microfluidics based magnetophoresis: A review*. Chemical Record **18**(11), 1596–1612 (2018).

[19] N. Apichitsopa, A. Jaffe, and J. Voldman, *Multiparameter cell-tracking intrinsic cytometry for single-cell characterization*. Lab on a Chip **18**(10), 1430–1439 (2018).

[20] A. Jaffe and J. Voldman, *Multi-frequency dielectrophoretic characterization of single cells*. Microsystems and Nanoengineering **4**(1), 23 (2018).

[21] D. G. Grier, *A revolution in optical manipulation*. Nature **424**(6950), 810–816 (2003).

[22] J. L. Thomas, R. Marchiano, and D. Baresch, *Acoustical and optical radiation pressure and the development of single beam acoustical tweezers*. Journal of Quantitative Spectroscopy and Radiative Transfer **195**, 55–65 (2017).

[23] T. Laurell and A. Lenshof (eds.), *Microscale Acoustofluidics* (Royal Society of Chemistry, Cambridge) (2015).

[24] P. J. Kenis, R. F. Ismagilov, and G. M. Whitesides, *Microfabrication inside capillaries using multiphase laminar flow patterning*. Science **285**(5424), 83–85 (1999), image taken by Felice Frankel, see https://felicefrankel.com/frankel_cover/science-1999/ (29 Feb 2020).

[25] P. B. Muller and H. Bruus, *Numerical study of thermoviscous effects in ultrasound-induced acoustic streaming in microchannels*. Phys. Rev. E **90**(4), 043016 (2014).

[26] H. Bruus, J. Dual, J. Hawkes, M. Hill, T. Laurell, J. Nilsson, S. Radel, S. Sadhal, and M. Wiklund, *Forthcoming lab on a chip tutorial series on acoustofluidics: Acoustofluidics-exploiting ultrasonic standing wave forces and acoustic streaming in microfluidic systems for cell and particle manipulation.* Lab Chip **11**(21), 3579–3580 (2011).

[27] M. A. Burguillos, C. Magnusson, M. Nordin, A. Lenshof, P. Augustsson, M. J. Hansson, E. Elme, H. Lilja, P. Brundin, T. Laurell, and T. Deierborg, *Microchannel acoustophoresis does not impact survival or function of microglia, leukocytes or tumor cells.* PLOS ONE **8**(8), e64233 (2013).

[28] M. Wiklund, *Acoustofluidics 12: Biocompatibility and cell viability in microfluidic acoustic resonators* (2014).

[29] F. Petersson, A. Nilsson, C. Holm, H. Jönsson, and T. Laurell, *Separation of lipids from blood utilizing ultrasonic standing waves in microfluidic channels.* Analyst **129**(10), 938–43 (2004).

[30] T. Laurell, F. Petersson, and A. Nilsson, *Chip integrated strategies for acoustic separation and manipulation of cells and particles.* Chem Soc Rev **36**(3), 492–506 (2007).

[31] M. K. Tan, R. Tjeung, H. Ervin, L. Y. Yeo, and J. Friend, *Double aperture focusing transducer for controlling microparticle motions in trapezoidal microchannels with surface acoustic waves.* Appl Phys Lett **95**(13), 134101 (2009).

[32] A. Lenshof and T. Laurell, *Continuous separation of cells and particles in microfluidic systems.* Chem Soc Rev **39**(3), 1203–1217 (2010).

[33] X. Ding, Z. Peng, S.-C. S. Lin, M. Geri, S. Li, P. Li, Y. Chen, M. Dao, S. Suresh, and T. J. Huang, *Cell separation using tilted-angle standing surface acoustic waves.* Proc. Natl. Acad. Sci. U.S.A. **111**(36), 12992–12997 (2014).

[34] M. Antfolk and T. Laurell, *Continuous flow microfluidic separation and processing of rare cells and bioparticles found in blood - a review.* Anal. Chim. Acta **965**, 9–35 (2017).

[35] M. Tenje, M. N. Lundgren, A. M. Swärd-Nilsson, J. Kjeldsen-Kragh, L. Lyxe, and A. Lenshof, *Acoustophoretic removal of proteins from blood components.* Biomedical Microdevices **17**(5), 95, 95 (2015).

[36] P. Augustsson, C. Magnusson, M. Nordin, H. Lilja, and T. Laurell, *Microfluidic, label-free enrichment of prostate cancer cells in blood based on acoustophoresis.* Anal. Chem. **84**(18), 7954–7962 (2012).

[37] A. Lenshof, A. Ahmad-Tajudin, K. Jaras, A.-M. Sward-Nilsson, L. Aberg, G. Marko-Varga, J. Malm, H. Lilja, and T. Laurell, *Acoustic whole blood plasmapheresis chip for prostate specific antigen microarray diagnostics.* Anal. Chem. **81**(15), 6030–6037 (2009).

[38] M. Grundy, W. Bolek, W. Coakley, and E. Benes, *Rapid agglutination testing in an ultrasonic standing wave.* Journal of Immunological Methods **165**(165), 47–57 (1993).

[39] T. Lilliehorn, U. Simu, M. Nilsson, M. Almqvist, T. Stepinski, T. Laurell, J. Nilsson, and S. Johansson, *Trapping of microparticles in the near field of an ultrasonic transducer.* Ultrasonics **43**(5), 293–303 (2005).

[40] M. Evander, L. Johansson, T. Lilliehorn, J. Piskur, M. Lindvall, S. Johansson, M. Almqvist, T. Laurell, and J. Nilsson, *Noninvasive acoustic cell trapping in a microfluidic perfusion system for online bioassays.* Anal. Chem. **79**(7), 2984–2991 (2007).

[41] B. Hammarström, M. Evander, H. Barbeau, M. Bruzelius, J. Larsson, T. Laurell, and J. Nillsson, *Non-contact acoustic cell trapping in disposable glass capillaries.* Lab Chip **10**(17), 2251–2257 (2010).

[42] B. Hammarström, T. Laurell, and J. Nilsson, *Seed particle enabled acoustic trapping of bacteria and nanoparticles in continuous flow systems.* Lab Chip **12**, 4296–4304 (2012).

[43] J. Lei, P. Glynne-Jones, and M. Hill, *Acoustic streaming in the transducer plane in ultrasonic particle manipulation devices.* Lab Chip **13**(11), 2133–2143 (2013).

[44] P. Mishra, M. Hill, and P. Glynne-Jones, *Deformation of red blood cells using acoustic radiation forces.* Biomicrofluidics **8**(3), 034109 (2014).

[45] I. Gralinski, S. Raymond, T. Alan, and A. Neild, *Continuous flow ultrasonic particle trapping in a glass capillary.* Journal of Applied Physics **115**(5), 054505 (2014).

[46] M. Tenje, H. Xia, M. Evander, B. Hammarström, A. Tojo, S. Belák, T. Laurell, and N. LeBlanc, *Acoustic trapping as a generic non-contact incubation site for multiplex bead-based assays.* Analytica Chimica Acta **853**, 682–688 (2014).

[47] M. Evander, O. Gidlof, B. Olde, D. Erlinge, and T. Laurell, *Non-contact acoustic capture of microparticles from small plasma volumes.* Lab Chip **15**, 2588–2596 (2015).

[48] N. Garg, T. M. Westerhof, V. Liu, R. Liu, E. L. Nelson, and A. P. Lee, *Whole-blood sorting, enrichment and in situ immunolabeling of cellular subsets using acoustic microstreaming.* Microsystems and Nanoengineering **4**(1), 17085 (9 pp.), 17085 (9 pp.) (2018).

[49] D. Baresch, J.-L. Thomas, and R. Marchiano, *Observation of a single-beam gradient force acoustical trap for elastic particles: Acoustical tweezers.* Phys. Rev. Lett. **116**, 024301 (2016).

[50] H. G. Lim, Y. Li, M.-Y. Lin, C. Yoon, C. Lee, H. Jung, R. H. Chow, and K. K. Shung, *Calibration of trapping force on cell-size objects from ultrahigh-frequency single-beam acoustic tweezer*. IEEE IEEE T. Ultrason. Ferr. **63**(11), 1988–1995 (2016).

[51] D. J. Collins, C. Devendran, Z. Ma, J. W. Ng, A. Neild, and Y. Ai, *Acoustic tweezers via sub-time-of-flight regime surface acoustic waves*. Science Advances **2**(7), e1600089 (2016).

[52] A. Riaud, M. Baudoin, O. Bou Matar, L. Becerra, and J.-L. Thomas, *Selective manipulation of microscopic particles with precursor swirling rayleigh waves*. Phys. Rev. Applied **7**, 024007 (2017).

[53] M. Wu, Z. Mao, K. Chen, H. Bachman, Y. Chen, J. Rufo, L. Ren, P. Li, L. Wang, and T. J. Huang, *Acoustic separation of nanoparticles in continuous flow*. Adv. Funct. Mater. **27**(14), 1606039 (2017).

[54] M. Antfolk, P. B. Muller, P. Augustsson, H. Bruus, and T. Laurell, *Focusing of sub-micrometer particles and bacteria enabled by two-dimensional acoustophoresis*. Lab Chip **14**, 2791–2799 (2014).

[55] Z. Mao, P. Li, M. Wu, H. Bachman, N. Mesyngier, X. Guo, S. Liu, F. Costanzo, and T. J. Huang, *Enriching nanoparticles via acoustofluidics*. Acs Nano **11**(1), 603–612 (2017).

[56] P. Thevoz, J. D. Adams, H. Shea, H. Bruus, and H. T. Soh, *Acoustophoretic synchronization of mammalian cells in microchannels*. Anal. Chem. **82**(7), 3094–3098 (2010).

[57] X. Ding, S.-C. S. Lin, B. Kiraly, H. Yue, S. Li, I.-K. Chiang, J. Shi, S. J. Benkovic, and T. J. Huang, *On-chip manipulation of single microparticles, cells, and organisms using surface acoustic waves*. Proc. Natl. Acad. Sci. U.S.A. **109**(28), 11105–11109 (2012).

[58] M. Kim, E. Huff, P. Bayly, and J. M. Meacham, *Living probes as calibration standards for acoustic microfluidics*. Journal of the Acoustical Society of America **145**(3), 1786–1786 (2019).

[59] D. J. Collins, B. Morahan, J. Garcia-Bustos, C. Doerig, M. Plebanski, and A. Neild, *Two-dimensional single-cell patterning with one cell per well driven by surface acoustic waves*. Nat. Commun. **6**, 8686 (2015).

[60] D. J. Collins, R. O'Rorke, C. Devendran, Z. Ma, J. Han, A. Neild, and Y. Ai, *Self-aligned acoustofluidic particle focusing and patterning in microfluidic channels from channel-based acoustic waveguides*. Phys. Rev. Lett. **120**(7), 074502 (2018).

[61] B. Vanherberghen, O. Manneberg, A. Christakou, T. Frisk, M. Ohlin, H. M. Hertz, B. Önfelt, and M. Wiklund, *Ultrasound-controlled cell aggregation in a multi-well chip*. Lab Chip **10**(20), 2727–2732 (2010).

[62] M. Wiklund, A. E. Christakou, M. Ohlin, I. Iranmanesh, T. Frisk, B. Vanherberghen, and B. Önfelt, *Ultrasound-induced cell-cell interaction studies in a multi-well microplate*. Micromachines **5**(1), 27 (2014).

[63] Y. Kurashina, K. Takemura, and J. Friend, *Cell agglomeration in the wells of a 24-well plate using acoustic streaming*. Lab on a Chip **17**(5), 876–886 (2017).

[64] A. Fornell, J. Nilsson, L. Jonsson, P. K. Periyannan Rajeswari, H. N. Joensson, and M. Tenje, *Controlled lateral positioning of microparticles inside droplets using acoustophoresis*. Analytical Chemistry **87**(20), 10521–10526 (2015).

[65] R. Barnkob, N. Nama, L. Ren, T. J. Huang, F. Costanzo, and C. J. Kähler, *Acoustically driven fluid and particle motion in confined and leaky systems*. Physical Review Applied **9**(1), 014027 (2018).

[66] P. B. Muller, R. Barnkob, M. J. H. Jensen, and H. Bruus, *A numerical study of microparticle acoustophoresis driven by acoustic radiation forces and streaming-induced drag forces*. Lab Chip **12**, 4617–4627 (2012).

[67] R. Barnkob, P. Augustsson, T. Laurell, and H. Bruus, *Acoustic radiation- and streaming-induced microparticle velocities determined by microparticle image velocimetry in an ultrasound symmetry plane*. Phys. Rev. E **86**, 056307 (2012).

[68] L. a. Kuznetsova, S. P. Martin, and W. T. Coakley, *Sub-micron particle behaviour and capture at an immuno-sensor surface in an ultrasonic standing wave.* Biosensors & bioelectronics **21**(6), 940–8 (2005).

[69] M. Wiklund, R. Green, and M. Ohlin, *Acoustofluidics 14: Applications of acoustic streaming in microfluidic devices*. Lab Chip **12**, 2438–2451 (2012).

[70] Lord Rayleigh, *On the circulation of air observed in Kundt's tubes, and on some allied acoustical problems*. Philos. Trans. R. Soc. London **175**, 1–21 (1884).

[71] W. L. Nyborg, *Acoustic streaming near a boundary*. J. Acoust. Soc. Am. **30**(4), 329–339 (1958).

[72] C. Lee and T. Wang, *Near-boundary streaming around a small sphere due to 2 orthogonal standing waves*. J. Acoust. Soc. Am. **85**(3), 1081–1088 (1989).

[73] C. P. Lee and T. G. Wang, *Outer acoustic streaming*. J. Acoust. Soc. Am. **88**(5), 2367–2375 (1990).

[74] J. Vanneste and O. Bühler, *Streaming by leaky surface acoustic waves*. Proc. R. Soc. A **467**(2130), 1779–1800 (2011).

[75] A. Y. Rednikov and S. S. Sadhal, *Acoustic/steady streaming from a motionless boundary and related phenomena: generalized treatment of the inner streaming and examples*. J. Fluid. Mech. **667**, 426–462 (2011).

[76] S. M. Hagsäter, T. G. Jensen, H. Bruus, and J. P. Kutter, *Acoustic resonances in microfluidic chips: full-image micro-PIV experiments and numerical simulations.* Lab Chip **7**(10), 1336–1344 (2007).

[77] M. W. H. Ley and H. Bruus, *Continuum modeling of hydrodynamic particle-particle interactions in microfluidic high-concentration suspensions.* Lab on a Chip **16**(7), 1178–1188 (2016).

[78] C. E. Bradley, *Acoustic streaming field structure: The influence of the radiator.* J. Acoust. Soc. Am. **100**(3), 1399–1408 (1996).

[79] J. T. Karlsen and H. Bruus, *Forces acting on a small particle in an acoustical field in a thermoviscous fluid.* Phys. Rev. E **92**, 043010 (2015).

[80] L. D. Landau and E. M. Lifshitz, *Fluid Mechanics*, vol. 6 (Pergamon Press, Oxford), 2nd edn. (1993).

[81] R. Barnkob, P. Augustsson, T. Laurell, and H. Bruus, *Measuring the local pressure amplitude in microchannel acoustophoresis.* Lab Chip **10**(5), 563–570 (2010).

[82] R. Moiseyenko and H. Bruus, *Mixed shear and longitudinal ultrasound wave resonances in polymer chips enabling microchannel acoustophoresis.* Lab Chip (in preparation), 1–8 (2016).

[83] M. Settnes and H. Bruus, *Forces acting on a small particle in an acoustical field in a viscous fluid.* Phys. Rev. E **85**, 016327 (2012).

[84] L. P. Gorkov, *On the forces acting on a small particle in an acoustical field in an ideal fluid.* Sov. Phys.–Dokl. **6**(9), 773–775 (1962), [Doklady Akademii Nauk SSSR **140**, 88 (1961)].

[85] *CRC Handbook of Chemistry and Physics* (CRC Press, Boca Raton, FL), 95th edn. (2014).

[86] L. Bergmann, *Der Ultraschall und seine Anwendung in Wissenschaft und Technik* (S. Hirzel Verlag, Stuttgart), 6th edn. (1954).

[87] P. H. Mott, J. R. Dorgan, and C. M. Roland, *The bulk modulus and poisson's ratio of "incompressible" materials.* J Sound Vibr **312**(4-5), 572–575 (2008).

[88] L. V. King, *On the acoustic radiation pressure on spheres.* Proc. R. Soc. London, Ser. A **147**(861), 212–240 (1934).

[89] K. Yosioka and Y. Kawasima, *Acoustic radiation pressure on a compressible sphere.* Acustica **5**, 167–173 (1955).

[90] A. A. Doinikov, *Acoustic radiation force on a spherical particle in a viscous heat-conducting fluid .1. general formula.* J. Acoust. Soc. Am. **101**(2), 713–721 (1997).

[91] A. A. Doinikov, *Acoustic radiation force on a spherical particle in a viscous heat-conducting fluid .2. force on a rigid sphere.* J. Acoust. Soc. Am. **101**(2), 722–730 (1997).

[92] A. A. Doinikov, *Acoustic radiation force on a spherical particle in a viscous heat-conducting fluid. 3. Force on a liquid drop.* J. Acoust. Soc. Am. **101**(2), 731–740 (1997).

[93] P. B. Muller, M. Rossi, A. G. Marin, R. Barnkob, P. Augustsson, T. Laurell, C. J. Kähler, and H. Bruus, *Ultrasound-induced acoustophoretic motion of microparticles in three dimensions.* Phys. Rev. E **88**(2), 023006 (2013).

[94] E. F. F. Chladni, *Die Acoustic* (Breitkopf und Hartel, Leipzig) (1802).

[95] H. C. Ørsted, *Forøg over klangfigurerne.* Det kongelige danske videnskabernes-selskabs skrivter **5 deels, 2. hefte**, 31–64 (1808), also published by A. G. Gehlen in Journal für die Chemie, Physik und Mineralogie, **8**, 223-254, Berlin 1809.

[96] F. Savart, *Mémoire sur la construction des instruments à cordes et à archets* (Deterville, Paris) (1819).

[97] M. Faraday, *On a peculiar class of acoustical figures; and on certain forms assumed by groups of particles upon vibrating elastic surfaces.* Philos. Trans. R. Soc. London **121**, 299–340 (1831).

[98] A. Kundt, *Ueber eine neue Art Akustischer Staubfiguren und über die Anwendung derselben zur Bestimmung der Shallgeschwindigkeit in festen Körpern und Gasen.* Annalen der Physik und Chemie **CXXVVII**(4), 497–523 (1866).

[99] H. Schlichting, *Berechnung ebener periodischer grenzeschichtströmungen.* Phys. Z. **33**, 327–335 (1932).

[100] J. Lighthill, *Acoustic streaming.* J Sound Vibr **61**(3), 391–418 (1978).

[101] C. Eckart, *Vortices and streams caused by sound waves.* Phys. Rev. **73**, 68–76 (1948).

[102] J. T. Karlsen, P. Augustsson, and H. Bruus, *Acoustic force density acting on inhomogeneous fluids in acoustic fields.* Phys. Rev. Lett. **117**, 114504 (2016).

[103] J. T. Karlsen, W. Qiu, P. Augustsson, and H. Bruus, *Acoustic streaming and its suppression in inhomogeneous fluids.* Phys. Rev. Lett. **120**(5), 054501 (2018).

[104] M. R. Maxey and J. J. Riley, *Equation of motion for a small rigid sphere in a nonuniform flow.* The Physics of Fluids **26**(4), 883–889 (1983).

[105] C. Oseen, *Über die Stoke'sche Formel und über eine verwandte Aufgabe in der Hydrodynamik: Mitteilung 2.* No. vb. 1 in Arkiv för matematik, astronomi och fysik (Almqvist & Wiksell) (1911).

[106] H. Faxén, *The resistance against the movement of a rigour sphere in viscous fluids, which is embedded between two parallel layered barriers.* Ann Phys **68**(10), 89–119 (1922).

[107] J. Hultström, O. Manneberg, K. Dopf, H. M. Hertz, H. Brismar, and M. Wiklund, *Proliferation and viability of adherent cells manipulated by standing-wave ultrasound in a microfluidic chip.* Ultrasound Med Biol **33**(1), 145–151 (2007).

[108] S. P. Martin, R. J. Towsend, L. A. Kuznetsova, K. A. J. Borthwick, M. Hill, M. B. McDonnell, and W. T. Coakley, *Spore and micro-particle capture on an immunosensor surface in an ultrasound standing wave system.* Biosens Bioelectron **21**, 758–767 (2005).

[109] P. Augustsson, R. Barnkob, S. T. Wereley, H. Bruus, and T. Laurell, *Automated and temperature-controlled micro-piv measurements enabling long-term-stable microchannel acoustophoresis characterization.* Lab Chip **11**(24), 4152–4164 (2011).

[110] R. Barnkob, I. Iranmanesh, M. Wiklund, and H. Bruus, *Measuring acoustic energy density in microchannel acoustophoresis using a simple and rapid light-intensity method.* Lab Chip **12**, 2337–2344 (2012).

[111] D. J. Collins, T. Alan, and A. Neild, *Particle separation using virtual deterministic lateral displacement (vdld).* Lab Chip **14**(9), 1595–1603 (2014).

[112] Z. Mao, P. Li, M. Wu, H. Bachman, N. Mesyngier, X. Guo, S. Liu, F. Costanzo, and T. J. Huang, *Enriching nanoparticles via acoustofluidics.* ACS Nano **11**(1), 603–612 (2017).

[113] M. Hoyos and A. Castro, *Controlling the acoustic streaming by pulsed ultrasounds.* Ultrasonics **53**, 70 (2013).

[114] P. B. Muller and H. Bruus, *Theoretical study of time-dependent, ultrasound-induced acoustic streaming in microchannels.* Phys. Rev. E **92**, 063018 (2015).

[115] W. Qiu, J. T. Karlsen, H. Bruus, and P. Augustsson, *Experimental characterization of acoustic streaming in gradients of density and compressibility.* Phys. Rev. Applied **11**, 024018 (2019).

[116] J. S. Bach, *Theory and simulation of microscale acoustic streaming in three dimensions: a study in effective modelling.* Master's thesis, Technical University of Denmark, www.fysik.dtu.dk/microfluidics (2019).

[117] P. Reichert, D. Deshmukh, L. Lebovitz, and J. Dual, *Thin film piezoelectrics for bulk acoustic wave (BAW) acoustophoresis.* Lab Chip **18**(23), 3655–3667 (2018).

[118] T. M. Squires and S. R. Quake, *Microfluidics: Fluid physics at the nanoliter scale.* Rev. Mod. Phys. **77**, 977–1026 (2005).

[119] J. Wu, *Acoustic streaming and its applications.* Fluids **3**(4), 108 (2018).

[120] N. Riley, *Steady streaming*. Annu. Rev. Fluid Mech. **33**, 43–65 (2001).

[121] S. M. Hagsäter, A. Lenshof, P. Skafte-Pedersen, J. P. Kutter, T. Laurell, and H. Bruus, *Acoustic resonances in straight micro channels: Beyond the 1D-approximation*. Lab Chip **8**(7), 1178–1184 (2008).

[122] COMSOL Multiphysics 5.4. http://www.comsol.com (2018).

[123] Matlab 2019b. http://www.mathworks.com (2019).

[124] H. Bruus, course notes for the course 10350 *Numerical studies in physics*, Technical University of Denmark, Department of Physics (2020).

[125] P. Augustsson, J. T. Karlsen, H.-W. Su, H. Bruus, and J. Voldman, *Iso-acoustic focusing of cells for size-insensitive acousto-mechanical phenotyping*. Nat. Commun. **7**, 11556 (2016).

[126] B. Hammarström, M. Evander, J. Wahlström, and J. Nilsson, *Frequency tracking in acoustic trapping for improved performance stability and system surveillance*. Lab Chip **14**, 1005–1013 (2014).

[127] B. W. Drinkwater, *Dynamic-field devices for the ultrasonic manipulation of microparticles*. Lab Chip **16**, 2360–2375 (2016).

[128] J. Lei, P. Glynne-Jones, and M. Hill, *Modal Rayleigh-like streaming in layered acoustofluidic devices*. Phys. Fluids **28**, 012004 (2016).

[129] P. Hahn and J. Dual, *A numerically efficient damping model for acoustic resonances in microfluidic cavities*. Physics of Fluids **27**, 062005 (2015).

[130] A. Riaud, M. Baudoin, O. Bou Matar, J.-L. Thomas, and P. Brunet, *On the influence of viscosity and caustics on acoustic streaming in sessile droplets: an experimental and a numerical study with a cost-effective method*. J. Fluid Mech. **821**, 384–420 (2017).

[131] CORNING, Houghton Park C-8, Corning, NY 14831, USA, *Glass Silicon Constraint Substrates*. http://www.valleydesign.com/Datasheets/Corning%20Pyrex%207740.pdf, accessed 29 February 2020.

[132] M. W. H. Ley and H. Bruus, *Three-dimensional numerical modeling of acoustic trapping in glass capillaries*. Phys. Rev. Applied **8**, 024020 (2017).

[133] E. Kreyszig, *Differential Geometry* (Dover Publications, New York) (1991).

[134] L. D. Landau and E. M. Lifshitz, *The Classical Theory of Fields* (Butterworth-Heinemann) (1980).

[135] A. Lenshof, C. Magnusson, and T. Laurell, *Acoustofluidics 8: Applications in acoustophoresis in continuous flow microsystems*. Lab Chip **12**, 1210–1223 (2012).

[136] M. Gedge and M. Hill, *Acoustofluidics 17: Surface acoustic wave devices for particle manipulation*. Lab Chip **12**, 2998–3007 (2012).

[137] E. K. Sackmann, A. L. Fulton, and D. J. Beebe, *The present and future role of microfluidics in biomedical research*. Nature **507**(7491), 181–189 (2014).

[138] N. Nama, R. Barnkob, Z. Mao, C. J. Kähler, F. Costanzo, and T. J. Huang, *Numerical study of acoustophoretic motion of particles in a pdms microchannel driven by surface acoustic waves*. Lab Chip **15**, 2700–2709 (2015).

[139] J. Lei, M. Hill, and P. Glynne-Jones, *Numerical simulation of 3D boundary-driven acoustic streaming in microfluidic devices*. Lab Chip **14**(3), 532–541 (2014).

[140] M. A. Hopcroft, W. D. Nix, and T. W. Kenny, *What is the Young's modulus of silicon*. J. Microelectromech. Syst **19**, 229–238 (2010).

[141] J. Dual and D. Möller, *Acoustofluidics 4: Piezoelectricity and application to the excitation of acoustic fields for ultrasonic particle manipulation*. Lab Chip **12**, 506–514 (2012).

[142] Meggit A/S, Porthusvej 4, DK-3490 Kvistgaard, Denmark, *Ferroperm Matdat 2017*. URL https://www.meggittferroperm.com/materials/, accessed 29 February 2020.

[143] F. Petersson, L. Åberg, A. M. Swärd-Nilsson, and T. Laurell, *Free flow acoustophoresis: microfluidic-based mode of particle and cell separation*. Anal. Chem. **79**(14), 5117–23 (2007).

[144] O. Manneberg, B. Vanherberghen, J. Svennebring, H. M. Hertz, B. Önfelt, and M. Wiklund, *A three-dimensional ultrasonic cage for characterization of individual cells*. Appl Phys Lett **93**(6), 063901–3 (2008).

[145] M. Antfolk, C. Magnusson, P. Augustsson, H. Lilja, and T. Laurell, *Acoustofluidic, label-free separation and simultaneous concentration of rare tumor cells from white blood cells*. Anal. Chem. **87**(18), 9322–9328 (2015).

[146] S. Li, F. Ma, H. Bachman, C. E. Cameron, X. Zeng, and T. J. Huang, *Acoustofluidic bacteria separation*. J. Micromech. Microeng. **27**(1), 015031 (2017).

[147] P. Westervelt, *The theory of steady rotational flow generated by a sound field*. J. Acoust. Soc. Am. **25**(1), 60–67 (1953).

[148] F. Busse and T. Wang, *Torque generated by orthogonal acoustic-waves - theory*. J. Acoust. Soc. Am. **69**(6), 1634–1638 (1981).

[149] S. B. Q. Tran, P. Marmottant, and P. Thibault, *Fast acoustic tweezers for the two-dimensional manipulation of individual particles in microfluidic channels*. Appl. Phys. Lett. **101**(11), 114103 (2012).

[150] J. Dual, P. Hahn, I. Leibacher, D. Möller, T. Schwarz, and J. Wang, *Acoustofluidics 19: ultrasonic microrobotics in cavities: devices and numerical simulation.* Lab on a chip **12**(20), 4010–4021 (2012).

[151] C. R. P. Courtney, B. W. Drinkwater, C. E. M. Demore, S. Cochran, A. Grinenko, and P. D. Wilcox, *Dexterous manipulation of microparticles using bessel-function acoustic pressure fields.* Appl. Phys. Lett. **102**, 123508 (2013).

[152] D. Baresch, R. Marchiano, and J.-L. Thomas, *Orbital angular momentum transfer to stably trapped elastic particles in acoustical vortex beams.* Physical Review Letters **121** (2018).

[153] P. L. Marston, *Axial radiation force of a bessel beam on a sphere and direction reversal of the force.* The Journal of the Acoustical Society of America **120**(6), 3518–3524 (2006).

[154] A. Marzo, S. A. Seah, B. W. Drinkwater, D. R. Sahoo, B. Long, and S. Subramanian, *Holographic acoustic elements for manipulation of levitated objects.* Nat. Commun. **6**, 8661 (2015).

[155] A. S. Dukhin and P. J. Goetz, *Bulk viscosity and compressibility measurement using acoustic spectroscopy.* J Chem Phys **130**(12), 124519 (2009).

[156] J. Shi, D. Ahmed, X. Mao, S.-C. S. Lin, A. Lawit, and T. J. Huang, *Acoustic tweezers: patterning cells and microparticles using standing surface acoustic waves (SSAW).* Lab Chip **9**(20), 2890–2895 (2009).

[157] Z. Gong and M. Baudoin, *Particle assembly with synchronized acoustic tweezers.* Phys. Rev. Applied **12**, 024045 (2019).

[158] M. Evander, A. Lenshof, T. Laurell, and J. Nilsson, *Acoustophoresis in wet-etched glass chips.* Analytical Chemistry **80**(13), 5178–5185 (2008), pMID: 18489126.

[159] D. Carugo, T. Octon, W. Messaoudi, A. L. Fisher, M. Carboni, N. R. Harris, M. Hill, and P. Glynne-Jones, *A thin-reflector microfluidic resonator for continuous-flow concentration of microorganisms: a new approach to water quality analysis using acoustofluidics.* Lab Chip **14**(19), 3830–3842 (2014).

[160] R. Yuan, J. Lee, H.-W. Su, E. Levy, T. Khudiyev, J. Voldman, and Y. Fink, *Microfluidics in structured multimaterial fibers.* Proceedings of the National Academy of Sciences **115**(46), E10830–E10838 (2018).

[161] P. J. Woodside SM, Bowen BD, *Measurement of ultrasonic forces for particle-liquid separations.* AIChE J. **43**, 1727–1736 (1997).

[162] D. Carugo, D. N. Ankrett, P. Glynne-Jones, L. Capretto, R. J. Boltryk, X. Zhang, P. A. Townsend, and M. Hill, *Contrast agent-free sonoporation: The use of an ultrasonic standing wave microfluidic system for the delivery of pharmaceutical agents.* Biomicrofluidics **5**(4), 044108 (2011).

[163] V. Dvořák, *Ueber die akustische Anziehung und Abstossung*. Ann. Phys. Chem. **157**, 42–72 (1876).

[164] T. Wang, E. Trinh, A. Croonquist, and D. Elleman, *Shapes of rotating free drops: Spacelab experimental results*. Phys. Rev. Lett. **56**(5), 452–455 (1986).

[165] J. Rooney, C. Smith, and R. Carey, *Acoustic streaming in superfluid-helium*. J. Acoust. Soc. Am. **72**(1), 245–249 (1982).

[166] G. Vishwanathan and G. Juarez, *Steady streaming flows in viscoelastic liquids*. J. Non-Newton. Fluid **271**, UNSP 104143 (2019).

[167] I. A. Ramadan, H. Bailliet, and J.-C. Valiere, *Experimental investigation of the influence of natural convection and end-effects on Rayleigh streaming in a thermoacoustic engine*. J. Acoust. Sos. Am. **143**(1), 361–372 (2018).

[168] J. G. Kaufmann, M. P. Y. Desmulliez, Y. Tian, D. Price, M. Hughes, N. Strusevich, C. Bailey, C. Liu, and D. Hutt, *Megasonic agitation for enhanced electrodeposition of copper*. Microsyst. Technol. **15**(8), 1245–1254 (2009).

[169] K. Sritharan, C. Strobl, M. Schneider, A. Wixforth, and Z. Guttenberg, *Acoustic mixing at low reynold's numbers*. Appl Phys Lett **88**(5), 054102 (2006).

[170] S. K. R. S. Sankaranarayanan, S. Cular, V. R. Bhethanabotla, and B. Joseph, *Flow induced by acoustic streaming on surface-acoustic-wave devices and its application in biofouling removal: A computational study and comparisons to experiment*. Phys. Rev. E **77**, 066308 (2008).

[171] P. Marmottant and S. Hilgenfeldt, *Controlled vesicle deformation and lysis by single oscillating bubbles*. Nature **423**(6936), 153–156 (2003).

[172] John D'Errico. Matlab file exchange (2012), https://www.mathworks.com/matlabcentral/fileexchange/8277-fminsearchbnd-fminsearchcon (2019).

[173] R. P. Moiseyenko and H. Bruus, *Whole-system ultrasound resonances as the basis for acoustophoresis in all-polymer microfluidic devices*. Phys. Rev. Applied **11**, 014014 (2019).

[174] L. Olesen, F. Okkels, and H. Bruus, *A high-level programming-language implementation of topology optimization applied to steady-state Navier-stokes flow*. Int. J. Numer. Meth. Eng. **65**(7), 975–1001 (2006).

[175] P. Augustsson and T. Laurell, *Acoustofluidics 11: Affinity specific extraction and sample decomplexing using continuous flow acoustophoresis*. Lab Chip **12**(10), 1742–1752 (2012).

[176] M. Engholm, H. Bouzari, T. L. Christiansen, C. Beers, J. P. Bagge, L. N. Moesner, S. E. Diederichsen, M. B. Stuart, J. A. Jensen, and E. V. Thomsen, *Probe development of CMUT and PZT row-column-addressed 2-D arrays*. Sensors and Actuators A: Physical **273**, 121–133 (2018).